Modelling, Simulation and Experimental Characterization of T-Jets Reactors

Ph.D. Dissertation
in
Chemical and Biological Engineering
by

Mohamed Ashar Sultan Mohamed Yousuf

Supervisors

Ricardo Jorge Nogueira dos Santos

José Carlos Brito Lopes

Laboratory of Separation and Reaction Engineering
Departamento de Engenharia Química
Faculdade de Engenharia
Universidade do Porto

January 2013

Acknowledgments

I would like to express the deepest appreciation and sincere gratitude to the people whose contribution was of immense importance in the completion of this work.

- Professor José Carlos Lopes, my Research advisor, for his guidance, support during this course of the work and giving an opportunity to be part of this Mixing Group.
- Dr. Ricardo Santos, my Research advisor, for his guidance, support, patience, time and effort during this course of this work and being a friend and inviting me to be part of this group.
- Professor Madalena Dias for the review of my work during my course of this thesis and for support and suggestions.

Without their persistent guidance who one way or another contributed and extended their valuable assistance in the preparation and completion of this thesis.

I wish to thanks Professor Alírio Rodrigues director of LSRE where this work carried out.

I would like to give special thanks to my friend and colleague Claudio Fonte and Kateryna Krupa, for their help, support and discussion during my experimental work.

I would like to thank Carlos Fonte, Anna Maria Karpsinka, Nuno Gomes, Marina V. Torres, Paulo Gomes, Ertugrul Erkoc, and Angela Novais, Enis Leblebici, for their help and friendship.

These people have shared valuable insights in the relevance of this study not just in the technology sector.

I would like to thank Telmo Santos for providing data acquisition part for this work.

I would like to thank Susana Cruz for providing administration support throughout the PhD.

I would like to thank Professor Tariq Mahmud, University of Leeds, U.K. whose advice and suggestion paved my way to Portugal to pursue my PhD.

I sincerely thank and acknowledge my Ph.D. scholarship by FCT- Fundação para a Ciência e a Tecnologia SFRH/BD/43879/2008.

To my family

“Be the change that you wish to see in the world .”- Mahatma Gandhi

Abstract

Mixing in T-jets reactors is studied using Planar Laser Induced Fluorescence (PLIF), 2D and 3D Computational Fluid Dynamics (CFD) simulation and test chemical reactions. The influence of geometrical and operational parameters on the flow regime in T-jets mixers is characterised. The following particular geometrical parameters are studied in ranges that are not available in the literature: mixing chamber width to the injectors width (W / w) ratio; mixing chamber width to the mixing chamber depth (W / d) ratio.

It is shown that the two geometrical parameters, (W / w) and (W / d) have an impact on the flow dynamics as important as the jets Reynolds number that here studied over a range of values from 50-600. The values of the geometrical and operational parameters that onset the transition of flow regime in the T-jets mixers are reported, and the impact of the geometry on such transition is analysed both experimentally and through CFD simulation. For the first time a particular flow regime in T-jets mixers, known as self-sustainable chaotic flow regime has been reported from experimental work and 3D CFD. Previously this flow regime identification was restricted to works with 2D CFD simulations. The main characteristics of the studied flow regimes are related with the mixing efficiency in the T-jets mixers.

The product distribution of the fast chemical reaction was used for the characterisation of micromixing in T-jets mixers. The geometrical parameters and operational parameter have a critical impact on the product distribution of the test reaction. Micromixing is shown to be related to the flow regime in each geometry and operational conditions, and the test reaction results are related to results from PLIF experiments. The results obtained show that for all the geometries mixing is enhanced at flow rate ratio close to unity, at larger Reynolds numbers and at larger (W / w) ratios and smaller (W / d) ratios.

The knowledge gathered on the effect of each geometrical parameter is applied on the definition of a new scale-up procedure that increases the T-jets throughput without compromising mixing.

Resumo

A mistura em reatores de jatos em T é estudada com a técnica experimental de *Planar Laser Induced Fluorescence* (PLIF), com simulações 2D e 3D com códigos de *Computational Fluid Dynamics* (CFD) e através de reações teste de micromistura. A influência de parâmetros operacionais e geométricos no regime de escoamento em misturadores de jatos opostos é caracterizada. Os seguintes parâmetros geométricos são estudados em gamas que não estavam disponíveis na literatura: razão entre a largura da câmara de mistura e da largura dos canais de entrada (W/w); e razão entre a largura da câmara de mistura e a profundidade da câmara (W/d).

É demonstrado que os dois parâmetros geométricos estudados, (W/w) e (W/d), têm um impacto significativo na dinâmica do escoamento, tão importante como o impacto do número de Reynolds na gama coberta nesta tese de 50-600. São reportados os valores dos parâmetros geométricos e operacionais que marcam a transição de regime de escoamento em misturadores de jatos em T, bem como é estudado experimental e numericamente o impacto dos parâmetros geométricos na referida transição. Nesta tese é reportado através de dados experimentais e de simulações numéricas tridimensionais pela primeira vez um regime caótico autossustentável em misturadores de jatos em T. Anteriormente este regime apenas estava identificado através de resultados de simulações bidimensionais. É estabelecida uma relação entre os regimes de escoamento e a eficiência de mistura nestes reatores.

A distribuição do produto duma reação química rápida foi usada para caracterizar a micro mistura em misturadores de jatos em T. Os parâmetros geométricos têm um impacto muito claro na distribuição de produtos da reação teste. A micromistura é relacionada com o regime de escoamento para cada geometria e condição de operação previamente caracterizada através de resultados experimentais de PLIF. Os resultados de com a reação teste de micromistura mostram que a mistura aumenta para maiores razões de (W/w) e menores razões de (W/d), e que independentemente da geometria a mistura aumenta com o número de Reynolds e com a operação do reator com razões de caudais entre os jatos opostos pertos da unidade. Os resultados do estudo da influência dos parâmetros geométricos na mistura em reatores de jatos em T, são usados para estabelecer um procedimento para aumento da produção destas unidades sem alteração das características da mistura.

Table of Contents

Table of Figures

Page

Table of Tables

Page

Notation

A	surface area [m^2]
C_A	local concentration of the species A [mol/m^3]
D_m	molecular diffusivity [m^2/s]
D_{vortex}	vortex diameter [m]
Dh_{in}	hydraulic diameter of the of the injectors/inlet channels [m]
D_H	hydraulic diameter of the mixing chamber [m]
d	depth of the T-jets mixers [m]
$F(\phi)$	is the generic function of ϕ
f	cell face
g	acceleration of gravity [m/s^2]
$\vec{g}$	gravitational acceleration vector [m/s^2]
H	height of the mixing chamber [m]
h	distance of injectors/inlet channels from the top of the mixing chamber [m]
I_s	intensity of segregation
K	identification number
L	length of the inlet jet [m]
l	length of the mixing chamber [m]
M	intensity of mixing
N_{faces}	number of faces
N_{xy}	total number of nodes in a 2D simulation
p	pressure [Pa.s]
q	volumetric flow rate [m^3/sec]
$q_{chamber}$	volumetric flow rate of the mixing chamber [m^3/s]
q_{inj}	volumetric flow rate of the injector [m^3/s]
Re	jets Reynolds number
Re_{Hjet}	hydraulic Reynolds number of the jets
Re_H	hydraulic Reynolds number of the mixing chamber
s_{ij}	fluctuating rate of strain
Sc	Schmidt number
t	time [s]
t_{mix}	time of mixing [s]
υ_{inj}	injector velocity [m/s]
$\upsilon_{chamber}$	mixing chamber velocity [m/s]
V	cell volume [m^3]
$V_{chamber}$	volume of the mixing chamber [m^3]
$V_{3Dvortex}$	vortex volume [m^3]
w	inlet injector width [m]

W	mixing chamber width [m]
W / w	ratio of mixing chamber width to jets width
W / d	ratio of mixing chamber width to depth
y	length of the mixing chamber through y direction [m]

Greek letters

α	first parameter of the identification number K
β	second parameter of the identification number K
γ	third parameter of the identification number K
ε	turbulent energy dissipation rate [m^2/s^3]
ζ	fourth parameter of the identification number K
λ	geometrical scaling factor
λ_k	Kolmogorov scale [m]
$\sigma^2_{C_A}$	variance of chemical species A
σ_A	standard deviation of chemical species A
σ_B	standard deviation of chemical species B
σT	standard deviation of fluid temperature
σ_x	standard deviation of the velocity x component
ΔT	temperature difference between the two inlet fluid [℃]
ϕ	scalar quantity
$\nabla\phi$	gradient of ϕ
$\nabla\phi_f$	gradient of ϕ at face f
Γ_ϕ	diffusion coefficient ϕ [m^2/s]
τ	passage time in the mixing chamber [s]
τ_{zz}	normal stress [Pa]
μ	viscosity [Pa.s]
ρ	density [kg/m^3]
ν	kinematic viscosity [m^2/s]
ω	vorticity [s^{-1}]
ω_y	y vorticity [s^{-1}]
ω_z	z vorticity [s^{-1}]

Indices

*	dimensionless variable
2D	for the 2D chamber
3D	For the 3D chamber
A	chemical species A
B	chemical species B
R	chemical species R
S	chemical species S
inj	at the injectors/inlet

Abbreviations

CFD	Computational Fluid Dynamics
DFT	Discrete Fourier Transform
DNS	Direct Numerical Simulation
EFD	Experimental Fluid Dynamics
FFT	Fast Fourier Transform
LIF	Laser Induced Fluorescence
PLIF	Planar Laser Induced Fluorescence
PIV	Particle Image Velocimetry
RTD	Residence Time Distribution
TEM	Transmission Electron Microscopy
AFM	Atomic Force Microscopy
DIN	Deutsches Institut für Normung (German Institute for standardization)
CNC	Computer Numerical Control

1. INTRODUCTION

1.1 Mixing Process and Its Importance

Mixing is one of the most important unit operations in the chemical, biological, pharmaceutical and food industries. Mixing is often the limiting step in a reactor design, for example when the chemical reaction is too fast and so the reaction time is shorter than the mixing time, or in the cases of very viscous fluids where mixing generally takes place under laminar flow regimes. Mixing covers the transfer of mass under a wide range of flow regimes, fluid types and geometries. In this work only single-phase mixing of liquids in opposed jets reactors is considered. The two most important mechanisms involved in mixing are convection and diffusion which includes molecular diffusion and eddy diffusion. The phases involved in mixing are of three scales:

- Macromixing is the mixing phenomenon associated with the large scale fluid motion also termed as convective mixing related to the mean concentration and concentration distribution throughout the reactor, generally assessed from the Residence Time Distribution (Bourne, 1997; Nguyen, 2007; Santos 2003). Macromixing is associated with overall circulation of fluid or particles in a reactor and so the typical scale is generally the reactor scale.
- Micromixing involves mixing of fluid in smallest scale referred as the molecular scale. (Nguyen, 2007). The homogenization of concentrations at the molecular scale is

the step that limits the chemical reaction, and so test chemical reactions are used to quantify micromixing. Micromixing is associated to Kolmogorov and Batchelor scales.

- Mesomixing is defined by some authors as the phenomenon between macromixing and micromixing scales, for example vortices that are much larger than the Kolmogorov scale but still much smaller than the reactor scale.

Therefore it could be summarized as: micromixing deals with homogenization of the fluid mixture at the smallest scales by small eddies and diffusion; macromoxing involves mixing with large circulation patterns around the reactor.

The widely used practice for mixing in industrial processes is the usage of tanks equipped with impellers or agitators. These mixers have limitations of high-energy consumption that is generally injected to a limited region of the tank, and fluid elements with very different ages are all being mixed in the same take, which makes the control of mixing poorer, and can lead to secondary often undesired products. Sometimes these limitations compromise the feasibility of a process. Opposing jets mixers which includes micro-scale devices, microreactors, etc., which promote direct contact of the reactant feed streams, can overcome most of these limitations, thus making several processes economically feasible, namely for the production of nanoproducts. Opposing jets mixers have been introduced in chemical engineering, mainly over the last two decade and preferred due to its simple geometry and operation. The advent of micromixers (Hessel and Löwe, 2003a, b, c) has been one of the major driving forces for the dissemination of this type of mixers.

1.2 Opposed Jets Reactors

Opposed jets reactors are devices consisting of two inlet jet streams that are impinged onto each other in a confined chamber. The main advantage of these reactors is the direct contacting of two pure streams of reactant that are mixed with times of the order of milliseconds (Liu and Fox, 2006). Opposed jets reactors geometries are generally of two types: cylindrical chamber geometries with round injectors (**Figure 1.1**a) generally referred to as confined impinging jets (CIJ) reactors (Santos et al., 2005; Johnson and Prud'homme., 2003); and prismatic chamber reactors with rectangular injectors (**Figure 1.1**b), generally referred in the literature as T-jets mixers (Wong et al., 2004 and Hoffman et al., 2006, Adeosun and Lawal., 2009).

The main difference between the two opposed jets reactors are their flow structure (Santos et al., 2010). In CIJ reactors, after the streams impinge onto each other, the jets spread around into a circle normal to the jets, a pancake like structure (Wood et al., 1991); vortices are formed immediately upstream and downstream of jets engulfing fluids in this pancake. In T-jets reactors after jets impingement, the jets bend $90°$ towards the outlet and flow with minimum deceleration. In upstream of jets impingement two vortices are formed, but only few particles break away from the injectors jet to the upper vortices.

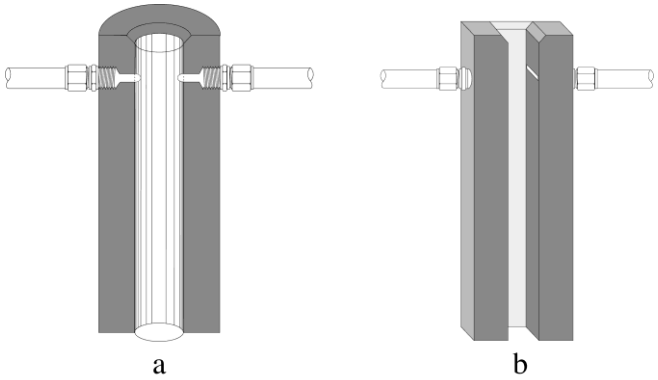

Figure 1.1 Schematic representation of opposed jets reactors: (a) cylindrical geometry (b) prismatic geometry.

Mixing in opposed jets reactors depends on many parameters, such as the momentum ratio of the jets, the jets Reynolds number and the chamber to injectors width or diameter ratios depending if the chamber geometry is prismatic or cylindrical, respectively. While these parameters have been characterized extensively for cylindrical geometries that were introduced for polymer processing since the 1970s (Keuerleber and Pahl, 1972) namely at LSRE over the last decade (Santos et al., 2002, 2003, 2005; Teixeira et al., 2005), on T-jets mixers most of the effect of these parameters remains unknown or unclear from different authors, as will be seen from the state of the art review in **Chapter 2**.

1.3 T-jets Mixers: Principle and Scope

In this Ph.D. thesis, the focus will be on the reactive processes in continuous Opposing Jets Reactor (OJR) namely having T-jets planar geometry shown in **Figure 1.2**. T-jets mixers are becoming increasingly studied with the wide spreading of microreactors in industrial applications. One of the main drivers for these reactors is the growing demand for nanoparticles in the market (BCC research, 2012) and consequently one of the big challenges nowadays is their production from continuous processes yielding large volumes of nanoparticles (Masala and Seshadri, 2004). This has led to the development in mixing

technologies with enhanced functionalities to meet the present demand in process industries especially in the nanoparticle production in continuous form (Silva et al., 2008). A continuous reactor already used in nanoparticles production is the T-jets reactor (Gradl et al., 2006; Gradl and Peukert, 2009).

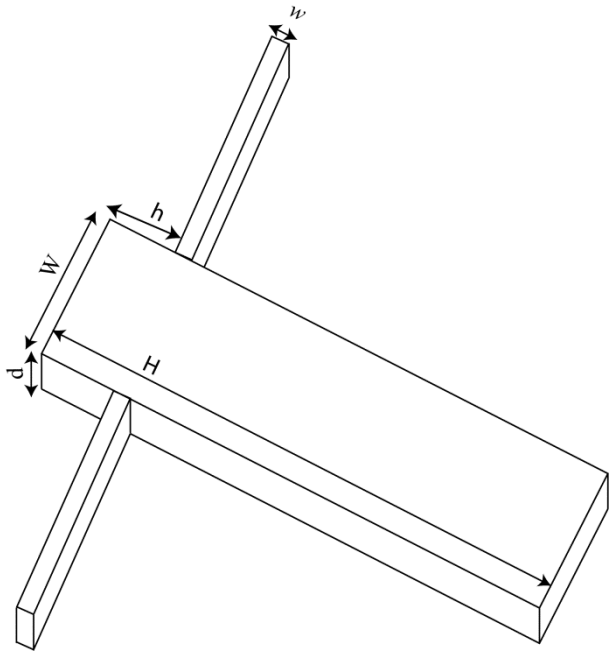

Figure 1.2 Schematic Representation of T-jets mixer.

The design of micromixers in general and of the T-jets mixers in particular, is a trade-off between several parameters, such as mixing time, pressure drop, reactor volume, throughput, feasibility of microfabrication, and integration with chemical detection devices (Jensen, 2001). The term microreactor refers to the systems or mixers with characteristics length scales that are in the micrometer range. The design of T-jets mixers in particular has more distinct advantages than other regular mixers for miniaturization: the absence of moving mechanical parts and the feasibility of this geometry to be constructed by most micro fabrication technologies. Due to small dimensions of the mixers, the flow behaviour are often controlled by viscous force relative to inertia (Brody et al., 1996), in this case the typical scale of mixing is half the width of the mixing chamber. Convective mixing patterns can occur in a T-jets mixer decreasing the thickness of the reactants laminae, which have a thickness equal to the width of the jets initially. The faster the thinning of the initial laminae the earlier the initially segregated fluids mix, yielding a higher local concentration, which is a key factor on the control of nanoparticles properties (Gradl et al., 2006). The path followed to assure the reduction of the initial scales is the miniaturization of the T-jets mixers that went down to the

micrometric scale many micro reactors are based on T-jets mixers geometries (Nguyen and Wu, 2005 and Mansur et al., 2008), but this compromises the reactors throughput. One of the main contributions of this thesis is on the study of the effect of several geometrical parameters and the results of this study offer new prospects for the scale up of micro-reactors.

1.4 Objectives and Thesis Organization

The scale issue is the main subject of this thesis. This work presents a study of the effect of the geometrical parameters of T-jets mixers and operational parameters on flow regimes and mixing using Experimental Fluid Dynamics (EFD) and Computational Fluid Dynamics (CFD) approaches.

There are very few works done in this area as can be seen in **Chapter 2** where the literature on T-jets mixers and its state of art is comprehensively reviewed and discussed. There the effect of operational and design parameters such as the momentum ratio of the jets, the jets Reynolds number and the chamber to injectors width ratio and depth of the geometry based on work of several authors is presented. From the literature, four different flow regimes are identified for T-jets mixers and the quantification of mixing in these flow regimes will be explained and summarised.

Chapter 3 comprises the hydrodynamic studies in the T-jets mixers using the experimental technique Planar Laser Induced Fluorescence (PLIF) to assess the dependence of mixing and flow regime on the mixers geometry, such as the ratio of the width of the chamber to the width of the injectors and the ratio of the width of the chamber to the chamber depth. Furthermore, operational parameters such as the Reynolds number will also be studied. Eight geometries covering several of the aforementioned geometrical parameters will be tested and studied and the mixing in these T-jets mixers will be quantified using the intensity of segregation that was originally defined by Danckwerts (1952). With this work, a new flow regime will be identified and reported. The main purpose of this study will be to compare the experimental study with the CFD simulations and predict the nature of flow in the mixer.

In **Chapter 4**, the flow in T-jets mixer is studied, first with 2D CFD simulations aiming to understand the flow mechanisms yielding different flow regimes at a fixed Reynolds number of 600 by sweeping the wide range of geometrical parameters similar to the experimental study with particular focus on chamber and inlet jets width. Then in order to study the effect

of depth and to get detail insight into the T-jets mixers, 3D CFD simulations are performed at different Reynolds numbers. The fact that from these CFD simulations time histories and the flow field are instantaneously derived gives the immediate relationships between typical flow frequencies and flow structures and enables a greater insight into the dynamic behaviour of the system. The mass transfer mechanism is then incorporated into 3D CFD simulation to give a greater degree of comprehension of the role played by the flow field and the geometrical and operational parameters in the T-jets mixers.

In **Chapter 5**, mixing in the T-jets mixers is experimentally and computationally studied through a test chemical reaction (Bourne et al., 1985). With experimental study the selectivity of the consecutive competitive chemical reaction introduced by Bourne et al. (1985) for mixing assessment is studied with different T-jets mixers. 2D CFD simulation was coupled to the chemical reaction introduced by Bourne et al. (1985), the numerical results were compared with experiments and found to be in good agreement.

Finally, in **Chapter 6**, based on the results of simulation and experimental observations made in this course of work, the knowledge gained on the influence of the operational and geometrical parameters for the T-jets mixers are presented. In addition, several conclusions about the mixing mechanism in the T-jets mixers are summarized and future paths to this investigation are proposed.

1.5 References

Adeosun, J.T., Lawal, A., 2009. Numerical and experimental studies of mixing characteristics in a T-junction microchannel using residence-time distribution. Chemical Engineering Science 64, 2422-2432.

BCC research, 2012. “Nanotechnology a realistic market assessment”. http://www.bccresearch.com/report/NANO31E.html

Bourne, J. R., 1997. Mixing in single-phase Chemical reactors. Mixing in the process industries, Nienow, A. W., et al. (ed.), Butterworth-Heinemann, Oxford.

Brody, J.P., Yager, P., Goldstein, R.E., Austin, R.H.,1996.Biotechnology at low Reynolds numbers. Biophysical journal 71, 3430-3441.

Danckwerts, P.V.,1952. The definition and measurement of some characteristics of mixtures. Applied Scientific Research 3, 279-296.

Gradl, J., Schwarzer, H.-C., Schwertfirm, F., Manhart, M., Peukert, W., 2006. Precipitation of nanoparticles in a T-mixer: Coupling the particle population dynamics with hydrodynamics through direct numerical simulation. Chemical Engineering and Processing 45, 908-916.

Gradl, J., Peukert, W., 2009. Simultaneous 3D observation of different kinetic subprocesses for precipitation in a T-mixer. Chemical Engineering Science 64, 709-720.

Hessel, V., Löwe, H., 2003a. Microchemical Engineering: Components, Plant Concepts User Acceptance - Part I. Chemical Engineering & Technology 26, 13-24.

Hessel, V., Löwe, H., 2003b. Microchemical Engineering: Components, Plant Concepts, User Acceptance - Part II. Chemical Engineering & Technology 26, 391-408.

Hessel, V., Löwe, H., 2003c. Microchemical Engineering: Components, Plant Concepts, User Acceptance - Part III. Chemical Engineering & Technology 26, 531-544

Hoffmann, M., Schlüter, M., Räbiger, N., 2006. Experimental investigations of liquid-liquid mixing in T-shaped micro-mixers using μ-LIF and μ-PIV. Chemical Engineering Science 61, 2968-2976.

Jensen, K.F., 2001. Microreaction engineering-is small better? Chemical Engineering Science 56, 293-303.

Johnson, B.K., Prud'homme, R.K., 2003. Chemical processing and micromixing in confined impinging jets. AIChe Journal 49, 2264-2282.

Keuerleber, R., Pahl, F., 1972. Device for feeding flowable material to a mold cavity. Krauss-Maffei, United States patent, 3706515.

Liu, Y., Fox, R. O., 2006. CFD predictions for chemical processing in a confined impinging-jets reactor. AIChe 52, 731-744.

Mansur, E. A., Wang, M. Ye. Y., Dai, Y., 2008. A State-of-the-Art Review of Mixing in Microfluidic Mixers. Chinese Journal of Chemical Engineering 16, 503-516.

Masala, O., Seshadri, R., 2004. Synthesis routes for large volumes of nanoparticles. Annual Review of Materials Research 34, 41-81.

Nguyen, C.T., Desgranges, F., Roy, G., Galanis, N., Mare, T., Boucher, S., Angue Mintsa, H., 2007. Temperature and particle-size dependent viscosity data for water-based nanofluids - Hysteresis phenomenon. International Journal of Heat and Fluid Flow 28, 1492-1506

Nguyen, N.T., Wu, Z., 2005. Micromixers-a review. Journal of Micromechanics and Microengineering 15(2), R1.

Santos, R.J., Teixeira, A.M.T., Costa, M. R. P. F. N., Lopes, J.C.B., 2002. Operational and Design Study of RIM Machines. International Polymer Processing 17, 387-394.

Santos, R. J., 2003. Mixing Mechanisms in Reaction Injection Moulding - RIM. An LDA/PIV Experimental Study and CFD Simulation. Departamento de Engenharia Química, Porto, Universidade do Porto.

Santos, R.J., Teixeira, A.M.T., Lopes, J.C.B., 2005. Study of mixing and chemical reaction in RIM. Chemical Engineering Science 60, 2381-2398.

Silva, V.M.T.M., Quadros, P.A., Laranjeira, P.E.M.S.C., Dias, M.M., Lopes, J.C.B., 2008. A Novel Continuous Industrial Process for Producing Hydroxyapatite Nanoparticles. Journal of Dispersion Science and Technology 29, 542-547.

Teixeira, A. M., Santos, R.J., Costa, M. R. P. F. N., Lopes, J.C.B., 2005. Hydrodynamics of the Mixing Head in RIM: LDA Flow-Field Characterisation. AIChE Journal 51(6), 1608-1619.

Wood, P., Hrymak, A.N., Yeo, R., Johnson, D.A., Tyagi, A., 1991. Experimental and Computational Studies of the Fluid Mechanics in an Opposed Jet Mixing Head. Physics of Fluids A 3, 1362-1368

Wong, S.H., Ward, M.C.L., Wharton, C.W., 2004. Micro T-mixer as a rapid mixing micromixer. Sensors and Actuators B 100, 359-379.

2. STATE OF THE ART ON T-JETS MIXERS

2.1 Introduction

In T-jets mixers, the most important parameter affecting mixing is the operation flow regime (Bothe et al., 2006; Soleymani et al., 2008a; Sultan et al., 2012 and Krupa et al., 2012). Due to the scale of most T-jets reactors, the Reynolds number associated with the flow regime is low and so most of the operation flow regimes are laminar. One of the most important parameters for the flow regime is the Reynolds number, Re, which can be defined as (Sultan et al., 2012)

$$Re = \frac{\rho w \upsilon_{inj}}{\mu} \tag{2.1}$$

where w is the width of the inlet jets, υ_{inj} the average velocity of the jets and ρ and μ the density and viscosity of the fluid, respectively. The definition of Reynolds number in T-jets is not universal, unlike the case of opposed jets with cylindrical geometries where all authors use the definition introduced by Malguarnera and Suh (1977). Some authors use the velocities in the mixing chamber and the hydraulic diameter of the mixing chamber to define the Reynolds number (Bothe et al., 2006; Soleymani et al., 2008a; Engler et al., 2004)

$$Re_H = \frac{\rho D_H \upsilon_{chamber}}{\mu} \tag{2.2}$$

where D_H is the hydraulic diameter of the mixing chamber, $\upsilon_{chamber}$ is the averaged velocity of the fluid in mixing chamber and ρ and μ the density and viscosity of the fluid, respectively. The hydraulic diameter is defined as

$$D_H = 4\frac{W\,d}{2(W+d)} \tag{2.3}$$

where W is the mixing chamber width and d is the depth. Because this definition of Reynolds number, Re_H, is the most common in literature in this chapter this is always the used definition. Later, in the chapter where results from this thesis are presented, the definition is the one in Equation (2.1). This was made in order to keep coherence between the present work and past works in the LSRE made with 2D CFD simulations that were the main motivation for this study (Santos et al., 2002, 2003, 2005, 2010; Teixeira et al., 2005).

Although many of the studies made on T-jets mixer focus mainly on the influence of Reynolds number on the flow features, the geometric parameters and other operation parameters also play a key role. In this chapter the different flow regimes in T-jets mixers will be characterized from the published literature; these studies have been performed using experimental techniques and Computational Fluid Dynamic (CFD) simulations. The studies on T-jets mixers have generally two objectives: a) characterize the mixing for each reactor at each specific flow regime and b) identify the design and operational parameters that determine the flow regime. **Table 2.1** and **Table 2.2** show the list of the studies concerning the mixing efficiency of T-jets mixers and effects of process and design conditions, which will be reviewed in the coming sections. Different operational conditions and reactor designs can be compared by the degree of mixing achieved in these devices.

Table 2.1. Summary of list of studies from different authors in T-jets mixers.

Author	Re_H	Re	W µm	w µm	d µm	Method	Flow regimes
Bothe, et al. 2006 and Bothe, et al. 2008	40	30	200	100	100	CFD	Segregated
	138	104					Vortex
	186	140					Engulfment
Bothe, et al. 2006	40	30	200	100	100	Experimental	Segregated
	138	104					Vortex
	186	140					Engulfment
Bothe, et al. 2010	40	30	200	100	100	CFD-Chemical reaction	Segregated
	138	104					Vortex
	186	140					Engulfment
Wong et al. 2004	50 - 1400	27 - 1200	200	100	82	Experimental	Segregated and Cross
			200	100	51		
			100	50	51		
			60	30	51		
Wong et al. 2004	489	362	100	50	51	CFD - steady	Segregated
	489[1]	362					Vortex
	121[1]	89.6					Segregated
	489	362					Segregated
	489[2]	362					Engulfment
	489[1]	362					Engulfment
Soleymani et al (2008a)	12	9	600	300	300	CFD	Segregated
	80	60					Vortex
	240	180					Engulfment
	120	1030	600	300	18	CFD	Segregated
		101			252		Vortex
		82			348		Engulfment
Soleymani et al (2008a)	2 - 308	2 - 231	600	300	300	Experimental	Segregated, Vortex and Engulfment mixing
			300	150	600		
Soleymani et al (2008b)	132	209	1600	400	300	CFD	Engulfment
	241.2	261	1000	500	300		
	270	135	200	200	200		
	273	137	300	300	300		
	278	139	100	100	100		
	477.2	358	200	200	100		
	141.3	71	400	400	400		

Table 2.2. Summary of list of studies from different authors in T-jets mixers.

Author	Re_H	Re	W µm	w µm	d µm	Method	Flow regimes
Hoffmann et al 2006	50 - 160	30 - 96	400	100	285	Experimental	Segregated
							Vortex
							Engulfment
Hoffmann et al 2006	242	121	200	100	200	Experimental	Engulfment
Hoffmann et al 2006	242	182	200	100	100	Experimental	Engulfment
Hoffmann et al 2006	186	140	200	100	100	CFD	Engulfment
Ito et al. 2006	6.7	3	500	1000	500	Experimental-Vibration Technique Applied	Chaotic Mixing
	67	34	500	1000	500		
	1.3	1	100	1000	100		
	6.7	3	100	1000	100		
	33	17	100	1000	100		
Engler et al.2004	7	5	600	300	300	CFD-ACE	Segregated
	60	45					Vortex
	199	149					Engulfment
Engler et al.2004	6.6 and 32	5 to 24	600	300	300	Experimental	Segregated
	60 and 142	45 and 107					Vortex
	157 and 199	118 and 149					Engulfment
Engler et al.2004	87	138	1600	400	300	Experimental	Engulfment
	235	255	1000	500	300		
	271	407	1000	500	200		
	147	110	600	300	300		
	75	56	400	200	200		
	135	101	200	100	100		
Schwarzer et al. 2006	250 and 15000	125 and 7500	1000	1000	1000	Experimental	Turbulent mixing

[1] – the jets have a non-zero velocity component on the direction of the chamber depth
[2] – dissimilar viscosities
W = Width of the mixing chamber
w = Width of the inlet jet
d = depth of the complete geometry

2.2 Quantification of Mixing

In this section, some experimental and computational works to determine the impact of operational and design parameters on the flow regimes in T-jets mixers are presented. Different operational conditions and reactor designs can be compared by the degree of mixing achieved in these devices. Although the most common quantification of mixing on the basis of tracer concentration spatial distribution is the intensity of segregation defined by Danckwerts (1952), not all authors used this definition or definitions that are related to it. Being that the case, before reviewing the literature on mixing in T-jets a quick review of the methods used to quantify mixing in these mixers is here made.

The quantification of mixing in the T-jets mixers was evaluated with the intensity of segregation (Danckwerts, 1952), I_s by a number of authors, namely Bothe et al. (2006, 2008), Hoffmann et al. (2006), and Sultan et al. (2012), according to the definition

$$I_s = \frac{\sigma_{C_A}^2}{\overline{C_A}(1-\overline{C_A})} \tag{2.4}$$

where C_A is the local concentration of the species A at each point in the probed line, $\sigma_{C_A}^2$ is

$$\sigma_{C_A}^2 = \overline{(C_A - \overline{C_A})^2} \tag{2.5}$$

Bothe et al. (2008) and Hoffmann et al. (2006) also used equivalent quantities to the intensity of segregation to determine the influence of the Reynolds number and the mixer dimensions in the degree of mixing achieved in T-jet mixers. As a measure of the impact of molecular diffusion, Bothe et al. (2006) and Hoffmann et al. (2006) used an intensity of mixing.

$$M = 1 - \sqrt{I_S} \tag{2.6}$$

where zero for M corresponds to totally segregated and a value of one corresponds to homogeneous mixture.

Soleymani et al. (2008) and Engler et al. (2004) quantified the mixing with mixing efficiency or quality derived from intensity of segregation. Mixing efficiency, α, is defined as follow

$$\alpha = 1 - \sqrt{\frac{\sigma_{C_A}^2}{\sigma_{C_A\max}^2}} \tag{2.7}$$

where $\sigma_{C_A\max}^2$ is the maximum value of the standard deviation of species A obtained for the less favourable mixing conditions. This definition does not enable the direct comparison of values of intensity of segregation if the $\sigma_{C_A\max}^2$ is not reported.

Tracer was also used to assess macromixing. Santos et al. (2005) and Adeosun et al. (2009) studied the mixing performance on T-jets mixers with CFD numerical simulation and characterised the flow behaviour with Residence Time Distribution (RTD). Adeosun et al. (2009) also conducted experimental work and compared with CFD tracer simulation for the validation of the numerical work.

Devahastin and Mujumdar (2002) and Srisamran and Devahastin (2006) performed numerical simulation to solve the time-dependent conservative equation for mass, momentum and energy of 2D laminar for a T-jet mixer. For the purpose of studying the mixing performance of the mixer with different operational and geometrical parameters they introduced the mixing index not based on the concentration of a tracer but on another scalar, the temperature, and define the mixing index $\left(\frac{\sigma T}{\Delta T}\right)$, which was based on temperature as it was employed as the tracer. Here the σT is the standard deviation of the fluid temperature and across the channel depth ΔT, is the temperature difference between the two inlet fluid. In this case when mixing is complete $\sigma T = 0$.

Other authors quantified mixing from chemical reaction. Aoki et al. (2006) quantified the mixing performance of the T-jets mixer with a parallel-competitive chemical reaction system called Villermaux/Dushman reaction. The mixing performance of the geometry was validated with the UV absorption of the end product obtained at the mixing outlet. Krupa et al. (2012) characterised micromixing in the T-jet mixers with Bourne test reactions with the selectivity, which was used to quantify the degree of mixing. Schwarzer et al. (2006) studied the precipitation of nanoparticle system that is sensitive to mixing, the barium sulphate. Mixing affects many of the BaSO4 properties (Steyer and Sundmacher, 2009). This work reports the

effect of mixing in more than one property. The particle size distribution PSD was measured with quasi-elastic light scattering, the specific surface area of dried samples obtained was determined through nitrogen adsorption, the X-ray diffraction and TEM were used for the determination of morphology and the measured sizes were then validated with AFM.

2.3 Flow Regimes Characterization

The flow regime in T-jets mixers has a strong effect on mixing, and this has been studied with several experimental techniques, and with numerical modelling of the flow. These flow regimes depend on many parameters, such as the momentum ratio of the jets, the jets Reynolds number and the chamber to injectors width or chamber width to depth ratios. The following flow regimes are identified in the literature and shown in **Figure 2.1**:

- **Segregated flow regime** - a steady flow regime where two parallel streams of fluid are formed, each stream is fed from each jet, the parallel streams flow from the injectors to the outlet without mixing. Shortly downstream of the jets impingement point the flow paths are all parallel (Aubin et al., 2005). Here mixing is only due to diffusion in the interface between the two streams issuing from each opposed jet. This flow regime occurs at lower Reynolds number, smaller than 100, and was identified in T-jets mixers by (Bothe et al., 2006; Soleymani et al., 2008a; Sultan et al., 2012).
- **Vortex flow -** Above a critical Reynolds number, i.e. Reynolds number at which the flow is no longer parallel, a double vortex pair is built up in each side of the mixing chamber. These vortices are helicoidal and have a rotation axis parallel to the mixing chamber axis. In this regime, symmetry between both sides of the mixing chamber is still maintained. This flow regime occurs at intermediate Reynolds numbers between the segregation flow regime and the engulfment flow regime. Here the mass transfer between both sides of the mixing chamber is diffusion dominated, but in each side of the chamber, there is flow rotation that promotes dragging of fluid between both sides (Bothe et al., 2006; Soleymani et al., 2008, Sultan et al., 2012).
- **Engulfment flow regime** - a flow regime where the flow pattern is not parallel from the inlet to the outlet, there is a rotation of each flow stream that is formed in each side of the chamber. The axis of the flow rotation is parallel to the mixing chamber axis,

i.e. aligned with the main flow direction, and the streams rotate in opposite directions. This rotation transports fluid from one half of the chamber to the other half. This flow regime is particularly clear from the PLIF image of Bothe et al. (2006) and CFD simulations of Soleymani et al.(2008) and is only observed in T-jets geometries.

- **Turbulent flow regime** – dynamic flow regimes where the jets are engulfed by action of the vortices that have a wide range of diameters. Schwarzer et al. (2006) reported this flow regime.

Segregated flow regime

Vortex flow regime

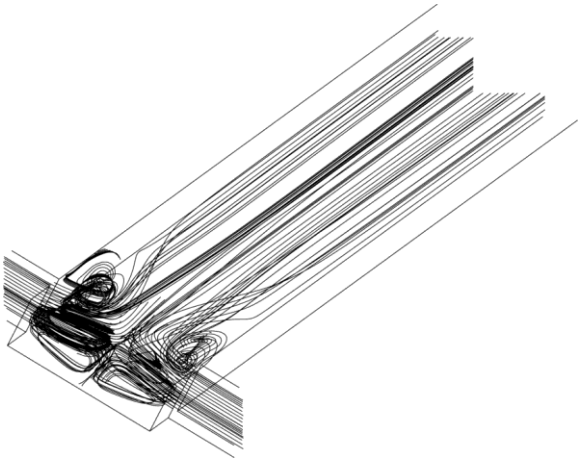

Engulfment flow regime

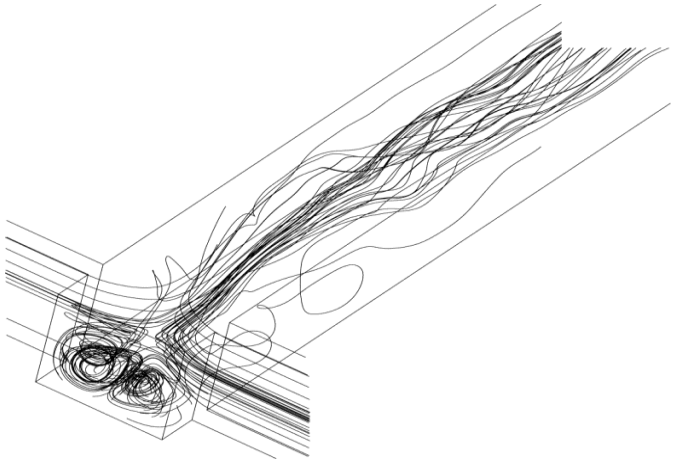

Figure 2.1 Path lines of segregated, vortex and engulfment flow regimes obtained in T-jets mixers from CFD simulation.

Engler et al. (2004) was, according to the surveyed literature the first author to report the three different flow regimes: segregated flow regime, vortex flow regime and the engulfment flow

regime. With experimental and numerical investigation, Engler reported that segregated flow regimes for Reynolds numbers ranging from 0-45; vortex flow regime at Reynolds number ranging from 45-150 and the engulfment flow regime from 150 and above.

For their study, Wong et al. (2004) fabricated the T-jets mixer with silicon substrate and Pyrex glass for the visualisation and observance of the mixing characteristics. They conducted experiments with a blue colour dye and a colourless liquid and with the chemical reaction experiment, namely hydrolysis reaction with dichloroacetyl phenol red (DCAPR) and NaOH solution, a distinct colour arises when the chemicals are completely mixed. Four different T-jets mixer were studied. They observed that for all the four T-jet mixers, a segregated unmixed fluid was visible at the outlet between blue dye and colourless liquid at low Reynolds number of 400 and below. With high Reynolds numbers ranging from 400 to 500 the onset of cross flow of the liquid between both sides of the mixing chamber, engulfment flow regime, this was observed from the blue colour dye that reached the wall in the opposed side of the mixing chamber, which is reported in this work as secondary flow creating vortices.

Bothe et al. (2006) made 3D CFD simulations and tracer experiment with PLIF technique at Reynolds number 40, 138, and 186 with the following dimensions, width of the mixing chamber, $W = 200$ μm , the width of both inlet jets, $w = 100$ μm and the depth of the complete geometry, $d =$ 100 μm. Segregated flow regime was reported at low Reynolds number, $Re_H = 40$, and the vortex flow regime was observed above a critical Reynolds number of 138. Then thereafter at $Re_H = 146$ and above, the transition from vortex to engulfment flow regime occurs. The scale of segregation for lower Reynolds numbers in the segregated flow regime was 200 μm which is the mixing chamber width, and decrease to less than 50 μm for larger Reynolds numbers when the flow turned to vortex flow. Then thereafter at $Re_H = 146$ and above, where transition from vortex to engulfment flow regime occurs the intensity of segregation increases significantly ranging from 0.01 to 0.09 approximately. At $Re_H = 186$, where the engulfment flow regime occurs the intensity of segregation reached a peak of approximately 0.2 and above. They concluded that the engulfment flow regime provides more efficient mixing than the segregated and the vortex regime.

Later, the same group, Bothe et al. (2008), performed 3D numerical simulation for T-jets micro-mixers with similar dimensions and Reynolds number as in Bothe et al. (2006), $W =$ 200 μm, $w = 100$ μm and, $d = 100$ μm. Three similar flow regimes were identified with the numerical simulation: segregated, vortex and engulfment flow regime at Reynolds number 40, 138 and 186.

Hoffmann et al. (2006) reported three different flow regimes for the T-jets mixer with dimensions, width of the mixing chamber, $W = 400$ μm, the width of both the inlet jets, $w =$ 100 μm, and depth, $d = 285$ μm. The three different flow regimes for this particular geometry were namely, segregated, vortex and engulfment flow regime at three Reynolds number ranges $Re_H \leq 50$, $50 \leq Re_H \leq 160$, and $Re_H \geq 160$, respectively

Soleymani et al.(2008a) performed numerical and experimental study of mixing in T-jets mixer. For the numerical simulation, the T-jet mixer with dimensions $W = 600$ μm, $w = 300$ μm and $d =$, $w = 300$ μm. The study was performed with Reynolds number ranging from 15 to 250. Between Reynolds number 15-80 the flow regime was segregated; in the Reynolds number range 80-140, vortex flow regime was observed; and from 140 onward engulfment flow regime occurs. Soleymani et al.(2008a) calculated the mixing efficiency, and the mixing in segregated flow regime was only due to diffusion and as the Reynolds number increases in this flow regime the mixing efficiency decelerates because the residence time decreases. For vortex flow regime mixing efficiency improves ranging from α =25-30 and maximum mixing efficiency occurs at engulfment flow regime starting from α =40 and above. Of all the flow regimes, engulfment flow achieved at high Reynolds number gives very good mixing compared to other flow regimes. The curves of mixing efficiency have the overall shape of the plot in **Figure 2.2** that is reprinted with permission from Soleymani et al. 2008a. Soleymani et al. (2008a) also studied the influence of flow regime on selectivity of fourth Bourne reaction (Baldyga et al., 1998). From the conversion plot the three flow regimes previously identified from PLIF experiments were clear.

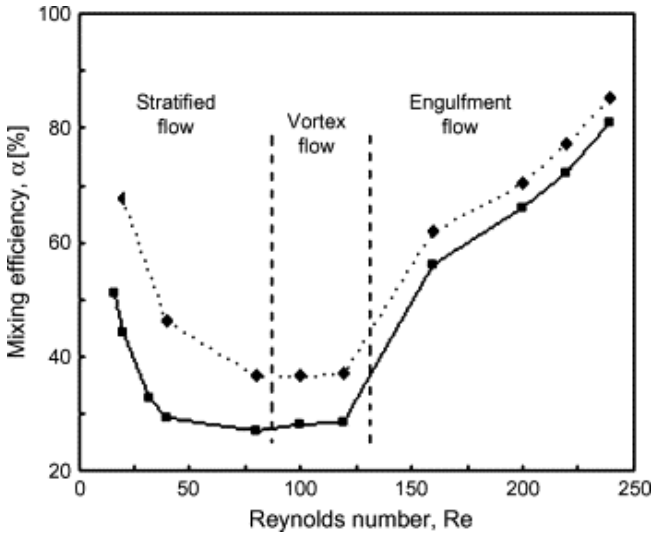

Figure 2.2 Trend showing Mixing efficiency vs. Reynolds number and flow regime. Reprinted with permission from Soleymani et al. 2008a.

Bothe et al. (2010) also studied fast irreversible second order chemical reaction with CFD simulation and identified the three flow regimes previously reported: segregated, at Reynolds number less than 40, vortex for Reynolds number 40 and 138, and engulfment if the Reynolds number is greater than 138 (Bothe et al., 2006, 2008). The PLIF experiment was conducted on T-jets mixer having the ratio 0.45 with dimensions $W = 600$ μm, $d = 270$ μm at $Re_H = 250$ that was reported as engulfment flow regime.

Sultan et al. (2012) characterised different flow fields using PLIF experiments with eight different T-jets mixers geometries. In this work, the influence of two geometrical parameters, ratios of W/w and W/d and operational parameters Re, on the flow field was reported. With the PLIF images, obtained for the eight T-jets mixers having a fixed $W/w = 6$ ratio and varying the depth ratio ranging from $W/d = 1$, 1.5, 2, 3 and 6 for different Reynolds number ranging from 50-600. A particular flow regime, namely self-sustainable chaotic flow regime was reported for the first time from experimental work including other flow regimes such as segregated and vortex flow regime. It was reported that at low Reynolds number for all the T-jets mixers studied the flow was segregated. For geometries having smaller ratio $W/d = 1$, 1.5 and 2 flow regime transition from segregated to chaotic flow regime with the formation of vortices was observed from Reynolds number 100 to 200. For $W/d = 3$ and 6, vortex and segregated flow regime was reported. 3D CFD simulation for a particular case with T-jets mixer dimension $W/w = 6$ and $W/d = 1$, was performed to have a better insight into the

fourth flow laminar regime reported for these mixers, the self-sustainable chaotic flow regime.

In addition to the laminar flow regimes, at larger Reynolds numbers the flow regime of operation is turbulent. Schwarzer et al. (2006) and Gradl et al. (2006) studied T-jets reactors for the precipitation of nanoparticles experimentally and performed simulations based on the population balance model coupled with CFD with barium sulphate and compared experimental and computational results. The Reynolds number was varied from 250 to 15000 and the mean residence time in the mixing chamber was 0.67 to 40 ms. In order to generate intense mixing small geometrical dimensions were preferred and the flow was set to be turbulent, with features differing from the four laminar flow regimes that occur in T-jets mixers as previously discussed. The main difference is the general spread of vortices formation having smaller sizes in the interface of the fluid streams generated from the opposed jets. The transition to turbulent flow was visualized to be around 400 to 500.

Adeosun et al. (2009) studied the macromixing performance in the T-jets mixer with CFD numerical simulation and experimental setup, and characterised the flow behaviour with Residence Time Distribution (RTD). The T-jets mixer studied had the following dimensions $W = 400$ μm, the inlet jets width, $w = 400$ μm and the depth of the complete geometry, $d =$ 250 μm. For this investigation tracer experiment was performed and the RTD data was extracted from experiments and CFD simulations. In their work, segregated flow regime was identified, at a volumetric flow rate of 0.20 and 0.40 mL/min, $Re_H < 50$. The RTD has a shape close to a piston reactor with axial dispersion, the Axial Dispersion Model (ADM) was used for the modelling of this RTD. Semi-Empirical Model (SEM) was also used. It was reported that the SEM fits better with experimental results than ADM, SEM enables to model asymmetric distribution, which predicts better the flow behaviour in the T-jets mixer. The results from both CFD and experimental were in good agreement. Santos et al. (2005) found similar RTD trend with 2D simulations of opposed jets reactors for segregated flow regimes. The RTD has a sharp increase on tracer concentration around the time the jets take to go from the inlet to the outlet without decelerating. After the maximum, the decrease in tracer concentration is also steep, but less sharp, and before reaching zero there is, a long tail associated with tracer that gets trapped in the headspace of the mixing chamber for the case

studied by Santos et al. (2005). This RTD showed a strong channelling from inlet to outlet for segregated flow regimes, which is associated to the decrease on mixing with increase in flow rate for this flow regime. For flow dynamic flow regimes, namely the self-sustainable chaotic flow regime, the RTD was adjusted to the model of a cascade with 3 CSTRs, which is evidence of strong back mixing in this reactor.

2.4 Influence of Geometry and Operation Conditions

In this section, some experimental and computational works from the published literature based on the impact of operational and design parameters on the mixing phenomena in T-jets mixers will be discussed. Some of the works on these mixers are from heat transfer studies, using air or water at different temperatures as working fluids. These works will be reviewed first and after the studies related to mass transfer and chemical reaction, which are related to chemical reactor applications.

2.4.1 **Heat Transfer**

3D CFD simulation performed by Gobby et al. (2001) studied the effect of design and operational parameters on the mixing characteristics of gaseous flow. Simulation were performed with the commercial software CFD-ACE^{TM} for two gases namely, methanol and oxygen. The inlet temperature was 400 K and diffusivity value $2.78\times10^{-5}\mathrm{m^2s^{-1}}$. The flow was considered to be laminar and adiabatic conditions were considered. In one of the simulation, different Peclet numbers ranging from 0.027 to 13.49 were studied. The results showed the variation of the mixing length as a function of outlet Peclet number. It was reported that the dependence of the mixing length on the Peclet number is linear. Further effect of the ratio (d/W) was studied, it was shown that as this ratio increases the mixing length decreases. Further, the simulation results were compared with the Fourier number, which provides limits for high flow rate where the mixing takes place in centre of the mixing chamber.

Devahastin and Mujumdar (2002) performed numerical simulation to solve the time-dependent conservative equation for mass, momentum and energy of a 2D laminar model of a T-jet mixer. Their main objective was to study the effect of inlet jets Reynolds number on

different geometries and then identify the transition Reynolds number. The T-jets mixer inlet jet width was half of the outlet and the range of Reynolds number simulated was from 500 to 10^4 for steady state simulations and 10 to 3500 with dynamic simulations. The length of the mixing channel was long and air at different temperatures was injected in each inlet. The ratio of the mixing chamber width and the inlet jets width, W/w, was varied from 1 to 4. (Devahastin and Mujumdar, 2002) reported that the transition Reynolds number depends strongly on the geometrical configurations particularly at low values of the ratio W/w. From the velocity component plots, it was shown that the fluctuations or degree of oscilliations is smaller at lower ratio regardless of the high Reynolds number at the inlet. Further studies were conducted with temperature as tracer. It was reported from steady state simulation results, at low ratio that no recirculating patterns inside the mixing chamber were observed at low and high Reynolds number. For higher ratio values of W/w vortices or recirculating bubbles as reported by the authors, were observed at very low Reynolds number and also the size of the vortices increased.

Srisamran and Devahastin (2006) studied the flow and mixing behaviour and various parameters such as inlet jets Reynolds number (Re_j) of a non-Newtonian fluid with steady state 2D laminar flow simulation for a T-jet mixer. The commercial software FEMLAB^{TM} 3.0. was implemented to solve the coupled heat, mass and momentum equation associated with numerical simulation to compute mixing from the spatial maps of a scalar, temperature. Since temperature was used as the tracer to monitor the fluid streams energy equation was also included. Only half of the geometry domain was simulated and the ratio of mixing chamber width of the mixing chamber to the injectors width W/w was always equal to 2 while the width of the inlet jets was half the mixing chamber width. The physical properties, such as density, specific heat and thermal conductivity for the simulation were constant and shear-thin fluid were considered while viscous dissipation was neglected. The Reynolds number defined in the inlet of the jets was defined as

$$\mathrm{Re}_j = \frac{w^n \upsilon_{inj} \rho}{8^{n-1} m} \left(\frac{4n}{3n+1} \right)^n \tag{2.8}$$

where w is the width of the inlet jet, υ_{inj} is the inlet jet velocity, ρ is the density of the fluid, n is the flow behaviour index and is considered 1 for water, consistency coefficient m is the viscosity of water. The Reynolds numbers studied were 10, 50,100 and 200. Water with temperature difference of 10 degrees was injected in each of the inlets. The results showed that as the Re_j increases the size of the two vortices placed immediately below the jets expand. Similarly, the results indicated that for the same, Re_j, low flow behaviour index causes smaller vortices, which are referred by the author as recirculating bubbles. Smaller recirculating bubbles induce good mixing. It was also demonstrated that a shorter mixing chamber was required for better mixing when the Re_j decreases, a result that holds good for both Newtonian and non-Newtonian fluids respectively.

Wang et al. (2006) in their work studied the effect of temperature on the mixing conditions. For this, air and water were used as working fluids to study the mixing efficiency at different temperatures. The air temperature was set to 20, 40 and 60 $°C$ and the water temperature to 10, 20 and 40 $°C$ considering equal velocities in both inlets. The results showed that temperature difference leads to an asymmetric flow field immediately after the jets impingement point, which results in vortex formation, and stronger shear, which in turns improves mixing. For different geometrical configurations studied and Reynolds numbers, it was reported that the length required for a specific mixing index increases as the temperature difference increases. The mixing index decreases as the ratio W/L increases, for a given Reynolds number and temperature difference, L is the length of the inlet jet. The length required to achieve complete mixing is greater for water than air.

2.4.2 **Mass Transfer and Chemical Reaction**

Hoffmann et al. (2006) conducted micro-Laser Induced Fluorescence and micro-Particle Image Velocimetry experiments. The main purpose of these flow visualization experiments was to analyse the flow properties such as concentration field and velocity field. The quality of mixing was quantified with intensity of segregation. The experiment was conducted with Rhodamine B dissolved in buffer solution injected through one inlet of the T-jets mixer and in the other inlet plain water, and the images obtained were then processed with Matlab. It was shown that the mixing quality improved along the mixing chamber with high mixing quality

achieved at the outlet where both the fluids are completely homogenised. Hoffmann et al. (2006) reported mixing quality with three different T-jets mixers having different W/d and W/w ratios. The mixing quality improved with increase of depth and increase of the W/w ratio. Furthermore, the quality of mixing increased regardless of geometry with the Reynolds number. In addition to the mixing quality, Hoffmann et al. (2006) computed a quantity related to the scale of segregation, the potential for diffusive mixing, which showed that the mixing quality has the same evolution of the mixing scales.

Bothe et al. (2006) conducted CFD simulations and experiments for Reynolds number 40, 138, and 186. Bothe et al. (2006) performed tracer simulations to study the effect of reactor scaling with regard to mass, momentum and heat transfer. In order to quantify the scaling effect, a geometrical scaling factor, λ, was introduced. By scaling down the reactor by a factor of λ at fixed Reynolds and Schmidt numbers it was shown that that the micro T-jets reactors enabled better thermal control and faster chemical reaction than their larger counterparts do.

Bothe et al. (2010) studied fast irreversible second order chemical reaction with CFD simulation for a T-jets mixer having dimensions, $W = 200$ μm, $w = 100$ μm, $d = 100$ μm and length of the mixing channel 1400 μm. The conversion values for this geometry at $Re_H = 120$ and 160 were computed, and it was reported that the maximum conversion of 0.10 at the outlet occurred at $Re_H = 160$ and smaller conversion occurred at low Reynolds number $(Re_H = 120)$ of around 0.02. Further study was conducted with varying mixing chamber width; $W =$ 200, 400 and 600 μm at engulfment flow regime achieved at $Re_H = 186$. It as reported that the geometry with $W =$ 200 μm had the highest conversion of around 0.45 near the outlet due to smaller diffusion time than the geometry with $W =$ 400 and 600 μm. The conversion values reported increased along the mixing channel for the three geometries studied. This observation conflicts with other authors reporting better mixing for larger ratio values of W/w, i.e. for the same inlet channel width the largest mixing chamber should present higher conversion values. This observation is only valid for segregated flow regimes, which are steady flows where diffusion is the main mixing mechanism and so narrower chambers yield better mixing.

Soleymani et al. (2008a) studied a T-jet mixer (1) with dimensions $W = 600$ μm, $w = 300$ μm, $d = 300$ μm and a second mixer (2) with $W = 300$ μm, $w = 150$ μm, $d = 600$ μm. With T-jet mixer (1) having its mixing chamber width twice wider than the T-jet mixer (2). It was shown that at a particular Reynolds number the mixing quality in the T-jet mixer (1) is better than the T-jet mixer (2). The results showed that the effect of vortices evolving in the T-jet mixer with wider mixing chamber have better mixing efficiency. Soleymani et al. (2008a) also performed a set of simulations with constant inlet velocity and inlet width but different depth to width ratio of the mixing chamber was tested. The results from the simulation showed that for low ratio of the depth to the width of the mixing chamber the flow is segregated, and as the ratio increased, they identified flow regimes, from vortex to engulfment flow regime, which is achieved at higher depth to width ratio. The mixing efficiency increased with the increase of this ratio. Therefore from their work it was concluded that the formation of vortices and different flow regimes not only depends on the operational parameter Reynolds number but also on the geometrical parameter.

Sultan et al. (2012) characterised different flow fields using PLIF experiments with eight different T-jets mixers geometries. The flow regimes were then related with the mixing efficiency computed from the intensity of segregation. In geometries with $W / w = 1$, 2 and 4 the change in intensity of segregation was mainly due to transition from segregated to dynamic state that occurs at Reynolds number around 200. The mixing was reported to be due to a boundary layer instability occurring in the interface of the two fluids, which exhibits very similar features to the Kevin-Helmholtz instability. For larger values of $W / w = 6$ a self sustainable chaotic flow regime is observed above the transition Reynolds number around 200. The onset of this flow regime marks a very steep decrease of the intensity of segregation. Furthermore, in Sultan et al. (2012) work, the influence of W / d was studied. For geometries having smaller ratio $W / d = 1$, 1.5 and 2, deeper mixing chambers, there was steep decrease in the intensity of segregation from Reynolds number 100 to 200. This steep decrease was related to the flow regime transition from segregated to chaotic flow regime with the formation of a vortex street. For $W / d = 3$ and 6, shallow chambers, the intensity of segregation decrease with the Reynolds number was not so steep and occurred at higher Reynolds numbers. Sultan et al. (2012) recommended a set of values for the geometrical

parameters as well as the operational parameters that enabled operation at self-sustainable chaotic flow regime with: $W/w=6$, $W/d\geq 2$ and Re above 300.

Krupa et al. (2012) used one of Bourne micromixing test reactions (Bourne, 1984), in this particular case of a consecutive-competitive reaction, and determined the influence of operational and geometrical parameters such as Reynolds number, W/w, W/d, and flow rate ratio on micromixing in eight T-jets mixers. The chosen test reaction involved two steps, where the first reaction was instantaneous and the second is fast, but slower than the first reaction. In the first step the first two reactant *A* and *B* react to yield *R*, which then reacts in a second step with *B* to form another product, *S*. *B* was set to be the limiting reactant, so the product *S* is only formed when an excess of *B* exists after *A* reacts with *B* to form *R*. If the mixing is fast, then all of the limited reactant *B* is consumed by *A*, and therefore the concentration of the product *S* is smaller for faster reaction conditions. At low Reynolds number, the flow regime was segregated, with mixing mainly occurring due to molecular diffusion and the selectivity value of the product *S* from the secondary reaction is high, which indicates poor mixing quality. Increasing the Reynolds number onsets the formation of vortices, this leads to faster mixing decreasing the selectivity of S for all geometries. The W/w ratio was studied, ranging from 1 to 4 for a constant depth of $d=4$ mm. When the reactors operate at chaotic or engulfment flow regimes, depending on the geometries, there is a significant improvement in the mixing quality seen from the decrease in the selectivity of *S*. Mixing is enhanced when increasing W/w values, at least up to 4, experiments with $W/w=6$ showed that this trend is limited to $W/w\leq 4$ and no significant evolution occurs thereafter. The transition Reynolds number for the studied geometries is reported to be roughly between 100 and 200, a range where the selectivity of *S* has a sharp fall. The W/d ratio effect for 1, 1.5, 2, 3 and 6 with constant $W/w=6$, was also studied. It was reported that the *S* selectivity decreases with decrease in the W/d ratio or increase in depth of the mixing geometry. For shallow geometries, $W/d=$ 3 and 6 the selectivity decreases only at very high Reynolds number greater than 500, where the flow regime is probably turbulent. It was also reported that the flow rate ratios between the two opposing jets must be close to unity in order to improve the micromixing in T-jets mixer.

One of main application of faster mixers is on nanoparticles production via wet chemistry methods, and most of the works exploiting actual application of T-jets on chemical processes are in this field. Schwarzer et al.(2006) studied T-jets reactors for the precipitation of nanoparticles experimentally and performed simulations based on the population balance model coupled with CFD with barium sulphate and compared experimental and computational results. The precipitation experiments with barium sulphate using aqueous solutions of barium chloride and sulphuric acid were conducted continuously at a temperature of $25\,°C$ on a T-jets mixer with width $W = 1000$ μm, inlet jets width $w = 500$ μm, and depth $d = 1000$ μm. The total flow rate ranged from 0.2 to 12 mL/s with equivolumetric flow rates in both the inlets. The Reynolds number was varied from 250 to 15000. In order to generate intense mixing small geometrical dimensions were preferred and the flow was set to be turbulent. The results for the barium sulphate particles precipitated from 0.5 M $BaCl_2$ and 0.33 M H_2SO_4 solutions studied at different flow rates showed that increase in Reynolds number increases the intensity of mixing yielding smaller nanoparticles. Poor mixing resulted in larger particles and the impact of agglomeration was found to increase with super saturation due to larger particles. This result evidences the application of this reactor for the production of nanoparticles under controlled mixing conditions.

The main objective of Lince et al. (2011) was to quantify the efficiency of T-jets mixer for the production of polymer nanoparticles and then to develop a mathematical model to be used for the design, optimization and scale up of mixers for nanoparticle productions. Two T-jets mixers were used, one with dimensions $W = 2000$ μm, $w = 1000$ μm, $d = 2000$ μm and other with dimensions $W = 2000$ μm, $w = 2000$ μm, $d = 2000$ μm. The two polymers used for this study were poly caprolactone (PCL) and the novel co-polymer widely known as poly (MePEGCA-co-HDCA). The two polymers PCL and co-polymer were studied with two different molecular weights 14000-80000 g/mol. These polymers are mixed with solvent and then with anti-solvent, for instance acetone and water. As these two solutions mix, nanoparticles are formed which are then dried in an evaporation unit. The particle size distribution and the mean particle size diameter were determined by dynamic light scattering. The experimental results highlight that as the flow rate increases the mean particle size diameter decrease, this were tested for four different flow rate ratios of water to acetone. Different flow rate ratios of water and acetones were studied, and the results showed that

these parameters affect the particle size diameter. It was also showed that the geometry with small injectors have faster mixing. To have better insight into the mixing phenomena Lince et al. (2011) conducted CFD simulation with a similar geometry. The contour plot results showed that the impingement point of the jets varies due to the momentum ratio caused by the different fluid properties namely density. It was also seen that as the inlet jets dimensions decrease the mixing efficiency improves and gets faster.

2.5 Active Mixing

Some authors try to overcome the limits of mixing in some T-jets reactors by imposing an external stimulus to the reactor. Ito et al. (2006) performed experiments in the T-jets mixer imposing an external vibration to the jets flow rate - active mixing, for promoting mixing and chemical reaction in the fluid. The device used to induce oscillation is a small vibrating motor. It was reported that the quality of fluid mixing and chemical reaction improved with this technique. At low frequency there was no change in the fluid motion and the mixing in the chemical reaction. However, with increase in frequency there was considerable improvement, with complete mixing leading to enhanced reaction between the studied chemicals taking place.

Qui et al. (2012) studied, using 2D CFD simulations, the effect of sinusoidal flow pulsations on mixing in T-jet mixers. In this work, fluid temperature was used as the passive tracer to assess the mixing efficiency in the T-jets mixer. Different pulsation amplitude and frequency was used to improve mixing efficiency at a particular Reynolds number. It was reported that the mixing performance could be improved by increasing the pulsation amplitude under a particular Reynolds number and the pulsation frequency should be in the range of vortex frequency for better mixing in T-jets mixer.

These works showed the possibility of onsetting dynamic flow regimes under flow conditions or geometeric configurations where flow regime is generally segregated.

2.6 Identification Number (K)

The parameters that set the flow regime are complex and interconnected: geometrical parameters and Reynolds number. Some authors have tried to propose identification numbers relating some design and operational parameters that could be used to predict the flow regime of operation.

Engler et al. (2004) in their study performed a dimensional analysis to obtain an identification number K, given as

$$K = \left(Eu \frac{D_H}{l_V} Re^3 \right)^{1/4} \tag{2.9}$$

where D_H is the hydraulic diameter, l_V is the ratio of control volume V and the cross sectional area of the mixing chamber A, and Eu is the Euler number, defined as

$$Eu = \Delta p / \rho \upsilon^2 \tag{2.10}$$

where Δp is the pressure loss per unit length, υ is the mean flow velocity, and ρ the fluid density. The identification number K was related to the Kolmogorov length scale λ_K, and to the hydraulic diameter D_H, this is the ratio of space available given as hydraulic diameter and the space required for the vortex formation represented as follows

$$K = \frac{D_H}{\lambda_K} \tag{2.11}$$

where $\lambda_K = \left(\frac{\nu}{\varepsilon} \right)^{1/4}$, ε being the specific energy dissipation inside the fluid, which is calculated as $\varepsilon = \frac{\Delta p V}{m}$, Δp is the pressure loss over the control volume V with corresponding mass m. This study was conducted at the onset of the engulfment flow regime. It was reported that the engulfment flow begins when the identification number is around 40,

which showed good agreement with the simulation results. This identification number does not account for the effect of parameters W/w and W/d on the Reynolds number for the transition flow regime.

The main purpose of the work by Soleymani et al. (2008b) was to establish an identification number for each flow regimes. Soleymani et al. (2008a) reported that good mixing occurs in the engulfment flow regime, and so the main goal in Soleymani et al. (2008b) was to introduce a dimensionless number that could identify transition from vortex to engulfment regime occurs. This number was tested on data from 3D CFD simulations of T-jets mixers. Soleymani et al. (2008b) used the following expression for the identification number K which describes the flow regime in the T-jets mixer

$$K = Re_H^{\alpha}\left(\frac{w}{W}\right)^{\beta}\left(\frac{D_{Hjet}}{D_H}\right)^{\gamma}\left(\frac{W}{d}\right)^{\zeta} \tag{2.12}$$

where W is the width of the mixing chamber, w width of the inlet jets, d depth of the geometry, D_H is the hydraulic diameter of the mixing chamber and D_{Hjet} is the hydraulic diameter of the inlet jets and mixing chamber respectively. The parameters $\alpha, \beta, \gamma, \zeta$ were had values 0.82, -0.79, -1.5 and 0.15. From CFD results the value of the identification number K marking the transition from vortex to engulfment flow regime is K_C=100. This parameter relates geometrical parameters and an operational parameter, the Reynolds number, for the case of equal flow rate in the opposed jets and fluid having equal physical properties. According to this number, transition to engulfment flow regime occurs at lower Reynolds numbers if the W/w ratio and the ratio W/d are larger. While the effect of W/w is according to the findings of this thesis, the W/d effect here was reported to be opposite. In **Chapter 3** of this thesis this parameter is applied to PLIF results and to results of other authors. The range of geometries covered in this thesis is larger than the one considered by Soleymani et al. (2008b).

2.7 Conclusion

The literature review on T-jets mixers showed that the main purpose of the study of T-jets mixers is to identify the different flow regime, which sets the mixing efficiency of these mixers. It was established through visualization experiments and CFD numerical simulation, the main parameters affecting mixing phenomena and flow dynamics have been geometrical and operational parameters. Reynolds number being the most important operational parameter, along with the geometrical parameters such as the interplay between the ratios namely, chamber width, injector's width and the chambers depth, which affects and initiates the different flow regime.

In the literature review, different flow regimes namely segregated, vortex, engulfment and turbulent flow were identified. These flow regimes arise because of effect of Reynolds number and geometrical parameters. At low Reynolds number segregated flow regime, in the intermediate Reynolds number range vortex regime and in high Reynolds number engulfment flow regime have been identified and in cases where the Reynolds number is extremely high turbulent flow regime is found. Also the effect of geometrical parameters, gives rise to different flow regimes with fixed Reynolds number as seen in the published literature. These studies were mostly based on the PLIF experiments and chemical reaction, 3D and 2D CFD simulation results. The range of geometrical parameters covered so far is yet limited, for example studied depth values were always smaller than the chamber width and so this thesis aims to contribute on the study of larger ranges of geometrical parameters, which could shed light on the goal of introducing small T-jets reactors with large throughput.

2.8 References

Adeosun, J.T., Lawal, A., 2009. Numerical and experimental studies of mixing characteristics in a T-junction microchannel using residence-time distribution. Chemical Engineering Science 64, 2422-2432.

Aubin, J., Fletcher, D.F., Bertrand, J., and Xuereb, C., 2005. Characterization of Mixing Quality in Micromixers. Chemical Engineering Science 60, 2503-2516.

Baldyga, B., Bourne, J.R., Walker, B., 1998. Non-isothermal micromixing in turbulent liquids: theory and experiment. Canadian Journal of Chemical Engineering 76, 641.

Bothe, D., Lojewski, A., Warnecke, H., 2010. Computational analysis of an instantaneous chemical reaction in a T-microreactor. AIChE Journal 56, 1406-1415.

Bothe, D., Stemich, C., Warnecke, H., 2006. Fluid mixing in a T-shaped micro-mixer. Chemical Engineering Science 61, 2950–2958.

Bothe, D., Stemich, C., Warnecke, H., 2008. Computation of scales and quality of mixing in a T-shaped microreactor. Computers & Chemical Engineering 32, 108-114.

Bourne, J. R., 1984. Micromixing Revisited. IChemE Symposium Series, (ISCRE 8), 797-813.

Danckwerts, P.V.,1952. The definition and measurement of some characteristics of mixtures. Applied Scientific Research 3, 279-296.

Devahastin, S., Mujumdar, A. S., 2002. A numerical study of flow and mixing characteristics of laminar confined impinging streams. Chemical Engineering Journal 85, 215-223.

Engler, M., Kockmann, N., Kiefer, T., Woias, P., 2004. Numerical and experimental investigations on liquid mixing in static micromixers. Chemical Engineering Journal 101, 315-322.

Gobby, D., Angeli, P., Gavriilidis, A., 2001. Mixing characteristics of T-type microfluidic mixers. Journal of Micromechanics and Microengineering 11, 126-32.

Gradl, J., Schwarzer, H.-C., Schwertfirm, F., Manhart, M., Peukert, W., 2006. Precipitation of nanoparticles in a T-mixer: Coupling the particle population dynamics with hydrodynamics through direct numerical simulation. Chemical Engineering and Processing 45, 908-916.

Hoffmann, M., Schlüter, M., Räbiger, N., 2006. Experimental investigations of liquid-liquid mixing in T-shaped micro-mixers using μ-LIF and μ-PIV. Chemical Engineering Science 61, 2968-2976.

Ito, Y. and Komori, S., 2006. A vibration technique for promoting liquid mixing and reaction in a microchannel. AIChE Journal 52, 3011-3017.

Krupa, K., Sultan, M.A., Fonte, C.P., Nunes, M.I., Dias, M.M., Lopes, J.C.B., Santos, R.J., 2012. Characterization of mixing in T-jets mixers. Chemical Engineering Journal 207-208, 931-937.

Lince, F., Marchisio, D. L., Barresi. A.A., 2009. Smart mixers and reactors for the production of pharmaceutical nanoparticles: Proof of concept. Chemical Engineering Research and Design 87, 543-549.

Malguarnera, S.C., Suh, N.P., Liquid Injection Molding I., 1977. An Investigation of Impingement Mixing. Polymer Engineering and Science 17, 111-115.

Qiu, S., Xu, P., Jiang, Z., Mujumdar, A.S., 2012. Numerical modeling of pulsed laminar opposed impinging jets. Engineering Applications of Computational Fluid Mechanics 6, 195-202.

Santos, R.J., Teixeira, A.M.T., Costa, M. R. P. F. N., Lopes, J.C.B., 2002. Operational and Design Study of RIM Machines. International Polymer Processing 17, 387-394.

Santos, R. J., 2003. Mixing Mechanisms in Reaction Injection Moulding - RIM. An LDA/PIV Experimental Study and CFD Simulation. Departamento de Engenharia Química. Porto, Universidade do Porto.

Santos, R.J., Teixeira, A.M.T., Lopes, J.C.B., 2005. Study of mixing and chemical reaction in RIM. Chemical Engineering Science 60, 2381–2398.

Santos, R.J., Teixeira, A.M.T., Ertugrul, E., Sultan, M.A., Karpinska, A.M., Dias, M.M., Lopes, J.C.B. 2010.Validation of a 2D CFD Model for Hydrodynamics Studies in CIJ Mixers. International Journal of Chemical Reactor Engineering 8 (A32).

Schwarzer, H.-C., Schwertfirm, F., Manhart, M., Schmid, H.-J. and Peukert, W., 2006. Predictive simulation of nanoparticle precipitation based on the population balance equation. Chemical Engineering Science 61, 167-181.

Soleymani, A., Kolehmainen, E. and Turunen, I., 2008a. Numerical and experimental investigations of liquid mixing in T-type micromixers. Chemical Engineering Journal 135, S219-S228.

Soleymani, A., Yousefi, H., Turunen, I., 2008b. Dimensionless number for identification of flow patterns inside a T-micromixer. Chemical Engineering Science 63, 5291-5297.

Srisamran, C., Devahastin, S., 2006. Numerical simulation of flow and mixing behaviour of impinging streams of shear-thinning fluids. Chemical Engineering Science 61, 4884-4892.

Steyer, C., Sundmacher, K., 2009. Morphology of Barium Sulfate Crystals from Seeded Precipitation. Chemical Engineering & Technology 32, 1127-1130.

Sultan, M.A., Fonte, C.P., Dias, M.M., Lopes, J.C.B., Santos, R.J., 2012. Experimental study of flow regime and mixing in T-jets mixers. Chemical Engineering Science 73, 388-399.

Teixeira, A. M., Santos, R.J., Costa, M. R. P. F. N., Lopes, J.C.B., 2005. Hydrodynamics of the Mixing Head in RIM: LDA Flow-Field Characterisation. AIChE Journal 51(6), 1608-1619.

Wang, S.J., Devahastin, S., Mujumdar, A.S., 2006. Effect of temperature difference on flow and mixing characteristics of laminar confined opposing jets. Applied Thermal Engineering 26, 519-529.

Wong, S.H., Ward, M.C.L., Wharton, C.W., 2004. Micro T-mixer as a rapid mixing micromixer. Sensors and Actuators B 100, 359-379.

3. T-JETS MIXER: PLIF EXPERIMENTAL STUDY

3.1 Introduction

This chapter presents the experimental study of the effect of the geometrical parameters of T-jets mixers on flow regimes and mixing.

An important aspect on mixing is the flow regime, from literature four flow regimes are identified for T-jets mixers. The following features are observed in all these flow regimes: the impinging of both jet streams on each other; the jets bend towards the outlet prior to the impingement point, and after impinging each other the jets initiate different flow patterns that depend on the operation flow regimes. The flow regimes were explained in **Section 2.1.**

A fifth flow regime has been observed from 2D CFD simulation of the T-jets flow fields in geometries that have ratios of the mixing chamber width to the jets width larger than six: the chaotic flow regime (Santos et al., 2005 and 2010). This flow regime is characterized by the self-sustainable oscillation of the jets impingement point and the formation of coherent vortices structures downstream the jets impingement point, originating a vortex street throughout the mixing chamber. The oscillations of the jets impingement point have typical frequencies that were related by Santos et al. (2009) with the formation rate of the vortices. The rotation axes of the vortices in the self-sustainable chaotic flow regime are in the normal

direction to the mixing chamber axis, unlike the vortices observed in the vortex and engulfment flow regimes that have rotation axes aligned with the mixing chamber axis. This flow regime (Santos et al., 2005) usually appears when the Reynolds number is above a critical value, larger than 100 that mark the transition from segregated steady to self-sustainable chaotic flow regime. The other conditions are opposed jets with flow rate ratio close to one and a mixing chamber width at least 6 times larger than the injectors. Up to now, this flow regime was only reported from 2D CFD simulations and some PIV and Laser Doppler Anemometry in Confined Impinging Jets reactor. This work reports for the first time experimental data on the self-sustainable chaotic flow regime in T-jets mixers, and in **Section 4.8,** 3D CFD data will be shown.

Other parameters, in addition to the operation Reynolds number that influence the flow regimes, are reported in the literature. Wong et al. (2004) studied different T-jets mixers geometries using tracer and CFD simulations, and also reported the flow features of the three flow regimes: segregated, vortex and engulfment. The best mixing indices in the work of Wong et al. (2004) were observed for the cases where the jets were better aligned, i.e. cases where the angle formed between the opposed injectors was closer to 180º. The strong impact of the alignment of the injectors on mixing was also observed in preliminary experiments made to prepare this study, for these reason, whenever dimensional precision of the T-jets made by CNC milling was not enough to ensure the jets alignment, a wire electro-erosion fabrication technique was used.

Another issue that has been observed to have an impact on the flow field in opposed T-jets mixers is the momentum ratio between the jets (Wong et al., 2004; Santos et al., 2010). In this work tight control of the flow rate of the two feed streams was made using liquid flow controllers that simultaneously measure and set the flow rate value. Furthermore, the liquid flow controllers have the advantage over other equipment, such as pumps, of not pulsating the flow and thus not inducing periodic perturbation to the jets, which are known to affect the flow field dynamics from results of studies on active mixing in T-jets mixers (Ito and Komori, 2006; Zhongliang et al., 2002).

Although there are several studies on mixing in T-jets mixers the mechanics underlying the different flow regimes that depend on operational conditions and T-jets geometrical

parameters are not yet established. Flow visualization experiments enable to get insight on the convective patterns that promote mixing up to a micro-scale level (Sinton, 2004). In this work, the effect of geometrical parameters of the T-jets mixers on mixing is studied experimentally with PLIF. Particular focus in this work will be given to the ratio of the width of the chamber to the width of the injectors, W / w, and the ratio of the width of the chamber to the chamber depth, W / d .

One of the most important parameters in T-jets mixers and opposed mixers in general is the operation Reynolds number, a known fact from the first works on mixing in these types of geometries (Malguarnera and Suh, 1979; Lee et al., 1980; Tucker et al., 1980). Although in cylindrical geometries the Reynolds number is always defined at the injectors using the hydraulic diameter, in T-jets reactors different authors define the Reynolds number differently. For example Soleymani et al. (2008a), defines the Reynolds number from the mixing hydraulic diameter. In this thesis the Reynolds number is consistently defined at the injectors (Santos et al., 2002, 2005 and 2010) as

$$Re = \frac{\rho w \upsilon_{inj}}{\mu} \tag{3.1}$$

where ρ and μ are the density and viscosity of the working fluid, υ_{inj} is the surface velocity at the injectors jets and w is the width of the injectors. In this work Reynolds number ranging from 50-600 were covered, according to the definition of Equation (3.1).

3.2 Experimental Setup

The experimental characterization of the flow field was made in eight T-jets mixers (**Figure 3.1**) with different geometrical parameters.

The complete list of the dimensions of the studied T-jets is in **Table 3.1**. W and w are the width of the mixing chamber and the injectors, respectively, and d is the depth of the entire T-jets mixers. The T-jets are replaceable parts made of aluminium or stainless steel that were sealed in a transparent acrylic block for visualization purposes. **Figure 3.1** shows drawing of the inner piece that defines the T-jets geometry and of the sealing acrylic block. Some T-jets

(see **Figure 3.2**), particularly those with thinner injectors jets had to be remade after dimensional control, instead of aluminium in those cases it was used a hardened stainless steel (DIN 1.2083), which enabled a better dimensional stability of the geometries. While in the cases where aluminium was used the milling of the material was made with CNC, the geometries made of steel were fabricated by wire-electro erosion, a technique that enabled alignment of the opposed injectors with precision of $\pm$ 5 μm.

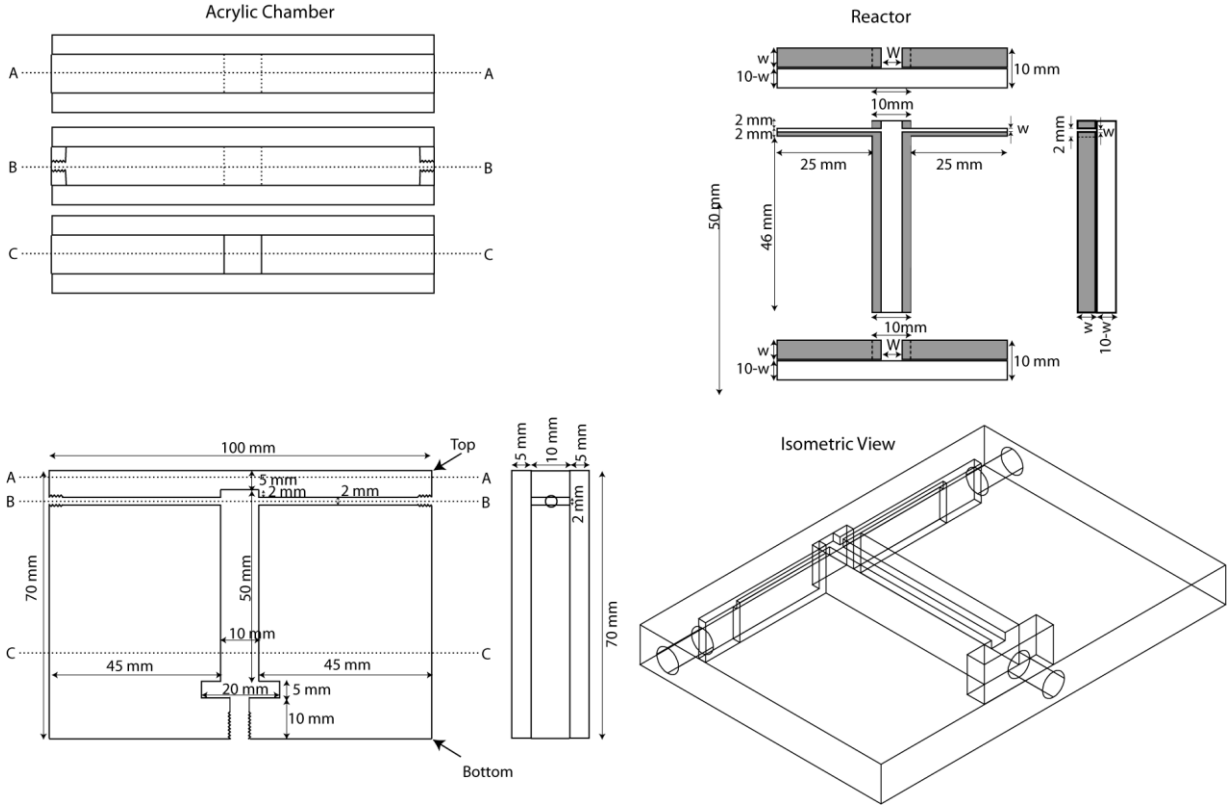

Figure 3.1 Drawing of T-jets mixers reactor and sealing acrylic block.

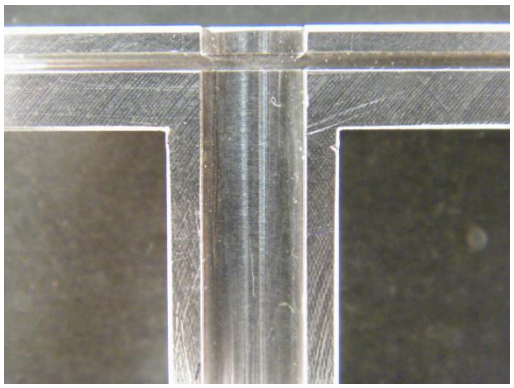

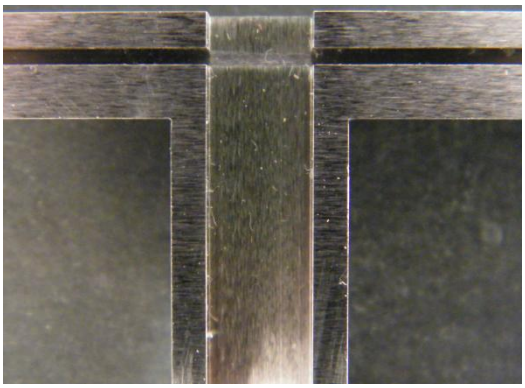

CNC technique-Aluminium **Wire-electro erosion technique-Stainless steel**

Figure 3.2 T-jets geometries built with different techniques.

Table 3.1. List of T-jets mixers geometrical parameters used in PLIF experiments.

Chamber Width (W) **mm**	**Jet Width** (w) **mm**	**Chamber Depth** (d) **mm**	W/w **ratio**	W/d **ratio**
2	0.5	4	4	0.5
2	1	4	2	0.5
2	2	4	1	0.5
6	1	1	6	6
6	1	2	6	3
6	1	3	6	2
6	1	4	6	1.5
6	1	6	6	1

The flow chart with the complete instrumentation used in the experiment is shown in the **Figure 3.3**. The fluids are stored in two pressurized tanks with a pressure regulator; these tanks deliver the fluids to two flow controllers from Alicat Scientific LC-200CCM-D (see **Figure 3.4**). The purpose of this flow controller is to deliver fluid with a tight control of the flow rate. These devices have an integrated valve whose aperture is changed by a PID controller to set the flow rate to the set point value. The flow controllers are actuated from a 0-10 V signal generated in a DAQ NI PCI-6221 National instruments data acquisition card. A program developed on LabView is controlling complete instrumentation. A data acquisition

card connected to the external board does the connection between the program and the instrument. The main feature of this program is the flow control based on the viscosity and density versus fluid composition and operating temperature. This program gives the desired flow rate by turning a single virtual knob and actuates the flow meter.

The fluids are delivered to the two injectors of the T-jets mixer. One tank is filled with clear water and the other tank is filled with water dyed with Rhodamine 6G. Complete installation of the experimental set-up is shown in **Figure 3.5**.

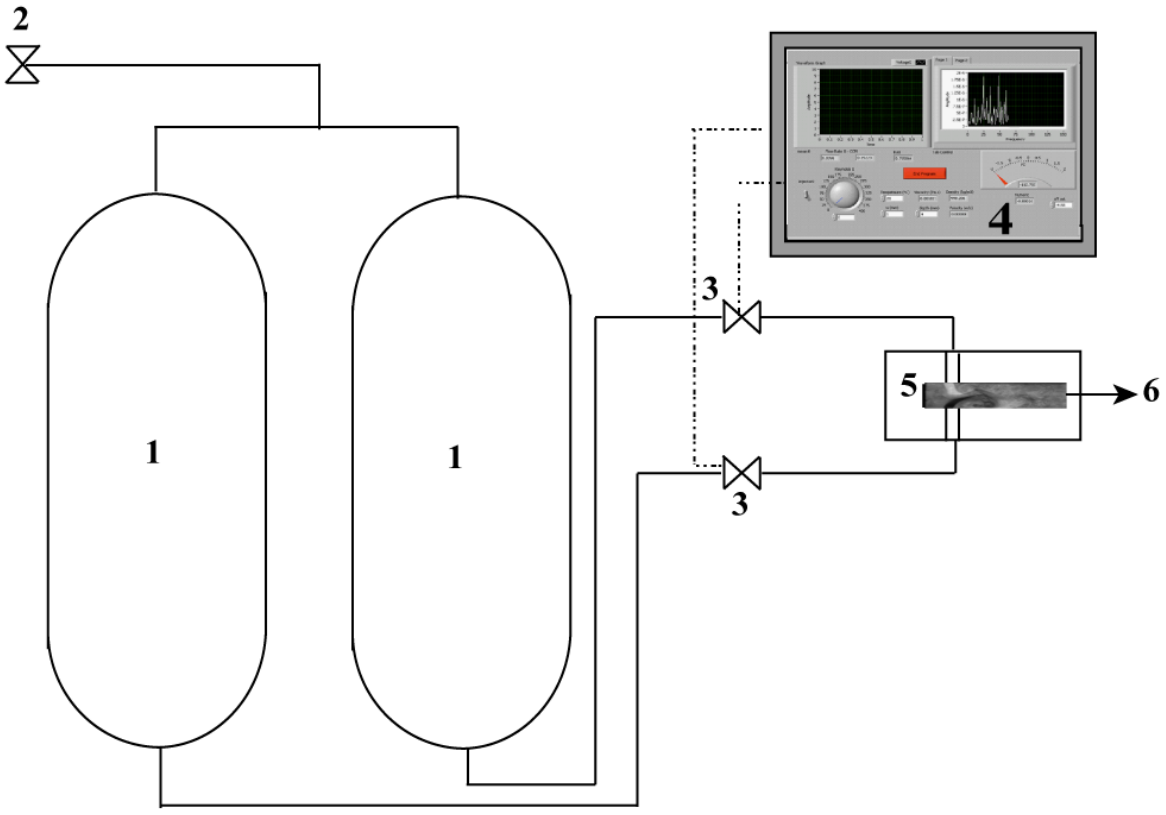

1. Tank **4. PC with Inbuilt flow controller software**

2. Pressure regulator **5. T-jet mixer in the acrylic chamber**

3. Flow controller **6- Outlet**

Figure 3.3 Flow chart of T-jets experimental set-up.

Figure 3.4 Close view of the Alicat Scientific –Flow controller

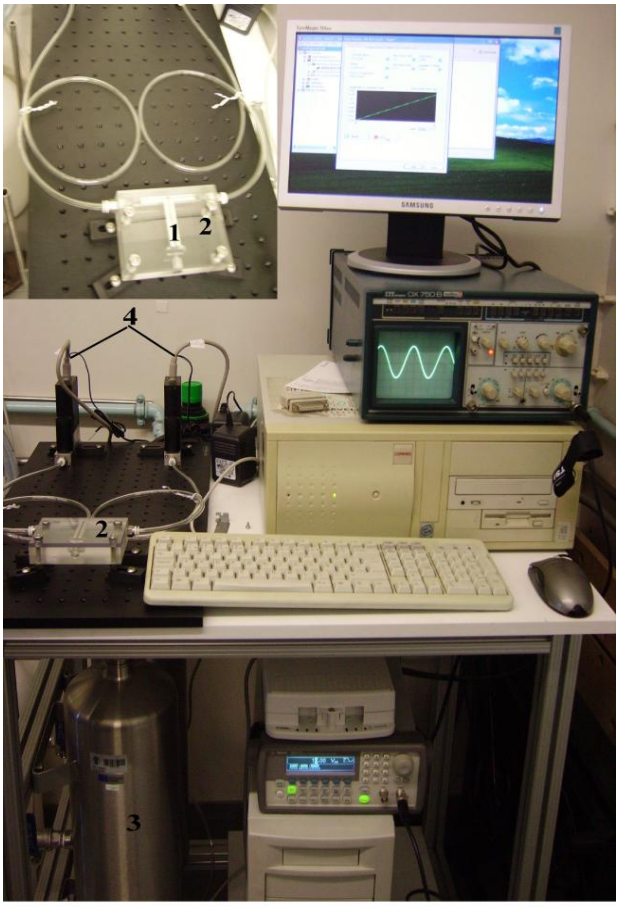

1-T-jets aluminium geometry **2- Transparent acrylic block**

3-Pressurised tank with fluids **4-Liquid flow controller**

Figure 3.5 PLIF experimental set-up.

The mixing of both streams in the T-jets was imaged with the PLIF technique that is shown in **Figure 3.6**. PLIF is an optical measuring technique used to measure the instant whole-field concentration and temperature maps in liquid flows. It has the following features such as: it is a non-intrusive technology, it provides quantitative, precise and accurate measurements of the concentrations or temperature fields in our case it is the concentration field.

The basic equipment required to carry out the PLIF measurements is the INSIGHT 3G software, used to capture, analyse and display the PLIF images. This software is functionally divided into two parts- acquisition and processing part. At first, it acquires an image and processes it to obtain properties such as concentration and temperature. In this work only the acquisition features were used, the data was post processed in Matlab®.

PLIF technique is effective for the study of small scale flow characteristics under a condition such that laser absorption by the working fluid is minimal, so that a low power laser can produce visualization with high resolution. The technique is most suitable in the study of mixing, where it is required to accurately measure concentration changes at a very small scale in fast phase. PLIF is based on the principle of electronic excitation of the molecules by an incident light beam and the measurement of the light intensity. This technique consists of fluorescent species or tracers, an incident light source and a camera for the measurement of fluorescent emission. The fluorescent tracers absorb photon at a particular wavelength and after a short period, it re-emits it in the form of longer wavelength. The fluorescent emission of the tracer is then measured by capturing the images with a high speed camera. The processing consists of converting the recorded raw images of the fluorescence to concentration maps. For liquid-liquid mixing, one of the fluids is marked with the dye while the other is clear water. When passing through the laser sheet, the dye is excited and re-emits fluorescent light. A camera captures the image of the plane illuminated by the laser sheet with a filter that blocks the wavelength of the laser and allows the passage of the fluorescent light. The light intensity is then processed to give concentrations.

A laser source (Nd:YAG laser) with appropriate optics to form a thin sheet of light is used to illuminate a plane that is parallel to the chamber top and bottom and cuts the T-jets geometry through its axis. The setup and controls for capturing the images with the INSIGHT 3G

software interface is shown in the **Figure 3.7**. The **Figure 3.7** shows the timing setting parameters used for the laser operation to help capture the desired images. In the interface:

- PIV Frame Mode- defines the number of frames the camera captures when it receives the trigger from the synchronizer. The single camera acquires a single frame image.
- Pulse Rep rate (HZ) - is the pulse repetition rate for the laser.
- Laser Pulse Delay- is the time to wait from the start of the sequence to the first laser pulse.
- Delta T (μs) - is pulse separation value between two pairs of pulses, only used for PIV when using pairs of images (frame straddle).
- PIV Exposure (μs) - is the time the camera shutters opens for each PLIF image.
- PLIF Camera Delay-is the time when the camera shutter opens after the sequence start.
- Num PLIF Laser Pulses- indicates the number of laser pulses within a single PLIF camera exposure.

In this work, the laser sheet illuminates the imaged plane is parallel to the chamber top and bottom and cuts the T-jets geometry through its axis. The laser sheet passes though a 0.5m m slit, that approximately sets the depth of the imaged plane. PLIF was made with:

- A fluorescent dye such as Rhodamine 6G that marks the fluid and is traced during the measurements. This chemical compound absorbs the laser light energy and re-emits the light at a longer wavelength that can be detected by a photo detector. This Rhodamine 6G fluorescent dye is used for the concentration measurements.
- A camera equipped with a sharp cut-off or narrow-band filter, so that only the fluorescent light is recorded. This camera acts as an array of light detectors (pixels) calibration. The level of fluorescence is known to vary with the concentrations in the experiment studied. The calibration procedure consists of determining the fluid clear water and fluorescence dyed water at every pixel of the camera.
- For the experiments, the concentration maps of the flow field were acquired using a camera connected to a computer at a rate of 15 frames per second. For each of the used geometries, a set of 16-bits grayscale images of the flow was captured storing the light intensity values for each pixel on a scale from 0 (black) to 2^{16} (white), proportional to the concentration of the dye.

At low concentrations of Rhodamine 6G, the intensity of the emitted light by the fluorescent dye when excited by the laser is linearly dependent on its concentration. The concentration of the Rhodamine 6G used in the PLIF experiments was 3.5×10^{-4} g/l, which is experimentally confirmed to be in a range where the relation between concentration and light emission intensity is linear, as shown in the **Figure 3.8**.

The light intensity values were converted into concentration values by using two calibration images: the first image was obtained with the maximum concentration of tracer; and the second image was obtained with clean water. The curve in **Figure 3.8** was obtained using the same concentration of Rhodamine 6G in both jets and using the average from 100 images. The working fluids for the experiment temperature of $24\,°C$ have a density of 997.38 kg/m^3 and viscosity of 9.11×10^{-4} Pa.s. The dye concentration that was used did not change the fluid properties.

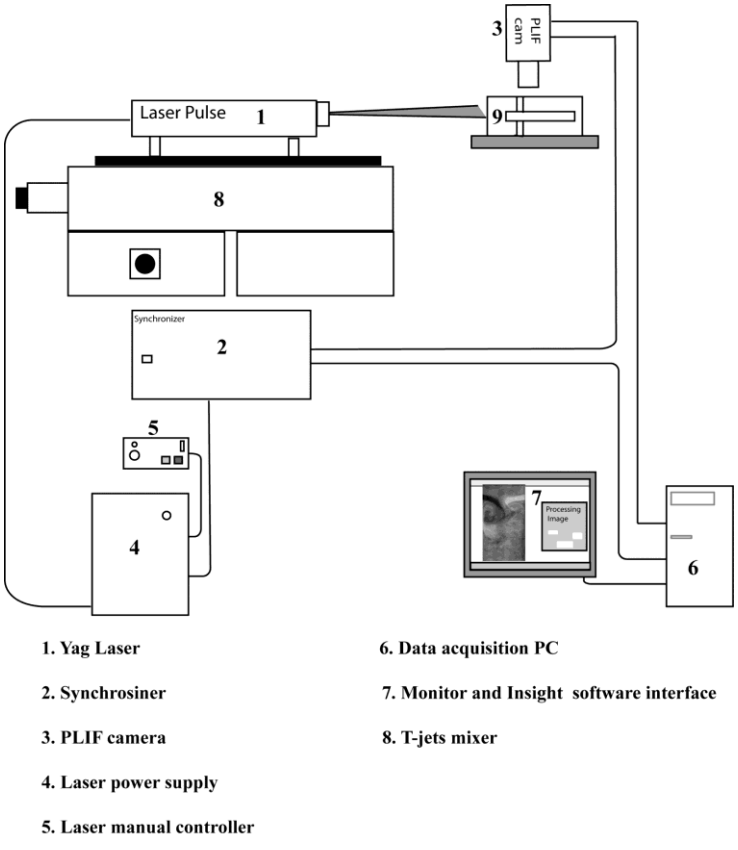

Figure 3.6 PLIF technique.

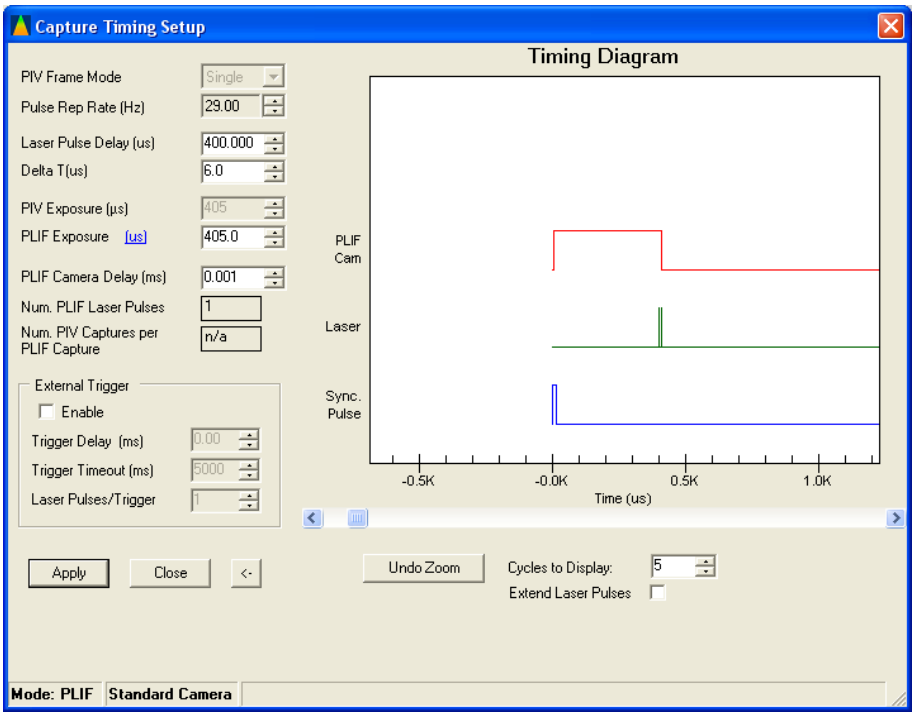

Figure 3.7 INSIGHT 3G timing setup parameters interface.

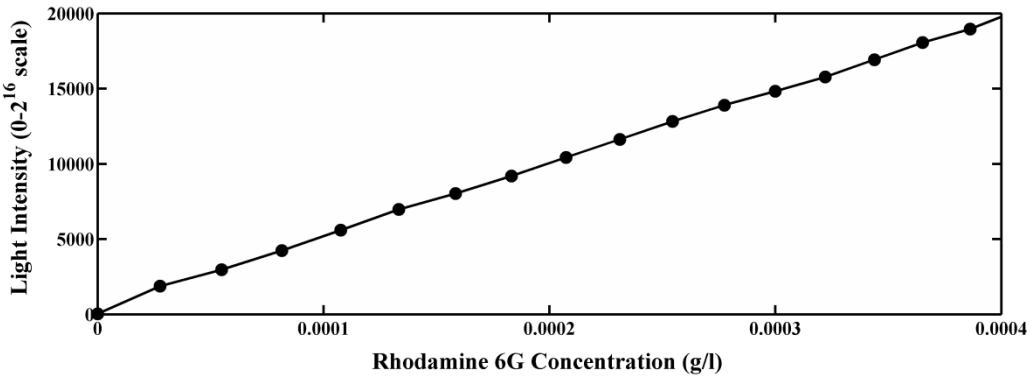

Figure 3.8 Calibration curve for pixel light intensity as a function of dye concentration.

3.3 Results

3.3.1 PLIF Images

PLIF images were obtained for the T-jets geometries listed in **Table 3.1. Figure 3.9** to **Figure 3.13** shows the PLIF images obtained for the geometries having a chamber width to jets width ratio of six, $W/w=6$, with varying depths, $W/d=1$, 1.5, 2, 3 and 6, for different Reynolds numbers starting at 50 up to 600. The PLIF images of the geometries with $W/w=1$, 2 and 4 for $W/d=0.5$ are shown in **Figure 3.14** to **Figure 3.16**. In the PLIF images the white refers to the Rhodamine 6G dyed stream and the black stream is clear water.

In **Figure 3.9** to **Figure 3.16** for lower Reynolds number, Re=50, two fluid streams are clearly visible from PLIF experiment; with the two streams flowing through segregated paths throughout the mixing chamber, i.e the dyed stream and clear water stream flow side by side and the interface between both streams does not change its position with time, and so this flow regime is termed as *segregated steady state flow regime*.

In the PLIF images obtained at $Re=50$ there is appearance of dark black streak regions, located in the white stream and vice versa. The intrusion of fluid having different colour in one of the jet streams enables the identification of the jets' paths and of the two upper vortices. The two upper vortices are symmetric and roundish. The jets bend before impinging each other, as previously reported in 2D simulations of Santos et al. (2005).

The images in **Figure 3.9** to **Figure 3.16** clearly show the dramatic change in flow field from Re=50 to high Reynolds number studied for each T-jet mixer geometry, with the onset of mechanisms such as the crossing of the jets from one side to the other side of the mixing chamber, generally transported by vortices that are formed downstream the injectors. The characteristic of the transient flow regimes observed at higher Reynolds number depends on the mixer geometry, particularly on the depth of the mixing chamber and on the ratio of mixing chamber width to jets width. These geometrical parameters are covered in the next sections. A third important geometrical parameter is the headspace above the jets that was previously studied by Santos et al. (2002) and Santos et al. (2010).

3.3.1.1 Effect of Depth Ratio (W/d)

Figure 3.9, **Figure 3.10** and **Figure 3.11** also shows PLIF images at Reynolds numbers below and above the flow regime transition. PLIF images show that before the flow regime transition, the flow has an increasing dynamics with the symmetry between both fluids being increasingly broken, nevertheless the onset of a vortex street clearly engulfing both streams are only observed at higher Reynolds number. The transition Reynolds numbers depends on the geometry.

For, $W/w = 6$, and, $W/d = 1$, 1.5, 2, the flow regime is chaotic after impingement of the jets, as showed in **Figure 3.9**, **Figure 3.10** and **Figure 3.11**. The jets impinge on each other close to the chamber axis and are directed towards the outlet, with formation of circular vortices on both sides of the jets. These vortices evolve throughout the mixing chamber towards the outlet. The interface between the two fluid streams, the black and white fluid, which was clearly seen for Re=50 is completely disturbed with the formation of these vortices that promote the engulfment of jets with the surrounding fluid. The upper vortices are disturbed at this flow regime by jets oscillations, which are a dynamic evolution of the jets impingement point location that is clearly observed from the dynamic visualization of several PLIF images. These oscillations are the underlying mechanism causing the impingement point of the jets to be off the chamber axis, as clearly seen from **Figure 3.9**, **Figure 3.10** and **Figure 3.11**.

For $W/w = 6$, and, $W/d = 3$ and 6 geometries the vortex street formation downstream the injectors is not taking place. For the $W/d = 3$ the oscillation of the jets is still observable at the lower half of the mixing chamber, but the flow keeps a markedly segregated pattern between the opposed streams at Re=300, a pattern which was already observed for Re=50. For $W/d = 6$ no or only very slight oscillations occur at Re=300 when compared with $W/d = 1$, 1.5, 2 at same Reynolds number. The flow is becoming increasingly steady and parallel for shallow mixing chambers.

The range of values of Re that comprise the flow regime transition for the $W = 6$ mm geometries are listed in **Table 3.2**. For the cases of the deeper chambers, the flow regime transition occurs at Re values in the range of 150 to 200. For the shallow chambers, the transition occurs at high Reynolds number and the flow regime has distinct features than those

described for the deeper chambers. The mixing of both fluids is not promoted by large coherent vortices engulfing both streams, but by flow structures that are not so clear from the PLIF images in the chosen plane. Bothe et al. (2008) reported flow patterns in the normal direction to this imaged plane, from where it is clear a rotation of the flow that caused a similar pattern to the one observed in **Figure 3.13** in the range of Reynolds numbers 400 to 548. The strias observed in this PLIF images are due to the rotation of the fluid: two symmetric hellicoidal vortices, one in each side of the mixing chamber. After this when increasing Re to 585 the flow regime goes to turbulent flow regime without going through chaotic regime.

The transition Reynolds number depends on the geometry, which can be due to the fact that the characteristic dimension chosen for the Reynolds number equation is the jets width (see (3.1)) and not the hydraulic diameter of the jet (D_{Hjet}). Other authors, such as Hoffmann et al. (2006); Engler et al. (2004); Bothe et al. (2008) and Soleymani et al. (2008) used the mixing chamber hydraulic diameter and average velocity in the mixing chamber for the computation of the Reynolds number.

$$D_{Hjet} = 2\frac{wd}{w+d} \tag{3.2}$$

The Reynolds number is then defined as

$$Re_{Hjet} = \frac{\rho \upsilon_{inj} D_{Hjet}}{\mu} \tag{3.3}$$

The range of values of Re and Re_{Hjet} that comprise the flow regime transition for the W = 0.006 m geometries are listed in **Table 3.2**.

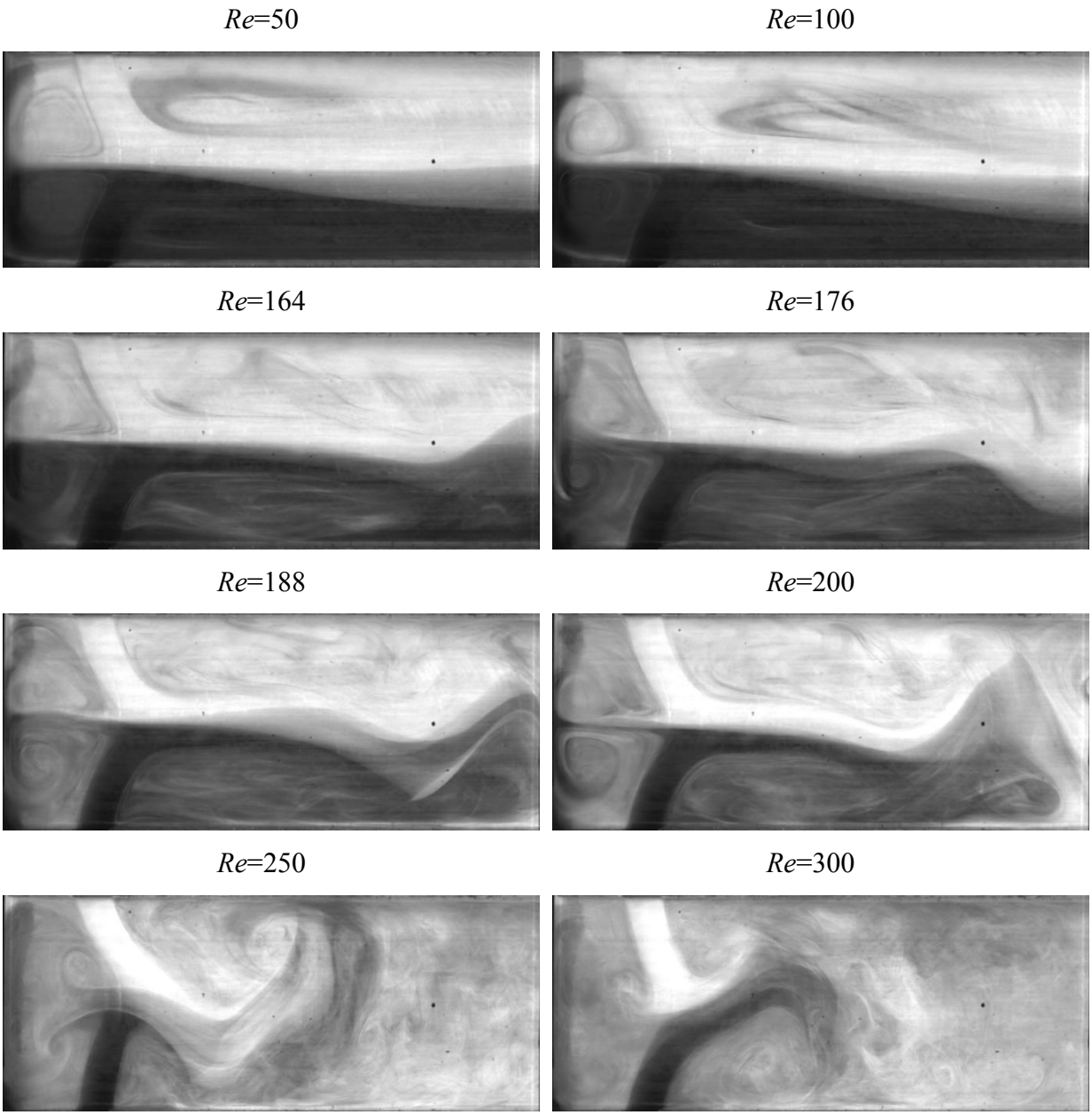

Figure 3.9 PLIF images of the T-jets mixer obtained for geometry with dimensions $W = 6$ mm; $w = 1$ mm and $d = 6$ mm with ratios W / w=6; $W / d = 1$ at different Reynolds number.

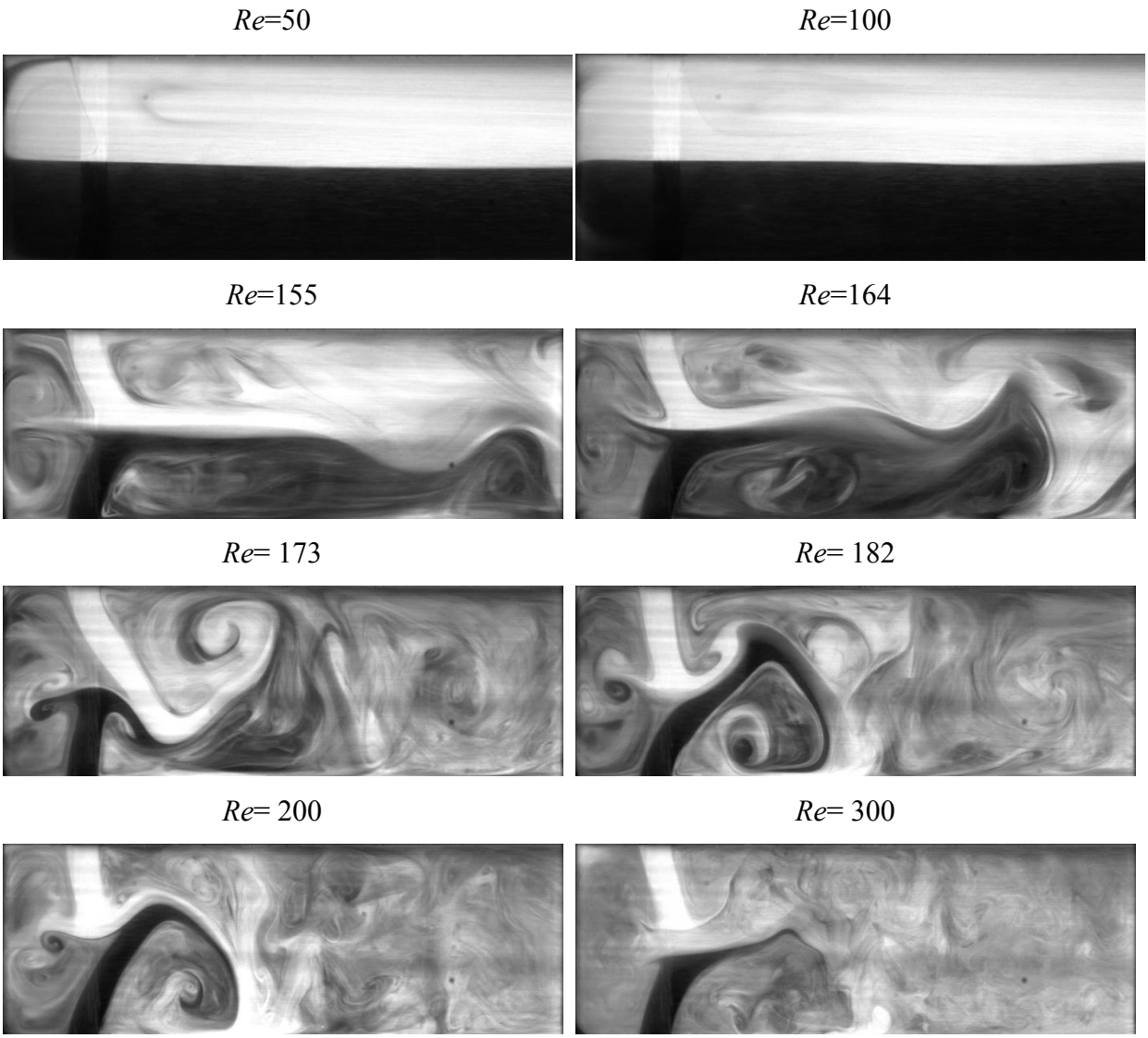

Figure 3.10 PLIF images of the T-jets mixer obtained for geometry with dimensions $W = 6$ mm; $w = 1$ m and $d = 4$ mm with ratios W / w=6; $W / d = 1.5$ at different Reynolds number.

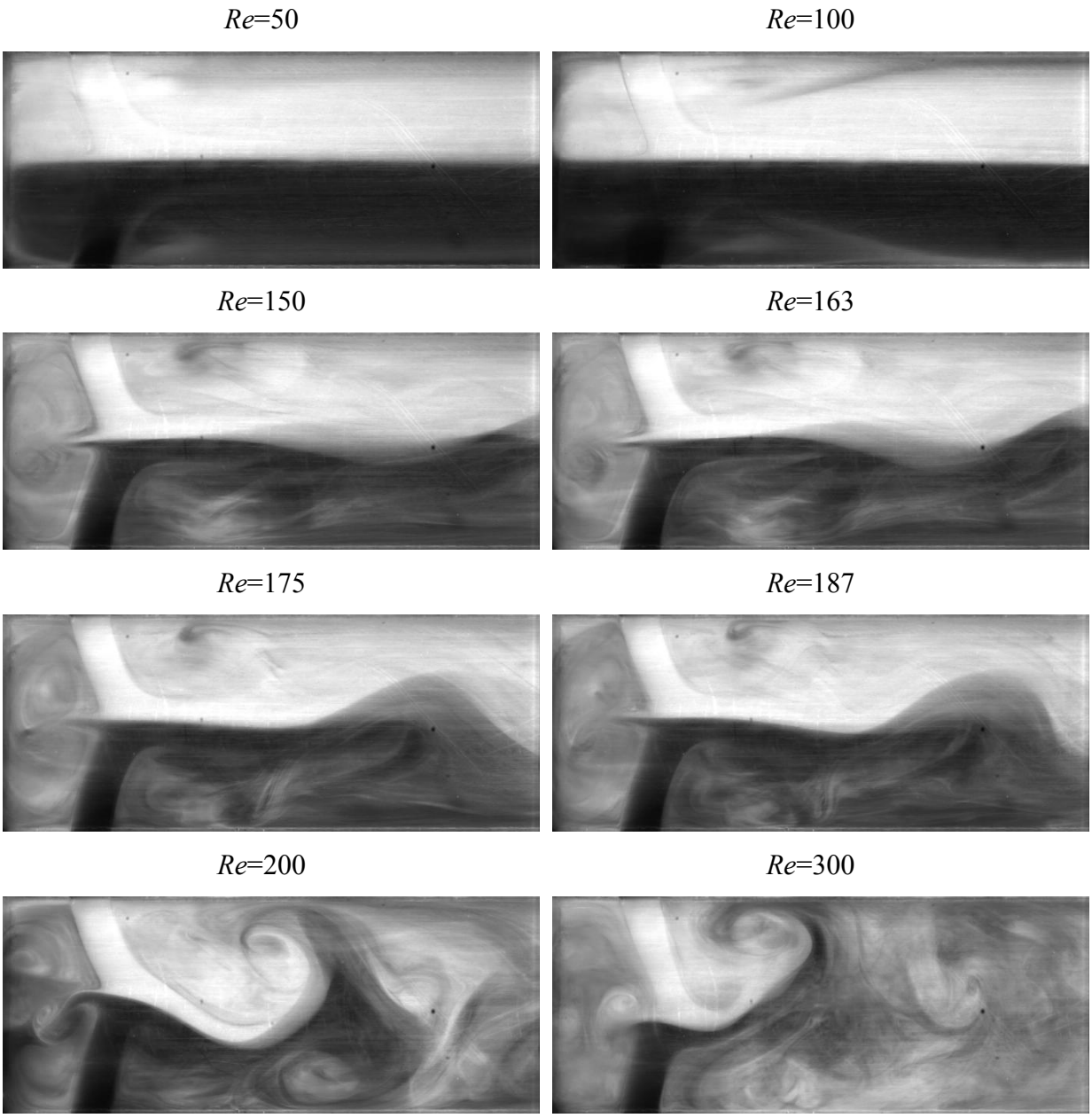

Figure 3.11 PLIF images of the T-jets mixer obtained for geometry with dimensions $W = 6$ mm; $w = 1$ mm and $d = 3$ mm with ratios $W / w = 6$; $W / d = 2$ at different Reynolds number.

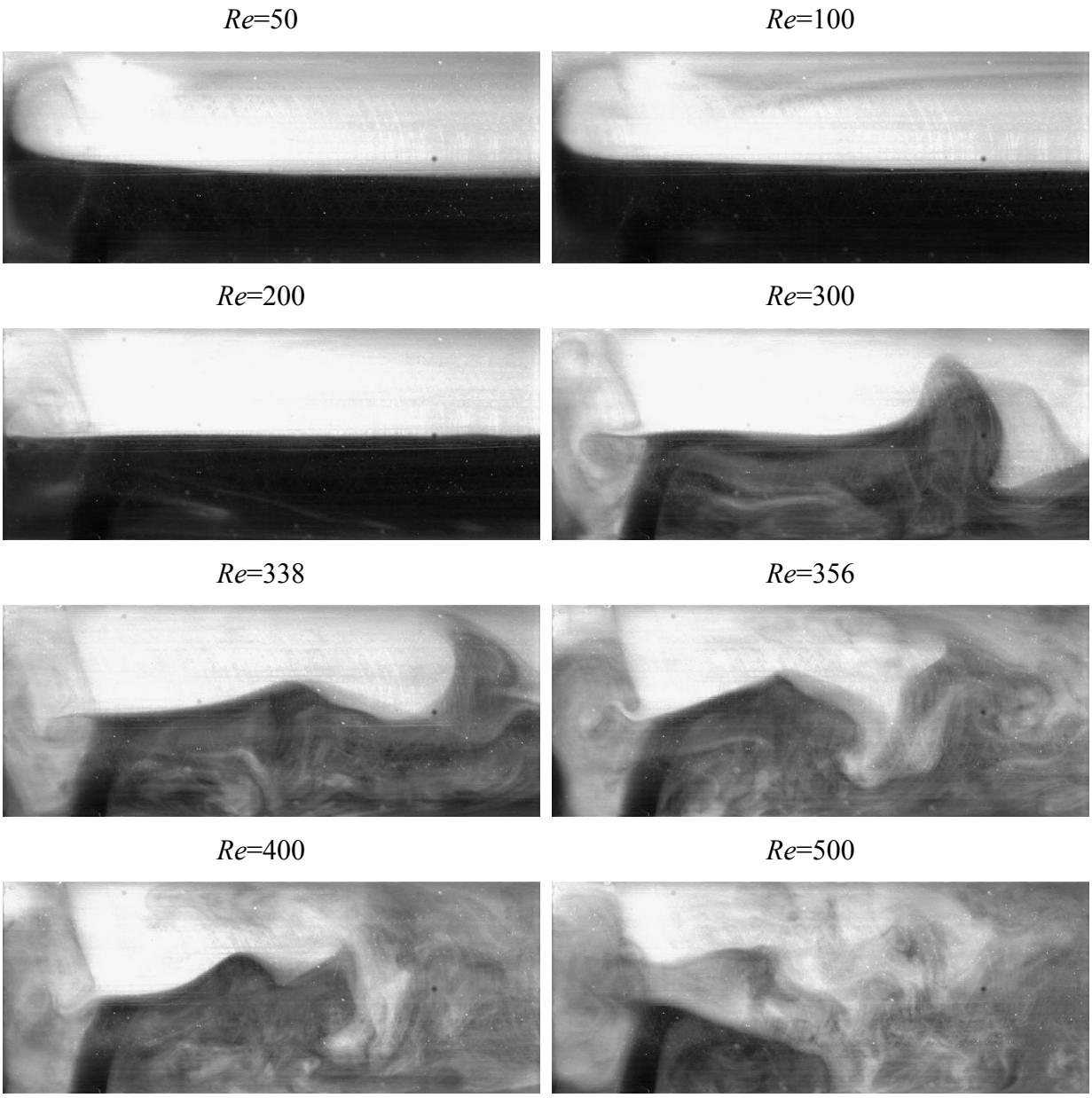

Figure 3.12 PLIF images of the T-jets mixer obtained for geometry with dimensions W = 6 mm; w = 1 mm and d = 2 mm with ratios W / w=6; W / d = 3 at different Reynolds number.

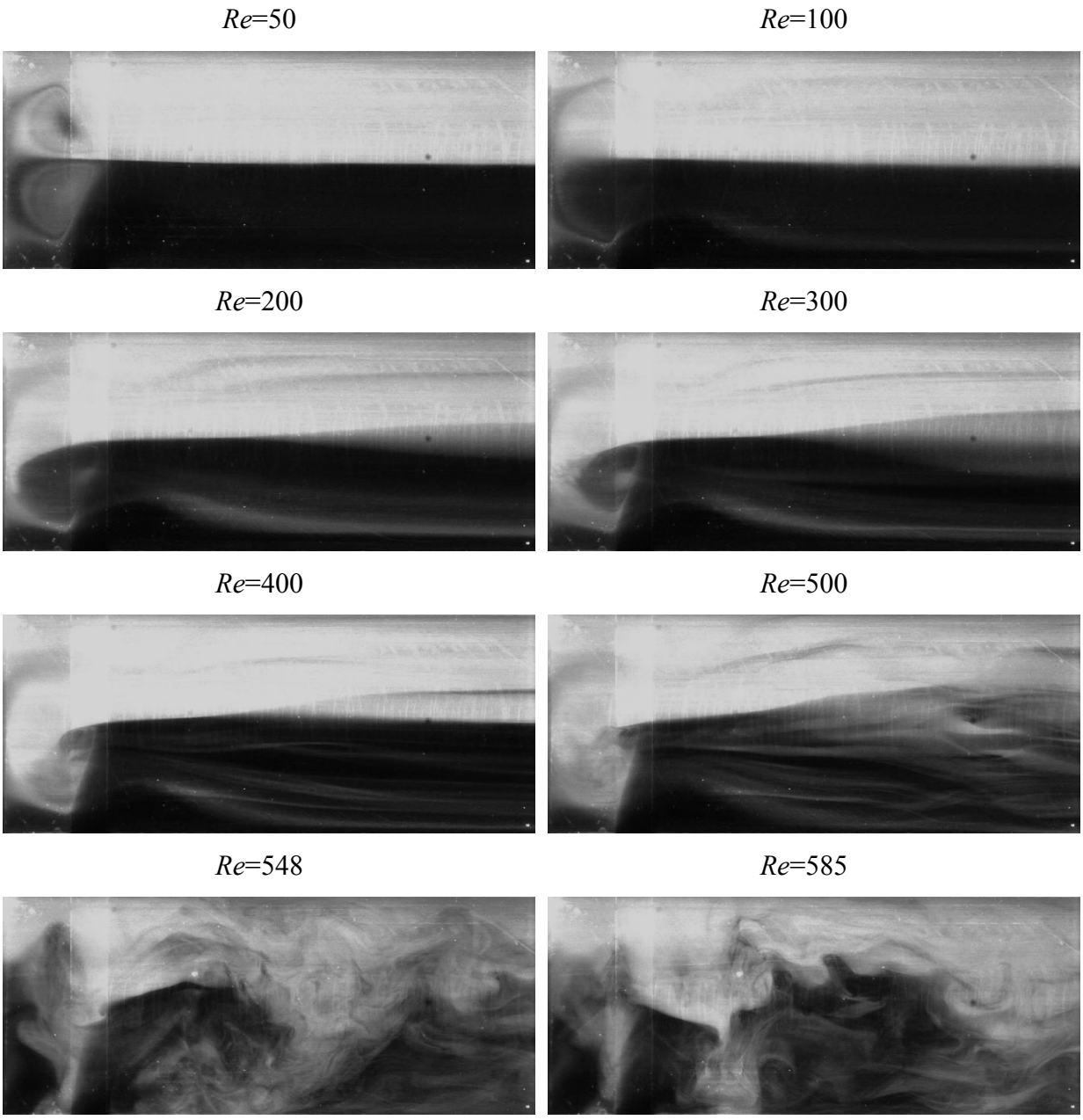

Figure 3.13 PLIF images of the T-jets mixer obtained for geometry with dimensions W = 6 mm; w = 1 mm and d = 1 mm with ratios W / w=6; W / d = 6 at different Reynolds number.

Table 3.2. Transition Reynolds numbers for the T-jets mixer geometries studied.

W/w **ratio**	W/d **ratio**	**Transition** Re	Re_{Hjet}
1	0.5	-	-
2	0.5	-	-
4	0.5	-	-
6	1	164 -200	281-343
6	1.5	164 – 173	262-277
6	2	187-199	281-299
6	3	338-356	451-475
6	6	500-548	500-548

3.3.1.2 Effect of Width Ratio (W/w)

In addition to the clear impact of the depth of the chamber on the flow regime, the ratio of injectors width to chamber width, W/w, was also observed to be a critical geometrical parameter (Sultan et al., 2009; Sultan et al., 2010). The images in **Figure 3.14**, **Figure 3.15** and **Figure 3.16** show different flow regimes, for several values of W/w, $W/w = 1$, 2 and 4 with $W/d = 0.5$, for a fixed depth value of $d = 4$ mm and width $W = 2$ mm. Although for the lower Reynolds number, Re=50, the flow is segregated, steady and symmetric regardless of the T-jets geometry, and for high Reynolds Re=300 and above the flow regime depends on the T-jets geometry. The effect of W/w on the flow regime are as follows:

Figure 3.14 for $W/w = 1$, the PLIF shows after the jets impinge on each other and bend towards the outlet the flow becomes unstable, and although the interface between the segregated streams is still clear, the location of the interface evolves dynamically. Furthermore, fluid from one side of the chamber appears close to the opposite side. There are no visible vortices engulfing both fluids in the imaged plane, so fluid transport namely convective mechanism is occurring through flow rotation that can only be observed in the normal plane to the imaged plane (Bothe et al., 2008).

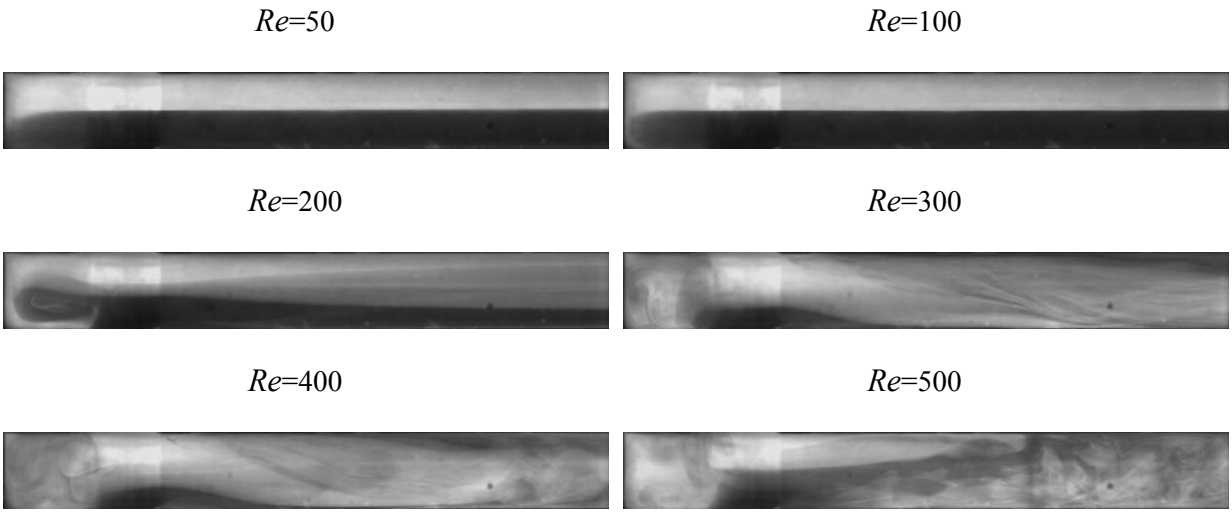

Figure 3.14 PLIF images of the T-jets mixer obtained for geometry with dimensions W = 2 mm; w = 2 mm and d = 4 mm with ratios W/w=1; W/d = 0.5 at different Reynolds number.

Figure 3.15 and **Figure 3.16** for $W/w = 2$ and 4, after the impingement point the jets bend towards the outlet and a boundary layer is formed in the contact region of the jets. The jets impingement point oscillations are not as clear from the dynamic observation of the PLIF images as those observed for $W/w = 6$ with deeper mixing chambers $W/d = 1$, 1.5, 2. The vortices having a scale of approximately half the chamber width that engulfs fluid from both jets, observed in $W/w = 6$ geometries, are not occurring in these geometries. In these cases, $W/w = 2$ and $W/w = 4$, mixing is promoted by smaller vortices formed in the contact region of both jets giving rise to a seemingly pattern with a Kelvin-Helmholtz instability although in these cases the two fluid streams have equal velocities. This instability grows throughout the T-jets mixer and consequently at downstream positions in the mixing chamber both fluids are increasingly homogenized. The main difference between $W/w = 2$ and $W/w = 4$, is the onset of the instability that occurs at upstream positions in the T-jets mixer for the $W/w = 4$ case.

When the jets collide and bend towards the outlet, the original width of the jets is roughly maintained, the small amount of thickening of the jets at the early stages is observed from **Figure 3.15** and **Figure 3.16**. If the jets keep the width w or are at most halved to $w/2$ shortly after impinging each other, the space occupied by the merged jet in the chamber axis is roughly $W-w$ to $W-w/2$, and the space for vortices formation in each side of the chamber is around $W-w/2$ to $(W-w/2)/2$. When the values of w are closer to the value of W the space for vortices formation is much smaller. This is clearly seen from **Figure 3.17**

that shows PLIF images of the flow in the T-jets mixer for the $W/w=2$ geometry and where the jets path are made clear by a dashed line. The case $W/w=1$ highlights these mechanisms in a clear way. From **Figure 3.14** is observed that for this specific case the initial width of the jets is equal to the width of the mixing chamber, the combined jet occupies the entire width of the mixing chamber, and so flow rotation can only occur in the normal direction to the imaged plane.

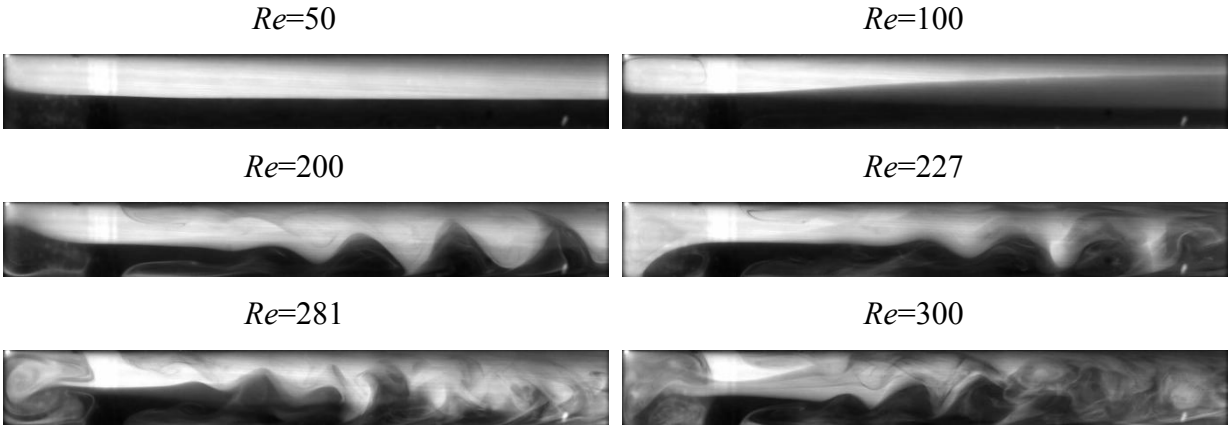

Figure 3.15 PLIF images of the T-jets mixer obtained for geometry with dimensions $W=2$ mm; $w=1$ mm and $d=4$ mm with ratios $W/w=2$; $W/d=0.5$ at different Reynolds number.

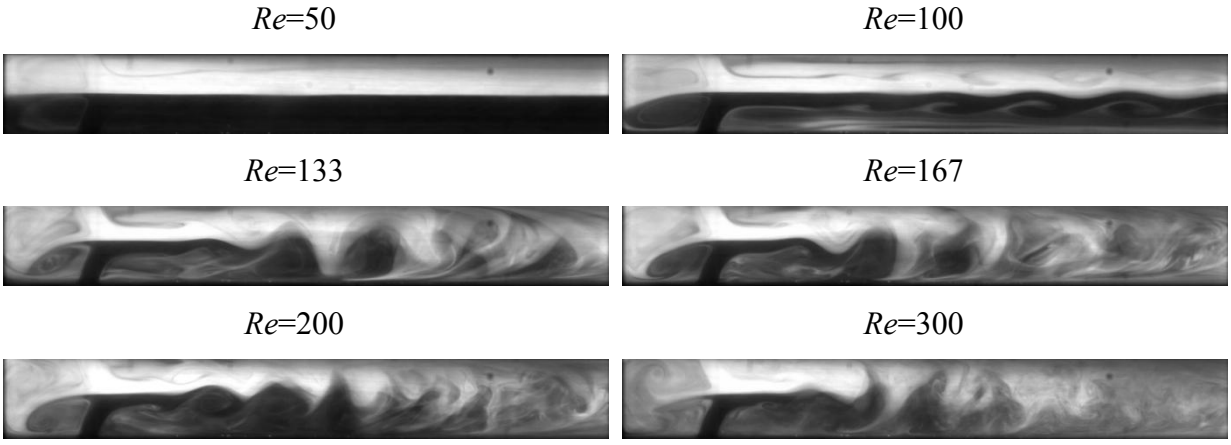

Figure 3.16 PLIF images of the T-jets mixer obtained for geometry with dimensions $W=2$ mm; $w=0.5$ mm and $d=4$ mm with ratios $W/w=4$; $W/d=0.5$ at different Reynolds number.

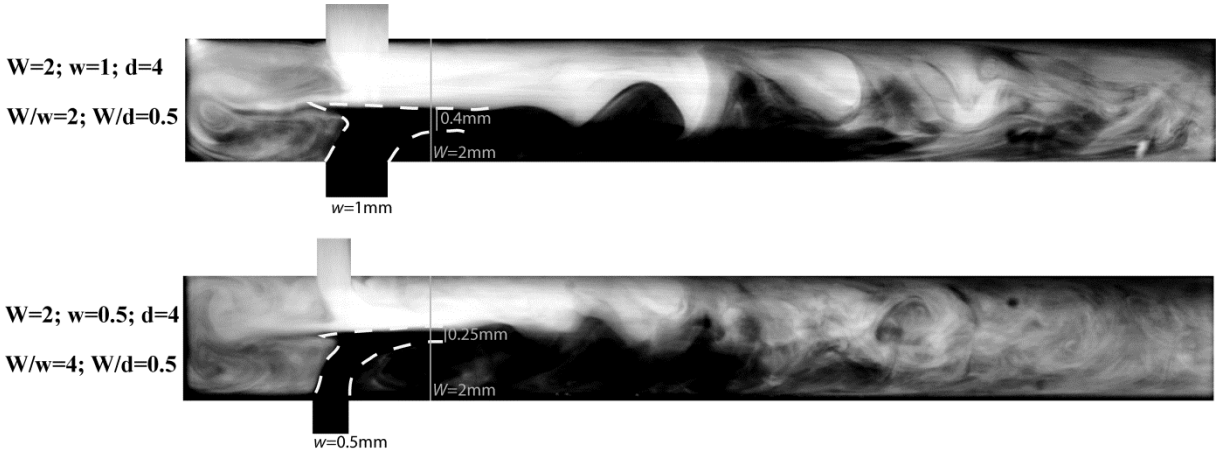

Figure 3.17 PLIF images of the T-jets mixer obtained for geometry with dimensions W/w=2 and 4 with fixed ratio W/d = 0.5 at *Re*=300.

3.3.2 Quantification of Mixing: - Intensity of Segregation (I_s)

The actual quantification of the effect of the Reynolds number in the range of 50 to 600 and the T-jets geometry on mixing is made from the computation of the intensity of segregation, I_s, defined by Danckwerts (1952) as

$$I_s = \frac{\sigma_{C_A}^2}{\overline{C_A}(1-\overline{C_A})} \tag{3.4}$$

where C_A is the local concentration of the species A at each point in the probed line, $\sigma_{C_A}^2$ is the variance of C_A, and $\overline{C_A}$ is the averaged concentration of A. , $\sigma_{C_A}^2$ is defined as

$$\sigma_{C_A}^2 = \overline{(C_A - \overline{C_A})^2} \tag{3.5}$$

The plots of the average intensity of segregation, computed from 50 images, versus the Reynolds number for different geometries are shown in **Figure 3.18**, **Figure 3.19** and **Figure 3.20**. Here, the intensity of segregation is calculated in a line of the imaged domain, normal to the T-jets axis, at a fixed distance of 14 mm from the top of the T-jets mixing chamber. The values of intensity of segregation reported in this work are the average values obtained from the 50 images that were captured at each studied Reynolds number and geometry.

3.3.2.1 Effect of Depth (W/d)

The maximum segregation between both fluids, that marks the onset of the flow regime transition, depends on the geometry. For the deeper chamber, from the plots of I_s in **Figure 3.18**, it is seen that the maximum segregation of both fluids occurs for $Re<100$. At low Reynolds numbers, the fluid streams introduced through each injector flow side by side with no convective mixing mechanisms being observed in the imaged plane (see **Figure 3.9-Figure 3.11**). When the fluid streams go through parallel paths the mixing between streams is mainly based on molecular diffusion through the concentration gradient. When vortex flow occurs there is also some convective mechanisms due to the vortices that have the rotation axis aligned with the T-jets mixing chamber axis. These vortices do not break the flow symmetry, and thus are not promoting mixing of both fluid streams significantly, as can be seen from the fact that the two fluids flow through the mixing chamber in the side they were originally introduced. The only visible effect of these vortices is from streaks of fluid introduced from the opposite side of the chamber that are observable in each stream.

For higher Reynolds numbers the I_s value decreases, the characteristics of the I_s evolution with the Reynolds number depend on the T-jets geometry. For the $W/w=6$ in the geometries having larger depths, $W/d=1$ to 2, a steep decrease of I_s occurs from $Re=100$ to $Re=200$. This steep decrease of I_s is clearly visible in **Figure 3.18** and is associated with a flow regime transition from segregated steady parallel flow at $Re<100$ to chaotic flow regime; characterized by the formation of vortices having rotation axis normal to the mixing chamber axis, these vortices promote a fast homogenization of both fluids as is seen from the PLIF images in **Figure 3.9** and so the onset of these vortices is related to a decrease of an order of magnitude of I_s.

$W/w=6$; $W/d=1$; W =6 mm; w =1 mm; d =6 mm

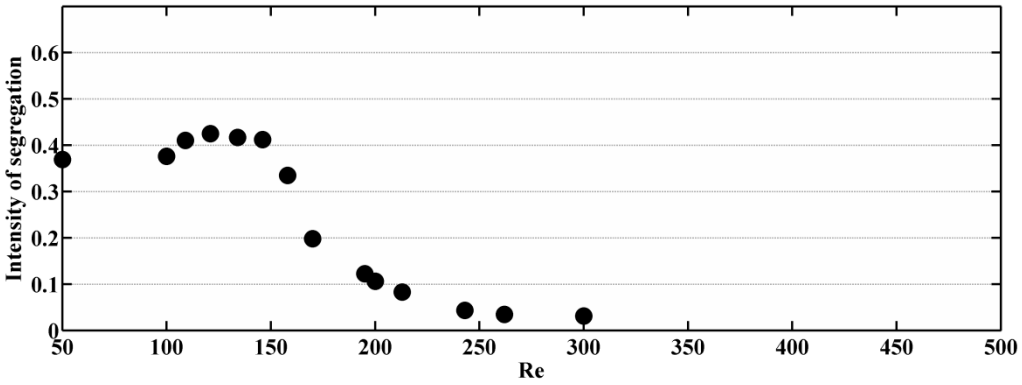

$W/w=6$; $W/d=1.5$; W =6 mm; w =1 mm; d =4 mm

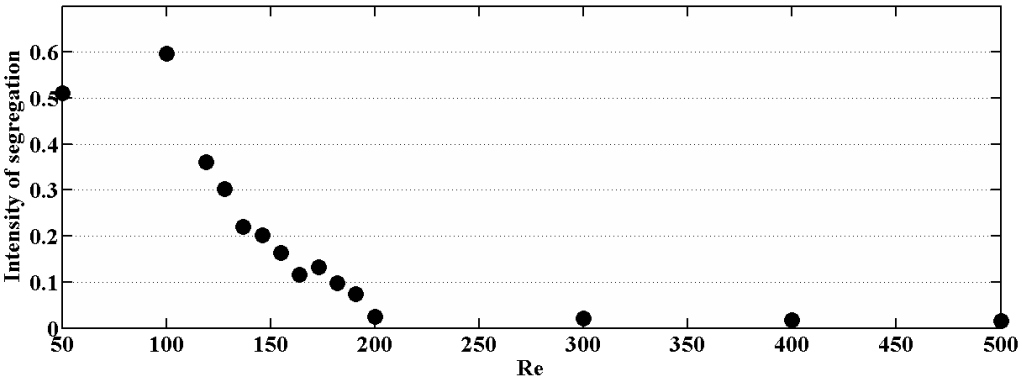

$W/w=6$; $W/d=2$; W =6 mm; w =1 mm; d = 3 mm

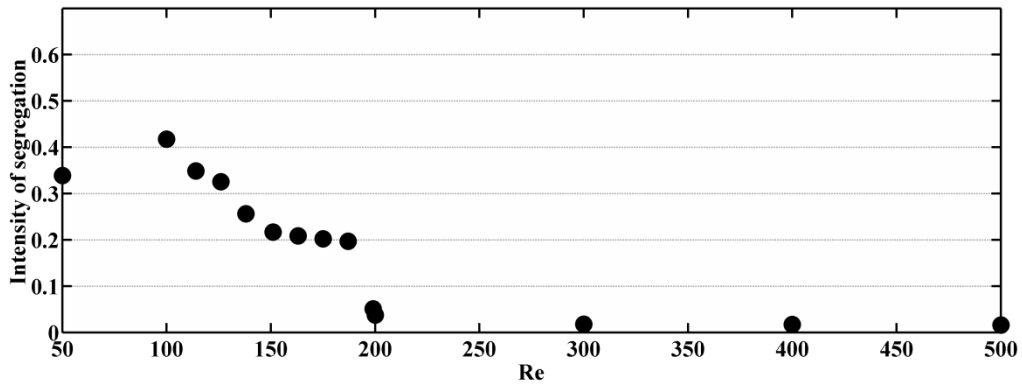

Figure 3.18 Intensity of segregation versus Reynolds number probed at y=14 mm in different geometries for $W/w=$ 6; with varying $W/d=1$; $W/d=1.5$; $W/d=2$.

For the shallow geometries, $W/d=3$ to 6, the I_s decrease is not as steep as observed in the deeper chambers, and the decrease of I_s seen in **Figure 3.19** occurs in a higher range Reynolds numbers. For these geometries, the transition of flow regime occurs above $Re=$

350 for $W/d=3$ and above $Re=500$ for $W/d=6$ as seen from **Figure 3.12** and **Figure 3.13** and **Table 3.2.**

In the geometries where the chamber depth is at least half the chamber width, it is observed the formation of coherent structures, larger vortices that are formed immediately downstream the injectors. These vortices are formed between the jets and the mixer walls and are associated with a fast decrease of the I_s.In these chambers, $W/d=1$ to 2, the values of I_s are 10 to 30 times lower than in the cases with width to depth ratios of $W/d=3$ and 6. A strong wall effect on the shallow geometries is restraining the vortex formation leading to higher values of I_s as seen in **Figure 3.18** and **Figure 3.19**, the values from **Table 3.3**.

$W/w=6;\ W/d=3;\ W=6$ **mm;** $w=1$ **mm;** $d=2$ **mm**

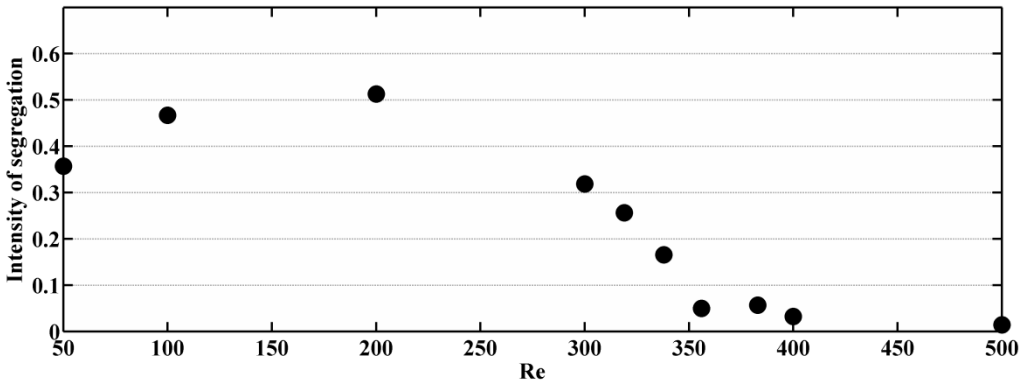

$W/w=6;\ W/d=6;\ W=6$ **mm;** $w=1$ **mm;** $d=1$ **mm**

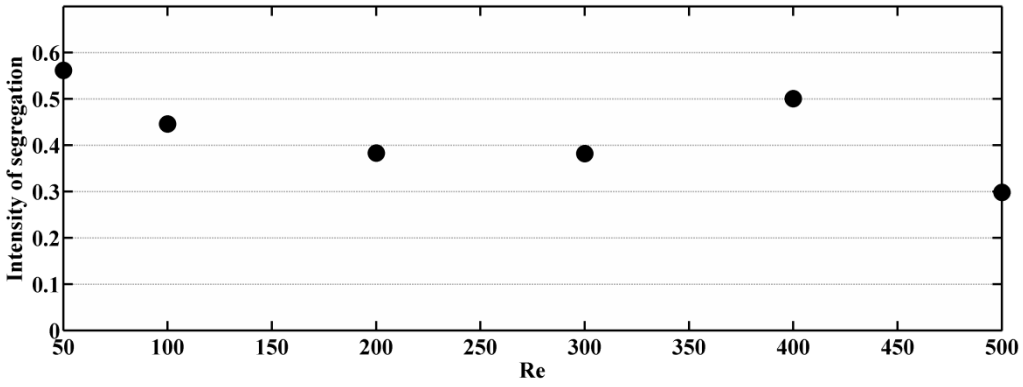

Figure 3.19 Intensity of segregation versus Reynolds number probed at y=14 mm in different geometries for $W/w=$ **6; with varying** $W/d=3;\ W/d=6$.

3.3.2.2 Effect of Width (W / w)

For the geometries, $W / w = 1$, 2 and 4 with fixed ratio $W / d = 0.5$, the evolution of I_s with the Reynolds number is also mainly affected by the transition from steady to dynamic flow regimes, as can be observed from the plots in **Figure 3.20**. The flow regime transition occurs at Reynolds number around 200. For $W / w = 1$, fluid mixing occurs in the normal plane to the imaged plane (Bothe et al., 2008), through helicoidal vortices that first are generated in each half of the mixing chamber (vortex flow regime) and later evolve to drag fluid from both sides of the mixing chamber (engulfment flow regime). The I_s values in the engulfment flow regime for $W / w = 1$, see **Table 3.3**, are slightly higher than those reported for the chaotic flow regimes in the $W / w = 6$ geometries, although the differences are not so clear. One should bear in mind that the line where I_s values are calculated is located at a distance from the jets of $12 / W = 2$ for the $W / w =$ 1 geometry and at $12 / W = 2$ for the $W / w =$ 6, i.e. in the $W / w =$ 1 the mixing length is larger.

In the case with $W / w = 2$ and $W / w = 4$, the smaller vortices formed in the contact region between the jets similar to Kelvin-Helmholtz pattern gives rise to instability which leads to homogenization of both fluids downstream and therefore it leads to decrease in the values of I_s.

Comparing the intensity of segregation of the geometries having a depth of 4 mm, i.e. the cases where W / w was in the range of 1 to 4 and the one with $W / w = 6$ and $W / d = 1.5$, the geometries where the jets expansion in the chamber is larger have better mixing performance, i.e. lower I_s values. The values of I_s at higher Reynolds numbers are two to four times higher for $W / w = 1$, 2 and 4, than in the $W / w = 6$ geometries with $W / d = 1$, 1.5 and 2, as showed in **Table 3.3.** Although the chamber with $W / w = 6$ is much larger, the fluid at the probed line was more homogenous than in the other geometries. Thus, the best degree of mixing is observed in the geometries having wider and deeper chambers compared to the jets width.

$W / w = 1$; $W / d = 0.5$; W =2 mm; w =2 mm; d =4 mm

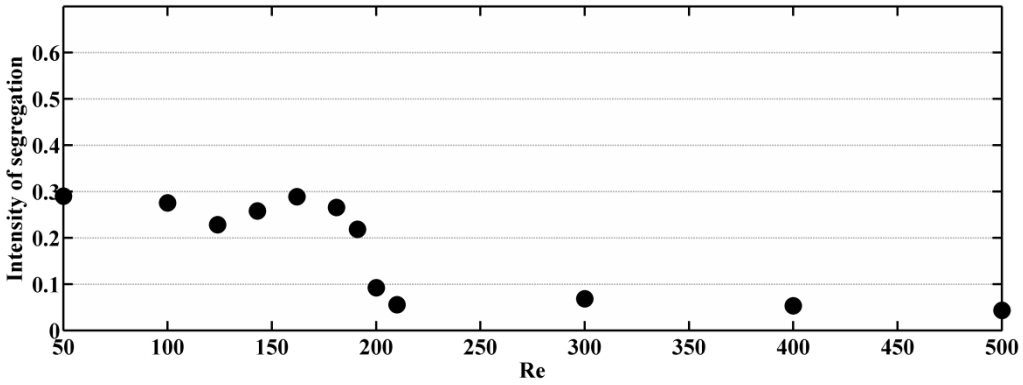

$W / w = 2$; $W / d = 0.5$; W =2 mm; w =1 mm; d = 4 mm

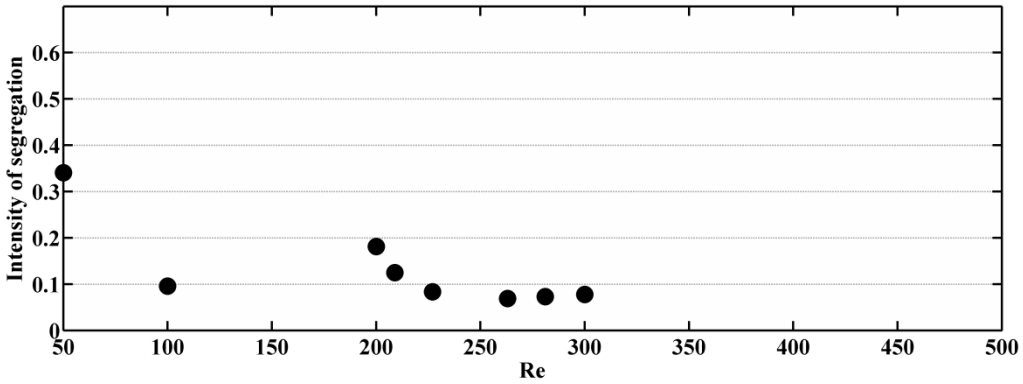

$W / w = 4$; $W / d = 0.5$; W =2 mm; w =0.5 mm; d =4 mm

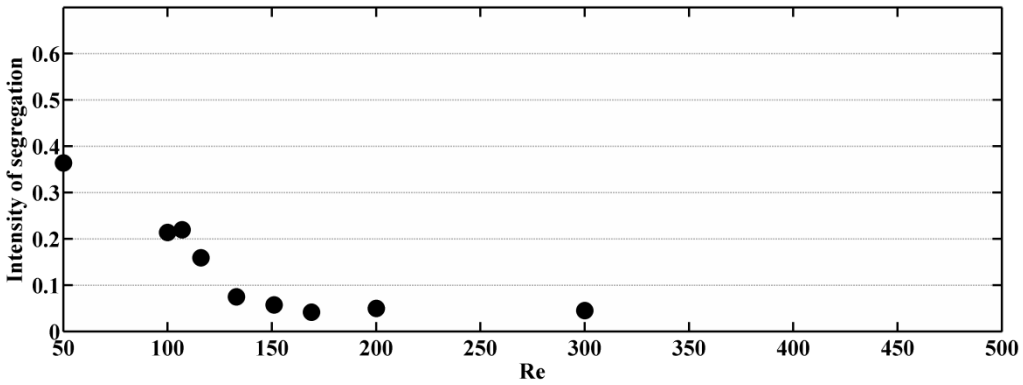

Figure 3.20 Intensity of segregation versus Reynolds number probed at y=14 mm for geometries for $W / d = 0.5$ with varying $W / w = 1$; $W / w = 2$; $W / w = 4$.

Table 3.3. Intensity of segregation for different geometrical ratios.

W/w ratio	W/d ratio	I_s	
		***Re* 200**	***Re* 300**
1	0.5	0.092	0.068
2	0.5	0.22	0.043
4	0.5	0.071	0.071
6	1	0.11	0.031
6	1.5	0.026	0.021
6	2	0.037	0.018
6	3	0.51	0.32
6	6	0.38	0.38

3.3.2.3 Segregation Profiles

The plots of the I_s computed from Equation (3.4) along the complete mixing chamber are represented in **Figure 3.21** and **Figure 3.22** for all the geometries studied at Reynolds number 300. It is visible from the plots that the I_s is maximum around $y = 2$ to 3 mm where the impingement of the jets occur, since both jets are positioned at $h = 2$ mm for all the geometries.

It is observed from **Figure 3.21** for $W/w = 6$ geometries having larger depths, $W/d =$ 1 to 2, has the steepest decrease of I_s along the mixing chamber after the jets impingement point. For the $W/w = 6$ geometry with shallow chamber $W/d = 3$ to 6 (see **Figure 3.21**) at high Reynolds number the I_s tends to decrease but not steep as observed in $W/d = 1$ to 2.

For $W/w = 1$, 2, 4 and 6 with fixed ratio $W/d = 0.5$ it is seen that the decrease in I_s is observed for $W/w = 6$ geometry (see **Figure 3.22**). The rate of I_s decrease for the other geometries is slower with decreasing W/w values.

The I_s tends to asymptotical values that are listed in **Table 3.4**. The location below the impingement point, $l = y - h$, where the asymptotical value of I_s is reached are also listed in **Table 3.4**. The values of l were normalized by the chamber width l/W that stands for the distance in number of chamber widths at which the asymptotical value of I_s was reached. The time for two fluids to mix, which here is assumed as the time the fluids take in the reactor to converge to the minimum observed value of I_s, in T-jets mixing chamber can be related to l both in terms of injectors velocity and Reynolds number as follows:

$$t_{mix} = \frac{lW/w}{2\upsilon_{inj}} \tag{3.6}$$

$$t_{mix} = \frac{\rho l W}{2\mu Re} \tag{3.7}$$

The t_{mix} is computed considering the distance for mixing to achieve the lowest I_s value, l, divided it by the average velocity in the mixing chamber. The average velocity is an assumption that does not consider the existence of heterogeneities, such as dead volumes in the mixer from the jets inlet up to l. The asymptotical values of I_s in **Table 3.4** are not coincident with the I_s values in **Table 3.3** due to the fact that the values in **Table 3.3** are obtained at a specific position y= 14 mm while the values in **Table 3.4** are obtained from a trend line drew after the values of I_s stop decreasing with the distance y from the jets impingement point.

From **Figure 3.22** it is observed that the I_s value decrease is steeper for $W/w = 6$ than for $W/w = 1$, 2 and 4. Even though the evolution of I_s differs with W/w the values, at $y =$ 14 mm they are very close. The length l at which the values of I_s start to decrease slowly is much shorter for $W/w = 6$ geometries. The I_s profile and the l value consistently show that mixing is faster in the $W/w = 6$ T-jets reactors having largest depth values. Thus, the geometries operating under chaotic flow regime have considerable advantage for fast

chemical reaction where mixing is affecting the reaction products (Johnson and Prud'homme, 2003; Pieper et al., 2011 and Schwarzer et al., 2006).

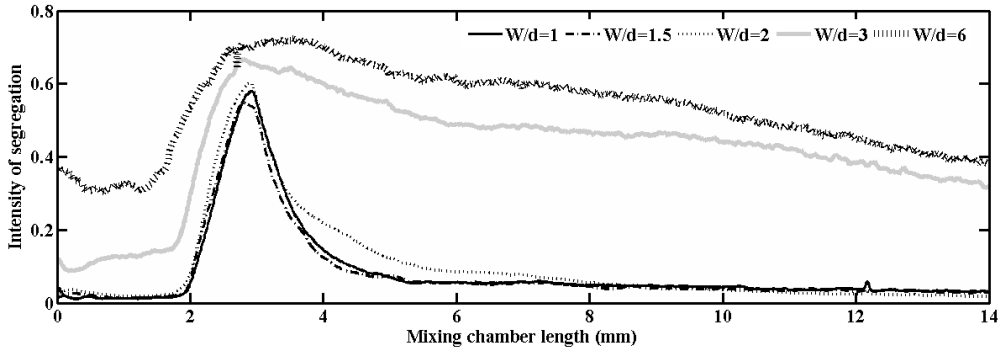

Figure 3.21 Intensity of segregation probed along the mixing chamber length at Re= 300 for different geometries for $W / w =$ 6; with varying $W / d =$ 1, 1.5, 2, 3 and 6.

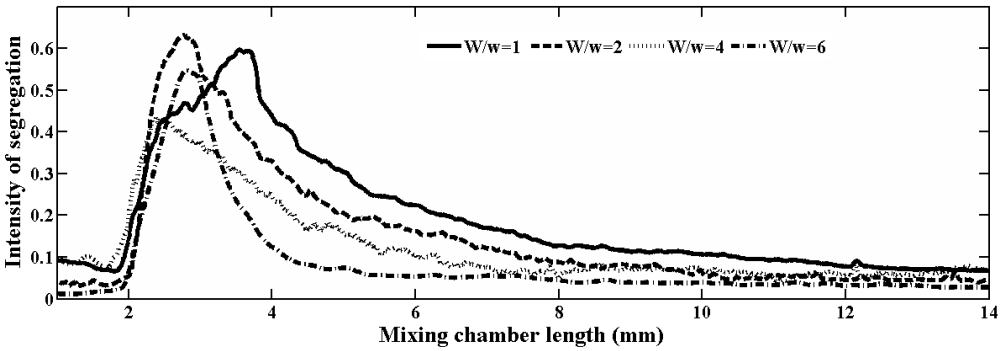

Figure 3.22 Intensity of segregation probed along the mixing chamber at different Reynolds number for different geometries for $W / w =$ 1, 2, 4 and 6 with fixed depth of $d =$ 4 mm.

Table 3.4. Decrease of intensity of segregation for different geometrical ratios.

W/w **Ratio**	W/d **ratio**	**Minimum** I_s	l **mm**	l/W
1	0.5	0.12	6	3.0
2	0.5	0.09	5.7	2.8
4	0.5	0.08	4.2	2.1
6	1	0.1	2.4	0.4
6	1.5	0.07	2.5	0.4
6	2	0.125	2.8	0.4
6	3	0.48	4	0.6
6	6	0.59	4.2	0.7

3.4 Results Discussion

From previous works of Hoffmann et al. (2006), Engler et al. (2004), Bothe et al. (2008) and Soleymani et al. (2008) on T-jets mixers the following flow regimes were identified: steady, vortex and engulfment. In these flow regimes, the main convective flow patterns promoting mixing of both fluid streams were perpendicular to the main flow direction, which is clear from the PLIF images of Hoffmann et al. (2006) and the pathlines from CFD simulation showed by Soleymani et al. (2008). **Table 3.5** has a complete list of works on the Reynolds number transition from vortex to engulfment flow. Soleymani et al. (2008) proposed a parameter for the identification of flow regime transition, which is also shown in **Table 3.5,** this parameter is computed as,

$$K = Re_H^{\alpha}\left(\frac{w}{W}\right)^{\beta}\left(\frac{D_{Hjet}}{D_H}\right)^{\gamma}\left(\frac{W}{d}\right)^{\zeta} \tag{3.8}$$

where D_H is the hydraulic diameter of the mixing chamber and D_{Hjet} is the hydraulic diameter of the jets inlets. The parameters $\alpha, \beta, \gamma, \zeta$ were find to be 0.82, -0.79, -1.5 and 0.15 by Soleymani et al. (2008), and the flow regime transition from vortex to engulfment flow occurs at $K = 100$. The Reynolds number Re_H is defined using the average velocity in the mixing chamber and the chamber's hydraulic diameter, and it is related to Re_{Hjet} as

$$Re = Re_{Hjet} \frac{D_H}{D_{Hjet}} \frac{2w}{W} \tag{3.9}$$

Table 3.5. Comparison of Reynolds number and identification number, K, at the onset of engulfment flow regime with other literature data.

Other authors	W	W / w	W / d	Re_H	Re_{Hjet}	K
Soleymani et al. (2008)	1.6	4	5.33	132	209	100
	1	2	3.33	241	261	98.2
	0.2	1	1	270	135	98.6
	0.3	1	1	273	137	99.5
	0.1	1	1	278	139	101
	0.2	1	2	477	358	101
	0.8	2	2	141	106	99.0
Bothe et al. (2008)	0.2	2	2	140	105	98.3
Hoffmann et al. (2006)	0.4	2	2	135	101	95.4
	0.4	2	2	150	113	104
	0.4	2	4	300	375	101
	0.4	2	4	315	394	105
	0.4	4	4	100	125	109
Engler et al.(2004)	0.6	2	2	145	108	101
This work	6	6	1	300	257	1641
	6	6	1.5	160	160	600
	6	6	2	133	150	360
	6	6	3	313	466	326
	2	1	0.5	400	200	152
	2	2	0.5	533	466	565
	2	4	0.5	266	177	1337

The values of Reynolds numbers for K computation were identified from **Figure 3.18** to **Figure 3.20** as the values that mark the onset of a steep decrease of I_s. This transition on mixing quality was proposed by Engler et al. (2004) to be the transition from vortex to engulfment flow regime. As can be seen in **Table 3.5** the value of K were very close to 100 for all works, except for this work. According to Soleymani et al. (2008) parameter criterion

of $K = 100$ the transition for the geometries, having $W / w = 6$ would be at Re in the range of 2 to 26, i.e. out of the range of studied Reynolds numbers, which was from 50 to 500. Furthermore, at $Re = 50$ a steady state is always observed from the PLIF experiments of the different geometries. The other authors had transition of flow regime associated with the $K =$ 100 identification numbers at Re_{Hjet} in the range of 100 to 400. The first observation when comparing this work and other works is that the geometrical parameters are quite distinct, the chambers width to jets width is larger in the present work for several cases where $W / w = 6$, and for the remaining cases where $1 \leq W / w \leq 4$ the chambers in the present work are always deeper than in other works. Both these geometrical parameters, W / w and W / d , were here observed to have a clear impact on the flow regime. Another important difference is that the T-jets geometries in this work have a headspace above the injectors, which was shown previously by Santos et al. (2002) to be a necessary condition to reach chaotic flow fields such as the ones here described. The two vortices formed upstream the jets when a headspace exists have a key role on the flow dynamics.

The chaotic flow regime that is here described has vortices with a rotation axis aligned with the z direction, and this flow regime is quite different from the engulfment flow regimes reported previously (Soleymani et al., (2008) and Engler et al., (2004)) where the vortices were helicoidal structures with the rotation axis aligned with the mixing chamber axis.

The identification number of Soleymani et al. (2008) is applicable to chambers that have engulfment flow regimes, which is not the case of the geometries here studied, which have chaotic flow regimes. From this work it is possible to set the design parameters for T-jets mixers to operate at chaotic flow regimes: $W / w = 6$ larger values were not tested, $W / w \leq 2$. The operation should be at Re_{Hjet} larger than 300, and only jets having equal momentum and viscosities were assessed in this study.

3.5 Conclusion

The PLIF experiments enabled a thorough characterization of the effect of the geometric parameter on the mixing degree. Nevertheless, the mechanisms underlying the dynamics of mixing, for the case of the self-sustainable chaotic flow regime are not fully accessible from

the PLIF experimental results that only show a particular plane of the flow field. From **Figure 3.9**, **Figure 3.10** and **Figure 3.11**, it is visible that for T-jets mixer $W/w=6$, $W/d=1.5$, the formation of vortices commences below $Re=200$, when compared to the T-jets mixers with ratios $W/w=6$, $W/d=1$, 2, where the formation of vortices occurs when $Re\geq 200$. Also the geometry with ratio $W/d=1.5$ achieves lowest I_s at $Re=200$ when compared with the geometries with ratios $W/d=1$ and 2 which achieves at $Re=300$ as seen in **Figure 3.10** and **Table 3.3** this could be due to self sustainable chaotic flow regime obtained at optimum value of W/d .The effect of chambers width to the chamber depth ratio W/d is thus quite clear and an important T-jets mixers design parameter. The complete structure of the flow will be characterized from 2D and 3D CFD simulation of the geometry in the next **Chapter 4** comprehensively. From PLIF results on T-jets mixer it was established the effect of geometrical and operational parameters on mixing and on the flow dynamics. The experiments showed the effect of chamber width to the injectors width, W/w, and the ratio of chambers width to the chambers depth, W/d on the flow regime. The different flow regimes obtained were described, with focus on a self-sustainable chaotic flow regime that differs from the other flow regimes previously reported in the literature (Bothe et al. 2006; Soleymani et al., 2008a). Values for the geometrical parameters as well as the operational conditions that enabled operation at flow regimes with high mixing dynamics were set for the generation of vortices : $W/w=6$, $W/d\geq 2$, *Re* must be 150 and above.

3.6 References

Bothe, D., Stemich, C., Warnecke, H., 2006. Fluid mixing in a T-shaped micro-mixer. Chemical Engineering Science 61, 2950-2958.

Bothe, D., Stemich, C., Warnecke, H., 2008. Computation of scales and quality of mixing in T shaped microreactor. Computers & Chemical Engineering 32, 108-114.

Danckwerts, P.V., 1952. The definition and measurement of some characteristics of mixtures. Applied Scientific Research 3, 279-296.

Engler, M., Kockmann, N., Kiefer, T., Woias, P., 2004. Numerical and experimental investigations on liquid mixing in static micromixers. Chemical Engineering Journal 101, 315-322.

Hoffmann,M., Schlüter,M., Räbiger,N., 2006. Experimental investigations of liquid-liquid mixing in T-shaped micro-mixers using μ-LIF and μ-PIV. Chemical Engineering Science 61, 2968–2976.

Ito, Y. and Komori, S., 2006. A vibration technique for promoting liquid mixing and reaction in a microchannel. AIChE Journal 52, 3011-3017.

Johnson, B.K., Prud'homme, R.K., 2003. Chemical processing and micromixing in confined impinging jets. AIChE Journal 49, 2264-2282.

Lee, L.J., Ottino, J.M., Ranz, W.E., Macosko. C.W., 1980. Impingement mixing in Reaction Injection molding. Polymer Engineering and Science 20, 868–874.

Malguarnera, S.C., Suh, N.P., 1977. Liquid injection molding I. An investigation of impingement mixing. Polymer Engineering Science 17,111–115.

Pieper, M., Aman, S., Hintz, W. And Tomas Jurgen., 2011. Optimization of continuous precipitation process to produce nanoscale $BaSO_4$. Chemical Enguneering and and Technology 34, 1567-1574.

Schwarzer, H.-C., Schwertfirm, F., Manhart, M., Schmid, H.-J. and Peukert, W., 2006. Predictive simulation of nanoparticle precipitation based on the population balance equation. Chemical Engineering Science 61, 167-181.

Santos, R.J., Teixeira, A.M.T., Costa, M. R. P. F. N., Lopes, J.C.B., 2002. Operational and Design Study of RIM Machines. International Polymer Processing 17, 387-394.

Santos, R.J., Teixeira, A.M.T., Lopes, J.C.B., 2005. Study of mixing and chemical reaction in RIM. Chemical Engineering Science 60, 2381–2398.

Santos, R.J., Ertugrul, E., Dias, M.M., Lopes, J.C.B., 2009. Dynamic behavior of the flow field in a RIM machine mixing chamber. AIChE Journal 55, 1338-1351.

Santos, R.J., Teixeira, A.M.T., Ertugrul, E., Sultan, M.A., Karpinska, A.M., Dias, M.M., Lopes, J.C.B., 2010.Validation of a 2D CFD Model for Hydrodynamics Studies in CIJ Mixers. International Journal of Chemical Reactor Engineering 8 (A32).

Sinton, D., 2004. Microscale flow visualization. Microfluidics and Nanofluidics 1, 2-21.

Soleymani, A., Kolehmainen, E. and Turunen, I., 2008a. Numerical and experimental investigations of liquid mixing in t-type micromixers. Chemical Engineering Journal 135, S219-S228.

Sultan, M.A., Monteiro, S.D., Dias, M.M., Lopes, J.C.B., Santos, R.J., 2009. Influência da geometria de misturadores em T na dinâmica do escoamento. Proceedings of the Third Conferência Nacional em Mecânica de Fluidos, Termodinâmica e Energia, Bragança, Portugal, 32-33.

Sultan, M.A., Fonte, C.P., Dias, M.M., Lopes, J.C.B., Santos, R.J., 2010. Effect of geometry on mixing in T-jets mixers. Proceedings of the Seventh European Congress of Chemical Engineering (ECCE 7) and Nineteenth International Congress of Chemical and Process Engineering (CHISA 2010), Summaries (3): Hydrodynamic Processes and System Engineering, Prague, Czech Republic, 889-890.

Tucker, C.L., Suh, N,P., 1980. Mixing for reaction injection molding. I. impingement mixing of liquids. Polymer Engineering Science 20,875–886.

Wong, S.H., Ward, M.C.L., Wharton, C.W., 2004. Micro T-mixer as a rapid mixing micromixer. Sensors and Actuators B 100, 359-379.

Zhongliang, T., Seungbae, H., Djordje, D., Vijay, M., Alan, C.W., James, Y. and Richard, M.O., 2002. Electrokinetic flow control for composition modulation in a microchannel. Journal of Micromechanics and Microengineering 12, 870.

4. DYNAMIC BEHAVIOUR OF FLOW FIELD IN T-JETS MIXER-3D and 2D CFD SIMULATIONS

4.1 Introduction

In this chapter, the analysis of the dynamic behaviour of the flow in T-jet mixers is made from the numeric simulation of the flow field. Taking into account that T-jets mixers are being widely used as micro mixers; a thorough study on the effect of the T-jet mixers geometry scale down on mixing is made using 2D and 3D Computational Fluid Dynamics (CFD) simulations.

This chapter starts (**Section 4.2**) by introducing and reviewing the governing continuity and conservation equations for fluid flow problems. A general overview of numerical CFD implementation, as applied by the commercial ANSYS FLUENT (version 14.0), is given in **Section 4.3**. Emphasis is given on the methods used in this work, namely a brief introduction to the available solvers, characterization of Direct Numerical Simulation (DNS) for laminar flows and of grid independent models.

This chapter is divided into two main parts, first part uses 2D CFD simulations to study the flow in the T-jets mixers, while in the second part 3D CFD simulations are used. The 2D model CFD simulations were made with the following purpose:

- To simulate the different flow fields with different values of W/w and under a range of values for the operational parameter Reynolds number between 100 and 600.
- To obtain dynamic data from the chaotic flow advection that will be analysed from particle tracking and spectral analysis techniques.

In **Section 4.8** 3D CFD model will be used to simulate the flow field, covering the following aspects:

- Different T-jets mixer geometries and geometrical parameters such as W/w and W/d at different Reynolds were simulated. The results obtained from the 3D CFD hydrodynamic simulation will then be analysed with the power spectra and Turbulence mixing intensity.
- The effect of the head space above the jets, is studied.
- The 3D CFD simulation of tracer being mixed will be conducted and with these results, mixing efficiency is quantified using the intensity of segregation.
- The main purpose of this study is to characterize the different flow regimes observed from the PLIF experiments in Section 3; and compare the PLIF images and the 3D CFD simulation results for the experimental validation of the simulations.

The conclusion from the analysis of the 2D and 3D CFD simulation are presented in the last section

4.2 Governing Equations

The CFD software, Ansys Fluent is used in various problems involving incompressible and compressible flows, laminar and turbulent fluid flow, steady and transient flow. Also with its mathematical modeling capability for transport phenomena involving heat and chemical reactions could be combined and utilized for solving complex geometries, simulations along with the conservative and momentum equations, transport equations such as the energy and

species transport equations with or without chemical reactions. CFD is a computer based numerical modeling approach for the study of fluid flow and associated heat and mass transfer problems. The modelling of numerical solutions of the governing equations includes:

- Continuity equation
- Navier-Stokes equations
- Thermal energy equation
- Species conservation equations (with or without chemical reactions)

The continuity equation for incompressible flow is given from the divergence of the velocity vector, $\vec{\upsilon}$:

$$\vec{\nabla} \cdot \vec{\upsilon} = 0 \tag{4.1}$$

and the equations governing the motion of fluids Navier-Stokes equations is given by:

$$\rho \frac{D\vec{\upsilon}}{Dt} = -\vec{\nabla} p + \mu \nabla^2 \vec{\upsilon} + \rho \vec{g} \tag{4.2}$$

where p is the pressure, t the time, $\vec{g}$ the gravitational acceleration vector, μ and ρ are the fluid viscosity and density, respectively.

The equations governing the motion of fluids are non-linear second-order partial differential equations; it consists of combinations of the flow variables $(\upsilon_x, \upsilon_y, \upsilon_z, P)$ and their derivatives. This consists of four equations with four flow variables and the system is mathematically closed. The exact solutions of the Navier-Stokes equation are not possible, except to a reduced form of Navier-Stokes equations for simple flows conditions. The behaviour of fluids in general is complex as it is time dependent, two and three dimensional and turbulent.

Nevertheless, the complete form of Navier-Stokes equations could be solved numerically using CFD codes. The problem solving in CFD generally involves following steps:

- The physical domain is divided into a number of cells or control volumes.
- The governing partial differential equations are then discretized with one of the following numerical methods: finite difference, finite element and finite volume.

- A set of algebraic equations for each of the variables such as velocity, temperature and concentration components is generated.

Finite volume introduces a control volume concept to generalize the finite difference method **Section 4.3.1** gives a description of finite volume method. It is been developed for fluid flow and is widely used in CFD.

4.3 Numeric Solutions of CFD

The CFD, ANSYS FLUENT uses finite volume method to study the flow field. In the following **Section 4.3.1**, the implementation and the solutions of the CFD is described (Ansys online manual, 14.0)

4.3.1 **Discretization**

In FLUENT, each grid element with general conservative equations is solved for scalar quantity ϕ, in integral form as follows

$$\int_V \frac{\partial \rho\phi}{\partial t} dV + \oint \rho\phi\vec{\upsilon} \cdot \vec{n} dA = \oint \Gamma_\phi \cdot \vec{n} dA + \int_V S_\phi dV \tag{4.3}$$

where $\rho =$ density, $\vec{\upsilon} =$ velocity vector, $\mathbf{A} =$ surface area vector where $\vec{n}$ is unit vector normal to the surface area , $\nabla\phi$ =gradient of ϕ, $\Gamma_\phi =$ diffusion coefficient of ϕ and $S_\phi =$ source of ϕ per unit volume. The terms in the equations are as follows: $\int_V \frac{\partial \rho\phi}{\partial t} dV$ is the unsteady term of ϕ accumulation in the control volume, $\oint \rho\phi\vec{\upsilon} \cdot \vec{n} dA$ is the convection term of ϕ over the control volume boundaries, $\oint \Gamma_\phi \cdot \vec{n} dA$ the diffusion term of ϕ over the control volume boundaries, and $\int_V S_\phi dV$ the generation or source term of ϕ over the control volume.

Different conservative equations are generated due to different scalar quantities ϕ Equation (4.3) : $\phi = 1$ for the continuity equation; $\phi = \upsilon_x$, υ_y or υ_z for the x, y or z momentum equations; and $\phi = h$ for the energy equation, where h stands for enthalpy.

4.3.2 **Discretization of Scalar Transport Equation**

4.3.2.1 Spatial Discretization

The governing integral equations for the conservation of mass and momentum, for energy and other scalar quantities such as turbulence and species is solved in Ansys Fluent using control-volume or finite volume method.

The discrete equation that represents the conservation law, Equation (4.3), is as follows

$$\frac{\partial \rho \phi}{\partial t} V + \sum_{f}^{Nfaces} \rho_f \mathrm{v}_f \phi_f \cdot \vec{n} A_{faces} = \sum_{f}^{Nfaces} \Gamma_\phi \nabla \phi_f \cdot \vec{n} A_{faces} + S_\phi dV \tag{4.4}$$

where N_{faces} = number of faces that create each cell domain; ϕ_f = value of ϕ convected through face f; $\rho_f \mathrm{v}_f \phi_f \cdot \vec{n} A_{faces}$ is mass flux through the face with area A_f and V is the cell volume and $\nabla \phi_f$ = gradient of ϕ at face f.

Each cell centre contains the discrete values of the scalar variable ϕ obtained from Fluent, and in some cases the values in the Equation (4.4) account to the faces shared between two cells in the domain. Thus, ϕ_f must be interpolated from the cell centre values. The interpolation methods for momentum and for gradients and derivatives are explained in detail in the next section.

Spatial discretization of momentum

Upwind scheme is applied to interpolate the momentum solutions, the scalar value on the face is obtained from the upstream cell centre, relative to the direction of the normal velocity υ_n. This leads to the diffusion term in the Equation (4.4) based on central-difference method to be second order accurate. Several upwind schemes options are available in Ansys Fluent to be chosen. In the following section, the schemes used are explained.

- **First-Order Upwind Scheme** - In this scheme, the ϕ_f value is equal to the cell-centre value on the upstream cell. This scheme assumes that all cell-centre values of

any scalar represent a cell-average value. For simple flow (laminar flow) that is aligned with the mesh, the numerical diffusion will be naturally low, so in this situation first-order scheme could be used.

- **Second-Order Upwind Scheme –** In this scheme, the Taylor-series expansion of the cell-centred solution about the cell centroid is used to compute the scalar quantities ϕ_f at the cell face. In this scheme, the determination of the scalar quantity gradient in each cell scheme is necessary.
- **Third-Order MUSCL Scheme –** This scheme arise from the combination of central differencing scheme and second order upwind scheme. This is more used for random meshes. This scheme has more scope for spatial accuracy, especially for three-dimensional flows by reducing numerical diffusion. This scheme could be applied for all type of meshes.

Power Law and Quick Law Upwind scheme are the other schemes available in Fluent.

Discretization of Gradients and Derivatives

Although the main purpose of the gradients is to correspond between the nearby cells but also for computing secondary diffusion terms and velocity derivatives. Three methods utilized by the gradients in Ansys Fluent to discretized are: Green-Gauss cell based; Green-Gauss node based; and Least squares cell based method. The convection and the diffusion term in the flow equations, mass and momentum conservation, are discretized by the gradients $\nabla\phi$ with these three methods. The Green-Gauss theorem solves the gradient of a scalar ϕ for any cell centre, C_o, and therefore has the discrete form

$$(\nabla\phi)c_0 = \frac{1}{V}\sum_f \bar{\phi}_f \vec{n} A_f \tag{4.5}$$

where ϕ_f is the value of the scalar ϕ at the cell face centroid, and the summation is over all faces enclosing the cell. In the Green-Gauss cell based, the face value $\overline{\phi_f}$ in the Equation (4.5) is acquired from the arithmetic average of the values at the adjacent cell centres. Green-Gauss node method solves $\overline{\phi_f}$ as the average of the nodal values on the face taken. The

default Least squares cell based gradient method, assumes that the scalar face values varies linearly with the values solved within the adjacent cells centres that share the face of interest. The change in the cell value between the cell centre value, C_o, and the adjacent or surrounding cell, C_i, along the vector δr_i, which is distance from the centroid of cell C_o to C_i, is given as

$$(\nabla\phi)C_o\Delta r_i = (\phi C_i - \phi C_o) \tag{4.6}$$

this equation could be extended for each cell adjoining the C_o and written as follows

$$[J](\nabla\phi)C_o = \nabla\phi \tag{4.7}$$

where $[J]$ is the coefficient matrix which is a function of geometry. The main aim is to find out the cell gradient $(\nabla\phi_0 = \phi_x\vec{i} + \phi_y\vec{j} + \phi_z\vec{k})$. The difference vector can calculate the gradient at the cell centre $\Delta\phi = (\phi_{Ci} - \phi_{Co})$.

4.3.2.2 Temporal Transient Discretization

In the transient simulations, the governing equations are discretized in both time as well in space. This discretization of the time-dependent equations is similar to the steady-state operation, except that it involves the integration of every term over a time step Δt. The integration of the transient term is straightforward as shown below.

The time evolution of a variable ϕ can be given as

$$\frac{\partial\phi}{\partial t} = F(\phi) \tag{4.8}$$

where $F(\phi)$ is the generic function that includes any spatial discretization. If the time derivative is discretized using backward differences, then the first order accurate temporal discretization is given by

$$\frac{\phi^{n+1}-\phi^{n}}{\Delta t}=F(\phi) \tag{4.9}$$

And the second order discretization is as follows

$$\frac{3\phi^{n+1}-4\phi^{n}+\phi^{n-1}}{2\Delta t}=F(\phi) \tag{4.10}$$

here the ϕ is the scalar quantity, n represents the current time level, t; $n+1$ is the next time level, $t+\Delta t$, and $n-1$ at the previous time level, $t-\Delta t$, respectively. After the discretization of the time derivative, the $F(\phi)$ needs to be calculated; there are two options of time levels values of ϕ to be used.

Implicit Time Integration

In this method, ϕ is calculated with a future time level:

$$\frac{\phi^{n+1}-\phi^{n}}{\Delta t}=F(\phi^{n+1}) \tag{4.11}$$

This is referred as implicit since ϕ^{n+1} in a given cell is related to ϕ^{n+1} in the adjacent cells through $F(\phi^{n+1})$:

$$\phi^{n+1}=\phi^{n}+\Delta t F(\phi^{n+1}) \tag{4.12}$$

This implicit equation is solved iteratively at each time step before moving further to the next time step.

Explicit Time Integration

The explicit time step exist only with density-based explicit solver, for this reason $F(\phi)$ is evaluated at the current time level

$$\frac{\phi^{n+1}-\phi^{n}}{\Delta t}=F(\phi) \tag{4.13}$$

This method is called as explicit, because the scalar variable at time $n+1$ can be expressed explicitly in terms of the known values of ϕ^{n}

$$\phi^{n+1}=\phi^{n}+\Delta t F(\phi) \tag{4.14}$$

This explicit formulation cannot be used for incompressible flows, as it is restrictive and should be used in cases such as transient behaviour of moving waves such as shocks.

4.4 Solvers

In Ansys Fluent, two numerical methods are available for flow solvers (ANSYS FLUENT., Section 20.1): pressure based solver and density based solver. In general pressure based solver is used for low speed incompressible flows and density based solver is used for high-speed incompressible flows, but with recent developments and enhancements both the solvers could be utilized in wide range of flow conditions. For both solvers, velocity field is computed from the momentum equations: in the density-based solver, the continuity equation is used to compute the density field while pressure field is determined from the equation of state. Meanwhile in the pressure-based solver, the pressure field is obtained by solving a pressure correction equation, by manipulating continuity and momentum equations.

These two solvers apply similar finite volume discretization method, but their ways to linearize and solve the discretized equations are different. Both the solvers are equipped with respective physical models for this purpose.

4.4.1 **Pressure-Based Solver**

Pressure based solver consists of two algorithms, which are used for solving the governing equations: segregated algorithm and coupled algorithm.

Segregated Algorithm

This algorithm solves the governing equations sequentially. Since the governing equations are non-linear and coupled to one another, therefore in order to obtain a converged solution, the solution loop must be done iteratively one by one. During the solving process the governing equations are segregated and solved. Due to this reason, segregated algorithm uses less computer memory. With this segregated algorithm, the convergence is slower as only one discretized equation is stored in memory at each time. In segregated algorithm method, the iterative solving is as follows: updating the fluid properties such as density, viscosity and specific heat based on the current solution or initialization values; solve the momentum equations one by one using the updated vales for pressure and mass fluxes; solve the pressure correction equation using the most recent velocity field and mass flux; correct face mass fluxes, pressure and velocity field using the pressure correction applied prior to this step; solve equations for additional scalars conservations, such as turbulent quantities, energy, species and radiation when it is active; update the source terms originated due to the communication between the different phases involved; check for the convergence of the equations involved. These steps are continued in loop until the convergence criteria is achieved.

Coupled Algorithm

This algorithm solves the momentum and pressure based continuity equations together at the same time, this involves more computer memory. As the discrete system of all the momentum and pressure based continuity equations must be stored in the memory when solving the velocity and pressure field, it consumes less time to achieve convergence. The steps involved in this algorithm are as follows: momentum and continuity equation are solved together, then the remaining iterative loops are solved similar to segregated algorithm.

Pressure Discretization

The solutions of pressure and velocity acquired on every iterative step are stored in each cell centre. The face values for these variables must be calculated; therefore appropriate interpolation schemes are used to solve the discretized continuity Equation (4.3). There are four schemes: linear, second-order, body-force-weighted and PRESTO (Pressure Staggering Option) schemes. In the linear scheme the face value is calculated as an average between the

two adjoining cell centres. In the second-order scheme, the convection term is utilized to attain the face value. This scheme must not be applied at the beginning of the simulation despite being more accurate than the linear scheme, and also in case, where the mesh is of poor quality. This scheme is not applicable for flows where the pressure gradient is discontinuous and forced by the presence of porous media or where Volume of Fluid (VOF) and mixture model are used. The body-force-weighted scheme computes the face value considering that the normal gradient of the difference between the pressure and body force is constant. Then the PRESTO scheme uses the discrete continuity balance on a control volume to compute the pressure. This PRESTO scheme is recommended for flows where high number of swirls and vortices are present, for natural convection and for strongly curved domains.

Density Interpolation Schemes

For incompressible flow, Fluent uses arithmetic averaging method for density. For compressible flow calculations, Fluent applies upwind interpolation of density at cell faces. There are several interpolation schemes available for density upwinding at cell faces: first order upwind, second order upwind, QUICK, MUSCL, central differencing and bounded central differencing.

First order upwind scheme sets the density at the cell face to be upstream cell-centre value. This scheme provides stability for the discretization of the pressure-correction equation, and provides good results for most flow cases. This scheme provides stability for compressible flow calculations; it is the default scheme for compressible flows.

Second order upwind scheme provides better stability for supersonic flows and captures shocks better than the first order upwind scheme.

Pressure-Velocity Coupling

Pressure-velocity coupling is achieved by deriving the additional condition for pressure by reformatting the continuity equations. Five pressure-velocity coupling algorithm are provided by Ansys Fluent: SIMPLE, SIMPLEC, PISO, Coupled and Fractional step. Only the schemes involving Coupled algorithm use the pressure-based coupled solver while the rest uses pressure-based segregated solver.

The SIMPLE algorithm uses the relationship between velocity and pressure corrections to enforce mass conservation and to obtain the pressure field. The SIMPLEC (SIMPLE Consistent) is similar to SIMPLE except that it introduces correction in the face flux. The modified correction of SIMPLEC obtains faster convergence than the SIMPLE for simple laminar flows without any additional flow models. PISO (Pressure-Implicit with Splitting of Operators) scheme is based on higher degree of the approximate relations between pressure and velocity corrections. Through this method additional correction is introduced in order to improve the efficiency of the flux calculations between the neighbouring cells. One of the limitations of SIMPLE and SIMPLEC is that the new velocities and corresponding fluxes do not satisfy the momentum balance after the pressure-correction equation is solved. Therefore the correction must be repeated for the balance to be satisfied; this deficiency is overcome by PISO algorithm with the introduction of neighbouring correction and skewness. The Coupled algorithm solves the momentum and pressure based continuity equations together. The full implicit coupling is achieved through implicit discretization of pressure gradient terms in momentum equations and an implicit discretization of face mass flux. The Fractional step algorithm uses a technique called operator splitting or approximate factorization to decouple the momentum equation from the continuity equation, this results in algorithm similar to segregated.

Under Relaxation Parameters

Due to the nonlinear equation solved by Ansys Fluent, it is necessary to control the change of scalar variable, ϕ. This is done by under-relaxation parameter, which reduces the change of ϕ, occurring during each iteration. The under-relaxation parameters is also referred as explicit relaxation of the variables and used in some material properties and in pressure based coupled algorithm for momentum and pressure. It also reduces the change of variables occurring during each iteration. It could be represented mathematically as follows, $\phi = \phi_{old} + \gamma \Delta\phi$, where ϕ_{old}, represent the old value of the scalar ϕ within the cell, $\Delta\phi$ is the computed change in scalar ϕ and γ the under-relaxation parameter set-up.

4.4.2 Direct Numerical Simulation and Grid Independent Model

Orszag (1970) introduced the Direct Numerical Simulation (DNS) which solves the complete incompressible Navier-Stokes equation without including turbulent model. Here the spatial and temporal scales are resolved for all range of flows including turbulence. The turbulence spatial scale range from smallest dissipative scales namely Kolmogorov scale (λ_K) (see Equation (4.15)) to the integral scale L, associated with the motion containing kinetic energy (Santos, 2003; Gomes, 2011). Kolmogorov scale value could be defined as the value of the same order of magnitude as the smallest scale for the hydrodynamics and thus the cell size characteristic dimensions should be smaller than the Kolmogorov scale to simulate even the smallest scales of the flow. The Kolmogorov scale for turbulent flows is defined as (Tennekes and Lumley, 1997).

$$\lambda_K = \left(\frac{\nu^3}{\varepsilon} \right)^{1/4} \tag{4.15}$$

where ν is the kinematic viscosity and ε is the turbulent energy dissipation rate

$$\varepsilon = 2\nu \overline{s_{ij} s_{ij}} \tag{4.16}$$

$\overline{s_{ij} s_{ij}}$ is the mean-square strain rate of the fluctuation rate-of-strain,

$$s_{ij} = \frac{1}{2} \left(\frac{\partial \upsilon_i'}{\partial x_j'} + \frac{\partial \upsilon_j'}{\partial x_i'} \right) \tag{4.17}$$

x_i and x_j are the Cartesian coordinates and, υ_i' and υ_j' are two fluctuation velocity components

$$\upsilon_i' = \upsilon_i - \overline{\upsilon_i} \tag{4.18}$$

where υ_i is a velocity component and $\overline{\upsilon_i}$ the corresponding time averaged velocity. The use of DNS can predict even the smallest of flow scales in detail. For this purpose, a sufficient fine mesh is essential to predict flow, but this affects the computer time for solving the

problem and uses more memory than simulation with subgrid turbulences modelling. Though in our work with T-jets mixer the flow is laminar, the flow is complex due to flow recombination, vortices, velocity vectors variations, and expansions. The DNS model setup would therefore support in studying the flow dynamics and other aspects of quantification study involved.

It is generally a pre-notion that a study with sparse grid will lead to faster solution than the dense but this leads to results where the smallest flow scales are not simulated, and even the flow dynamics (Santos et al., 2010). So a measure should be taken to select an appropriate grid. Therefore, a grid independent model study should be done which is obtained when the simulation results do not vary more than a fixed small amount with the grid refinement which is dependent upon the user. As mentioned earlier that the DNS predicts the smallest of scales associated with it, without including the averaging physical models.

For the mass transfer simulation the necessary number of nodes for a 3D CFD simulation of a turbulent flow scales with the Reynolds number, *Re*, and the Schimdt, *Sc*, numbers as (Baldyga and Bourne, 1999) is given as

$$N_{xyz} \infty Re^{9/4} Sc^{3/2} \tag{4.19}$$

where the Schmidt number is defined as

$$Sc = \frac{\mu}{\rho D_m} \tag{4.20}$$

here D_m is the molecular diffusivity of a chemical species in a fluid with viscosity μ and density ρ. Based on the Kolmogorov and Batchelor scales, for 2D geometries the number of nodes scales as

$$N_{xy} \infty Re^{3/2} Sc \tag{4.21}$$

A realistic order of magnitude of the Schmidt number for liquids is 10^3, which would require an increase in the number of nodes for the 3D and 2D simulation of three orders of magnitude relative to the problems where mass transfer is not simulated. Due to the limitations of

computer memory, an increase in the number of nodes is not recommended, and therefore artificial low values for the Schmidt number are incorporated.

The Kolmogorov scale provides a limit where turbulent forces are balanced by viscous forces. Below this scale, appears the Batchelor scale that provides a limiting scale where the rate of molecular diffusion is equal to the rate of dissipation of turbulent kinetic energy (Kresta and Brodkey, 2004).

Here the diffusion and convection of chemical species within the flow fluid is included in the simulation. With this approach there is a possibility of coupling chemical reaction with mass transfer, which can give further insight into mixing mechanism which is presented in **Chapter 5**.

4.5 Species Transport

Ansys Fluent can model the mixing and transport involving chemical species by solving conservation equations describing convection, diffusion and reaction sources for each component species. Even multiple simultaneous chemical reactions can be modelled with reactions occurring in the bulk phase (volumetric reactions) which will be studied in **Chapter 5**. In this section species transport modelling both with and without reactions is explained.

4.5.1 Species Transport Equations

In order to solve the conservation equations for chemical species, Ansys Fluent calculates the mass fraction of each species, Y_i, with the solution of the convection-diffusion equation for the i^{th} species. This conservation equation is represented form as follows

$$\frac{\partial}{\partial t}(\rho Y_i) + \nabla \cdot (\rho \vec{\upsilon} Y_i) = -\nabla \cdot \vec{J}_i + R_i + S_i \tag{4.22}$$

where R_i is the net rate of production of species i by chemical reaction and S_i is the rate of formation by addition from the dispersed phase plus any user-defined sources. This form of equation will be solved for $N-1$ species where N is the total number of fluid phase chemical reaction present in the system. As the sum of the mass fraction of the species must

be unity, the *Nth* mass fraction is calculated as one minus the sum $N-1$ of the solved mass fractions. In order to reduce the numerical error, the *Nth* species should be selected with the overall largest mass fraction, such as N_2 when the oxidizer is air.

4.5.1.1 Species Transport in the Energy Equation

For many multi component mixing flows the transport of enthalpy due to species diffusion can have significant effect on the enthalpy field and should not be neglected. ANSYS FLUENT will include this energy equation term by default.

4.6 2D CFD Study of T-jets Mixers

In this section, the effect of the T-jet mixers geometry scale down on mixing is studied with 2D CFD simulations. With the purpose of clearly showing the critical impact of the T-jets geometry on the mixing and flow dynamics several T-jets geometries were simulated. The mixer scale and the ratio between the jets and chamber widths are varied yielding different flow regimes for the same Reynolds numbers and jets momentum ratios.

4.6.1 **Model Description**

The basic T-jet mixer geometry here used is 2D comprising two injectors connected at opposite sides of a square chamber with a closed top and an outlet, as shown in **Figure 4.1**(a). The axes of the opposite injectors are aligned and above the injectors it is formed a headspace with a height $h=2$ mm. The width of the injectors, w, was varied within the range of 0.125 mm to 1 mm. The chamber has a height of $H=50$ mm and the width of the chamber W was varied in the range of 1 mm to 6 mm. The list of T-jets mixers studied with 2D CFD simulation is summarised in **Table 2.1** with the dimensions, the width of the injectors jets, w, the width of the mixing chamber, W.

The described model and finite element grid shown in **Figure 4.1** (b) was generated with the pre-processing software from ANSYS: GAMBIT (version 2.3.16). GAMBIT stands for *Geometry And Mesh Building Intelligent Toolkit*.

Table 4.1. List of T-jets mixers dimensions studied with 2D CFD simulations.

Chamber Width (W) mm	**Jets Width (w) mm**	**W/w ratio**
1	0.5	2
1	0.25	4
1	0.125	8
2	1	2
2	0.5	4
2	0.25	8
4	0.5	8
6	1	6

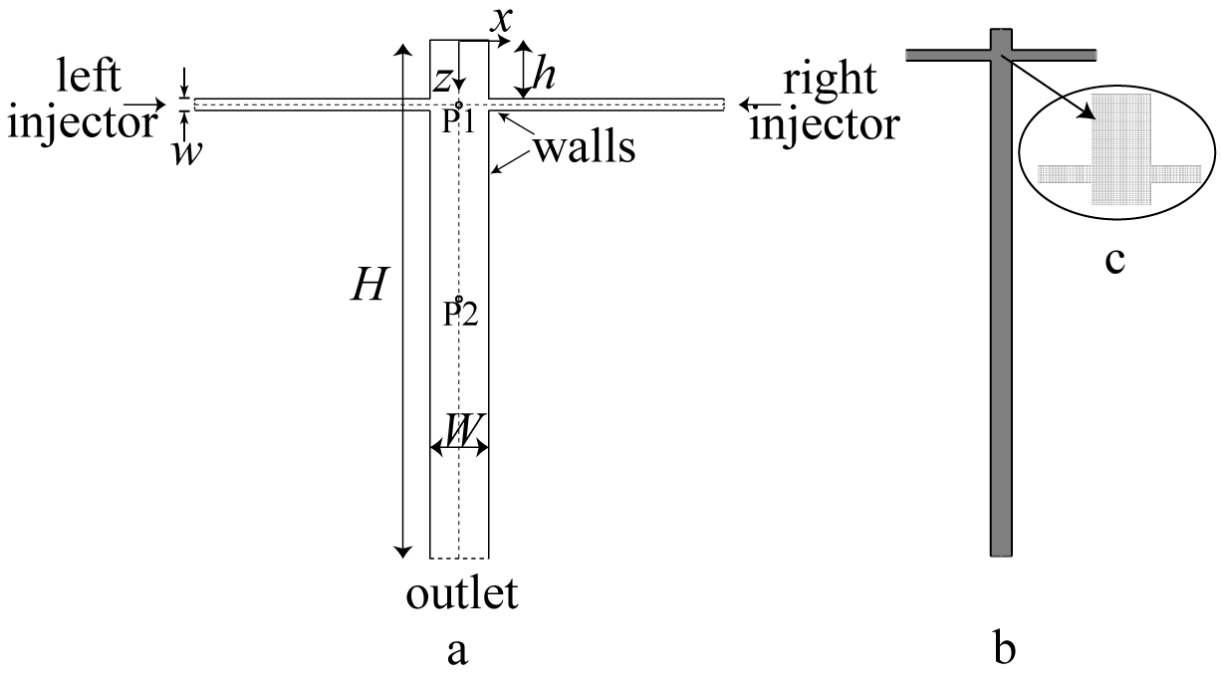

Figure 4.1 T-jets mixer geometry used in CFD simulation : a) 2D Model b) Computational grid c) close view of grid.

4.6.2 **Governing Equations**

For the flow field simulation the continuity and the Naviers-Stokes equations were solved numerically – see Equation (4.1) and (4.2)

4.6.3 **Boundary and Initial Conditions**

In this Section, the boundary conditions at the chamber walls, the injectors, and chamber outlet are presented. These conditions are used for the start up the simulation.

4.6.3.1 Inlet Boundary Conditions

The direction of the flow in the inlets is normal to the direction of the chambers wall $\upsilon_z = 0$, therefore at the injectors the velocity components was set, at left injector $\vec{\upsilon} = (\upsilon_{inj}, 0)$ and at right injector $\vec{\upsilon} = (-\upsilon_{inj}, 0)$. The used fluid is water at 24ºC, having viscosity $\mu = 1.003$ mPa.s, and density $\rho = 998.2$ kg/m^3 The Reynolds number is 600 for all the simulations and is defined at the injector as,

$$\mathrm{Re} = \frac{\rho \upsilon_{inj} w}{\mu} \tag{4.23}$$

where w is the width of the jets and υ_{inj} is injector velocity.

4.6.3.2 Chamber Outlet Boundary Conditions

In the chamber outlet the flow is assumed to be parallel and the velocity gradient is zero, which is given as $\upsilon_x = 0$ and $\tau_{zz} = -p_0$, where the normal total stress at the chamber outlet τ_{zz} and p_o is the pressure outlet. Therefore, for a Newtonian fluid τ_{zz} is defined as

$$\tau_{zz} = 2\mu \frac{\partial \upsilon_z}{\partial z} - p \tag{4.24}$$

where p is the pressure and μ the fluid viscosity. At the outlet $p = p_0$, $\tau_{zz} = -p_0$ and therefore we have zero velocity gradient.

$$\frac{\partial \upsilon_z}{\partial z} = 0 \tag{4.25}$$

So therefore pressure outlet was set for all the simulation conducted in this work (0 Pa gauge). The pressure outlet boundary has two advantages over outflow outlet boundary conditions:

- It does not fix, the condition of the flow rate that exits through the boundary nor the exiting velocity vectors;
- It allows backflow, which is the direct outcome of the primary statement, since the fluid may enter the system through this boundary condition or exit as vortices.

The pressure outlet boundary condition often leads to better convergence when backflow occurs during iterations.

4.6.3.3 Chamber Walls Boundary Conditions

- **No slip wall boundary conditions-** the two velocity components υ_x and υ_z are equal to the walls velocity in each direction. Both the velocity components are set to zero at the walls.

- **Slip wall conditions-** In slip wall boundary conditions, these walls are null shear walls and is set-up in the symmetry axis of each chamber centre, dividing the chamber in two parts, each having an injector and an adjacent outlet in the downstream direction. These slip walls are only used in steady state simulations. The main purpose of this wall is to avoid the fluid contact from the two injectors and therefore prevent fluid crossing from injectors to opposing outlets and thus a segregated steady state is obtained. The steady state results will be used as starting point for the corresponding Re transient state simulation. When in transient state simulations, the slip internal walls are changed to default interior walls and thus disappear to no longer influence the results: fluid can cross the chamber freely, according to the flow velocity vectors.

4.6.3.4 Initial Conditions

Initially for steady state simulations, solution is obtained with a first order momentum spatial discretization scheme and standard discretization scheme for pressure. Then the momentum discretization algorithm is modified to second-order upwind and the pressure is also changed to second order and Least Squares Cell based algorithm for Gradient spatial discretization. This final converged result was the starting point for transient simulation. These discretization schemes were maintained for the subsequent transient state.

For the transient simulations, a second order implicit formulation was set. The time step was set as recommended for better solution with transient simulation. For all the simulations 2D and 3D CFD simulation, the time step size was defined so that a fluid particle can only move an average of one finite element cell for each time step, according to the definition

$$\Delta t = \frac{\overline{\Delta x}}{\bar{\upsilon}} \tag{4.26}$$

where $\overline{\Delta x}$, represents the average cell size and $\bar{\upsilon}$, the local average velocity. For all values of *Re*, the time step size was 1000 times smaller than the unit cell passage time. Further 20 iterations per time step was fixed from the Fluent heuristic rule.

For all the transient simulation, the under relaxation parameters were set at default values: 0.3 for pressure, 1 for density (the density was constant in the entire domain as fluid was considered incompressible), 1 for body forces and 0.7 for momentum. As per the absolute convergence criteria, the residuals were set at 10^{-4} for continuity, x and y velocity. For transient simulation, the residuals were set to 10^{-5}.

4.6.4 **Analysis Method**

4.6.4.1 Spectral Analysis Method

The flow dynamics is assessed from the normalized standard deviation of the x component of the velocity, $\upsilon_x(t)$, at points P1 and P2 as shown in the **Figure 4.1**,

$$\sigma = \frac{1}{2}\ln\frac{\overline{\left(\upsilon_x - \bar{\upsilon}_x\right)^2}}{\upsilon_{inj}^2} \tag{4.27}$$

where $\bar{\upsilon}_x$ is the time average of υ_x, which is the instantaneous velocity value at the point P1 and P2.

The time histories of υ_x at P1 and P2 were transformed into the frequency domain using the Discrete Fourier Transform, DFT:

$$G\left(f = \frac{k}{N\Delta t} \right) = \sum_{i=1}^{N-1} \upsilon_x(i\Delta t) e^{\frac{-j2\pi ik}{n}}, k = 1, 2.., n-1 \tag{4.28}$$

For the case where $\upsilon_x(i\Delta t)$ is the datum of periodic velocity time series, Δt is the periodic time series interval, f is the frequency, N is the total number of points in the time series and $e^{\frac{-j2\pi ik}{n}}$ is the Euler formula for complex numbers where j is the imaginary part. In this work, the FFT was used, for series with 2^N numbers, the FFT and DFT yield the same result. The modulus of the complex number series that is obtained in the Fourier domain, $|G|$, is used in the power spectra presentation.

4.6.4.2 Particle Tracking Method

To assess the effect of the flow dynamics on the actual mixing of the fluids, particle tracking method can be performed (Aubin et al., 2005). This section explains the particle tracking method in ANSYS.

Equations of Motions for Particles

Particle Force Balance

Ansys Fluent calculates the trajectory of a discrete phase particle by integrating the force balance on the particle. The particle inertia connects to the force balance with the forces acting on the particle and can be written as

$$\frac{d\upsilon_p}{dt} = F_D(\vec{\upsilon} - \vec{\upsilon}_p) + \frac{g(\rho_p - \rho)}{\rho_p} + \vec{F} \tag{4.29}$$

where $\vec{F}$ is an additional acceleration (force/unit particle mass) term, $F_D(\vec{\upsilon} - \vec{\upsilon}_p)$ is the drag force per unit particle mass and

$$F_D = \frac{18\mu}{\rho_p d_p^2}\frac{C_D Re}{24} \tag{4.30}$$

here $\vec{\upsilon}$ is the fluid phase velocity, $\vec{\upsilon}_p$ is the particle velocity, μ is the molecular viscosity of the fluid, ρ is the fluid density and ρ_p is the density of the particle and d_p is the particle diameter. Re is the relative Reynolds number which is defined as

$$Re = \frac{\rho d_p \left|\vec{\upsilon}_p - \vec{\upsilon}\right|}{\mu} \tag{4.31}$$

The Equation (4.29) also includes additional force in the particle $\vec{F}$, in the particle force balance which could be important under certain situations. The first of these is the virtual mass force, the force required to accelerate the fluid surrounding the particles which can be given as

$$F = \frac{1}{2}\frac{\rho}{\rho_p}\frac{d}{dt}(\vec{\upsilon} - \vec{\upsilon}_p) \tag{4.32}$$

and is important when $\rho > \rho_p$. Another force arises due to the pressure gradient in the fluid:

$$F = \left(\frac{\rho}{\rho_p}\right)\upsilon_p \nabla \upsilon \tag{4.33}$$

The particles were assumed spherical with the same density of the fluid and having a diameter of 10^{-9}m, and Stokes law was used for drag. The particle and fluid densities were matched in addition to the small dimensions of the particles, which assured the paths of particles and fluid coincide.

4.7 2D Dynamic Simulation Analysis

In this section, results from 2D CFD simulations are studied with the purpose of clearly showing the critical role of the T-jets geometry on the mixing and flow dynamics. The mixer

scale and the ratio between the jets and chamber widths are varied yielding different flow regimes for the same Reynolds numbers and jets momentum ratios.

4.7.1 **Flow Field**

Figure 4.2 and **Figure 4.3** shows the streamline maps from the CFD simulations using the 2D model for the cases of the T-jets mixers with widths $W = 1$ mm and $W = 2$ mm, respectively, and for chamber to jets widths ratio $W / w = 2$, 4 and 8. The streamline maps are obtained from the dynamic CFD simulations at $t = 0.5$ *s*. For the same Reynolds number three flow regimes are observed differing only on their features after the jets impingement point. In the three flow regimes, the jets enter perpendicularly to the mixing chamber axis bending towards the outlet just before impinging each other. The impingement point is slightly offset to downstream the point P1 (see **Figure 4.1**), which is located at the intersection of the axes of the mixing chamber and of the injectors. After impinging each other the opposed jets merge into a single jet that has approximately twice the width of the original jets; this merged jet flows towards the outlet forming different patterns that depend on the value of W / w ratio.

4.7.1.1 Effect of Width Ratio

For $W / w = 2$, after the impingement point the merged jet bends firstly to one side of the chamber and then to the opposite side. There is some rippling of the jet after its second turn whilst flowing to the outlet.

For $W / w = 4$, the merged jet bends consecutively to right and left and vortices are formed around it – between the path of the merged jet and the sidewalls.

For $W / w = 8$, after the jets impingement point two vortices are formed, one in each side of the chamber: vortices having width around half the chambers width. Immediately downstream of these vortices there is the formation of larger vortices that occupy almost entirely the chamber width, these larger vortices evolve in a well-defined vortex sequence to the outlet. The merged jet meanders around these consecutive larger vortices street.

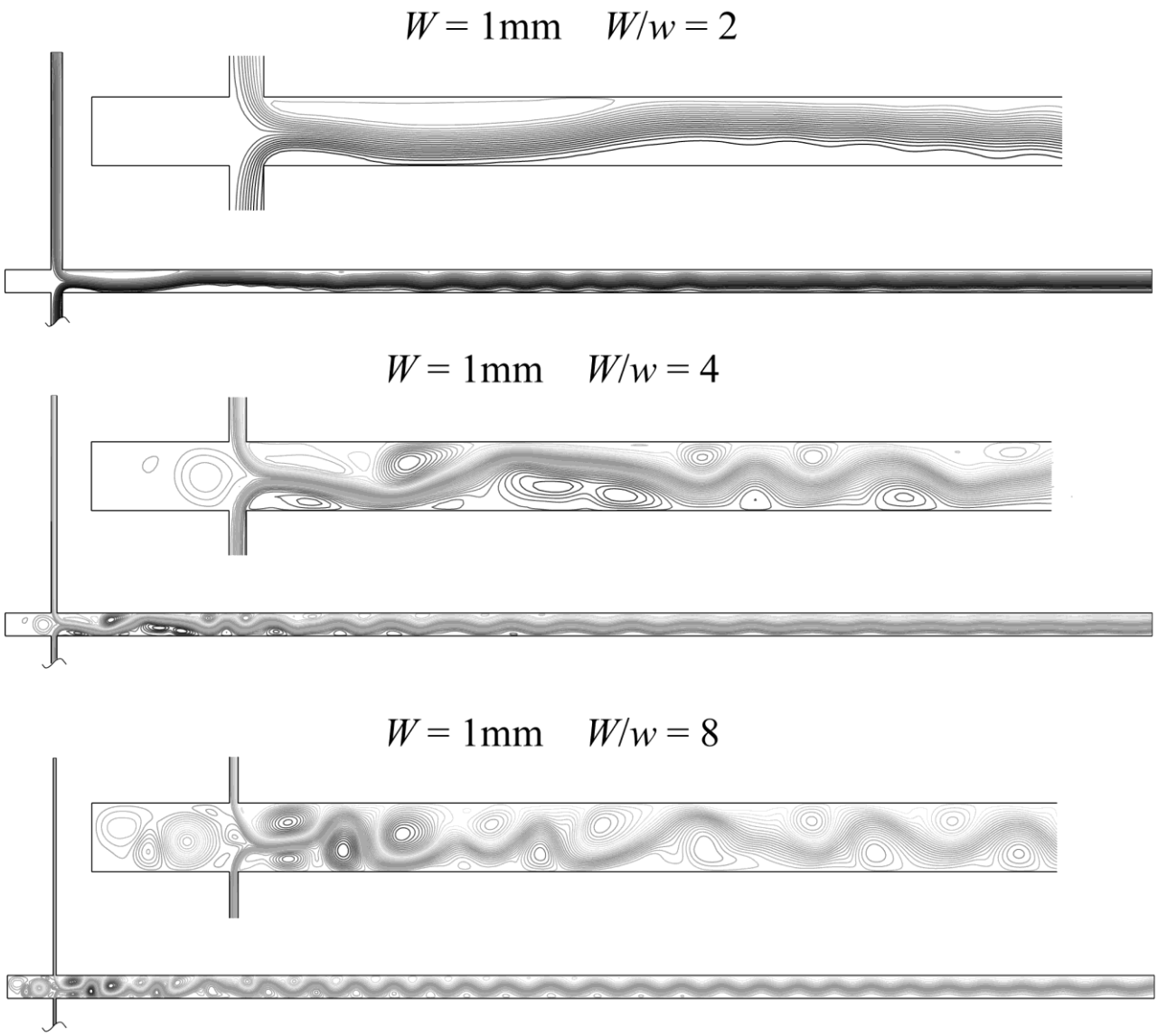

Figure 4.2 Streamline maps of the 2D CFD simulation of the geometries having $W = 1$ mm, $W / w = 2$, 4 and 8 at $t = 0.5$ *s* at *Re*=600.

4.7.1.2 Effect of Mixing Chamber Scale

Flow patterns for the larger mixing chamber are shown in **Figure 4.4**, $W = 4$ mm and $W = 6$ mm, it is seen that for $W / w \geq 6$ the flow features do not differ from the cases of $W / w = 8$ and $W = 2$ mm. For the larger values of jets to chamber width ratios, $W / w \geq 6$, on the range of chamber widths 2 mm$\leq W \leq$8 mm, a flow field with the generation of a vortex street that is formed downstream the jets impingement point is always observed. The overall flow features are independent on the chamber width, the key issue setting the operation flow regime is the ratio of chambers to jets width. Thus, the reactor can be scale down and still operate under

chaotic flow regime, stipulating that with the specified dimensions it is possible to operate above the transition Reynolds number.

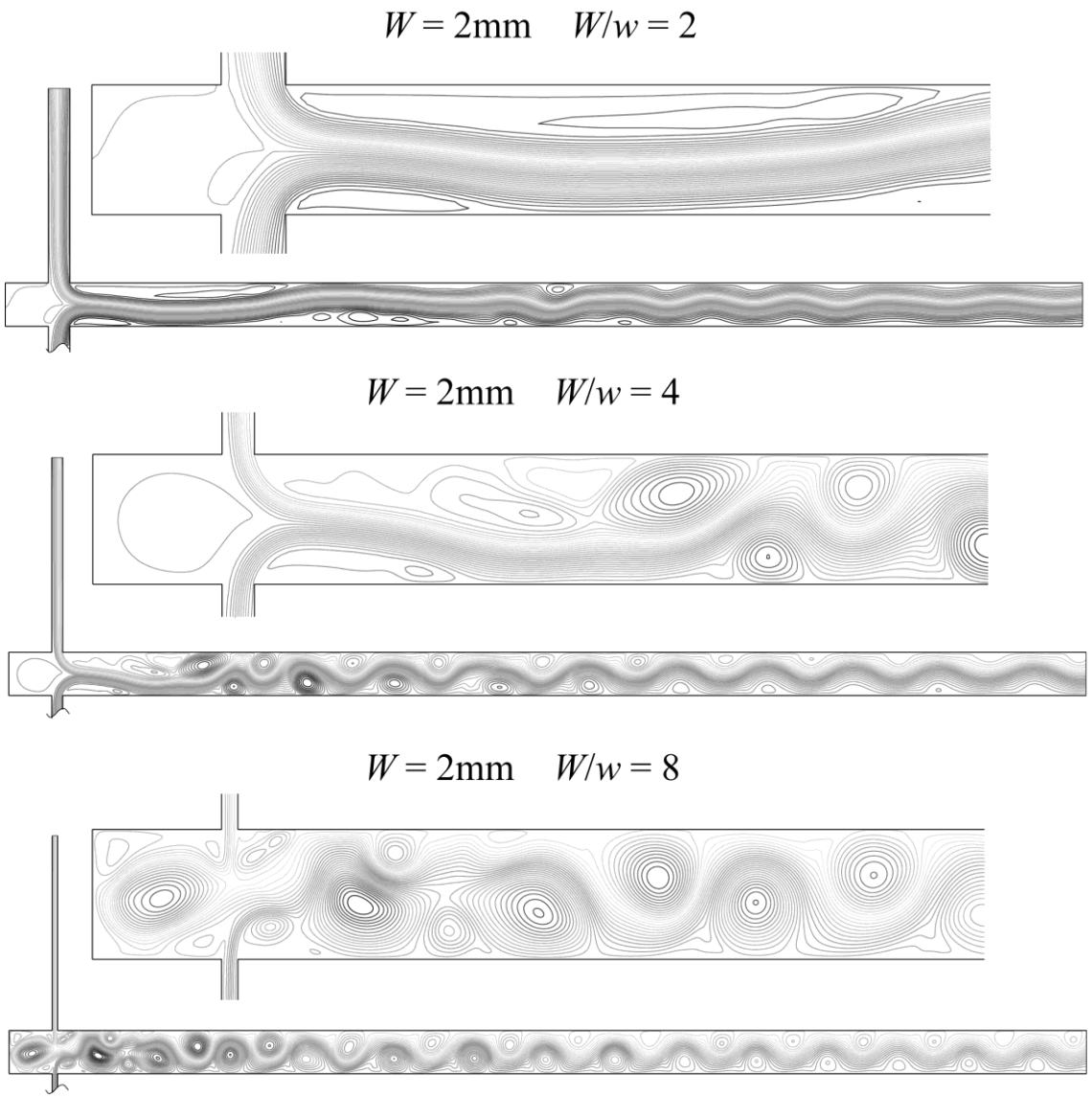

Figure 4.3 Streamline maps of the 2D CFD simulation of the geometries having W = 2 mm W/w = 2, 4 and 8 at t = 0.5 *s* at *Re*=600.

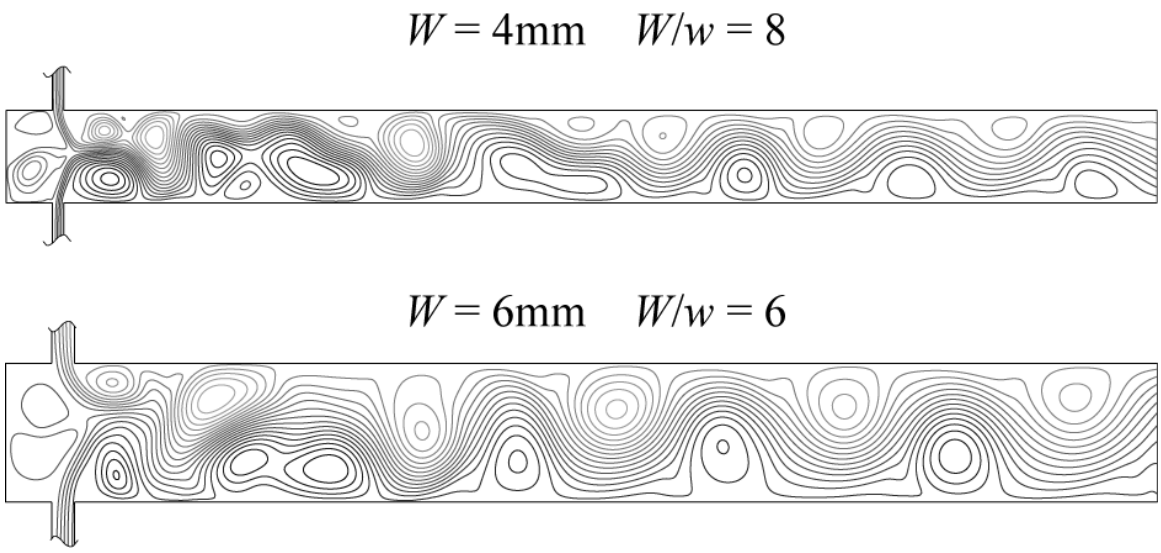

Figure 4.4 Streamline maps of the 2D CFD simulation of the geometries having $W = 4$ mm and $W / w = 8$; $W = 6$ mm and $W / w = 6$ at $t = 0.5$ *s* at *Re*=600.

4.7.1.3 Effect of Head Space

The chamber width only affects the flow in the cavity at the top of the mixing chamber. Previously Santos et al. (2002 and 2005), among others, observed that in the top of the mixing chamber is formed a pair of side by side vortices. Here the mixing chambers top have a fixed height, h, thus the aspect ratio of the chambers top, h/W, varies with the width, W. Santos et al. (2002) studied the influence of the chamber tops aspect ratio on the flow dynamics, on a range of h/W values from zero to 0.75. Santos et al. (2002) observed an increase in the flow dynamics with h/W. Here h/W is one for the $W = 1$ mm and two for the $W = 2$ mm chamber. A single vortex occurs over the jets impingement point both for the $W = 1$ mm and the $W = 2$ mm chambers. Only when h/W is less than 0.5, see **Figure 4.4**, a pair of vortices is formed over the jets. The vortices that are formed upstream the opposed jets tend to be circular, and thus their number and arrangement depends only on the h/W ratio. Although the geometry of the vortices upstream the jets influences the flow dynamics this will be the subject of future work, here the focus is mainly on the chambers width and the chamber to jets widths ratio.

4.7.2 **Dynamic Analysis of the Flow Field**

The flow dynamics in the T-jets mixers is identified for the different flow patterns or regimes previously described. The flow dynamics is analysed at points P1 and P2: P1 is at the

intersection of the jets and chambers axes, while P2 is at the chambers axis equidistant from the chambers top and outlet see **Figure 4.1**. The flow at P1 and P2 has markedly different features: P1 is close to the jets impingement point; while P2 is in the middle of the chamber where the flow patterns depending on the mixer geometry can be such as a vortex street, for $W/w=8$, or a rippling jet, for $W/w=2$. The x velocity component, υ_x, is the analyzed variable due to the fact that the transport mechanisms between both sides of the mixing chamber are in the x direction. The velocity values are normalized by the jets injector velocity, $\upsilon_x^* = \upsilon_x / \upsilon_{inj}$, for direct comparison between different geometries having different jets injector velocities. For a constant Reynolds number of 600 the υ_{inj} depends on the jets width, see Equation (4.23), and so υ_{inj} varies with the values of W/w for a fixed W.

Figure 4.5 shows the time histories of υ_x^* at P1. Only the $W/w=8$ cases have a clear dynamic evolution of υ_x^* at P1, with oscillations of the value of υ_x in the range of $-1.5\upsilon_{inj}$ to $1.5\upsilon_{inj}$. The jets enter the mixing chamber with a 2D parabolic profile having peak values of $\pm 1.5\upsilon_{inj}$ at the injector's axis. The jets keep their velocities up to the jets impingement point. The location of the impingement point oscillates from one side to the other of the chamber axis; the value of υ_x is set from the dominant jet at each instant, i.e. when one jet pushes the opposite jet to its side of the chamber the observed value of υ_x at P1 is the maximum velocity value of the dominant jet. Santos et al. (2009) proved that the oscillations of the jets impingement point are caused by the formation of vortices immediately downstream the injectors. Here, the cases having υ_x oscillations at P1 are the ones where two circular vortices form immediately downstream the jets, as seen from **Figure 4.2** and **Figure 4.3**.

The chamber width influences the flow dynamics, for the $W/w=8$ geometries, the flow dynamics is higher for the $W=2$ mm chamber than for the $W=1$ mm chamber: there are more frequent observation of extreme values of υ_x in the $W=2$ mm case. Since the value of h is fixed the values of W/h are different for different chamber's widths, and so here it is not possible to clearly ascertain the contribution of each of these parameters: W and W/h. Santos et al. (2002) showed that the flow dynamic increases with h for a fixed chamber width.

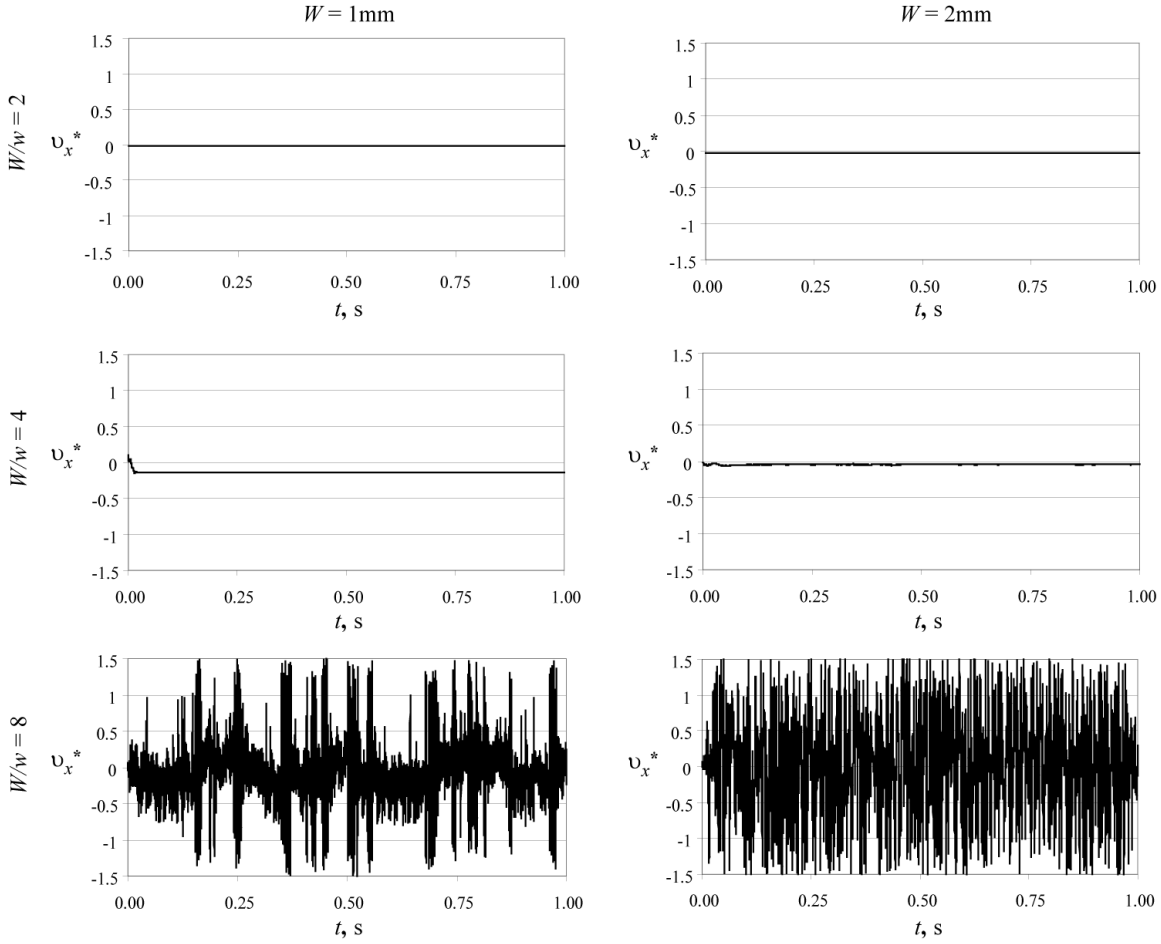

Figure 4.5 Time histories of υ_x^* at the impingement point, P1, for the T-jets mixing chambers with $W = 1$ mm $W = 2$ mm, and ratios $W / w = 2, 4$ and 8.

Figure 4.6 shows the time histories of υ_x^* at P2, a location where the flow oscillations are observed for all the simulated values of W / w. The flow oscillations have different patterns, higher amplitude for the wider chamber and more repetitive at $W / w = 4$. The chamber width influences the flow dynamics, for the $W / w = 2$, 4 and 8 geometries; the flow dynamics is higher for the $W = 2$ mm chamber than for the $W = 1$ mm chamber: there is more frequent observation of extreme values of υ_x in the $W = 2$ mm case.

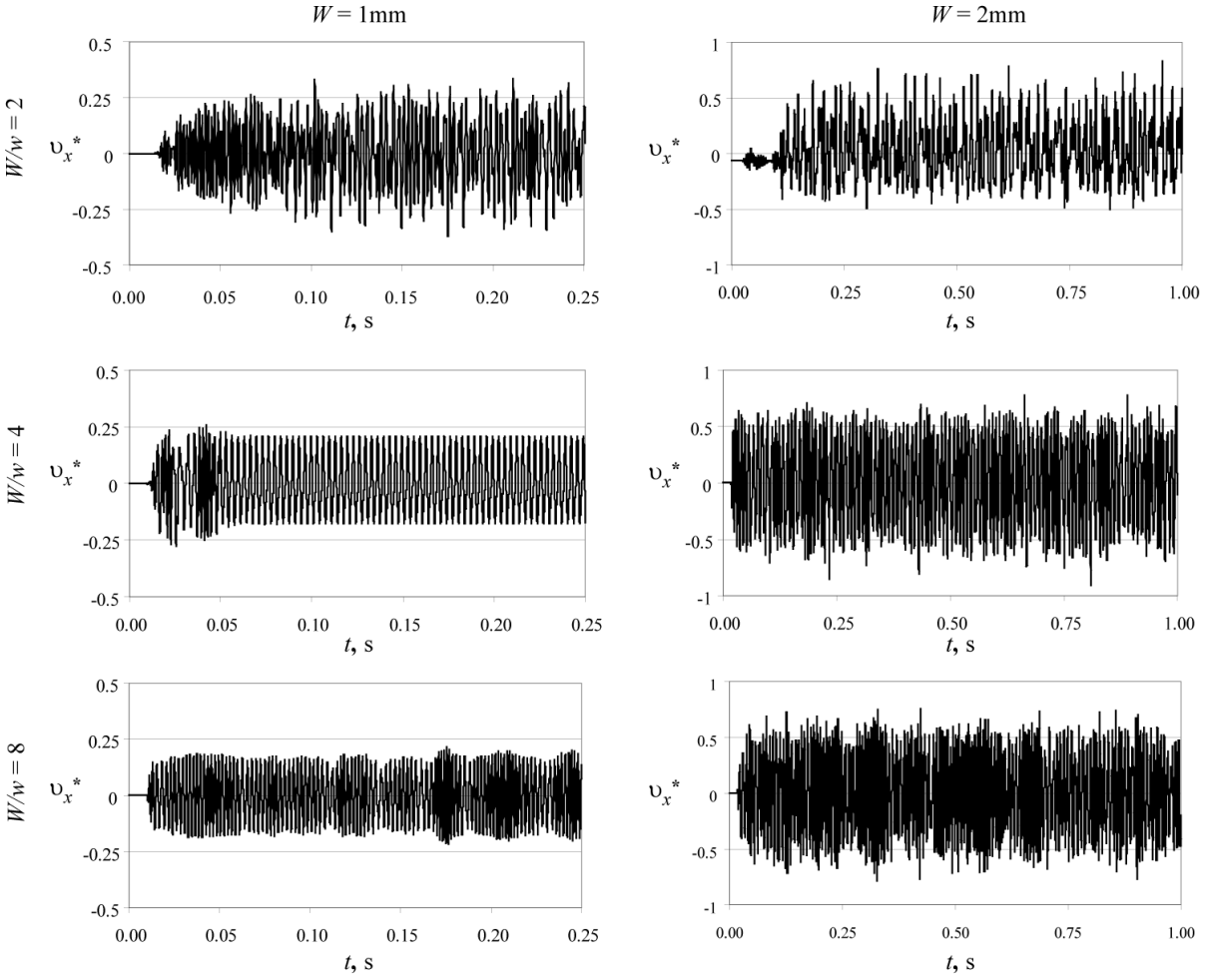

Figure 4.6 Time histories of υ_x^* at the impingement point, P2, for the T-jets mixing chambers with $W = 1$ mm $W = 2$ mm, and ratios $W/w = 2$, 4 and 8.

At P2 the flow has higher dynamics for all geometries than at P1. From the streamline maps of **Figure 4.2**, **Figure 4.3**, and **Figure 4.4** is seen that the main feature at P2 is the sequential passage of vortices. The width of the merged jets flow stream that passes through P2 sets the flow dynamics at this region. When W/w is smaller, i.e. the flow stream occupies most of the mixing chamber, the vortices are smaller, more separated between them and evolve closer to the walls making the merged jet to ripple. The chambers having larger values of W/w have a thinner merged jet that circulates around vortices evolving throughout the chamber axis towards the outlet.

The local flow dynamics for the different geometries are first compared from the values of the logarithm of the standard deviation of υ_x^*, σ, see Equation (4.27), at P1 and P2 that are shown in **Figure 4.7**. The higher values of σ, lighter tones of gray, are observed for the larger

values of W/w. P1 is closer to the jets impingement point and so the values of σ at P1 are a direct measure of the earliness of mixing, i.e. of how soon the fluids are mixing after entering the mixing chamber. The key role of W/w is clear at P1 from the alignment between the isolines of σ and the W/w lines, and so the mixing dynamics is growing exponentially with W/w see Equation (4.27).

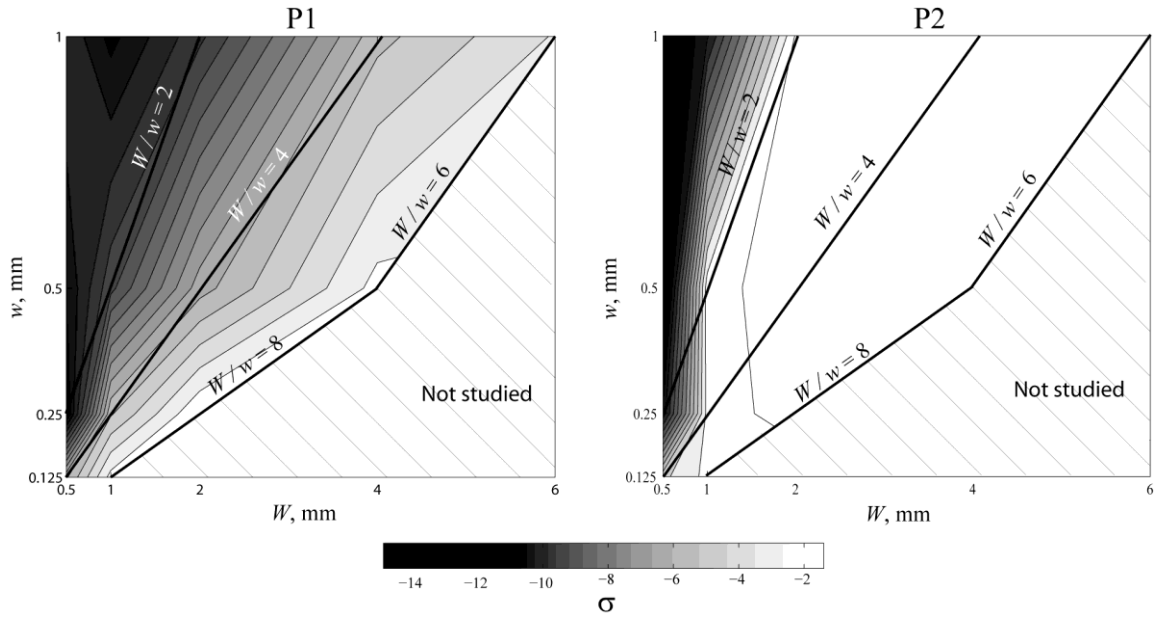

Figure 4.7 Maps of the logarithm of the standard deviation of υ_x^*, σ, at, P1 and P2 obtained from the 2D CFD simulations at different values of jets width, w, mixing chamber width W.

The dynamics of the flow oscillation are clear on the frequency domain, and so the power spectra obtained from the υ_x^* time histories are going to be analysed in this work.

The power spectra of υ_x^* at P1 and P2 that are shown in **Figure 4.8** and **Figure 4.9** that provide further details of the flow dynamics not accessible from data in time domain. Energy peaks in those power spectra at a frequency value stand for an oscillatory behaviour having that same frequency; the amplitude of the oscillation is related to the energy level of the peak. The way energy spreads around the energy peak is a measure of flow repetitiveness: a narrow energy peak stands for a pure oscillatory flow, while a larger distribution of energy around the local maximum (peak) is generally associated with chaotic flows where the oscillation have a frequency around a typical value called *typical frequency*.

The power spectra differ from P1 to P2 and among the several studied geometries. To facilitate the power spectra analysis the following discussion is grouped by W/w values.

4.7.2.1 Power Spectra Analysis for $W/w=2$

The power spectra for the $W/w=2$ cases at P1 have the lowest energy levels; the flow oscillations are not clear from the time histories of υ_x^* in **Figure 4.5**. Nevertheless, a typical frequency is observed at P1 for $W/w=2$ for both cases $W=1$ mm and $W=2$ mm; this typical frequency has values approximately equal to those observed at P2 (see **Figure 4.9**), although the energy levels at P1 are four to five orders of magnitude lower than at P2. The oscillation of the flow at P2 disturbs the opposite jets equilibrium at P1, although this perturbation is not perceptible from the υ_x^* time histories. The flow at the jets impingement point keeps itself almost steady although it is under the constant perturbation from the downstream flow structures, a phenomenon that is only observable from the results in the frequency domain.

At P2 the frequency of the flow oscillations are four times higher for the $W=1$ mm chamber, $\approx$400 Hz, than for the $W=2$ mm chamber, $\approx$100 Hz (see **Figure 4.8** and **Figure 4.9**). The flow oscillations are caused by the spatial evolution of the small vortices formed between the jets flowing through the mixing chamber axis and the wall see **Figure 4.2** and **Figure 4.3**; when the chamber width doubles the diameter of these vortices also doubles. According to the findings of Santos et al. (2009) the frequency of the flow oscillations scales inversely with the area of these vortices for a constant flow rate in a 2D geometry. The Reynolds number is 600 for all simulations in this work, thus the $w\upsilon_{inj}$ value, which stands for flow rate in the 2D geometries, is always the same because the fluid properties are constant see Equation (4.23). The original expression proposed by Santos et al. (2009) for the frequency of a vortex street of consecutive vortices occupying the entire chamber width and having circular shape is:

$$f=\frac{4\upsilon_{inj}w}{\pi D_{vortex}^2} \tag{4.34}$$

where D_{vortex} is the diameter of the vortices. On the present case the frequency at P2 is not given by Equation (4.34) because the vortices only occupy part of the chambers width. Nevertheless, the frequency scales inversely with the square of the vortices diameter as proposed in Equation (4.34). The present result, the fourfold increase of frequency when halving the chamber width, provides further evidence to the thesis of Santos et al. (2009): the frequencies in the mixing chamber are dictated from the geometry of the flow, namely the vortices.

Between the simulations of the cases having $W = 1$ mm and $W = 2$ mm there is an important difference on energy spreading and oscillation amplitude. The amplitudes are higher at the larger chamber, $W = 2$ mm, and the energy is more spread around the typical oscillation frequency. On one hand the flow dynamics grows with W (fact 1), on the other hand the thinner chamber presents higher frequencies and smaller initial scales (fact 2) - the impact of W on mixing will be a trade-off between these two facts, although the accounting of the influence of each fact is not yet made in the present work.

4.7.2.2 Power Spectra Analysis of $W/w=4$

The flow dynamics evolves from $W/w=2$ to $W/w=4$; the main evolution occurs at P1 where the typical oscillation frequencies do not coincide with those at P2. The energy peaks of the typical frequencies at P1 for the $W/w=4$ geometries are two orders of magnitude higher than for the $W/w=2$ geometries, thus the amplitude of the jets impingement point oscillations increases, although, likewise for the $W/w=2$ geometry, these oscillations are hardly observable from the time histories of v_x^* in **Figure 4.5**. The energy peaks are extremely well defined at P1 for $W = 1$ mm indicating pure oscillatory flow behaviour, while for $W = 2$ mm is observed a spread of energy around the typical frequency denoting a chaotic behaviour of the flow. The flow regularity is thus enhanced on the smaller geometries.

The typical frequencies at P1 are 1200Hz for $W = 1$ mm and 300Hz for $W = 2$ mm, at P2 are 300Hz for $W = 1$ mm and 100 Hz for $W = 2$ mm. The changes on the typical frequency values at different locals are due to the changes of the vortices scales throughout the mixing chamber: at the jets impingement region there is one vortex in each side of the mixing chamber while the jets flow through the chamber axis; at downstream locations, such as P2,

the vortices evolve sequentially forming a vortex street and a single vortex is observed at each section of the mixing chamber. The flow oscillations from the vortex street region are not driving the small oscillations of the jets impingement point - contrary to what happened in the $W/w=2$ geometries where the same typical frequencies are observed at P1 and P2. The flow structures around the jets are inducing new frequencies, which will only be clear for the power spectra of the $W/w=8$ geometries, where the jets impingement point clearly oscillates - see the v_x^* time histories of **Figure 4.5**.

The typical frequencies at P2 do not scale with a factor of four when going from $W=1$ mm to the $W=2$ mm: the typical frequencies scale factor is three thus the vortices diameter is not scaling as directly with the chamber width as in the previous case: $W/w=2$. Nevertheless, the ratio of the diameters of the vortices between the different geometries, that were inferred from the ratios of the typical frequencies, are not much different when the frequency ratio is 4 or 3: for a frequency ratio of 4 the vortices diameter ratio is 2, while for a frequency ratio of 3 the vortices diameter ratio is 1.7.

4.7.2.3 Power Spectra Analysis $W/w=8$

For $W/w=8$ the typical frequencies at P1 keep in the same range observed for $W/w=4$: $\approx$ 1200 Hz for $W=1$ mm and in the range of 100Hz to 200Hz for $W=2$ mm where a well-defined typical value does not exist. The main evolution is the increase on the energy levels of the typical frequencies, caused by the oscillation amplitudes that are much higher at $W/w=8$ than at $W/w=4$, and the energy is much more spread around the typical value. Thus, the oscillations of the jets have higher amplitude, as was seen from the time histories of **Figure 4.5**, and are more chaotic – the oscillation frequency is not so fixed and is varying within a range of values.

At P2 the oscillation typical frequencies are ≈ 500 Hz for $W=1$ mm and ≈ 125 Hz for $W=2$ mm, i.e. the frequencies are slightly higher at P2 for $W/w=8$ than for $W/w=4$, this is more clear for the $W=1$ mm geometry. The frequencies are related to the vortices diameters according to the relation found by Santos et al. (2009), i.e. the flow frequency increases fourfold when the chamber width is halved. The vortices on the T-jets geometry with $W=1$ mm and $W/w=8$ are larger than on the $W/w=4$ and $W/w=2$ geometries, as clearly seen

from the streamline maps in **Figure 4.2**. An increase on the vortices diameter, according to Equation (4.34), should decrease the oscillation frequency, which is not the case, the frequencies at P2 increase from the $W/w=4$ to the $W/w=8$ geometries. Although the vortices are larger in the $W/w=8$ geometries, they are closer or more packed, i.e. there are more vortices flowing on each period at a fixed point. For these geometries, the frequencies predicted by Equation (4.34) that considers round vortices occupying the entire chamber width are 760Hz for $W=1$ mm and 190Hz for $W=2$ mm, i.e. the deviation from the model of Santos et al. (2009) is around 30%.

4.7.2.4 Power Spectra Analysis Summary

From the above discussion, we can summarize geometry influence on the flow patterns and flow dynamics as follows:

1. the increase of the chamber to jets width ratio, W/w, reduces the chamber section occupied by the jets favouring the appearance of vortices with increased size;
2. the chamber width, W, favours the flow dynamics and the formation of vortices at upstream locations of the chamber; furthermore the chamber widths also favoured an earlier onset of local chaotic behaviours of the flow dynamics, Eullerian Chaos (Moon, 2004).

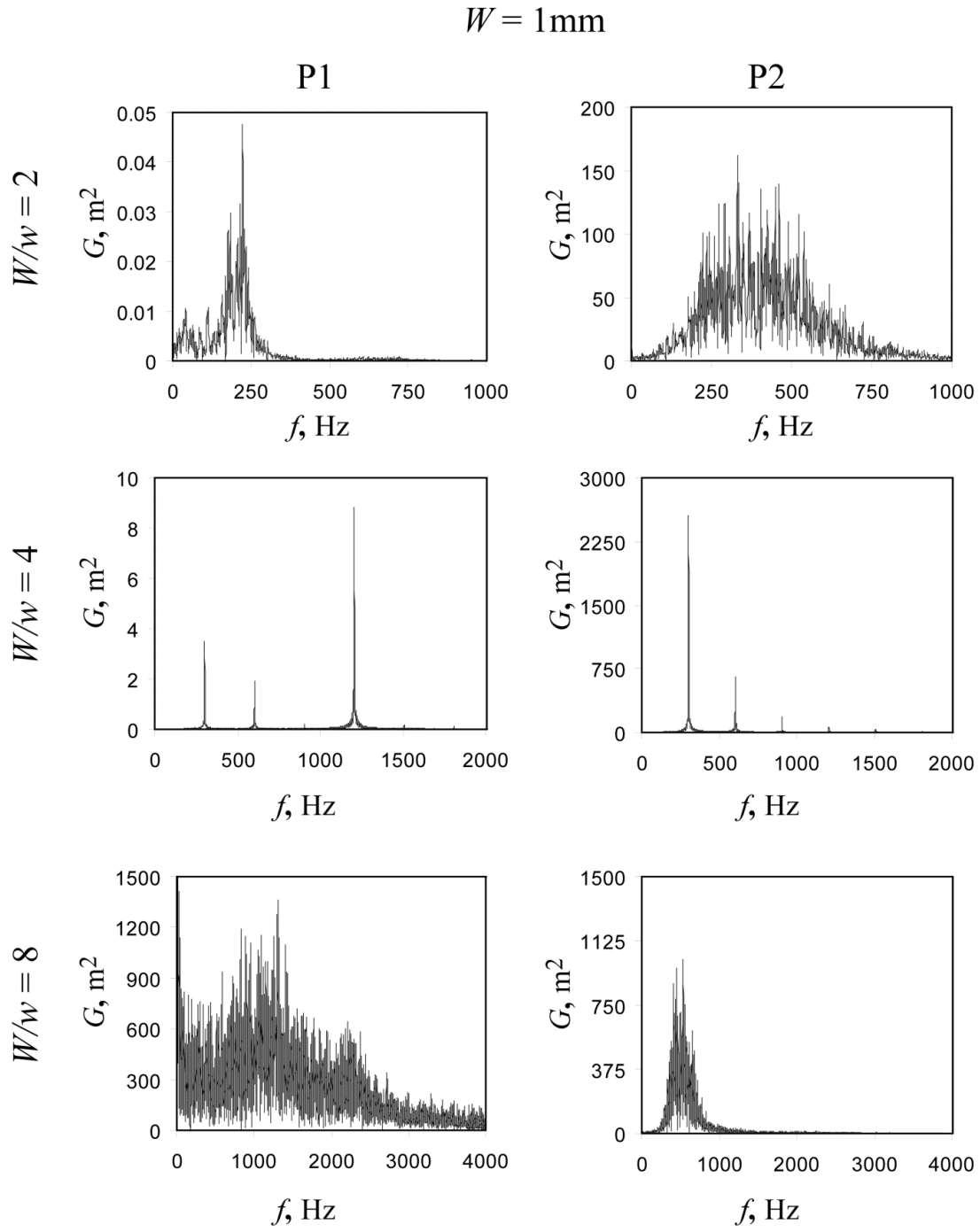

Figure 4.8 Power spectra of υ_x^* at the impingement point, P1, and middle point, P2, for the T-jets mixing chambers with $W = 1$ mm, and with width ratios $W / w = 2$, 4 and 8.

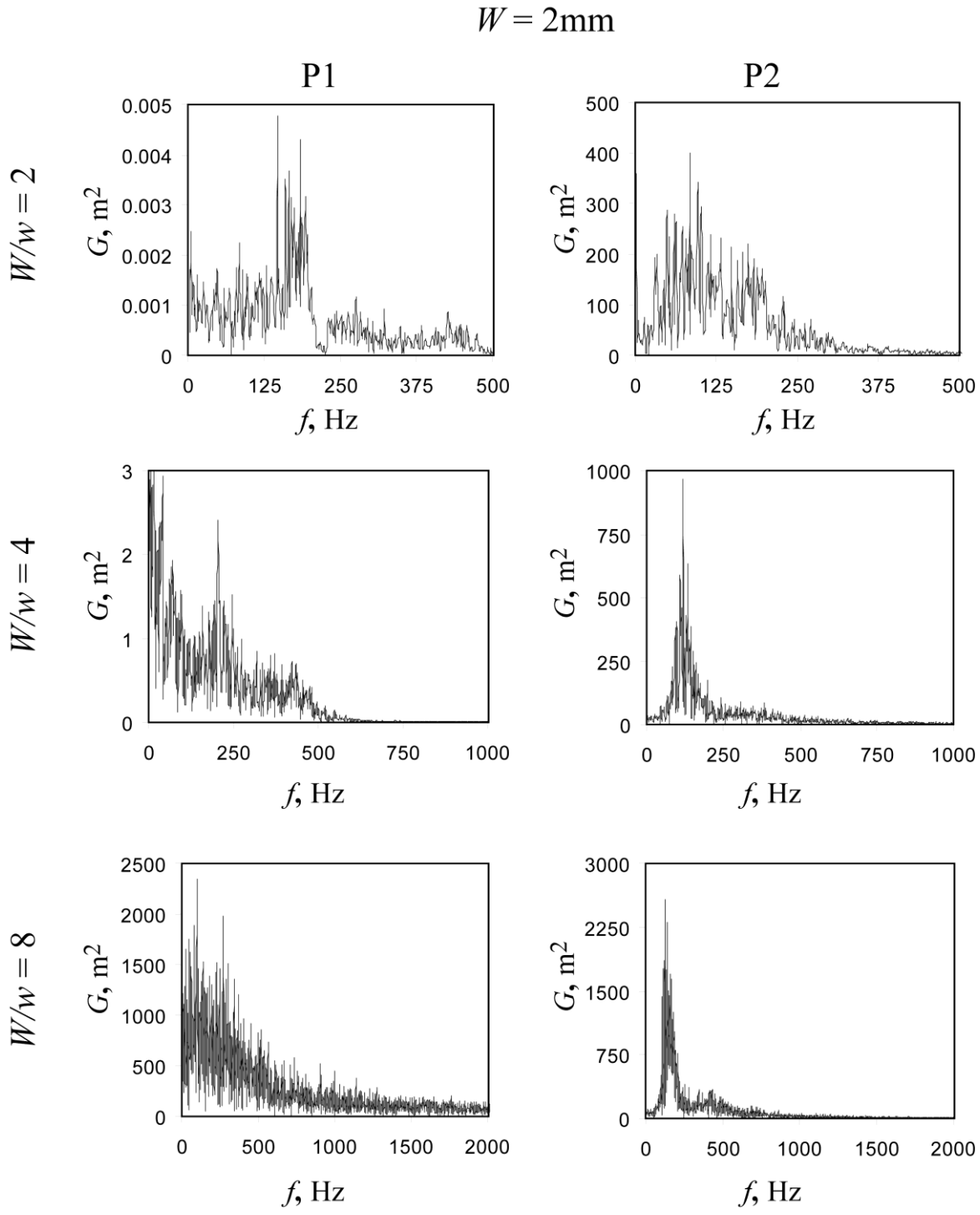

Figure 4.9 Power spectra of υ_x^* at the impingement point, P1, and middle point, P2, for the T-jets mixing chambers with $W = 2$ mm, and with width ratios $W / w = 2$, 4 and 8.

4.7.3 **Chaotic Advection Analysis**

In this section, the effect of W/w on the mixing was also studied with the 2D CFD model using the trajectories of discrete particles. Particles are injected on the mixing chambers for a short period to quantify mixing (Aubin et al., 2003) as described in the previous Section 4.6.4.2. Here, the mixing is seen from the evolution of the maps with the particles positions for the geometries with $W/w=2$ in **Figure 4.10**, $W/w=4$ in **Figure 4.11** and $W/w=8$ in **Figure 4.12** all at a fixed $Re=600$. The time on the maps, ti, is set to zero at the instant of the particles injection, which is after one second of the dynamic simulation. The particles are injected through a line occupying the entire jets width and located at the junction of the injector and the mixing chamber. The particle maps clearly show the initial scales of mixing and their evolution: the initial scale is the jets width that is sheared throughout the chamber with different intensities depending on the flow patterns and dynamics.

For the $W/w=2$ case the jets bend to the outlet before the actual impingement point; after the jets thin slightly due to the velocity profile - the jets have higher velocity on the central regions. Downstream the impingement point jets are surrounded by small vortices that capture portions of fluid from the jets, nevertheless the bulk of the flow occurs through the jets within the axial region of the chamber, and scale reduction of the initial lamina is mainly due to the jets velocity profile.

The geometry with $W/w=4$ differs from the $W/w=2$ particularly at downstream locations on the greater influence that the surrounding vortices have upon the jets, forcing them to meander throughout the chamber more pronouncedly at $W/w=4$ than at $W/w=2$. The thinning of the jets occurs mainly after the onset of the vortex street, at a distance $\approx 3W$ downstream the jets impingement point. The particles are now more frequently dragged into the vortices. The dragging of fluid from the jets into the vortices is the main mechanism engulfing fluid entered separately from each jet into the mixing chamber; as demonstrated from CFD simulations of mixing and chemical reaction by Santos et al. (2005).

The geometry with $W/w=8$ has the most generalized flow dynamics with vortices being formed immediately downstream the jets' impingement point. The thinning of the initial lamina, the jets, is made by the vortices that engulf the opposite jets immediately after their

impingement point. Within 2 ms the particles are completely spread throughout the chamber and the initial structure, the jet, is no longer identifiable.

The mixing is faster and more intense, i.e. with stronger reduction of the initial mixing scales, with the increasing flow dynamics occurring, when the W/w increases from $W/w=2$ to $W/w=8$.

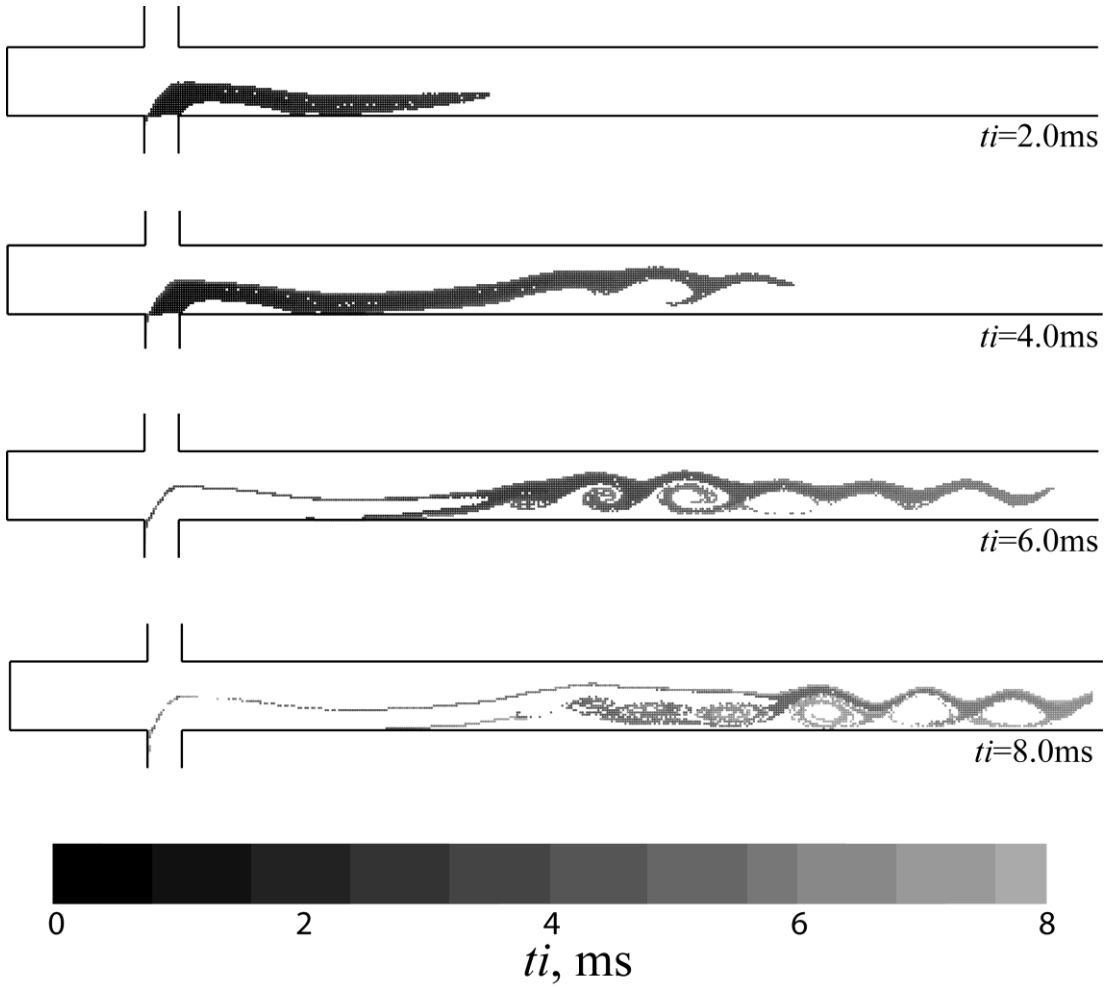

Figure 4.10 Maps with the evolution of particles positions for the T-jets mixing chambers with $W=1$ mm and ratios $W/w=2$ at $Re=600$.

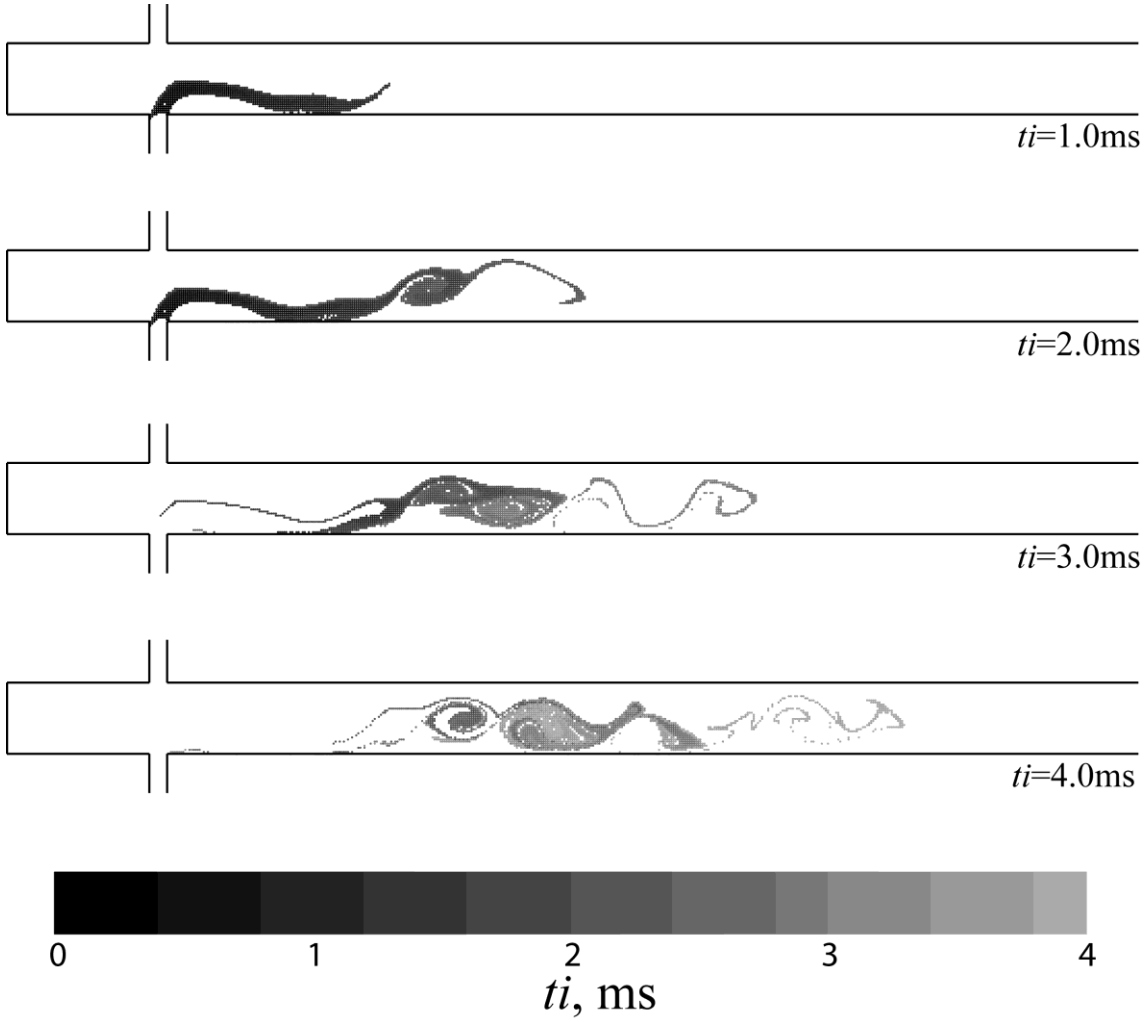

Figure 4.11 Maps with the evolution of particles positions for the T-jets mixing chambers with $W = 1$ mm and ratios $W / w = 4$ $Re = 600$.

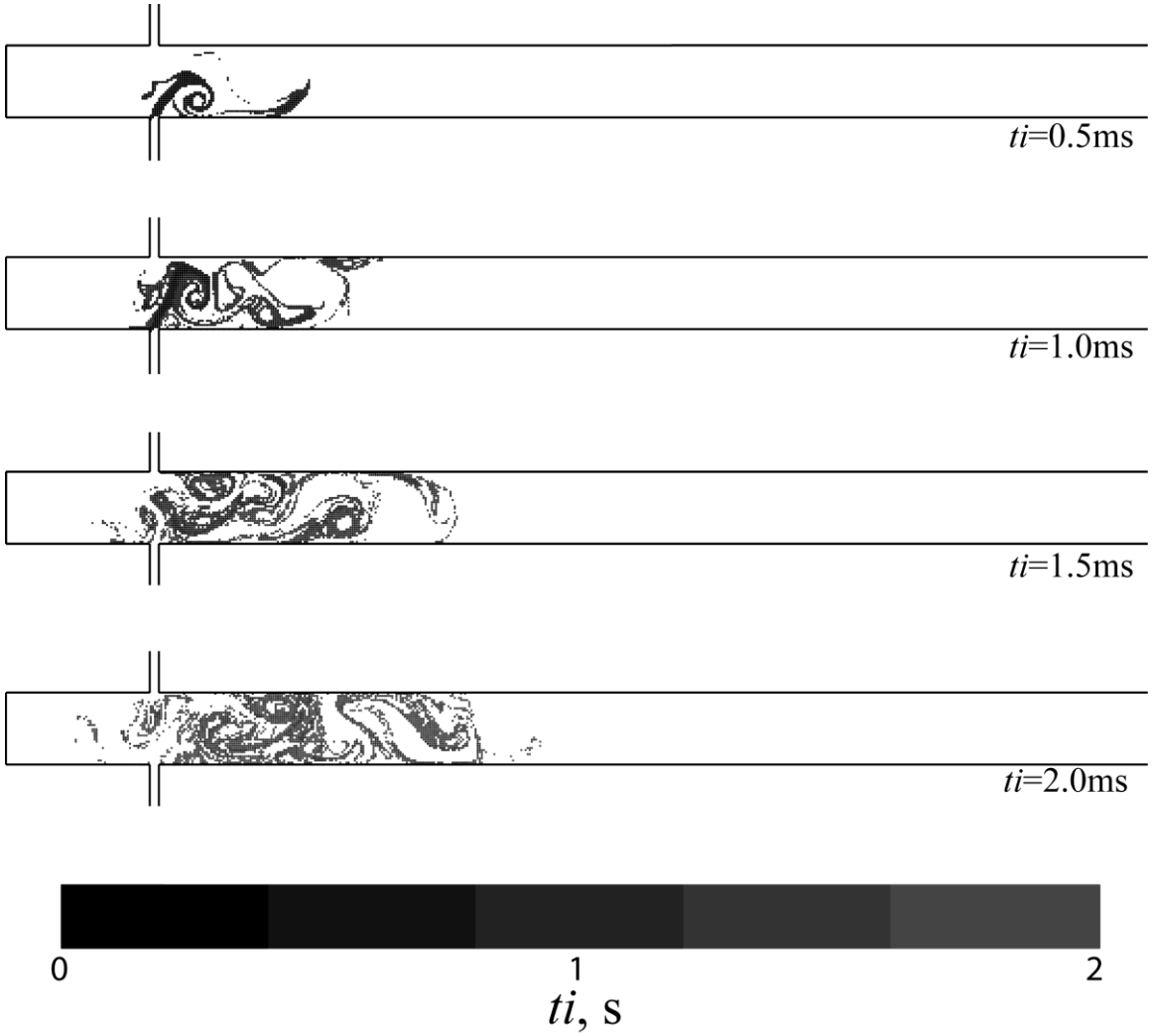

Figure 4.12 Maps with the evolution of particles positions for the T-jets mixing chambers with W = 1 mm and ratios W / w = 8 at Re = 600.

4.7.4 Comparison with Experimental Results

The 2D CFD results have shown with detail some mixing mechanism observed from experimental PLIF data reported in **Chapter 3**. For the comparison between CFD results and experiments a relation between the Reynolds numbers for the experimental T-jet mixer and the CFD simulation model is developed. With the hydraulic diameter for the prismatic cross section channel the Reynolds number is defined as

$$Re_{Hjet} = \frac{\rho \upsilon_{inj}}{\mu} \frac{2wd}{(w+d)} \tag{4.35}$$

For the 2D CFD, the depth or the thickness is infinite .i.e. $d \to \infty$. The Reynolds number calculated for the infinite model $Re_{CFD_{2D}}$, is therefore defined as

$$Re_{CFD_{2D}} = \lim_{d \to \infty} \frac{\rho \upsilon_{inj}}{\mu} \frac{2wd}{(w+d)} \tag{4.36}$$

which simplifies to

$$Re_{CFD_{2D}} = \frac{\rho \upsilon_{inj}}{\mu} 2w \tag{4.37}$$

For the experimental results the Reynolds number was calculated with Equation (3.1) see **Chapter 3** which is same as the Equation (4.23) in **Chapter 4** which is

$$Re = \frac{\rho w \upsilon_{inj}}{\mu}$$

Therefore the relation between the

$$Re_{CFD_{2D}} = 2Re \tag{4.38}$$

Here, in the **Figure 4.13** for the purpose of comparison with the 2D CFD results are shown three images of the mixing patterns obtained with PLIF; the three 3D chambers have the injectors width, $w = 1$ mm and $w = 0.5$ mm, and depth, $d = 4$ mm, and different mixing chambers width, $W = 2$ mm and $W = 6$ mm. PLIF images shown above have Reynolds number of 300, which is defined with Equation (4.23) and the 2D CFD flow fields show above have the Reynolds number of 600.

The mixing chamber having $W = 2$ mm and $W / w = 2$ from 2D CFD results is observed to have the same flow behaviour described earlier in PLIF results: the jets flow side by side to the outlet without engulfing each other. The Reynolds number of the experiments is lower, and for this geometry, the flow field is steady.

The mixing chamber having $W = 2$ mm and $W / w = 4$ has the similar flow pattern with vortices seen at the lower half in the downstream of the mixing chamber, which is initiating mixing.

The mixing chamber having $W / w = 6$, has the same flow behaviour described from the 2D CFD results for the geometries having $W / w = 6$, the jets engulf each other immediately after their impingement point.

Maintaining the Reynolds number of the experiments and changing the T-jets geometry clearly yielded three different flow regimes. The same influence of the geometry on the flow regime is observed from the experiments and from the 2D CFD simulations.

In the experiments, there is the influence of the third dimension: the depth of the T-jets mixer. The experimental results shown above had a depth, $d = 4$ mm, this was chosen from preliminary studies that showed a critical influence of the depth only for values smaller than 4 mm. A detailed 3D CFD study on the effect of the T-jets chamber is presented in the next section.

$W = \mathbf{2\ mm}; w = \mathbf{1\ mm}; W / w = \mathbf{2}$

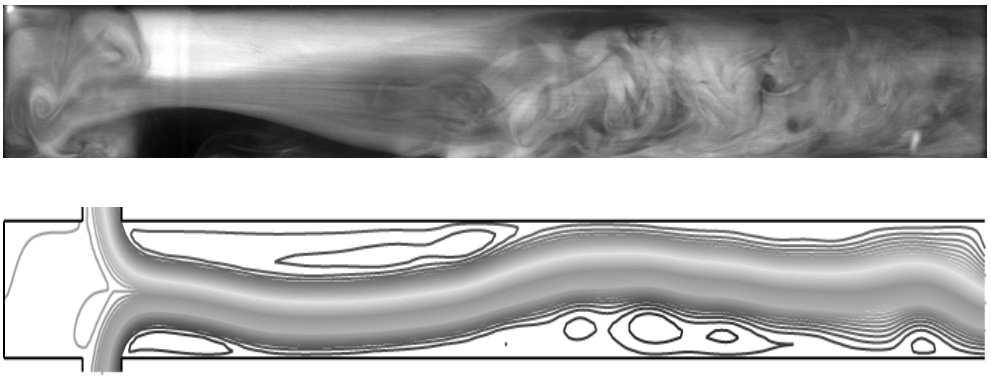

$W = \mathbf{2\ mm}; w = \mathbf{0.5\ mm}; W / w = \mathbf{4}$

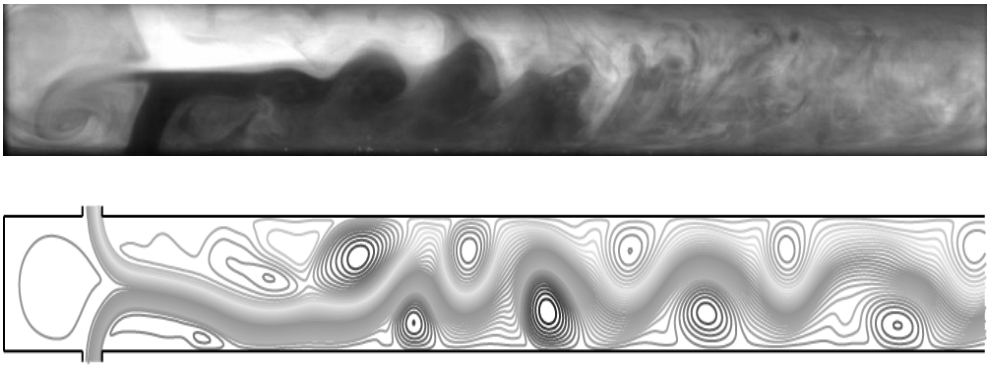

$W = \mathbf{6\ mm}; w = \mathbf{1\ mm}; W / w = \mathbf{6}$

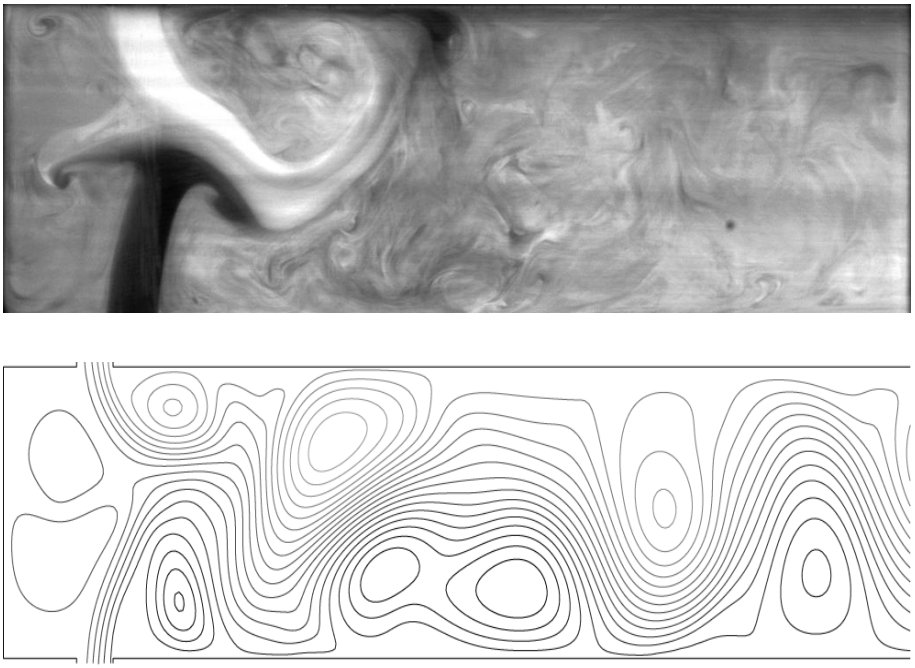

Figure 4.13 PLIF images of the three T-jets mixers having different geometries at *Re*=300 and 2D CFD simulation results at *Re*=600.

4.8 3D CFD Study of T-jets Mixers

In this section, the 3D CFD simulation of the flow field in the T-jets mixers was conducted. The 3D geometry studied here has the same dimensions as the 2D model excepting the addition of third dimension, the depth d. Therefore, this study will get detailed insight into the flow dynamics in the T-jets mixers and will be compared directly with experimental results. Furthermore, 3D CFD simulation with tracer is studied in Section 4.11. **Figure 4.14** shows the 3D geometry studied with top and front view.

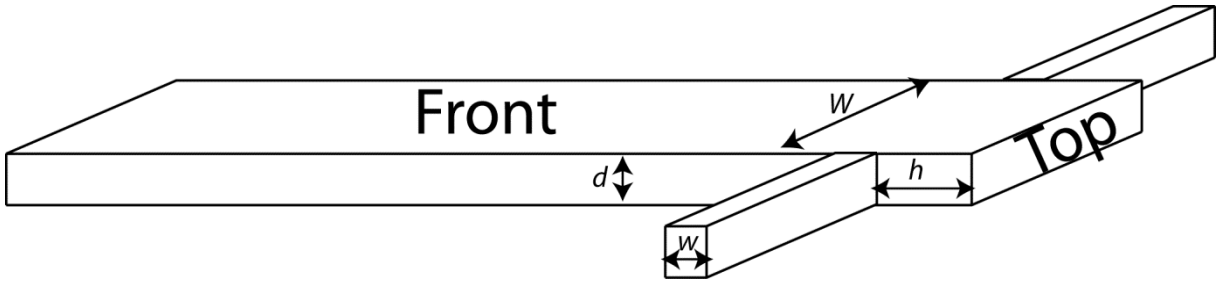

Figure 4.14 3D Schematic representation of the T-jets mixer.

4.8.1 3D-Model Description

The CFD simulations were made with a three-dimensional model of the T-jets mixers as depicted in the **Figure 4.15**. With the 3D model of the T-jets mixers, the significant geometrical parameters, the ratio of the chambers width to the jets injector width, W/w and chambers width to the chambers depth, W/d geometrical parameter, which is not studied with 2D CFD simulation is also incorporated. All the geometrical conditions studied here are similar to 2D CFD simulation, with the injector jets positioned at 2 mm from the closed top of the mixing chamber, the chamber has a height of *H*=50 mm. The lists of T-jets mixers geometries simulated with 3D simulations are shown in **Table 4.2**.

4.8.2 Boundary Conditions

All the boundary conditions are similar to the 2D CFD simulation with the exception of addition third dimensions. No slip conditions at the walls of the mixing chamber, i.e., the three velocity components were set to zero at the wall, and at the chamber outlet a constant pressure value was set, left injector jets velocity is defined as $\vec{\upsilon} = (-\upsilon_{inj}, 0, 0)$ and in the right

injector $\vec{\upsilon} = (\upsilon_{inj}, 0, 0)$, the injector velocity, υ_{inj}, is defined by the Equation (4.23) similar to the equation used in 2D CFD simulations and PLIF experiments. The model and boundary conditions are shown in **Figure 4.15**.

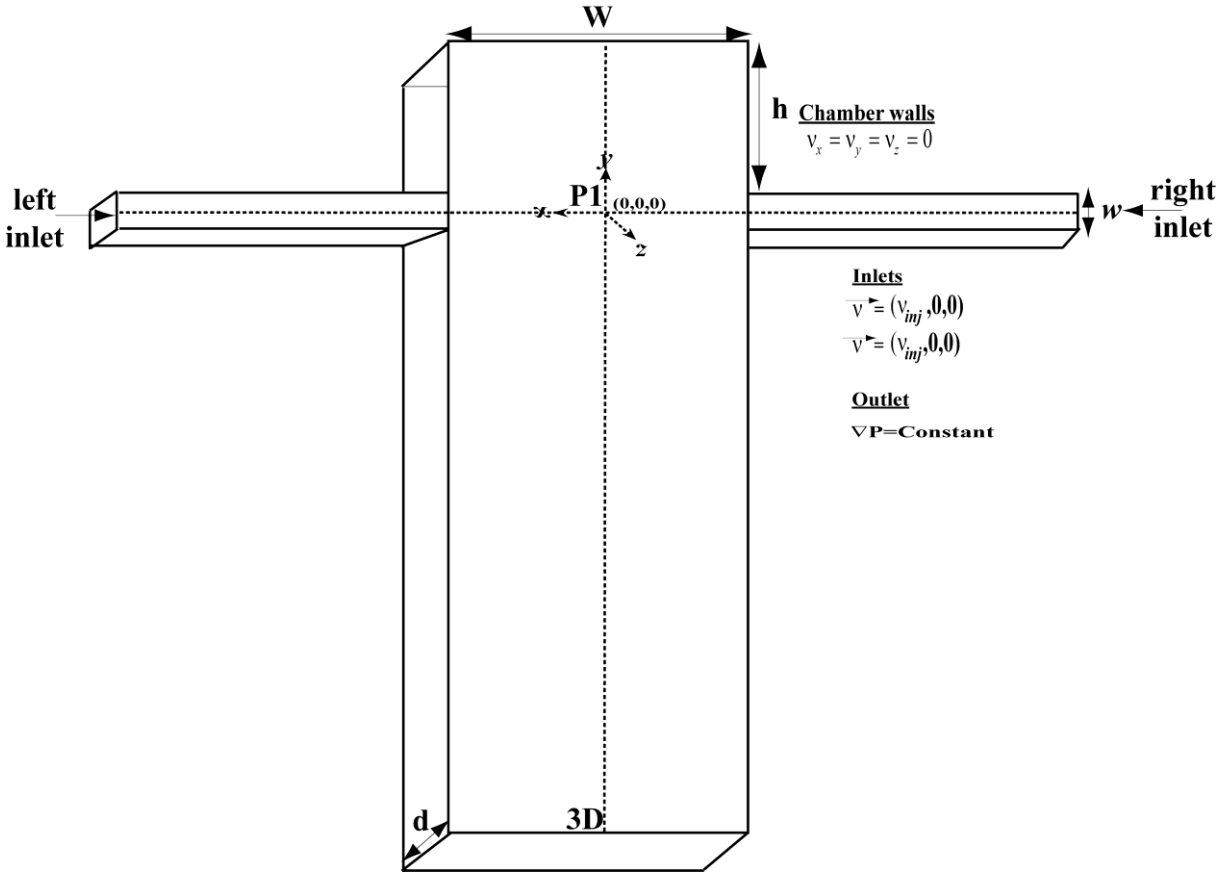

Figure 4.15 3D CFD model of T-jets mixers with boundary conditions.

Table 4.2. List of T-jets mixers geometrical parameters studied in 3D CFD dynamic simulations.

Chamber Width (W) mm	**Jets Width (w) mm**	**Chamber Depth (d) mm**	W/w **ratio**	W/d **ratio**
2	0.5	4	4	0.5
2	1	4	2	0.5
6	1	1	6	6
6	1	2	6	3
6	1	3	6	2
6	1	4	6	1.5
6	1	6	6	1

4.8.3 **Governing Equations**

For the flow field simulation the continuity (see Equation (4.1)) and Naviers-Stoke equation (see Equation (4.2)) were numerically solved as explained earlier in Session **4.2**.

4.8.4 **Initial Conditions**

The solver used for the simulation was Pressure based solver for both steady and transient state simulation. The residuals of the solution of the Equations (4.1) and (4.2) were converged to 10^{-5}, for the steady state simulations as per the absolute convergence criteria.

All the simulations were converged to a steady state, which was used as the initial solution for the dynamic simulations. The solution method was Pressure-Velocity coupling; Coupled scheme was set for both steady and transient simulation. The spatial discretization gradient was Least Squares Cell based, Pressure spatial gradient was Second order for both steady state and transient state and for spatial momentum discretization Third Order MUSCL was set. For the transient simulations, a second order implicit formulation was set. For all the transient simulations, the residuals were converged to 10^{-6}.

4.9 3D Dynamic Simulation Analysis

The results of the simulations are shown using the vorticity, $\vec{\omega}$, which is the curl of the velocity vector,

$$\vec{\omega} = \nabla \times \vec{\upsilon} \tag{4.39}$$

Two components of this vector are shown: ω_y and ω_z for cuts of the mixing chamber in the xz and xy planes, respectively.

4.9.1 Grid Independent Model

In order to assess the hydrodynamics independency on the grid, two different mesh sizes were tested. The T-jets mixers geometry with dimensions $W = 6$ mm, $w = 1$ mm and $d = 4$ mm and with ratios chamber width to jets width $W / w = 6$ and chamber width to chamber depth $W / d = 1.5$ was chosen. The boundary and initial conditions are similar to the ones explained in Section **4.8.2**. The Reynolds number studied for comparison was 300. The variable studied to evaluate the grid independency is the standard deviation of the x velocity component dynamic data, σ_x, from 0 to 2 seconds, at the impingement point. The difference between the standard deviations obtained with a grid of 0.3 and 0.4 mm is less than 5%. **Table 4.3** summarizes these results. The grid independent simulation considered was achieved when the variables did not vary more than 5%. Such imposition was verified for average grid densities between 0.4 and 0.3 mm. When the average cell sizes change from 0.4 to 0.3 mm the number of cell elements increases and consequently the computational effort increases greatly.

It is also observed from z vorticity shown in **Figure 4.16** for the grid size 0.4 to 0.3 mm that the flow characteristics were similar without any observable change and maintain similar flow characteristics. After the jets impingement, a vortex street evolves continuously throughout the mixing chamber until the outlet.

Power spectra of υ_x at impingement point P1 was also analysed as shown in **Figure 4.17** the energy peak is around 1300 at a frequency of ≈20 Hz for both the cell size considered. The energy peaks shown in this power spectra at a frequency value stand for an oscillatory

behaviour having the same frequency. The power spectra compares result from both grids at higher statistical order than the previous comparisons, so one can say that the flow dynamics are intact without changes for the different cell size used in the simulation. So for the purpose of consuming time, the geometry with low cell size of 0.4 mm was used for the 3D CFD simulation for all the T-jets mixers geometries involving hydrodynamic studies.

Table 4.3. Grid independence evaluation for geometry with ratio $W/w=6$ and $W/d=1.5$

Average cell size (mm)	Total number of cells	Total number of faces	Total number of nodes	σ_{v_x}	%
0.3	50440	162142	61464	0.129436	
0.4	22980	75268	29461	0.135902	5

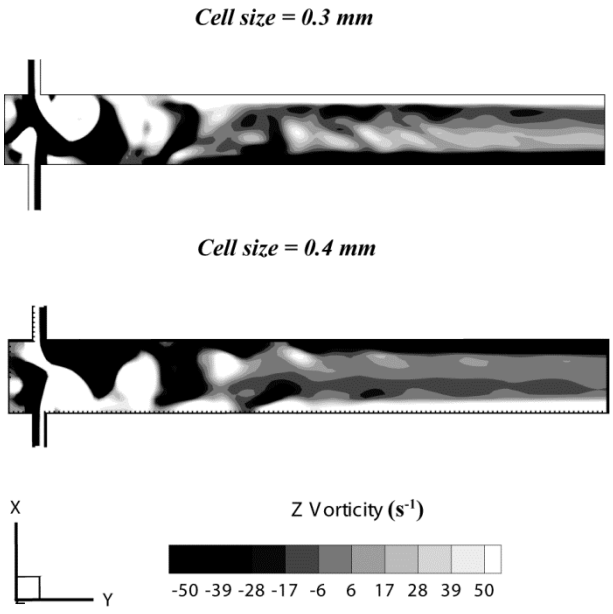

Figure 4.16 Z vorticity map for the geometries with ratio $W/w=6$ and ratios of $W/d=1.5$ at different grid size 0.3 mm and 0.4 mm for Re=300.

$W/w=6$; $W/d=1.5$; W=6 mm; w=1 mm; d=4 mm; Cell size=0.3 mm

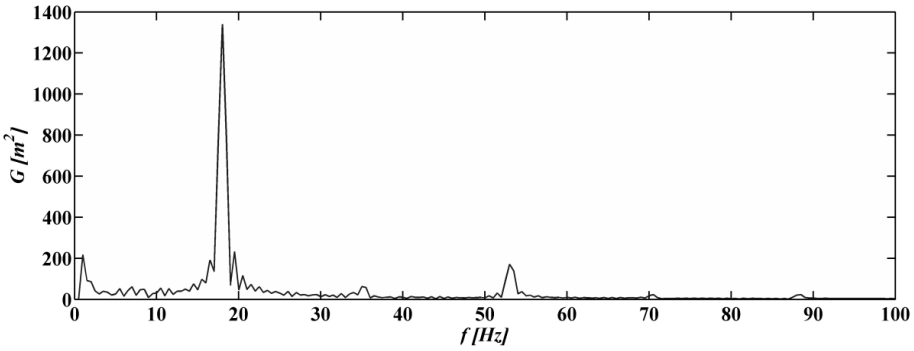

$W/w=6$; $W/d=1.5$; W=6 mm; w=1 mm; d=4 mm; Cell size=0.4 mm

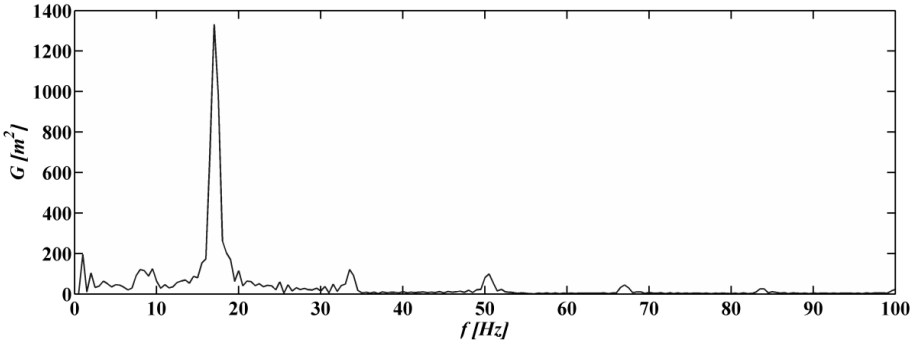

Figure 4.17. power spectra of v_x at the impingement point for the for geometries with ratios $W/w=6$ and $W/d=1.5$ at different grid size 0.3 mm and 0.4 mm for Re=300.

4.9.2 Flow Field

4.9.2.1 Effect of Depth Ratio (W/d)

Here all the simulations were performed for *Re* = 300 and critical Reynolds number, as it was seen from experimental results in **Chapter 3,** at low Reynolds number .i.e. $Re \leq 100$, the flow dynamics was segregated for all the geometries studied.

Figure 4.18 shows two y vorticity maps and velocity vectors in a plane parallel to the top and bottom planes of the mixing chamber, i.e., a plane normal to the mixing chamber axis, for the geometries having ratio $W/w=6$; and ratios $W/d=1$, 1.5, 2, 3 and 6 at *Re* = 300. The first column of the y vorticity maps shows flow dynamics near the impingement point while the right column shows a plane at the centre of the mixing chamber; different flow dynamics are observed at these planes depending on the T-jets geometries:

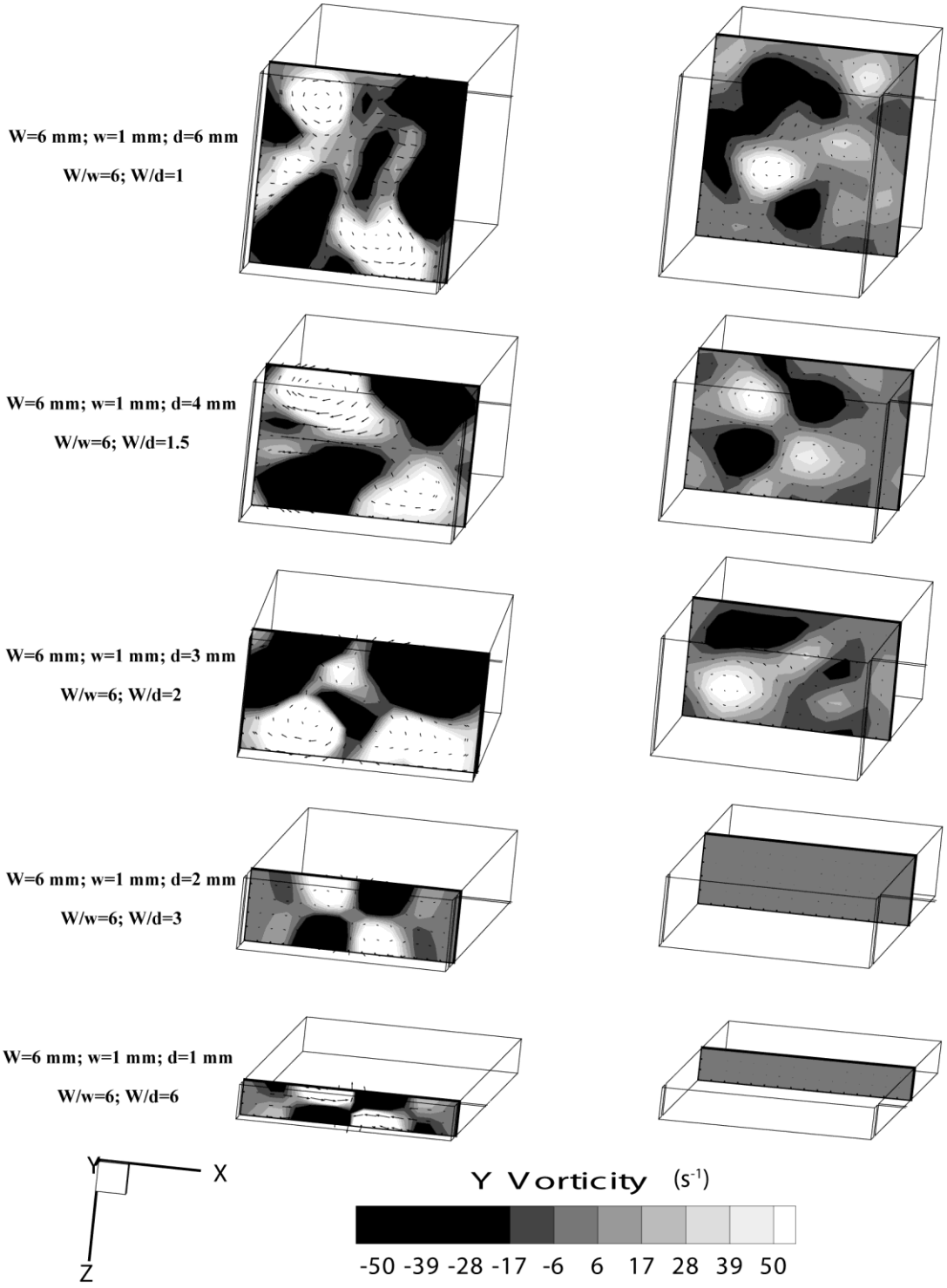

Figure 4.18 y **vorticity map and 2D velocity vector map after the impingement point and in the center of the chamber for the geometries with ratio** $W/w=6$ **and ratios of** $W/d=$ **1, 1.5, 3 and 6 for *Re*=300.**

For $W/w=6$ and $W/d=1$, 1.5 and 2, subsequent to the jets impingement four complete circular vortices are observed on both sides of the jets. Each of these vortices approximately occupies half of the mixing width and depth of the mixing chamber. These vortices have opposite rotation directions, as can be seen from the positive and negative values of the y vorticity. In the plane located in the middle of the T-jets mixers shown in the right hand side column, the vorticity values are smaller than the plane near the impingement point, thus the fluid rotation diminishes throughout the mixing chamber showing a decrease on mixing dynamics.

For $W/w=6$ and $W/d=3$, 6 geometries, one observes that the four vortices formed in the plane subsequent to the jets impingement do not occupy the complete section of the mixing chamber. Furthermore, these vortices do not cross the middle lines of the mixing chamber section, both vertical and horizontal, thus keeping the flow segregated in each side of the camber. When compared to the vorticity maps from geometries with ratios $W/d=1$ and 1.5 and 2 there is a strong wall effect, very narrow space is available between the top and bottom planes of the mixing chamber. This weaker dynamics of mixing close to the impingement point evolves to a parallel flow observed at the mid plane of the geometries $W/d=3$ and 6, where no flow rotation can be observed from the vorticity maps in **Figure 4.18**.

The CFD simulation clearly shows the rotation of fluid in the normal direction to the main flow direction. The vorticity is twice the angular velocity, and thus from the vorticity maps where the core of the vortices exhibit vorticity values of $50s^{-1}$, the angular speed is around $25s^{-1}$(=1500rpm). The rotation has the same order of magnitude in the two planes, *xy* and *yz*, close to the region where the jets impinge. The complete rotation pattern of the flow was not visible from the PLIF images due to the fact that is occurring in the plane normal to the imaged plane. Although other authors reported this rotation movement (Bothe et al., 2006; Wong et al., 2004; Soleymani et al., 2008), this was only made for the vortex and the engulfment flow regimes. The rotation in the normal planes to the chamber axis is important and is the main mixing mechanism in narrower mixing chambers, $W/w=1$, and is probably the mechanism underlying the effect of depth on flow regime for the geometries for mixing chambers with larger widths, $W/w=6$.

Figure 4.19 shows z vorticity, plane normal and parallel to the flow from entrance to the outlet, which illustrates better the flow dynamics evolving in the complete geometry and also the formation of vortices after the jets impingement.

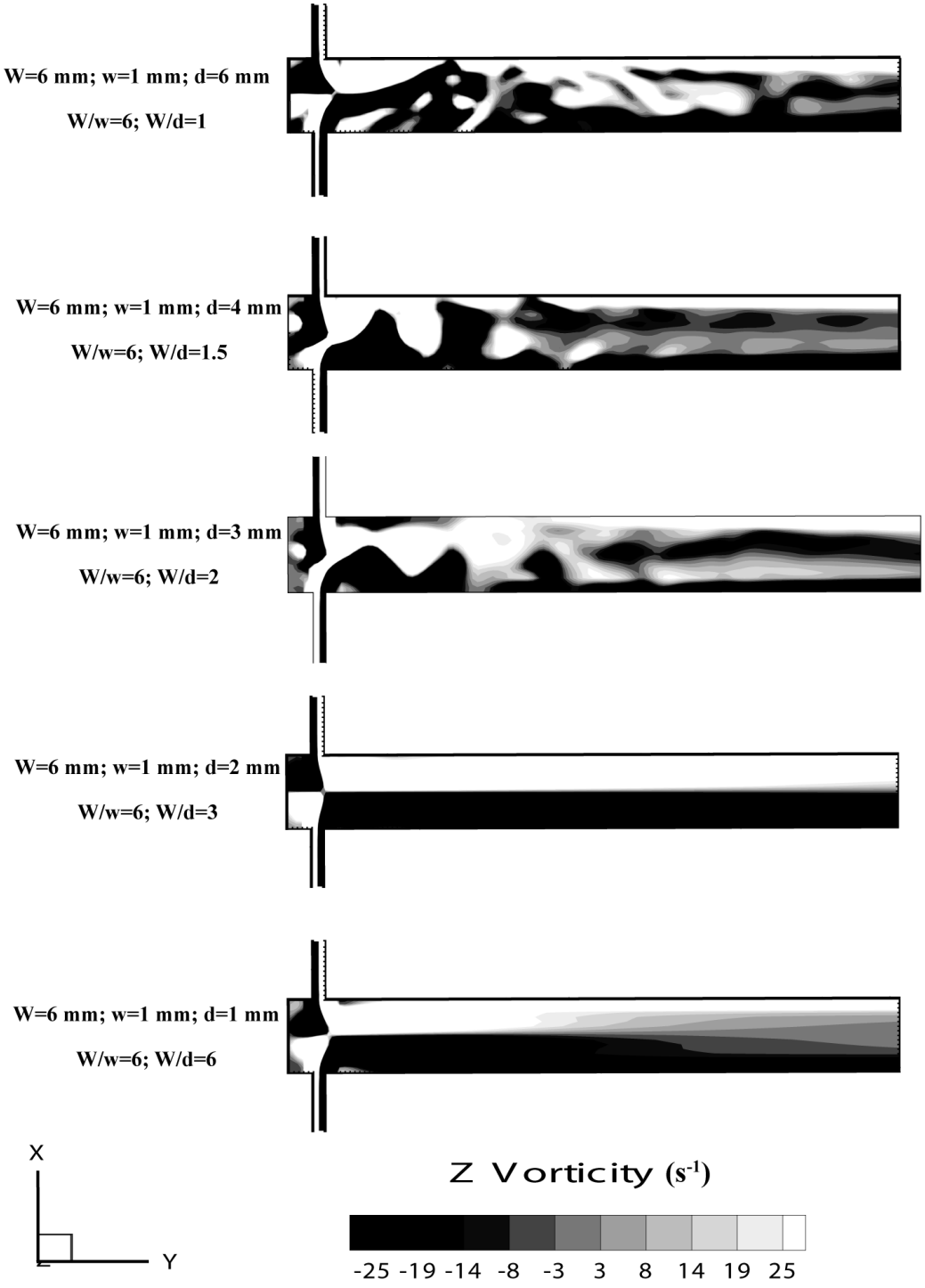

Figure 4.19 Z vorticity map for the geometries with ratio $W / w = 6$ and ratios of $W / d = 1$, 1.5, 3 and 6 for *Re*=300.

For the geometry with ratio $W/w=6$ and $W/d=1.5$, 2 the flow is completely disturbed immediately after the fluids enter the mixing chamber with the emergence of *vortex street*, formed with the engulfing of the fluids from both jets. The vortex street is clear from the alternate sequence of counter rotating vortices: white and black circular regions in the vorticity maps. For the geometry with ratios $W/w=6$ and $W/d=1$ it is visible that the onset of the vortex street occurs at downstream positions from the jets impingement point. In geometries with ratio $W/w=6$ and $W/d=1$, 1.5 and 2, after the jets impingement the vortices are evolving continuously throughout the mixing chamber until the exit of the outlet.

For $W/w=6$ and $W/d=3$, 6 geometries, it is observed that a complete steady segregated flow is being maintained throughout the chamber with absence of any sort of vortex street as seen in **Figure 4.19**.

Figure 4.20 shows the *pathlines,* which are the trajectories that individual fluid particles describe if the flow field instantaneous values were frozen in time. For steady state these line coincide with the trajectories of said particles. **Figure 4.20** has two views of the pathlines, left column (a to e) showing the top view from the mixing chamber top, see **Figure 4.14**, and the right column (f to j) shows the front view.

Figure 4.20 (b, g and c, h) for $W/w=6$ and $W/d=1.5$, 2 shows two vortices in either side of the mixing chamber downstream of the injector jets that are completely disturbed by an intense cross flow; as observed from the path lines crossing each other and reaching the opposite side of the mixing chamber. This flow regime is termed as *self-sustainable chaotic flow regime*.

Figure 4.20 (a and f) representing the T-jets mixer with ratios $W/w=6$ and $W/d=1$, shows similar patterns to $W/d=1.5$ with two vortices one in each side of the mixing chamber (front view). Nevertheless the flow field observed in **Figure 4.20** (f) is more symmetric than $W/d=1.5$ and 2, particularly in the mixing chamber head space (top view) where a pair of vortices is observed. For both these geometries $W/d=1.5$ and 2, the vortices are formed in pairs downstream the injectors in a chaotic sequence that is clear from the simulation dynamic visualization (front view). On the other hand for $W/d=1$, the vortices sequence is not so clear and the path lines pattern is closer to those reported in the work of (Bothe et al., 2006;

Soleymani et al., 2008) as *engulfment flow regime*. In this geometry the mixing is due to convective mechanism. It is observed for $W/d=1$ that the vortices formation may be affected in deeper mixing chambers. So it is probable that there is an optimum value for W/d .

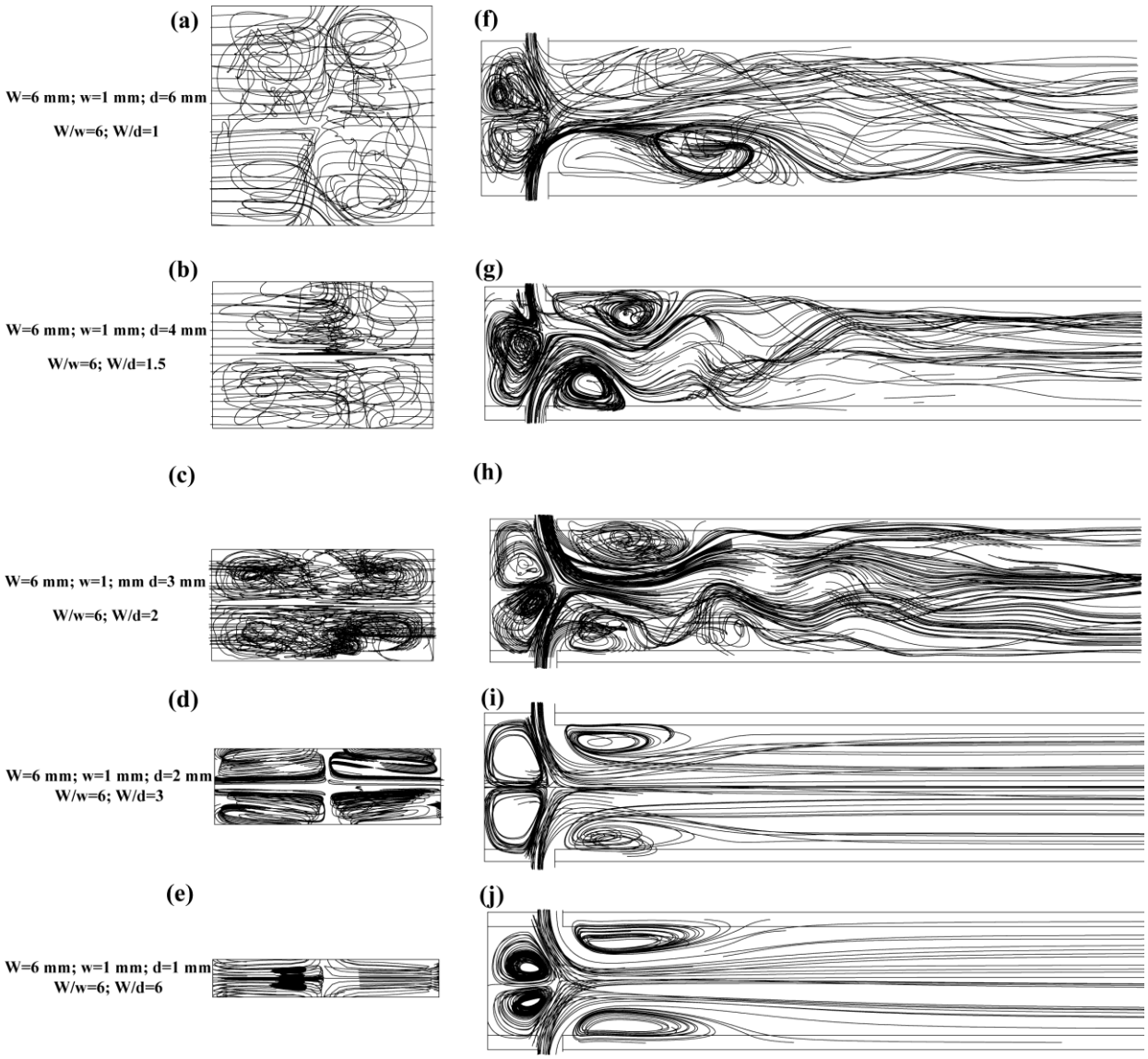

Figure 4.20 Path lines for the T-jets geometries with ratio $W/w=6$ and ratios of $W/d=1$, 1.5, 2, 3 and 6 at *Re*=300, viewed from the mixing chamber top (left column) and from the front (right column).

Figure 4.20 (d and i) for $W/w=6$ and $W/d=3$, two vortices are seen in either side of the chamber from the top view. This flow regime is termed as *vortex flow regime*. **Figure 4.20** (i) front view shows the flow from the entrance to the outlet is completed steady and straight without any cross flow or swirling of the two opposed injector streams. This flow regime is

similar to the maps reported for vortex flow regime by Bothe et al. (2006) and Soleymani et al. (2008).

For $W/w=6$ and $W/d=6$, **Figure 4.20** (e and j), does not show any vortices in the mixing chamber (top and front view), the flow is completely symmetrical and steady. Straight path lines are observed similar to those in the $W/d=3$, T-jets mixer. This flow is termed as *segregated flow regime*.

Figure 4.21 shows z vorticity maps representing critical Reynolds number where the transition occurs from segregated steady state to unsteady dynamic state. For the ratio $W/w=6$ in the geometries having larger depths, $W/d=1$, 1.5 and 2, transition occurs at low Reynolds number around *Re*=200 for $W/d=1$, *Re*=180 for $W/d=1.5$, and Re=190 for $W/d=2$. In the shallow geometries, $W/d=3$ and 6, the transition of flow regime occurs at *Re*=390 for $W/d=3$ and for *Re*=548 for $W/d=6$.

From this flow field results it could be inferred that for the T-jets mixers with ratios $W/w=6$ and $W/d=1$, 1.5, 3 and 6, as the depth of the mixing chamber decreases the formation of vortices diminishes and the transition occurs at high Reynolds number as in the case of $W/d=$ 3 and 6. The transition Reynolds numbers were chosen from the experimental results in **Chapter 3**, which have similar flow patterns to those from CFD simulations.

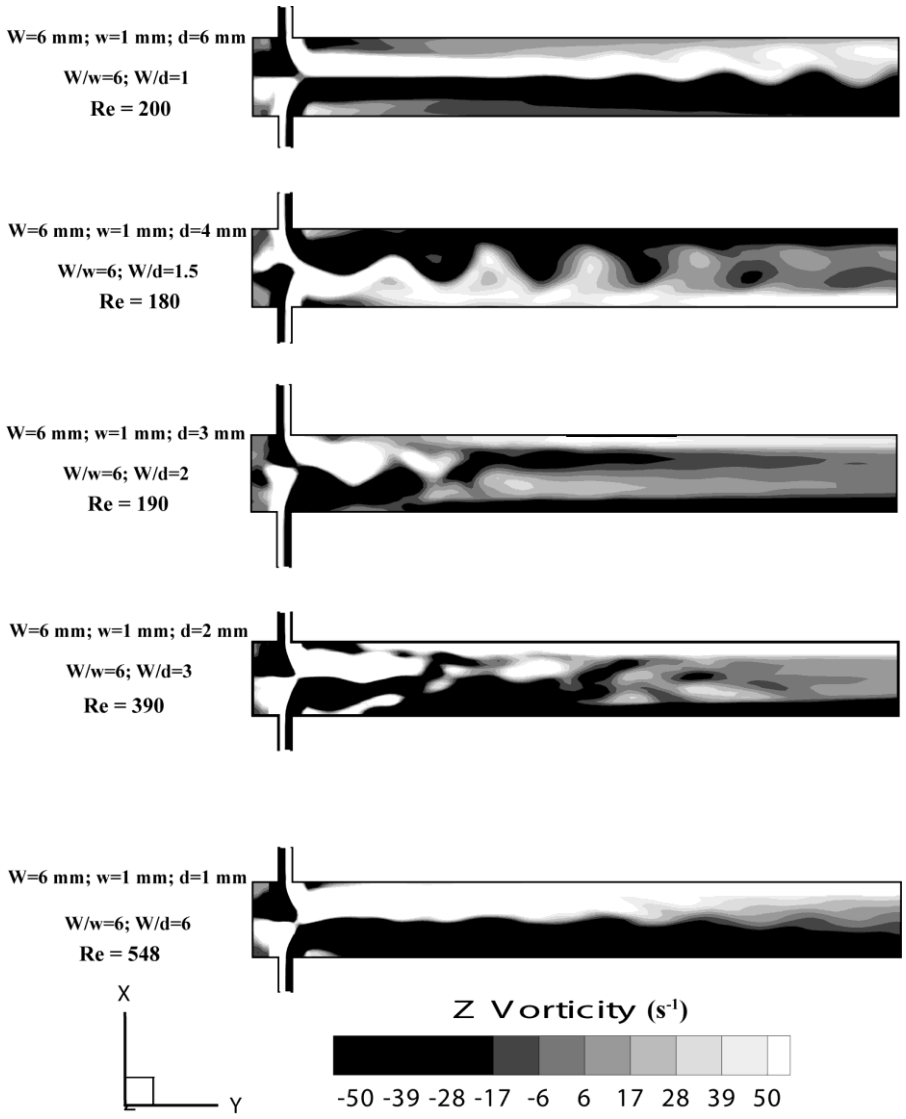

Figure 4.21 Z vorticity for the geometries with ratio $W/w=$ 6 and ratios of $W/d=$ 1, 1.5, 2, 3 and 6 for critical Reynolds number.

4.9.2.2 Effect of Width Ratio (W/w)

The impact of ratio of injectors width to chamber width, W/w, was also studied with 3D simulations and was observed to be an important geometrical parameter in addition to the initial study on the impact of depth in flow dynamics.

Figure 4.22 show y vorticity maps for ratios $W/w=2$ and 4 with $W/d=0.5$, for a fixed chambers depth of $d=4$ mm and chambers width, $W=2$ mm. It is seen that after the jets impingement, the widths of the jets are being kept until the outlet. For $W/w=2$, and 4, it is observed a segregated flow with clear interface between the fluids from opposed jets. This is

quite different from the flow patterns observed when $W/w=6$ and $W/d=1$, 1.5 where the mixing is initiated immediately after the jets impingement with the formation of 4 vortices. In the cases $W/w=2$, 4, vortices form making the fluid rotate with a rotation axis parallel to the mixing chamber axis. These vortices refresh the fluid in the contact region of both jets, their effect was visible from PLIF results of **Chapter 3**, when streaks of fluid were observed in the opposed side of the chamber from where the fluid was injected. These vortices are thus dragging small amounts of fluid from the opposed jet. As visible in the centre and downstream of the mixing chamber.

For ratios $W/w=2$ and 4 when the jets collide and bend towards the outlet, the original width of the jets is roughly maintained. In the plane located in the middle of the T-jets mixers shown in the right hand side column, the vorticity values are smaller than the plane near the impingement point, thus the fluid rotation diminishes throughout the mixing chamber showing a decrease on mixing dynamics.

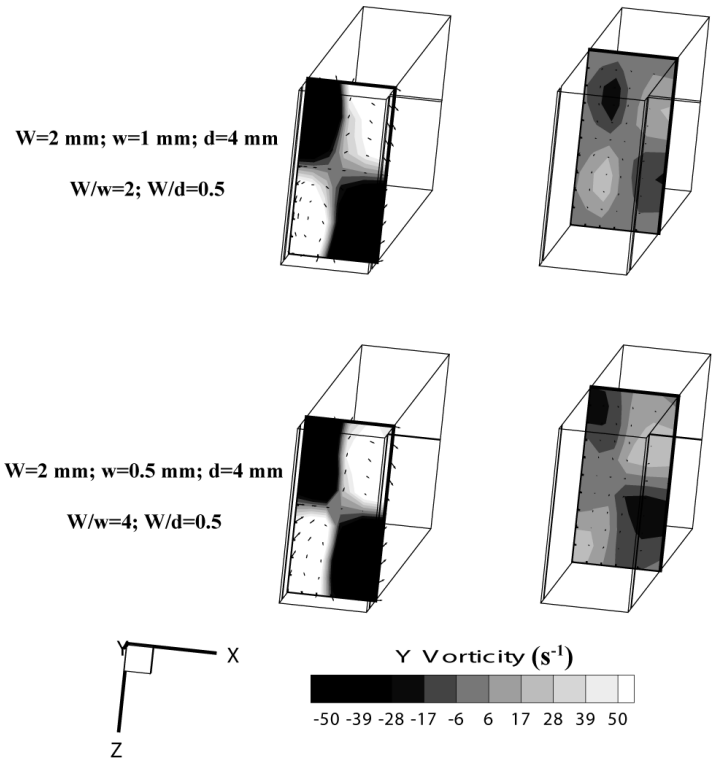

Figure 4.22 y **Vorticity map and 2D velocity vector map after the impingement point and in the center of the chamber for the geometries with ratios** $W/d=$ **0.5 and** $W/w=$ **2 and 4 for *Re*=300.**

Figure 4.23 shows z vorticity maps for the geometries $W/w = 2, 4$. For both geometries, the flow is segregated and steady except in $W/w = 4$ where slight ripple is visible downstream the jets impingement point in the interface of the two fluid streams.

Figure 4.24 shows the pathline for the geometries $W/w = 2$ with the jets $w = 1$ mm and $W/w = 4$ with the jets $w = 0.5$ mm. From the pathlines are not visible any flow patterns that engulf flow from both streams. The pathlines show strong channelling of the flow through the mixing chamber axis.

With the expansion of jets twofold, $W/w = 4$, the flow instability at upstream positions in the T-jets mixer are observed, nevertheless the flow does not evolve to a fully chaotic pattern as those seen in $W/w = 6$ geometries. This is due to the fact that the vortices formed in chaotic flow regimes have a diameter equal to half the width of the mixing chamber minus the width of the jets; when the jets width is larger the free space for formation of vortices decreases.

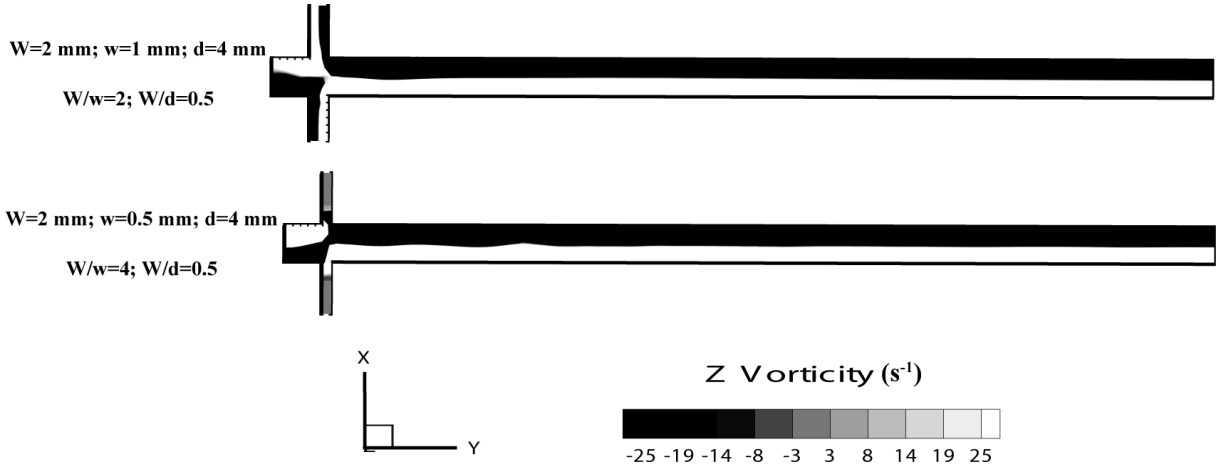

Figure 4.23 Z Vorticity map for the geometries with ratio $W/w = 0.5$ and ratios $W/w = 2$ and 4 for *Re*=300.

Figure 4.24 . Path lines for the T-jets geometries with ratio $W/d = 0.5$ and ratios of $W/w = 2$ and 4, at *Re*=300, viewed from the mixing chamber top (left column) and from the front (right column)

4.9.3 Analysis of Time Histories and Power Spectra

To analyse the flow dynamics in the different T-jets mixers geometry studied, a point P1 is defined at the intersection of the jets and the chambers axis-see **Figure 4.15** at the jets impingement point. Here x velocity component, υ_x, is analyzed as the transport mechanisms between both sides jets are in the x direction. For the Reynolds number studied υ_{inj} depends on the jets width, see Equation (4.23) and so υ_{inj} varies with the w. For a direct comparison between different cases the normalized velocity, $\upsilon_x^* = \upsilon_x / \upsilon_{inj}$, is used.

4.9.3.1 Time Histories

Figure 4.25, **Figure 4.26**, **Figure 4.27** and **Figure 4.28** shows the time histories of υ_x^* at P1 (see **Figure 4.15**). The location of the impingement point oscillates from one side to the other of the chamber axis; the value of υ_x^* is set from the dominant jet at each instant, i.e. when one jet pushes the opposite jet to its side of the chamber the observed value of υ_x^* at P1 is the maximum velocity value of the dominant jet. The jets keep their velocities up to the jets impingement. The formation of vortices immediately after the impingement of the jets is and the oscillations of the jets are related as shown in Santos et al. (2009). Here, the cases having υ_x^* oscillations at P1 are the ones where large circular vortices are formed immediately downstream of the jets as seen from **Figure 4.18** and **Figure 4.19**.

Only the $W/w=6$ with $W/d=1$, 1.5 and 2 cases have a dynamic evolution of υ_x^* at P1, with the oscillations of the value of υ_x^* in the range of $-\upsilon_{inj}$ to υ_{inj} and these oscillations are more periodic for $W/d=1.5$ and 2. For $W/d=1$ the oscillations range $-\upsilon_{inj}/4$ to $\upsilon_{inj}/4$ and are not as periodic as observed for $W/d=1.5$ and 2.

From the oscillation of jets that can be seen from the time histories of υ_x^*, it is observed a *warm-up time*, of around 0.8 sec after the initial steady state at t=0. This period is the time that the system requires to evolve from initial steady state solution to a fully developed chaotic state. The warm-up time is associated with the development of the instability inside the system. This dynamics is observed in T-jet mixer with ratio $W/d=1.5$ and 2, where fully developed chaotic with self sustainable jets oscillations can be seen.

In $W/d=1$, the jets oscillation is consistently dampened in time, this could be due to the deeper mixing chamber. To verify if the dynamics will evolve to a clear chaotic flow regime, with similar dynamic features as $W/d=1.5$ and 2 cases, this simulation was extended up to 5 sec as seen in **Figure 4.26**. The system kept a flow behaviour for the complete simulation that is distinct from the other mixing chambers with larger depth values, particularly regarding the oscillations periodicity and the maximum values of the oscillation. This will be clear from power spectra analysis in Section 4.9.3.2.

From **Figure 4.27** for the $W/w=6$ geometries with ratios $W/d=3$ and 6, no clear oscillation of the jets is observed from the time histories; this type of behaviour confirms the effect of the chamber depth on mixing dynamics that was already reported from PLIF experimental results in **Chapter 3**.

$W/w=6;\ W/d=1;\ W$ =6 mm; w=1 mm; d =6 mm

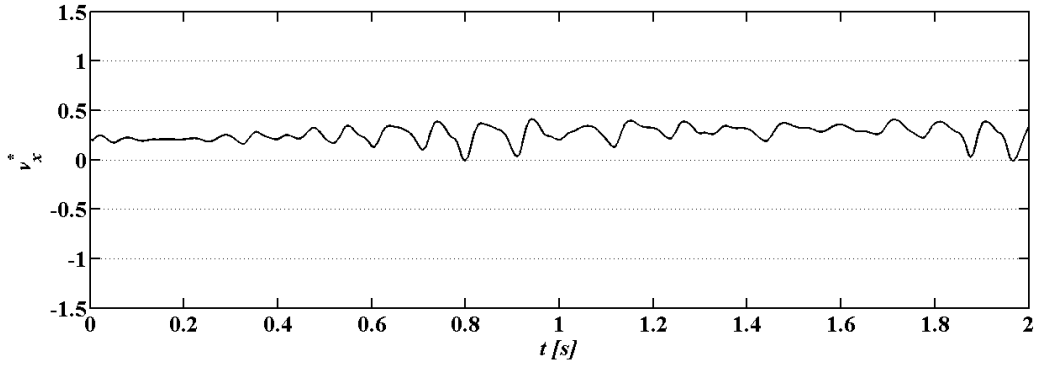

$W/w=6;\ W/d=1.5;\ W$ =6 mm; w=1 mm; d =4 mm

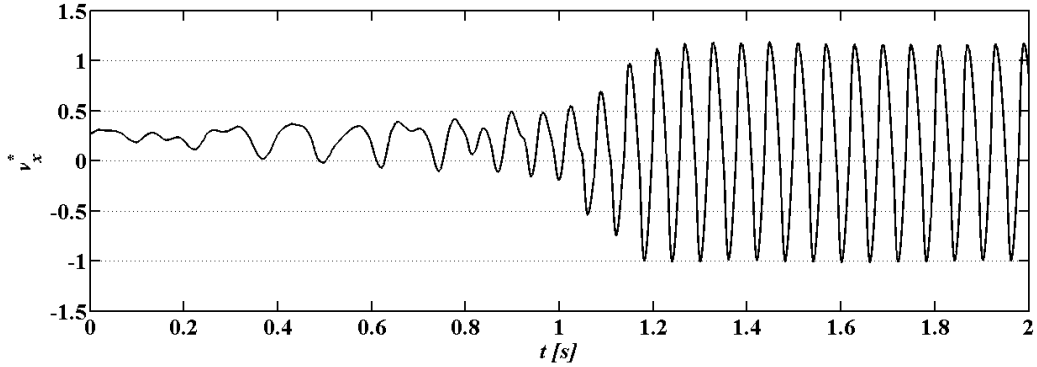

$W/w=6;\ W/d=2;\ W$ =6 mm; w=1 mm; d =3 mm

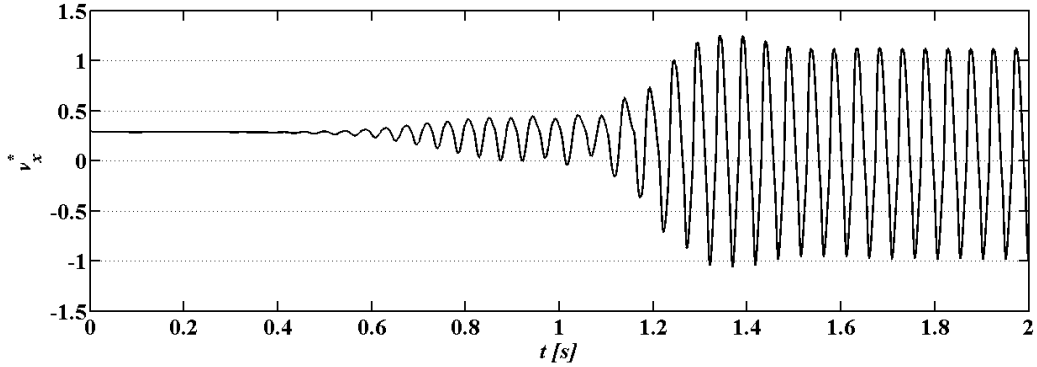

Figure 4.25 Time histories of U_x^* at the impingement point for the different geometries with ratio $W/w=6$ and $W/d=1$, 1.5 and 2 for *Re*=300 at 2 sec.

$W/w=6;\ W/d=1;\ W$ **=6 mm;** w**=1 mm;** d **=6 mm**

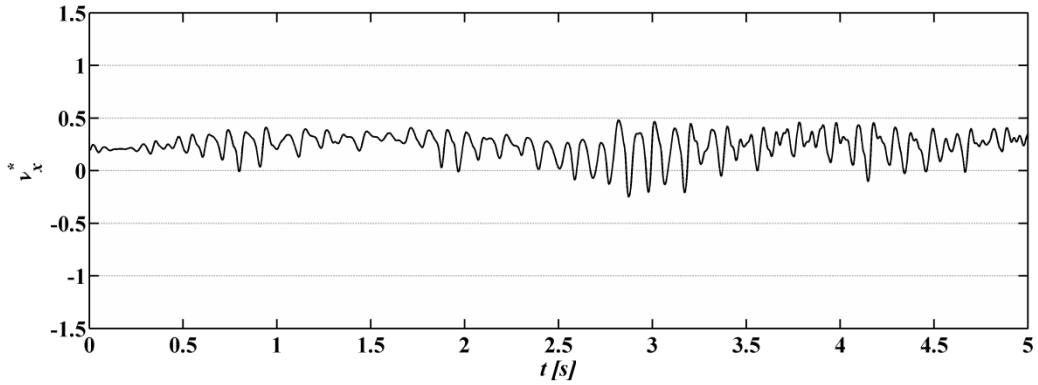

Figure 4.26 Time histories of U_x^* **at the impingement point for the geometry with** $W/w=6$ **and ratios** $W/d=1$ **for *Re*=300 at 5 sec.**

$W/w=6;\ W/d=3;\ W$ **=6 mm;** w**=1 mm;** d **=2 mm**

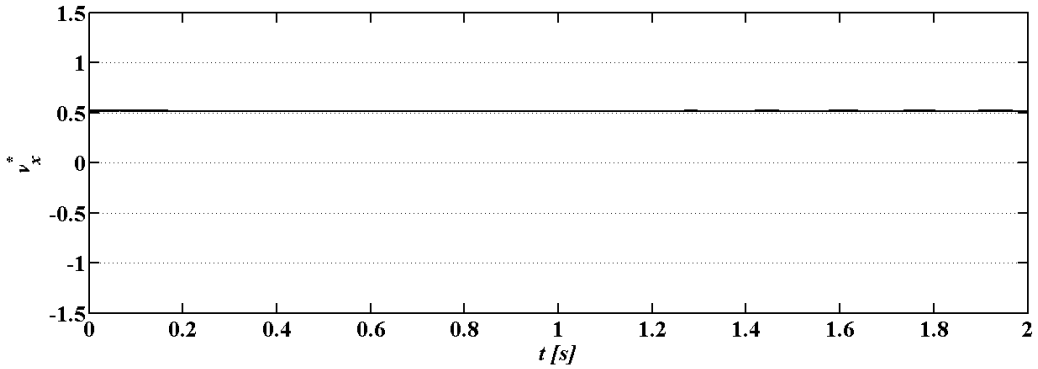

$W/w=6;\ W/d=6;\ W$ **=6 mm;** w**=1 mm;** d **=1 mm**

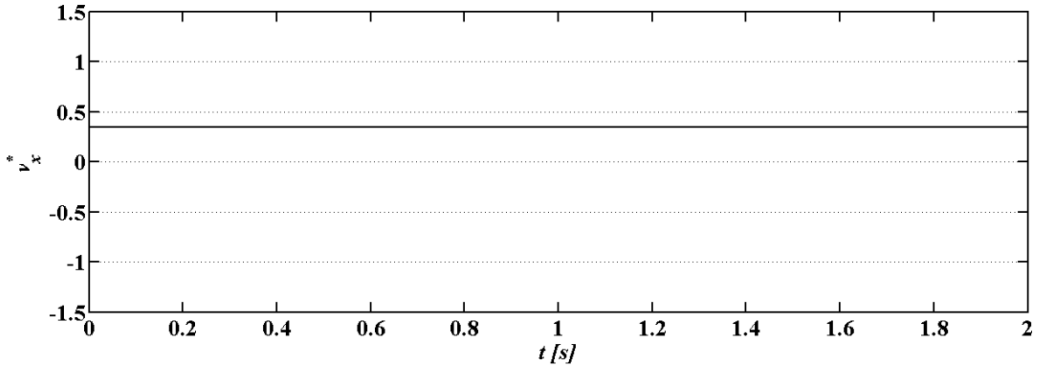

Figure 4.27 Time histories of U_x^* **at the impingement point for the different geometries with ratio** $W/w=6$ **and** $W/d=3$ **and 6 for *Re*=300 at 2 sec.**

$W/w=2$; $W/d=0.5$; W=2 mm; w=1 mm; d=4 mm

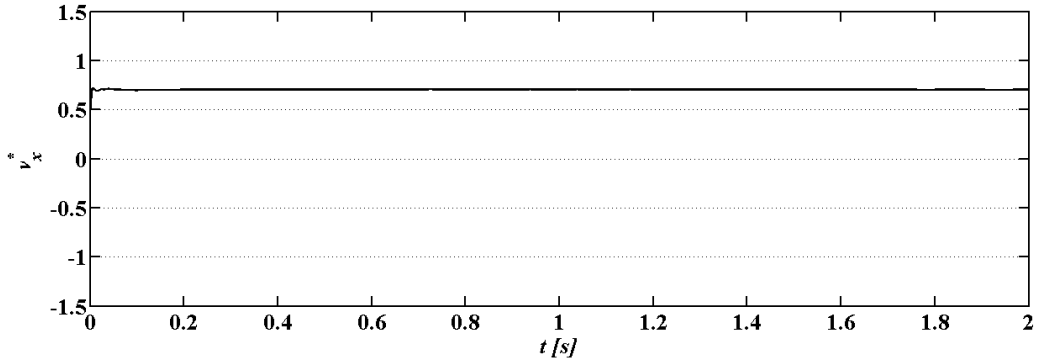

$W/w=4$; $W/d=0.5$; W=2 mm; w=0.5 mm; d=4 mm

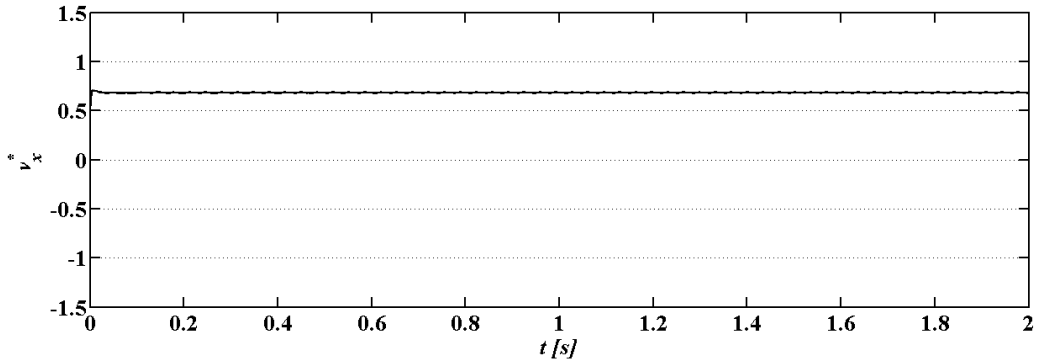

Figure 4.28 Time histories of U_x^* at the impingement point for the different geometries with ratio $W/w=2$, 4 and $W/d=0.5$ for *Re*=300 at 2 sec.

Figure 4.28 shows time histories for other W/w ratios. Non-oscillatory behaviour is observed for the geometry with ratio $W/w=2$, 4 and $W/d=0.5$; this behaviour was predicted already from 2D CFD simulations and is in accordance with the PLIF results of Chapter 3, where no vortices were observed around the jets impingement region for values of W/w =2 and 4.

For geometry $W/w=4$ and $W/d=0.5$ with $w=0.5$ mm slight rippling is visible, this is due to the jets from the injector are smaller when compared to $W/w=2$ with width $w=1$ mm. This flow behaviour gives rise to small vortices appearing downstream the jets which are just enough to initiate slight rippling (see **Figure 4.22**). The vortices formed in $W/w=4$ and $w=$ 0.5 mm have a diameter equal to one fourth the width of the mixing chamber; when the jets width is larger the free space for formation of vortices decreases. This behaviour was particularly clear from 2D simulation results, which could be regarded as not so representative

of the actual flow field being a simplified physical model, but give us access to a clear view of some flow mechanisms.

4.9.3.2 Power Spectra Analysis

To get a detailed analysis of the flow dynamics, the power spectra of υ_x at P1 are shown in **Figure 4.29**. The energy peaks shown in these power spectra at a frequency value stand for an oscillatory behaviour having that same frequency. The amplitude of the oscillation is related to the energy level of the peak. The spread of energy level around an energy peak is the measure of the repetitiveness; a narrow energy peak stands for an oscillatory flow, while a large distribution of energy around the local maximum energy peak is generally associated with chaotic flows having a frequency energy distribution around a typical value: Eullerian chaos (Moon, 2004). The power spectra for $W/w=6$ and $W/d=1.5$ and 2 shown in **Figure 4.29**, have the highest energy level at the typical frequency, while for $W/d=1$ the oscillation amplitude was smaller and so the associated energy. The values of typical frequency and associated energy value are listed **Table 4.4**.

The frequency power spectra of υ_x, for geometries $W/w=6$ with ratios $W/d=3$ and 6 and $W/d=0.5$ with ratios $W/w=2$, 4 were not computed since the oscillatory behaviour is very weak or not present.

In this work the vortices formation is also related with the jets oscillation frequency, testing the model proposed in Santos et al. (2009). The vortices are formed in pairs immediately downstream the jets injector, each oscillation wavelength is generated by the formation of consecutive vortices pairs of alternating vortices with a diameter equal to half the chamber width. So the jets oscillation frequency, f, is given by the flow rate of both jets divided by the volume of four vortices,

$$f=\frac{2}{4}\frac{q_{inj}}{V_{3Dvortex}} \tag{4.40}$$

$$q_{inj} = \upsilon_{inj}\, wd \tag{4.41}$$

where w is the jets width, d the depth, q_{inj} and υ_{inj} are the volumetric flow rate and velocity of the jets, $V_{3Dvortex}$ is the volume of each vortex. The structure of the vortex is assumed cylindrical shaped and its volume is given as

$$V_{3DVortex} = \frac{\pi}{4} D_{vortex}^2 d \tag{4.42}$$

D_{vortex} is the diameter of the vortex, therefore

$$f = \frac{2\upsilon_{inj}}{\pi D_{vortex}^2} \tag{4.43}$$

If we assume the vortex occupies half of the mixing chamber, $D_{vortex} = \frac{W}{2}$, then we get

$$f = \frac{8\upsilon_{inj} w}{\pi W^2} \tag{4.44}$$

where W is the width the mixing chamber. For these geometries, $W/w = 6$ and $W/d = 1$, 1.5 and 2 the frequencies predicted by Equation (4.44) correspond to 20 Hz. The frequency is close to the values obtained from the simulation, see **Table 4.4**, and so the vortices formation rate is defining the jets oscillation frequency. It may be concluded that the main feature and structure of the vortices formed in the geometries $W/w = 6$ and $W/d = 1.5$ and 2 are similar, while for $W/w = 6$ and $W/d = 1$ the oscillations frequency deviate from the prediction of the model that was demonstrated for chaotic flow regimes (Santos et al., 2009).

$W / w = 6$; $W / d = 1$; W =6 mm; w =1 mm; d =6 mm

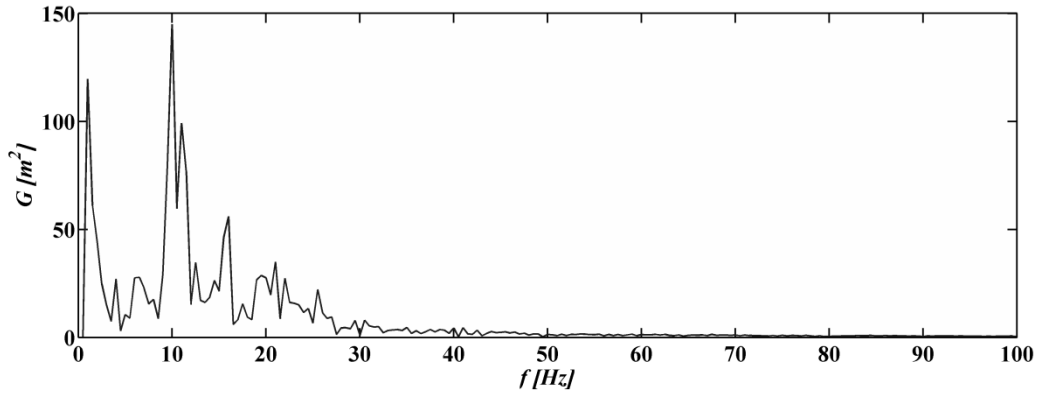

$W / w = 6$; $W / d = 1.5$; W =6 mm; w =1 mm; d =4 mm

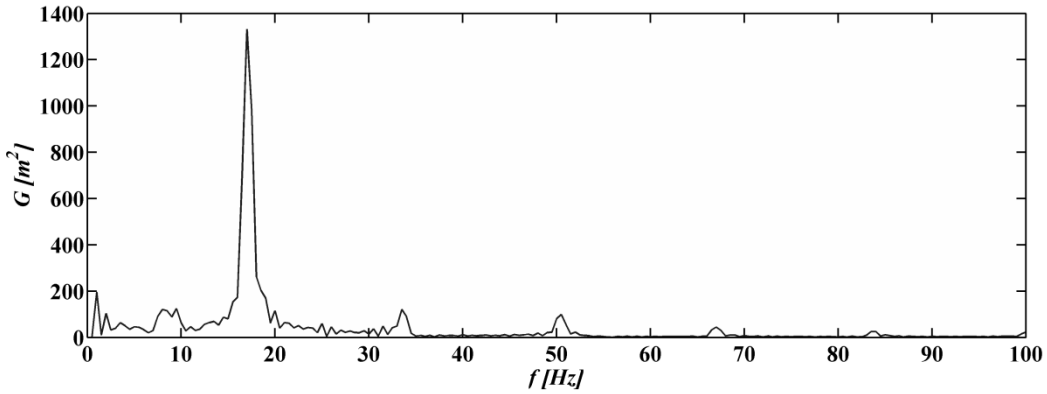

$W / w = 6$; $W / d = 2$; W =6 mm; w =1 mm; d =3 mm

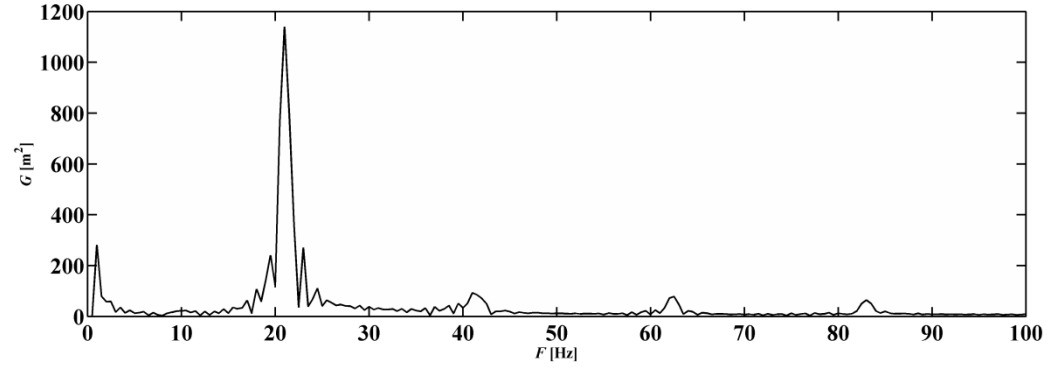

Figure 4.29 Power spectra of v_x at the impingement point for the different geometries with $W / w = 6$ and ratios $W / d = 1$, 1.5 and 2 for *Re*=300.

The energy peak of the frequency for $W / d = 1.5$ and 2 are similar and have approximately 10 times more energy than the one for $W / d = 1$ geometry. The simulation for $W / d = 1$ has been continued for 5 sec and respective power spectrum of the complete time history with 5

seconds is shown in **Figure 4.30**. In $W/d=1.5$ and 2, geometry the vortices formed are closer and more packed, i.e. there are more vortices flowing on each period at fixed point than in $W/d=1$. The increase in depth affected the flow in a complex way, the jets oscillations are not so clear probably because the vortices formation rotating with an axes normal to the chamber axes is not so repetitive. The increase in depth increases the weight of the inertial effects, due to increase of distance from the walls, this is rendering more complex flow behaviours, which is demonstrated from the fact that the power spectra in **Figure 4.30** has two typical frequencies: one close to the frequency that would be generated by the formation of cylindrical vortices occupying half the chamber width (close to 20Hz), and another frequency that would be caused by formation of larger vortices.

Table 4.4. Max energy values from power spectra for the six T-jets mixers studied for 2 sec

W/w **ratio**	W/d **ratio**	f **Frequency (Hz)**	**Max energy value (m^2)**
6	2	20	1140
6	1.5	17	1332
6	1	10	138.94

$W/w=6$; $W/d=1$; W **=6 mm;** w**=1 mm;** d **=6 mm**

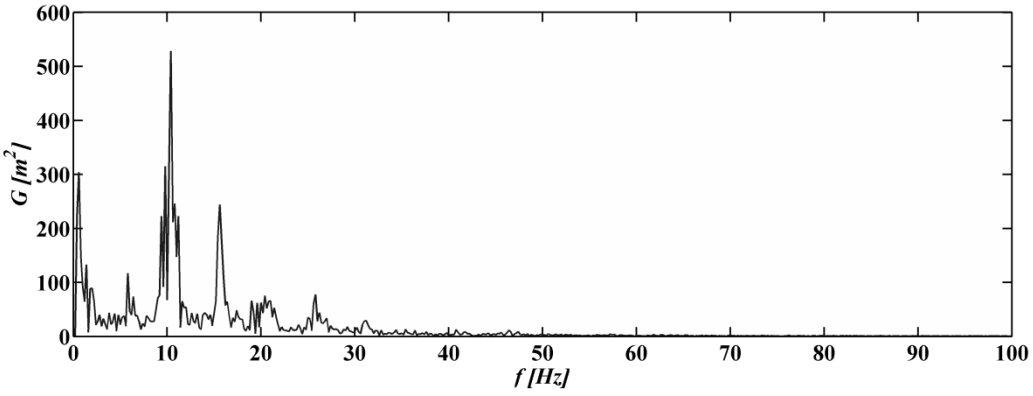

Figure 4.30 Power spectra of v_x at the impingement point for the geometry with $W/w=6$ and ratios $W/d=1$ for *Re*=300 at 5 sec.

4.9.3.3 Turbulence Intensity

The turbulence intensity is computed from the standard deviation of x velocity component as it is normal to main the flow direction and aligned with mixing, which occurs from one side of the chamber to the other. The turbulence intensity is thus defined as,

$$\sigma_x = \frac{1}{n_{samples}} \sqrt{\sum_{i=1}^{n_{samples}} (\upsilon_x(i) - \langle \upsilon_x \rangle)^2} \tag{4.45}$$

Where $n_{samples}$ is the total number of time instants considered, $\upsilon_x(i)$ is the x velocity component at a time instant i, and $\langle \upsilon_x \rangle$ is the average value of $\upsilon_x(i)$, calculated as

$$\langle \upsilon_x \rangle = \frac{1}{n_{samples}} \sum_{i=1}^{n_{samples}} \upsilon_x(i) \tag{4.46}$$

Higher values of the turbulence intensity from higher velocity fluctuations are directly associated with mixing phenomenon, given that these fluctuations promote the mixing of fluid with its surrounding fluid.

In **Figure 4.31** the turbulence intensity calculated from Equation (4.45) is presented for geometries with different depth. It is observed that the turbulence intensity is higher for $W/d = 1$, 1.5 and 2 than for $W/d = 3$ and 6. The $W/d = 1.5$ geometry has the highest turbulence intensity than $W/d = 1$ and $W/d = 2$. This confirms evidence from the power spectra analysis showing that there is probably an optimum depth to chamber width value, as far as the flow dynamics is regarded.

In **Figure 4.32** is presented for geometries with different jets width to mixing chamber width ratio, and similar depth. It is observed that as the W/w ratio increases the turbulence intensity increases. The turbulence intensity is highest for $W/w = 6$, a result that also confirms data from 2D CFD simulations and PLIF results of **Chapter 3**.

Figure 4.33 represents the turbulence intensity for geometry $W/w = 6$ and $W/w = 1.5$ for *Re*=100, 180 and 300. It is observed that the turbulence intensity increases with *Re*, quite steeply after a critical value. The existence of critical Reynolds number after which the flow

dynamics dramatically changes over a short range of Reynolds number is a wide spread observation in opposed jets mixers literature (Lee et al., 1980; Santos et al., 2010; Unger and Muzzio, 1999; Harris et al., 1992).

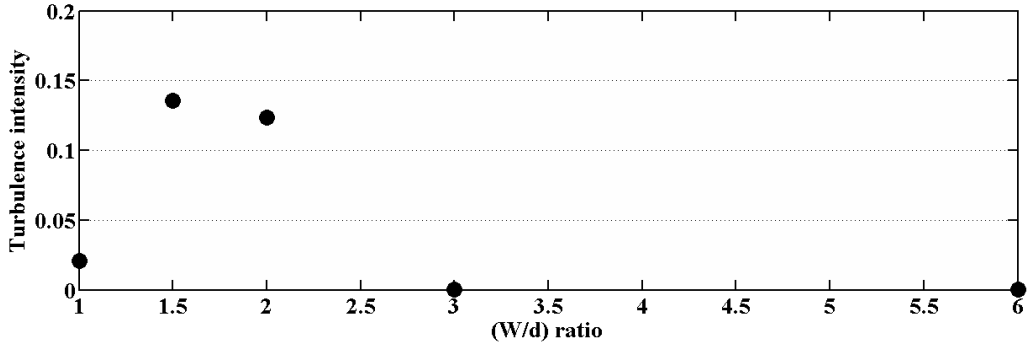

Figure 4.31 Turbulence intensity of different geometries with ratio $W/w=6$ and $W/d=1$, 1.5, 2, 3 and 6 for *Re*=300.

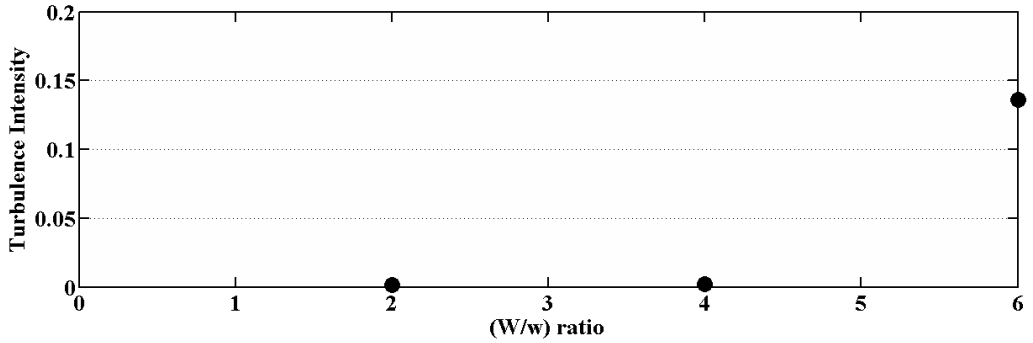

Figure 4.32 Turbulence intensity of different geometries with ratio $W/d=1.5$ and $W/w=2$, 4 and 6 for *Re*=300.

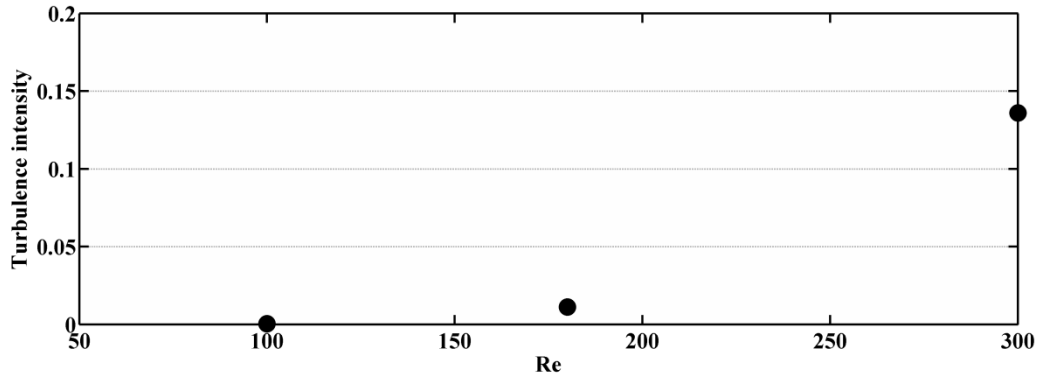

Figure 4.33 Turbulence intensity geometry with ratio $W/w=6$ and $W/d=$ 1.5 at different *Re*=100, 180 and 300.

4.9.4 **Influence of the Head Space**

To study the effect of headspace above the jets in the system dynamic behaviour, two cases $W/w=6$ and $W/d=1.5$ and 3 at Re=300, were simulated without headspace in addition to the cases studied above which had a space of 2 mm above the jets injector. There are two purposes for these simulations: first is to assess the impact in the flow dynamics of the upper vortices and compare with the earlier studies; second is to find any oscillatory behaviour that could be induced from the upper vortices.

Figure 4.34 and **Figure 4.35**, shows the y and z vorticity maps and **Figure 4.36** pathlines for the two cases without headspace. The time histories and power spectra of υ_x, time series at the jets impingement for these two cases are shown in **Figure 4.37** and **Figure 4.38**.

4.9.4.1 Vorticity Maps

Figure 4.34 for $W/w=6$ and $W/d=1.5$, shows four vortices after the impingement point. In the plane located in the middle of the mixing chamber shown in the right hand side column, the vorticity values are smaller than for the plane near the impingement point, thus the fluid rotation diminishes throughout the mixing chamber showing mixing dynamics similar to the geometry with head space.

In $W/w=6$ and $W/d=3$ no vortices are visible after the jets impingement but cross flow of fluid is observed from the velocity vector maps, when compared to the geometry with head space (see **Figure 4.18**) where two vortices in each side of the mixing chamber were observed. In the case without headspace one small vortex is observed in the centre of the mixing chamber, as seen in **Figure 4.34**.

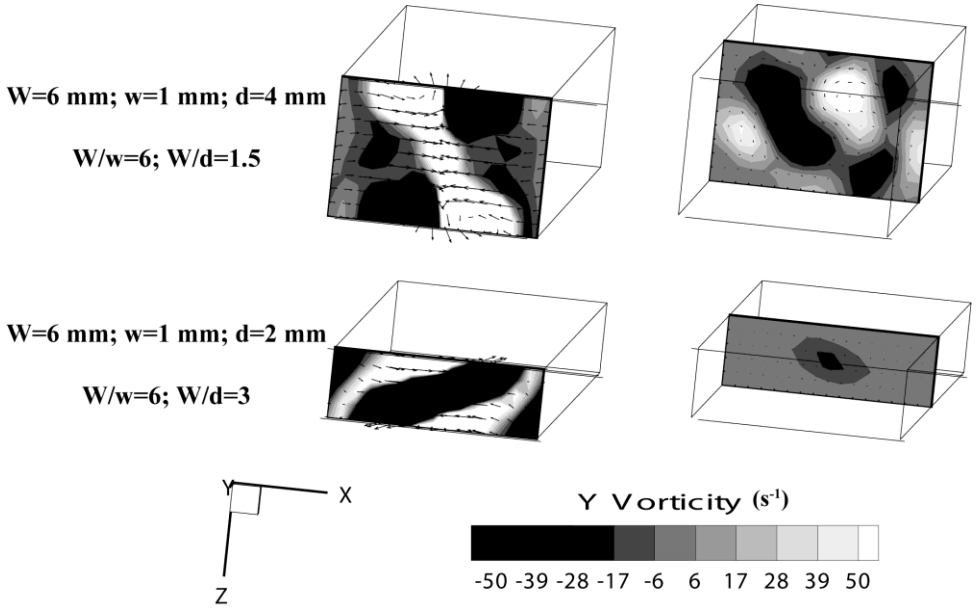

Figure 4.34 y **vorticity map and 2D velocity vector map after the impingement point and in the center of the chamber for the geometries with ratio** $W/w=6$ **and ratios** $W/d=1.5$ **and 3 for *Re*=300 without head space.**

Figure 4.35 shows the z vorticity map in an axial plan of the mixing chamber, from which it is seen the formation of vortices after the jets impingement point. In the geometries without head space and with, $W/w=6$ and $W/d=1.5$ the onset of the vortex street occurs at downstream positions and does not display the same chaotic pattern as previously observed in mixing chambers with the headspace (see **Figure 4.19**). The flow patterns are closer to the case $W/w=6$ and $W/d=1$ that is closer to engulfment flow than to chaotic flow. T-jets mixers had been studied without headspace, and this is one of the likely reasons that the chaotic flow regime was not previously reported (Hoffmann et al., 2006; Bothe et al., 2006; Soleymani et al., 2008). The other reason is that generally the W/w ratios are below 6 (Bothe et al., 2006; Soleymani et al., 2008; Wong et al., 2004).

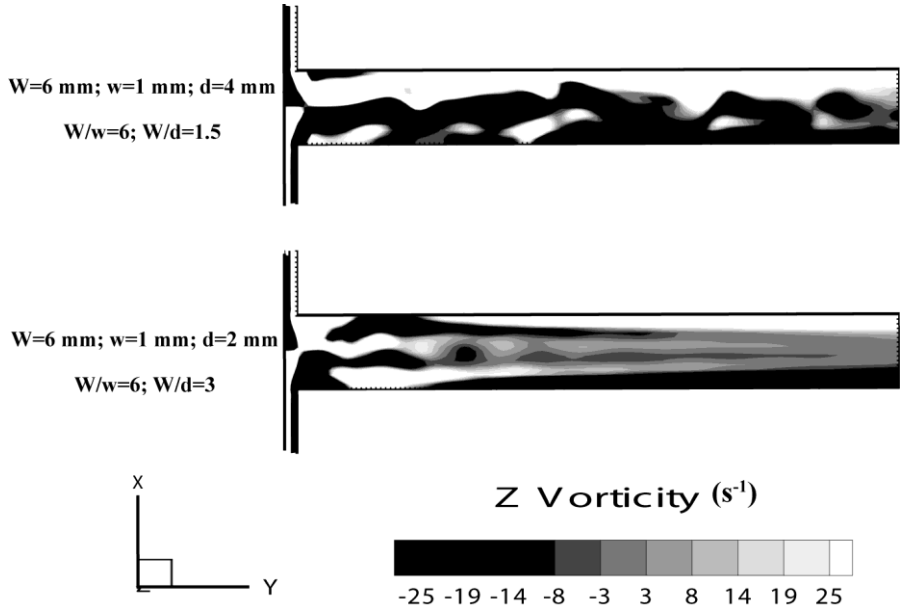

Figure 4.35 Z vorticity map for the geometries with ratio $W/w=6$ and ratios $W/d=1.5$ and 3 for *Re*=300 without head space.

The case with $W/w=6$ and $W/d=3$ also displays a dramatic effect of the headspace on the flow regime. The mixing chamber with headspace exhibited a segregated steady flow regime, see **Figure 4.19**, removing the headspace causes secondary flow with some rotation around the mixing chamber axis; see **Figure 4.34** and **Figure 4.35**.

4.9.4.2 Pathlines

The pathlines in **Figure 4.36** (a and c) for $W/w=6$ and $W/d=1.5$, show a more symmetric flow field than in the chamber with headspace (see **Figure 4.20** (b)), particularly from the top view of the chamber. From **Figure 4.36** (c) it is observed the vortices sequence is not so clear and the path lines pattern is closer to those reported in $W/d=1$ (see **Figure 4.20** (a) and (e)).

For $W/w=6$ and $W/d=3$ the pathlines in **Figure 4.36** (b and d) clearly show cross flow or swirling of the jets around the mixing chamber axis. The pathlines viewed from the mixing chamber top also show this swirling of the jets. The headspace has an effect on flow regime, not only on chaotic flow regimes, but also on other regimes such as the segregated steady regime.

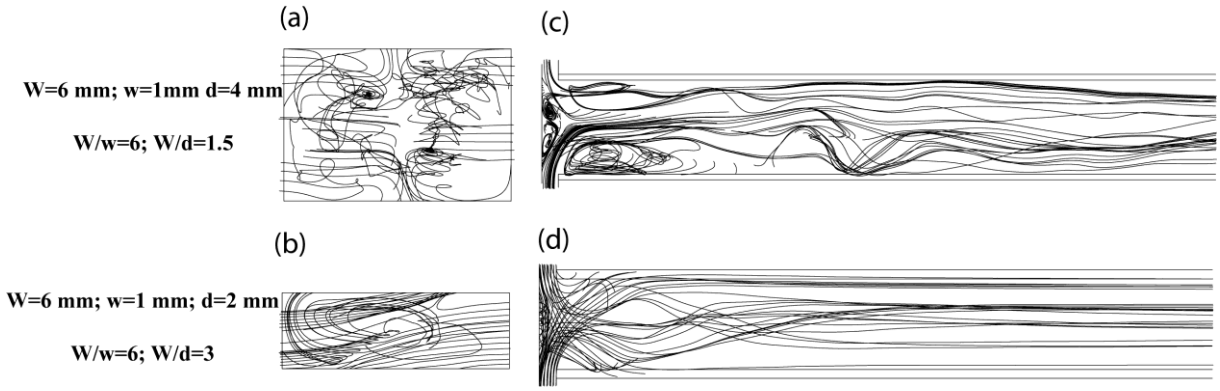

Figure 4.36 Path lines for the geometries with ratio $W/w=6$ and ratios $W/d=1.5$ and 3 for *Re*=300 without head space viewed from the mixing chamber top (left column) and from the front (right column).

4.9.4.3 Analysis of flow dynamics

Figure 4.37 shows the time histories of υ_x^* for geometry $W/w=6$ and $W/d=1.5$, it is observed the jets oscillations have much less amplitude. The chaotic flow regimes lay on two phenomenon, one is the formation of vortices formed immediately below the jets that engulf both jets, the other is the oscillation of the jets impingement point driven by the vortices formation (Santos et al., 2009). Placing the top wall of the mixing chamber immediately above the jets imposes a viscous force that dumps the jets oscillations, as can be seen from the time history in **Figure 4.37**. On the other hand as seen from the vorticity maps and pathlines this has a negative effect on the formation of a vortex street that was reported by Santos et al. (2005) as the main mixing mechanisms in 2D opposed jets geometries.

In both cases without head space, $W/w=6$ with $W/d=1.5$ and $W/d=3$ (see **Figure 4.37**), similar time histories to that of the geometry $W/w=6$ and $W/d=1$ (see **Figure 4.25**), are observed where the flow regime is quite similar to the engulfment flow regime.

The power spectra **Figure 4.38** for $W/w=6$ and $W/d=1.5$ and for $W/d=3$, show an energy peak around the frequency 12 Hz, while for the geometry with headspace the typical value was around 20 Hz. The energy peak value for $W/d=1.5$ case is 10 times less than in this geometry with head space (see **Figure 4.29**). The power spectra for both geometries without headspace proves the similar dynamics of these flows with the one observed in $W/w=6$ and $W/d=1$ geometry having headspace that had close frequency and energy value.

$W / w = 6$; $W / d = 1.5$; W =6 mm; w=1 mm; d =4 mm

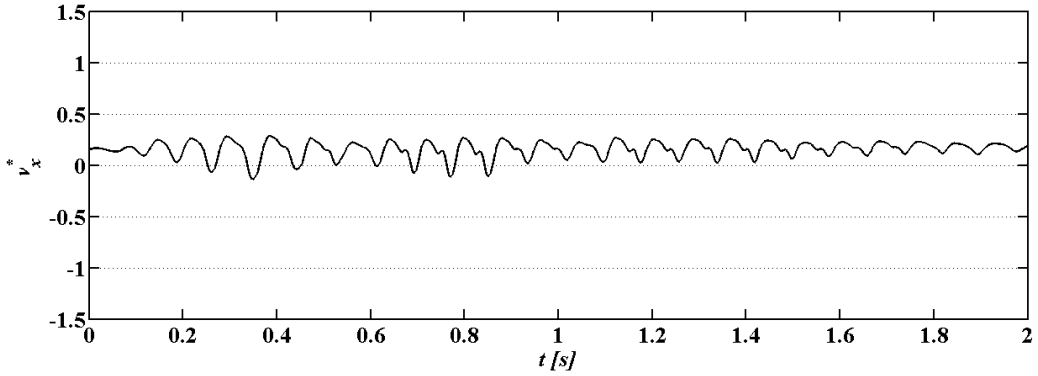

$W / w = 6$; $W / d = 3$; W =6 mm; w=1 mm; d =2 mm

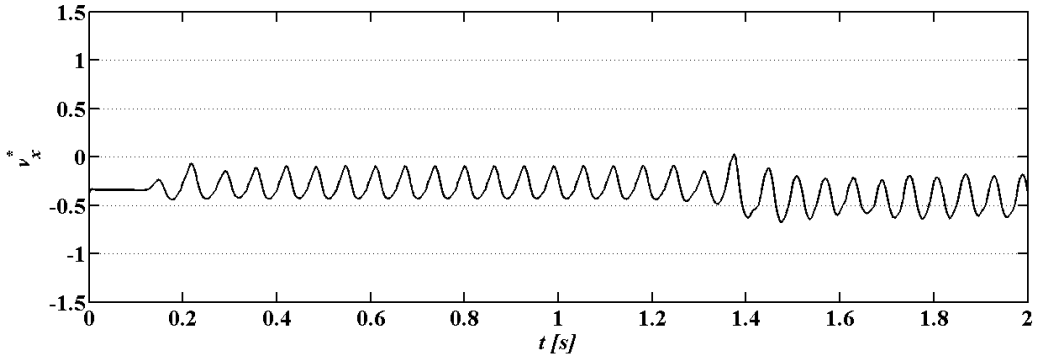

Figure 4.37 Time histories of υ_x at the impingement point for the T-jets geometries with ratio $W / w = 6$ and ratios $W / d =$ 1.5 and 3 for *Re*=300 without head space.

$W / w = 6$; $W / d = 1.5$; W =6 mm; w=1 mm; d =4 mm

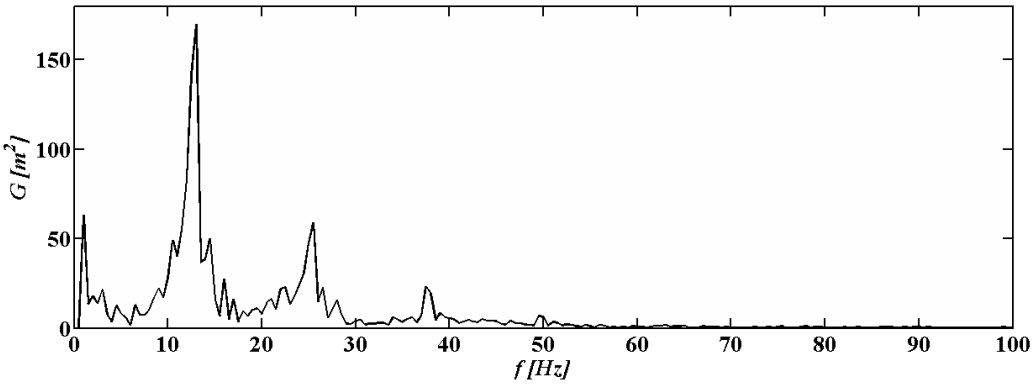

$W / w = 6$; $W / d = 3$; W =6 mm; w=1 mm; d =2 mm

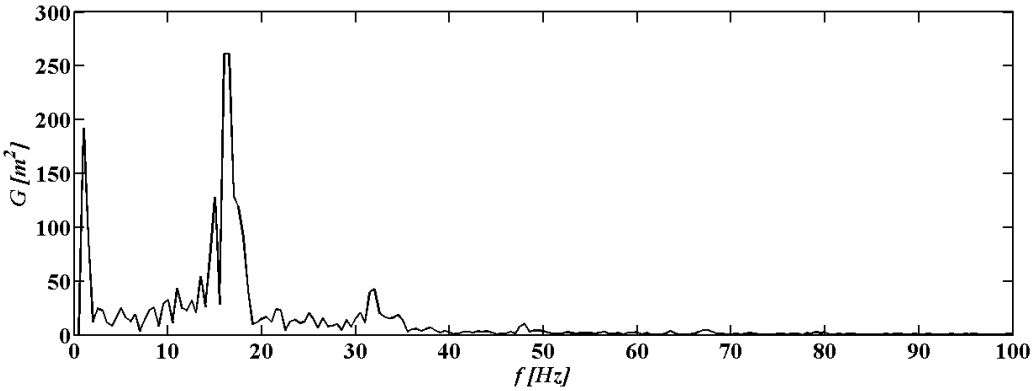

Figure 4.38 Power spectra of υ_x at the impingement point for the T-jets geometries with ratio $W / w = 6$ and ratios $W / d =$ 1.5 and 3 for *Re*=300 without head space.

4.10 Tracer or Species Transport Simulation

The 3D model correctly simulates the flow field in the different T-jets mixers namely the main flow structures, as can be seen by comparing the results in **Chapter 4** with the PLIF experiments of **Chapter 3**. Thus, the next step is to use this model for the study of the mass transfer mechanisms in the T-jets mixers, which will enable a better insight into the effect of flow regime on mixing and better comparison with PLIF results.

4.10.1 **Model and Equations for Mass Transfer Study**

The 3D model earlier described in this chapter for the simulation of the hydrodynamics is used for the mass transfer simulation in this section by coupling the advection-diffusion-reaction equation to this 3D model. The geometry with boundary conditions is shown in

Figure 4.39 with the specific boundary conditions for the mass transfer simulation. All the tracer simulations in this chapter are made with a passive tracer; which has no influence on the fluid properties or in the flow field.

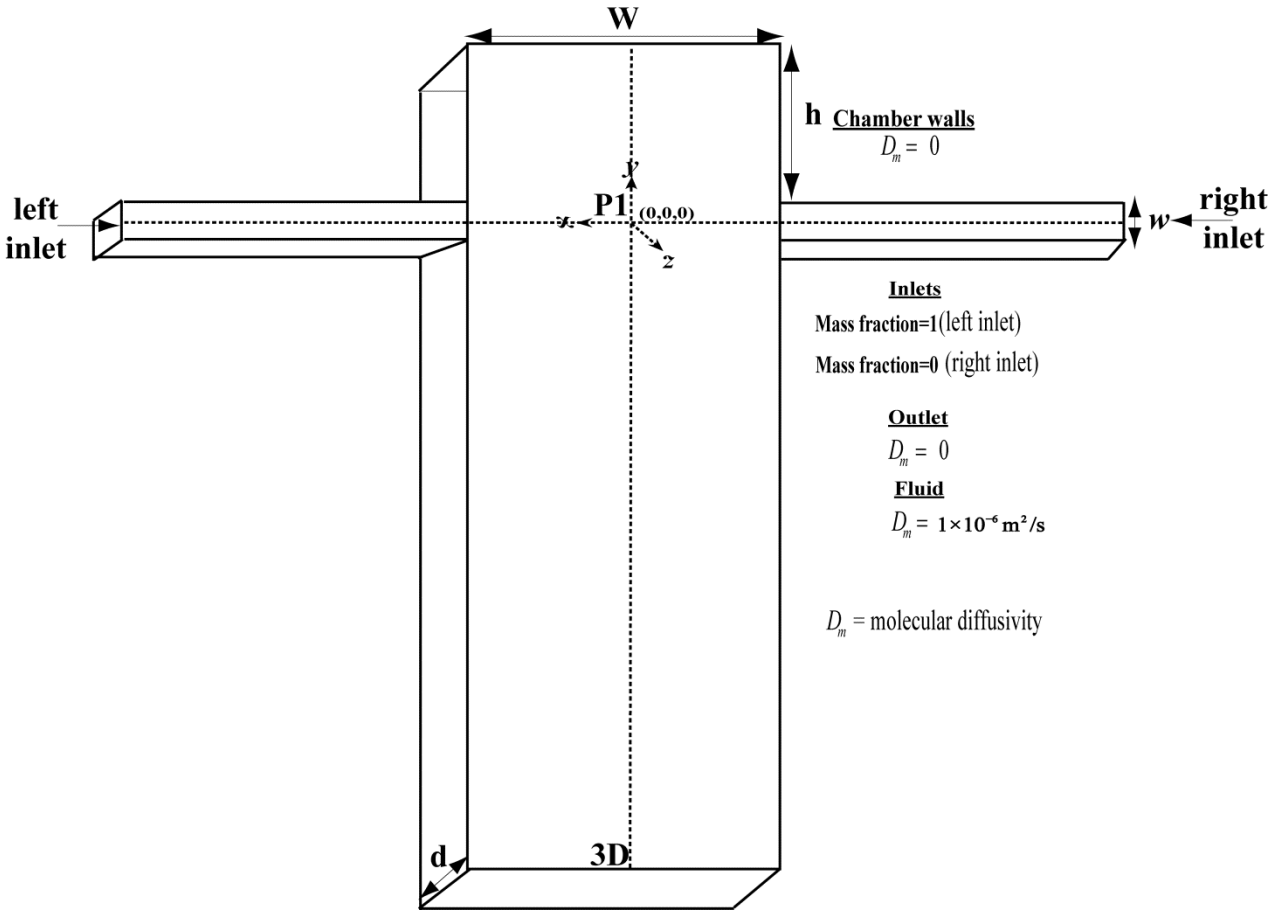

Figure 4.39 3D CFD model of T-jets mixers with boundary conditions for the mass transfer of species A in the tracer simulation.

4.10.2 **Mass Transfer Model**

The hydrodynamic model described earlier in the **Section 4.2** of this chapter is coupled with the advection-diffusion-reaction equation for a species with or without chemical reaction is

$$\frac{\partial c}{\partial t} + \vec{\upsilon}\vec{\nabla}c = D_m \nabla^2 c + r \tag{4.47}$$

where c is the concentration of the chemical species, $\vec{\upsilon}$ is the velocity vector field at time t and D_m is the molecular diffusivity and r is the rate of formation by chemical reaction.

For a n order elementary chemical reaction the net rate of reaction of the chemical species is

$$r = kC^n \tag{4.48}$$

where k is specific reaction rate.

4.10.3 **Geometry and Boundary Conditions**

The boundary conditions for the mass transfer are represented in term of diffusivity coefficients D_m, and mass fluxes. At the boundaries of the mixing chamber interior, walls, injectors and the outlet, D_m is set to zero. The mass fluxes are set to zero at the chamber walls. The mass diffusivity of the fluid is set as, $D_m = 1\times10^{-6} m^2/s$.

For the tracer simulation, the species A concentration is set 1 at the left injector and zero at the right injector. This 3D tracer simulation was performed with the fluid having the Schmidt number, $Sc = \dfrac{\mu}{\rho D_m} = 1.002$ for the mass transfer process.

4.10.4 **Initial Conditions**

The solver used for the simulation was Pressure based solver for both steady and transient state simulation. The residuals of the solution of the Equations (4.1) and (4.2) were converged to 10^{-5}, for the steady state simulations.

All the simulations were converged to a steady state, which was used as the initial solution for the dynamic simulations. The solution method was Pressure-Velocity coupling with Coupled scheme for both steady and transient simulation. The spatial discretization gradient was Least Squares Cell based; Pressure gradient used was Second order for both steady state and transient state; spatial momentum, species and energy discretization was set as Third Order MUSCL. For the transient simulations, a second order implicit formulation was used, and all the residuals were converged to 10^{-6}.

4.11 3D Tracer Dynamic Simulation Analysis

The following T-jets mixers cases were studied for mixing of a passive tracer, see **Table 4.5**.

Table 4.5 List of T-jets mixers geometrical parameters used in tracer simulation

Chamber Width (W) (mm)	Jets Width (w) (mm)	Chamber Depth (d) (mm)	W/w ratio	W/d ratio
2	1	4	2	0.5
6	1	1	6	6
6	1	3	6	2
6	1	4	6	1.5
6	1	6	6	1

4.11.1 Species Concentration Maps

The species A concentration maps are shown in **Figure 4.40** to **Figure 4.44**, in an axial plane, front view (left side of figures) and three planes normal to the mixing chamber axis, top view (right side). The tracer maps enable a clear view of the complete mixing effectiveness and mechanisms. The concentration maps show the dynamic sequence of mixing for a period of 2 secs, $t = 0$, 0.5, 1, 1.5 and 2 secs, at *Re*=300, for the geometries $W/w = 6$ and $W/d = 1$, 1.5, 2 and 6; $W/w = 2$ and $W/d = 0.5$. The mixing chamber from the top to the outlet has an height $H = 50$ mm, the planes normal to the mixing chamber axis where tracer maps are shown, are located close to jets impingement (3.1 mm), the second plane is at the centre of the mixing chamber (25 mm) and the last plane near the outlet (40 mm).

From **Figure 4.40** to **Figure 4.44** for all the geometries studied, two fluid streams are clearly visible from tracer images at $t = 0$ sec, where a steady state solution was used. In steady states two streams flow through segregated paths throughout the mixing chamber, i.e. the white and

black stream flow side by side and the interface between both streams does not change its position for all the geometries studied.

It is observed that at the centre of the mixing chamber and plane near the outlet from $t = 0.5$ sec onwards in geometries $W / w = 6$ and $W / d = 1$, 1.5 and 2 that a dynamic flow regime is initiated immediately downstream of the impingement point of the jets with formation of vortices, as shown in **Figure 4.40** to **Figure 4.42**. The jets impinge on each other close to the chamber axis and are directed towards the outlet. Two circular vortices are formed in both sides of the chamber immediately below the jets entrance. These vortices will detach and evolve throughout the mixing chamber towards the outlet forming a *vortex street* (Santos et al., 2005). The interface between the two fluid streams, the black and white fluid, which was clearly seen for $t = 0$ sec is completely disturbed with the formation of vortices that promote the engulfment of jets with the surrounding fluid. The upper vortices are disturbed at this flow regime by jets oscillations, which consist on a dynamic evolution of the jets impingement point location that is clearly observed from the dynamic visualization of the concentration maps. These oscillations are the underlying mechanism causing the impingement point of the jets to be off the chamber axis, as clearly seen from **Figure 4.40**, **Figure 4.41** and **Figure 4.42**. This image clearly depicts the role played by the vortices in mass transfer process by engulfing fluid from both jets throughout the mixing chamber (Santos et al., 2005).

From **Figure 4.43** for $W / w = 6$ and $W / d = 6$ geometry it is seen that the vortex street formation downstream the injectors is not taking place. The oscillation of the jets is observed at the interface of both fluids, this shows instabilities at the jets impingement that are not propagating to the whole flow field as they were in deeper geometries. The flow keeps a markedly segregated pattern between the opposed streams at $t = 2$ sec a pattern which was initially observed at $t = 0$ sec. The flow is becoming increasingly steady and parallel for shallow mixing chambers, which is due to a strong effect of the wall increasing the impact of viscous forces.

For $W / w = 2$ and $W / d = 0.5$ geometry shown in **Figure 4.44**, a segregated flow is observed from the front and top view throughout the T-jets mixer along with the time. The flow is steady and parallel for mixing chamber with smaller width. Although the chamber is deep enough for the onset of dynamic flow regimes, the expansion of the chamber width is equal to

the combined width of the opposed jets. This was previously seen in Section 4.7.1 to prevent the onset of dynamic flow regimes with sequential formation of vortices issuing from the jets impingement point.

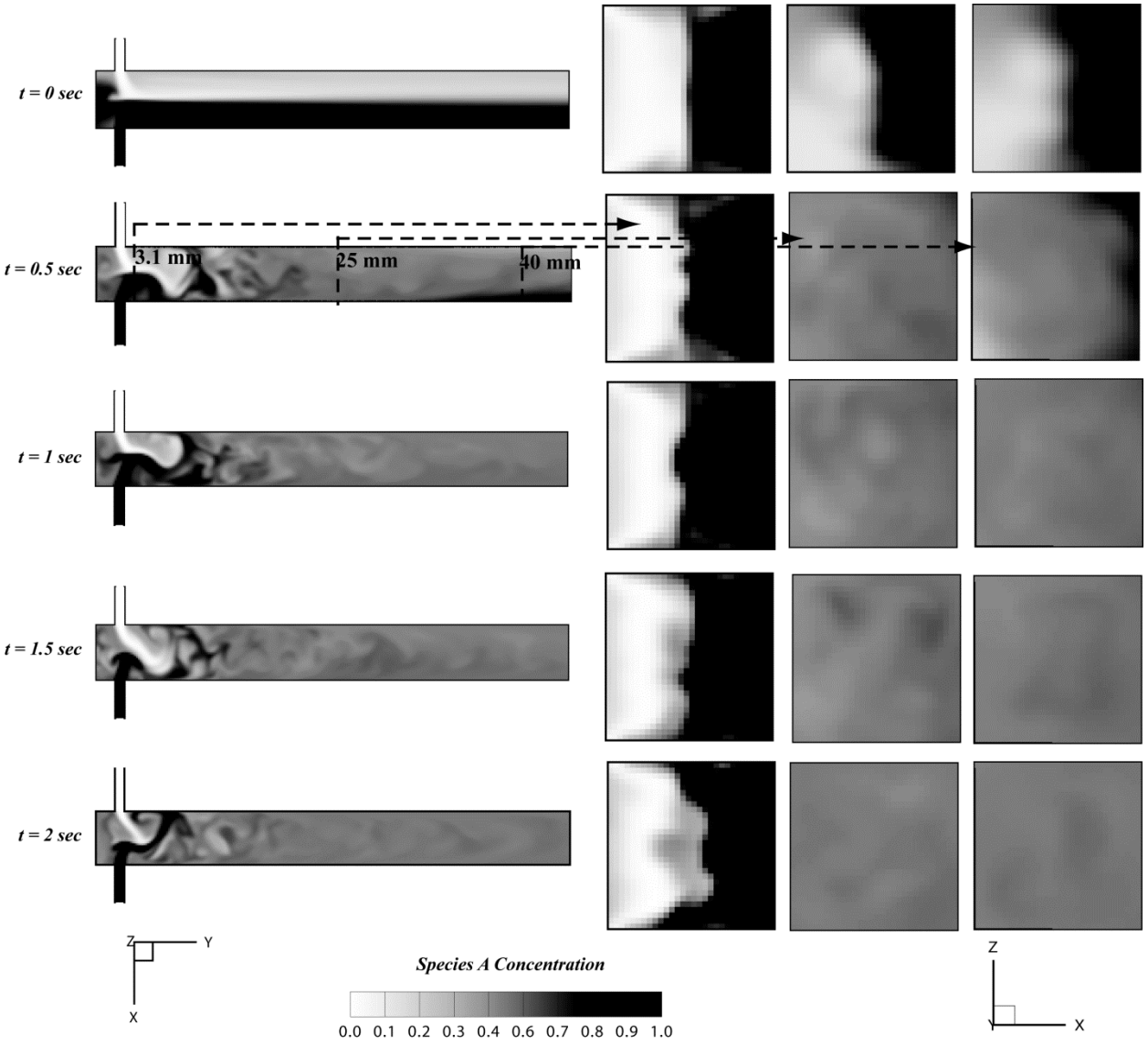

Figure 4.40 Dynamic sequence of tracer maps from 3D CFD simulation at *Re*=300 for $W / w = 6$ and $W / d = 1$ at various time step in front view (left side) and top view (right side).

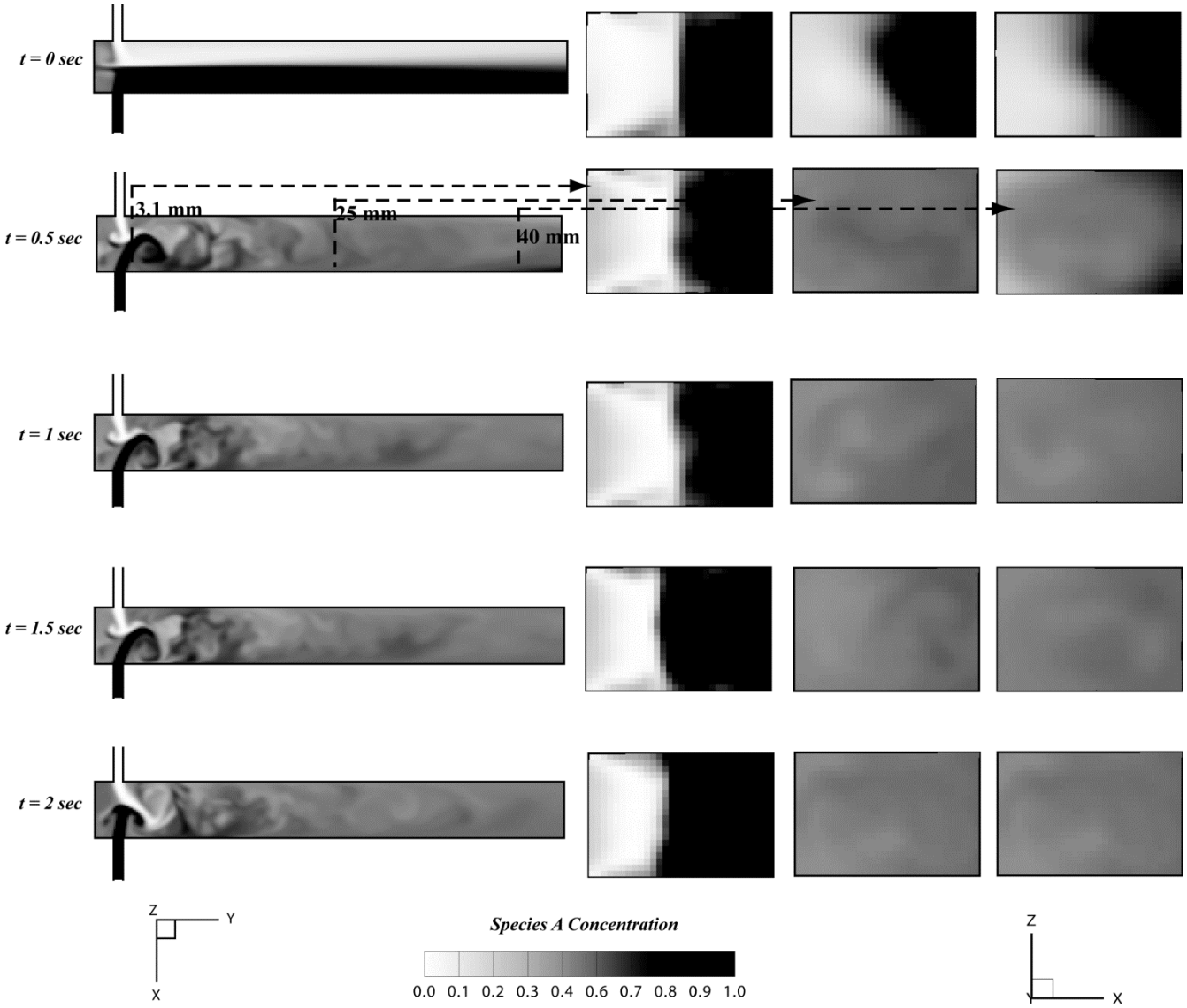

Figure 4.41 Dynamic sequence of tracer maps from 3D CFD simulation at *Re*=300 for $W / w = 6$ and $W / d = 1.5$ at various time step in front view (left side) and top view (right side).

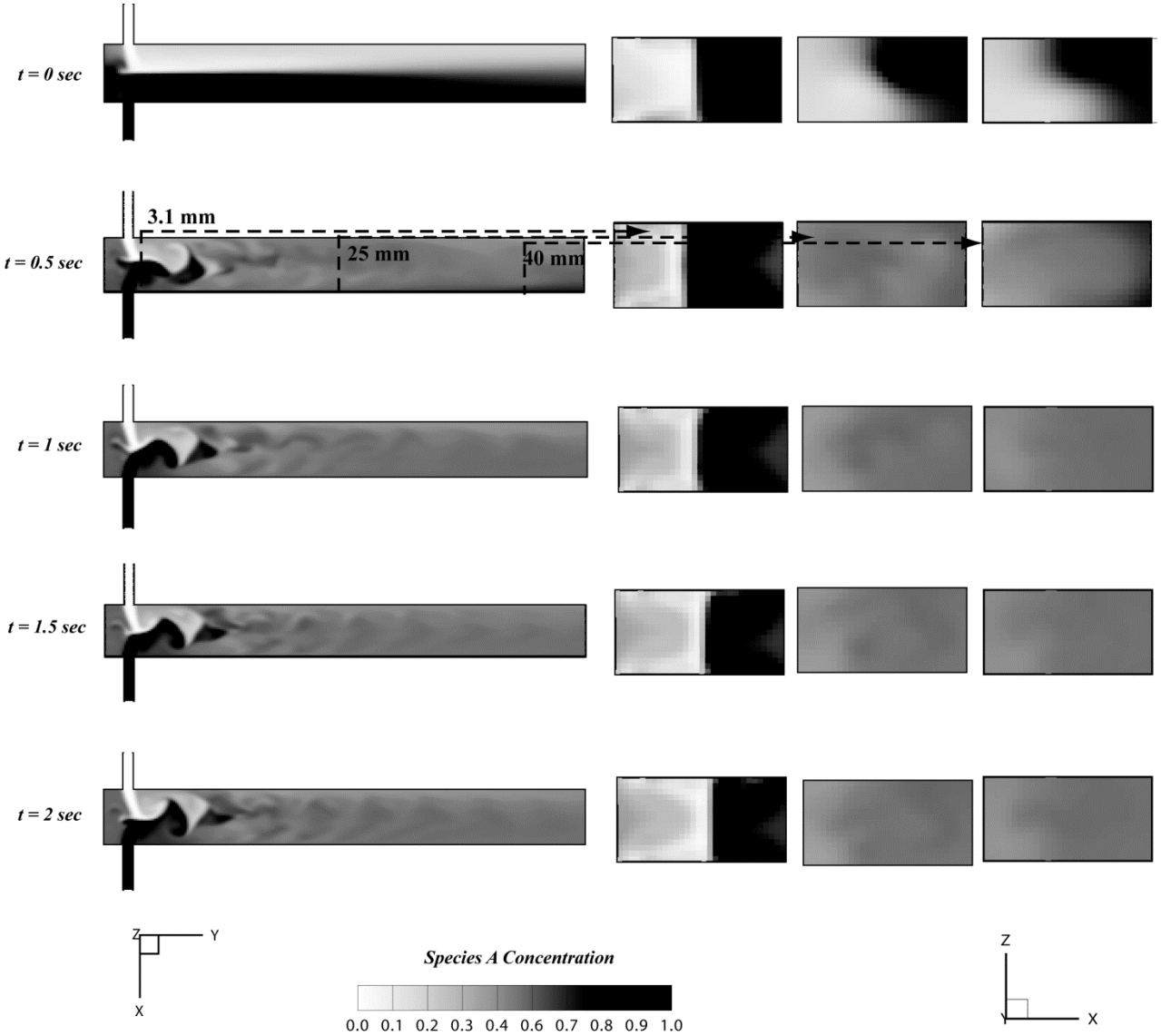

Figure 4.42 Dynamic sequence of tracer maps from 3D CFD simulation at *Re*=300 for $W / w = 6$ and $W / d = 2$ at various time step in front view (left side) and top view (right side).

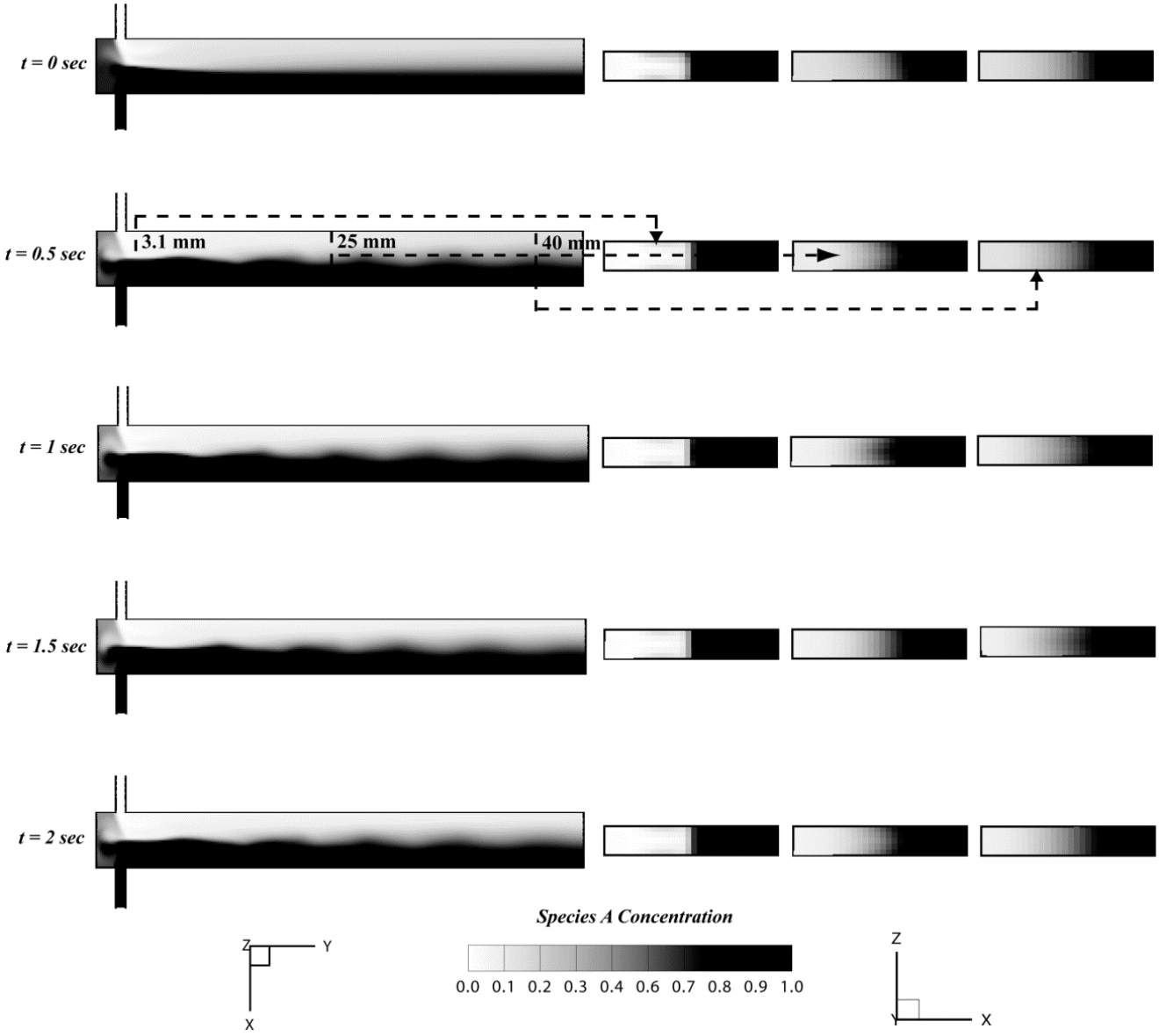

Figure 4.43 Dynamic sequence of tracer maps from 3D CFD simulation at *Re*=300 for $W / w = 6$ and $W / d = 6$ at various time step in front view (left side) and top view (right side).

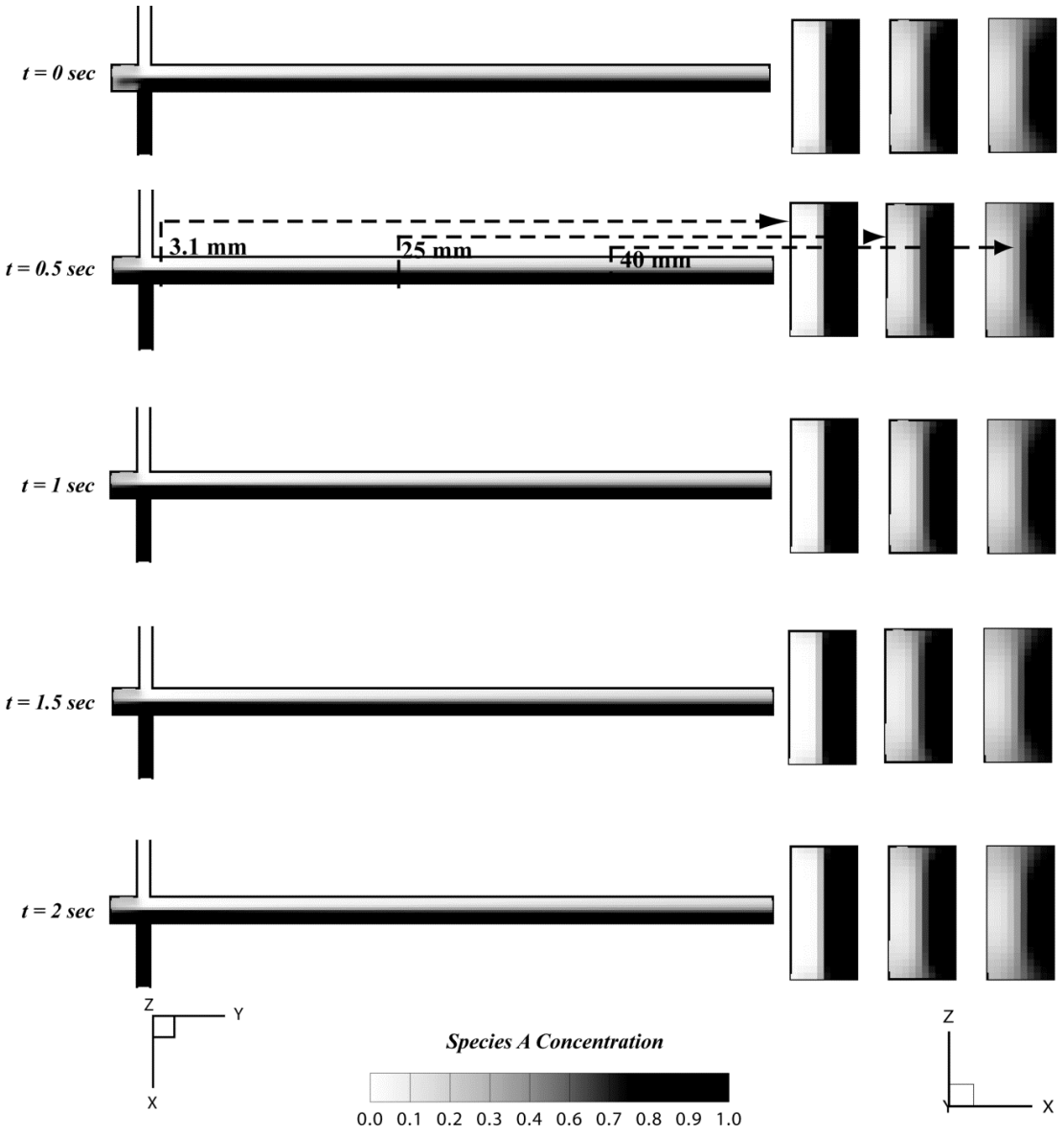

Figure 4.44 Dynamic sequence of tracer maps from 3D CFD simulation at *Re*=300 for $W/w=2$ and $W/d=0.5$ at various time step in front view (left side) and top view (right side).

For geometries $W/w=6$ and $W/d=6$; $W/w=2$ and $W/d=0.5$ mixing is due to diffusion of tracer or other small scale instabilities at the interphase formed by fluid from each jet along the plane located throughout the mixing chamber axis, as it could be seen in the top view from $t=0.5$ sec. The mixing of both fluids is not promoted by large coherent vortices engulfing both streams, which makes the fluids to be much more segregated at the reactor outlet.

4.11.2 **Intensity of Segregation**

The intensity of segregation in a binary mixture of A and B is given as (Danckwerts, 1952),

$$I_s = \frac{\sigma_A^2}{\bar{C}_A.\bar{C}_B} \equiv \frac{\sigma_B^2}{\bar{C}_A.\bar{C}_B} \equiv \frac{\sigma_A^2}{\bar{C}_A.(1-\bar{C}_A)} \equiv \frac{\sigma_B^2}{\bar{C}_B.(1-\bar{C}_B)} \tag{4.49}$$

where C_A and C_B is the species average concentration over the probed plane, and σ_A and σ_B refer to the respective standard deviation. The intensity of segregation assumes the value 1 if the fluid is completely segregated and 0 if it is completely mixed. The intensity of segregation was computed for each time instant from the dynamic simulations at three planes normal to the mixing chamber axis: 14 mm, 25 mm (centre of the mixing chamber) and 50 mm at the outlet of the mixing chamber. The time histories of the intensity of segregation are shown in **Figure 4.45** to **Figure 4.47** for the planes at 14 mm to 50 mm, respectively. The time in these plots is normalized by the passage time or residence time , which is defined as

$$\tau = \frac{V_{chamber}}{q_{chamber}} \tag{4.50}$$

$$q_{chamber} = 2\upsilon_{inj} A_{inj} \tag{4.51}$$

$$V_{chamber} = WdH \tag{4.52}$$

Where $V_{chamber}$ is the volume of the mixing chamber, $q_{chamber}$ is the volumetric flow rate in the mixing chamber, υ_{inj} is the jet velocity in injector. Then W , d and $H = 50$ mm are the width, depth and height of the mixing chamber respectively.

For the geometries $W/w = 2$ and $W/d = 0.5$; $W/w = 6$ and $W/d = 6$ the intensity of segregation is very close to 1 at all the planes measured as shown, this is due to the operation at the same flow regime, segregated flow regime, with reduced mechanisms that engulf fluid injected from opposite inlet channels.

The intensity of segregation for the geometries $W/w = 6$ and $W/d = 1$, 1.5 and 2 decreases for different planes from the planes at 14 mm until the outlet at 50 mm, see **Figure 4.45**,

Figure 4.46 and **Figure 4.47**. At the 14 mm plane, close to jets impingement, the intensity of segregation values evolve to approximately zero for $W/w=6$ and $W/d=1$ and 1.5, whereas for $W/d=2$ geometry the I_s value is around 0.15 see **Figure 4.45**. At the mixing chamber planes located at 25 mm and 50 mm the I_s values coincide and are almost zero, which stand for complete mixing of two inlet streams, see **Figure 4.46** and **Figure 4.47**. The lower values of the intensity of segregation for the $W/d=$ 1 and 1.5 geometries, provides further evidence of an optimum range of value for depth of the mixing chamber.

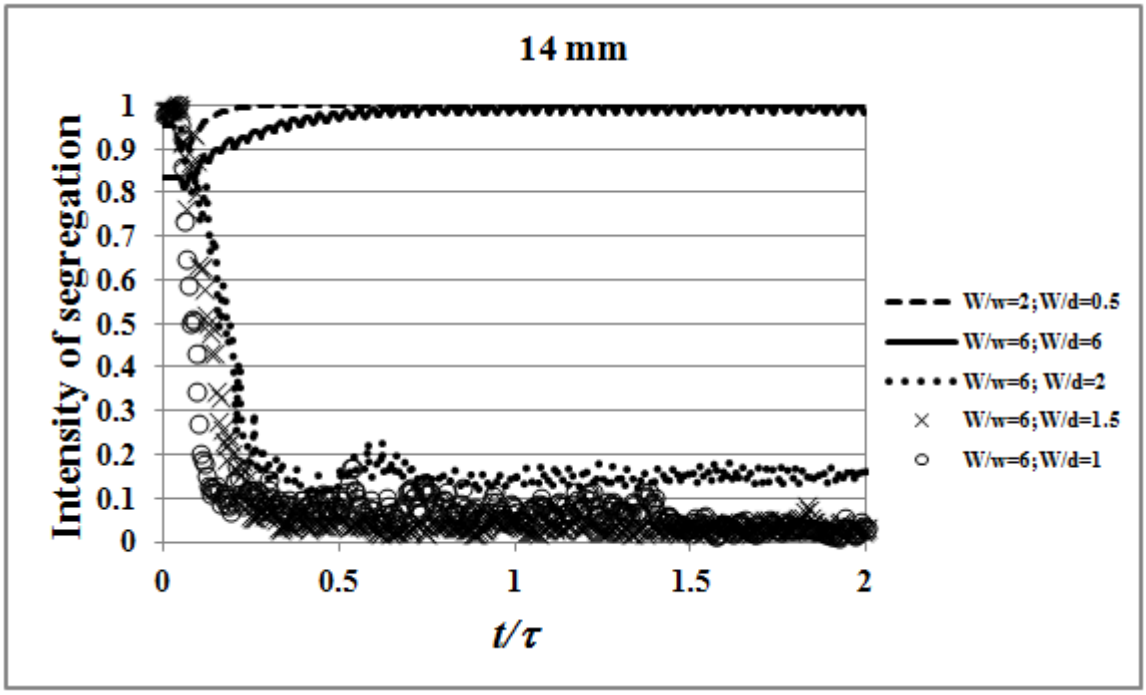

Figure 4.45 Intensity of segregation at z=14 mm, as a function of passage time

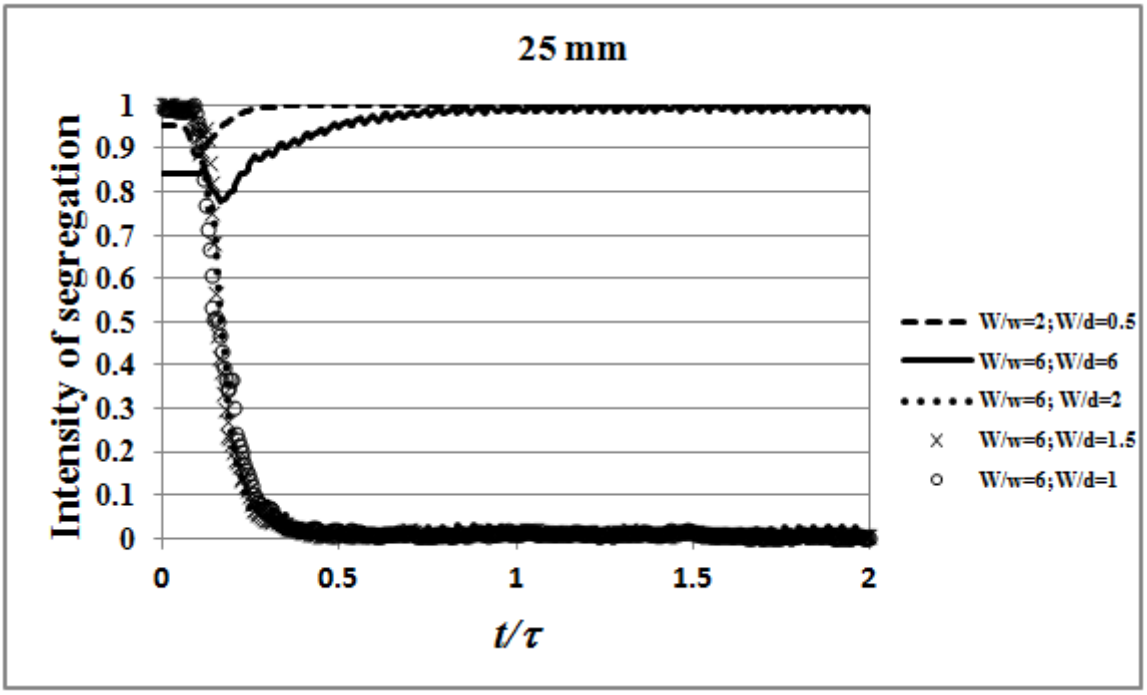

Figure 4.46 Intensity of segregation at z=25 mm, as a function of passage time

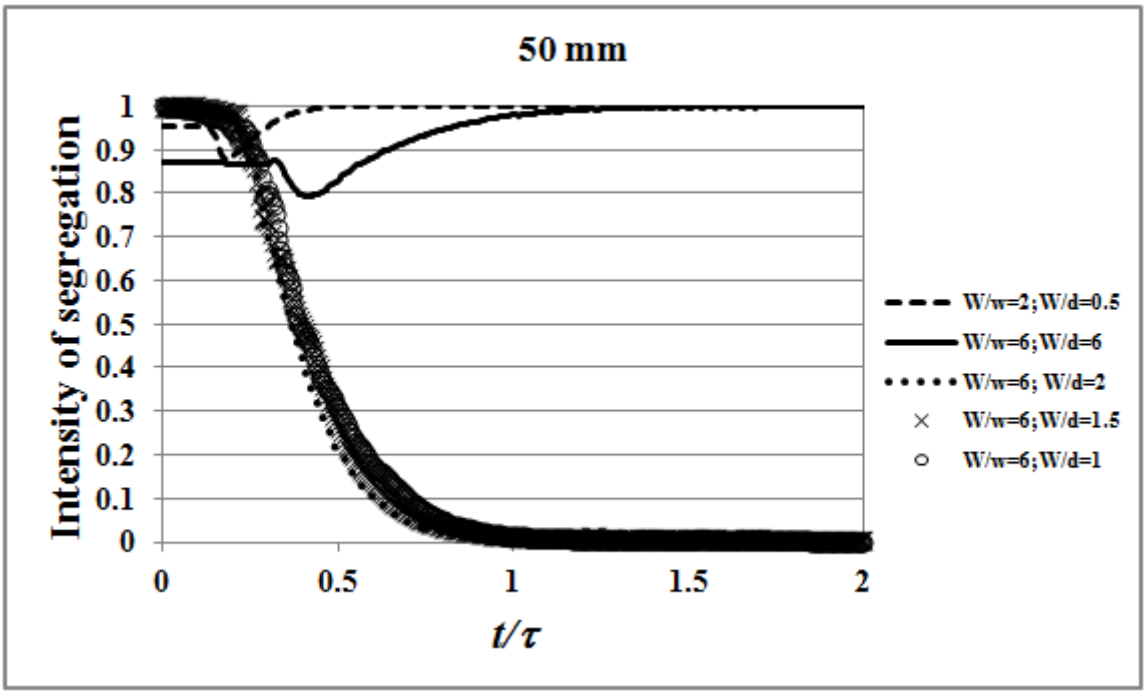

Figure 4.47 Intensity of segregation at z=50 mm, as a function of passage time.

4.11.3 **Comparison of 3D CFD and Experimental results**

The results obtained from 3D CFD simulation has shown detail of mixing mechanism that can be easily compared with the experimental PLIF data of **Chapter 3**. **Figure 4.48** and **Figure 4.49** compares the result obtained from 3D CFD simulation and PLIF tracer experiments for four different geometries at *Re*=300.

For $W/w=6$ and $W/d=1$ geometry, both images show similar flow patterns, after the jets impingement point it is clearly seen a vortex street flowing along the mixing chamber towards the outlet.

For $W/w=6$ and $W/d=$ 1.5 and 2, after the jets impingement a s*elf-sustainable chaotic flow regime* is observed with vortices evolving along the mixing chamber towards the outlet.

In the $W/w=6$ and $W/d=6$ geometry, from both the images the oscillation of the jets is still observable at the lower half of the mixing chamber, but the flow keeps a markedly segregated pattern between the opposed streams. This flow regime is *segregated*.

The maps of tracer concentration exhibit for the four cases in **Figure 4.48** and **Figure 4.49** similar patterns to the experimental PLIF results. One of the main differences is some increased impact of diffusion in the CFD results.

The intensity of segregation results obtained for the geometries $W/w=6$ and $W/d=1$, 1.5 and 2 from PLIF experiments and CFD show similar trends of low values of intensity of segregation. Similar trend is observed for the geometry $W/w=6$ and $W/d=6$, where the intensity of segregation values from experimental results at *Re*=300 are very high from both CFD and experimental results, with improvement is observed at high Reynolds number from experimental results.

$W = 6$ mm; $w = 1$ mm; $d = 6$ mm; $W / w = 6$; $W / d = 1$

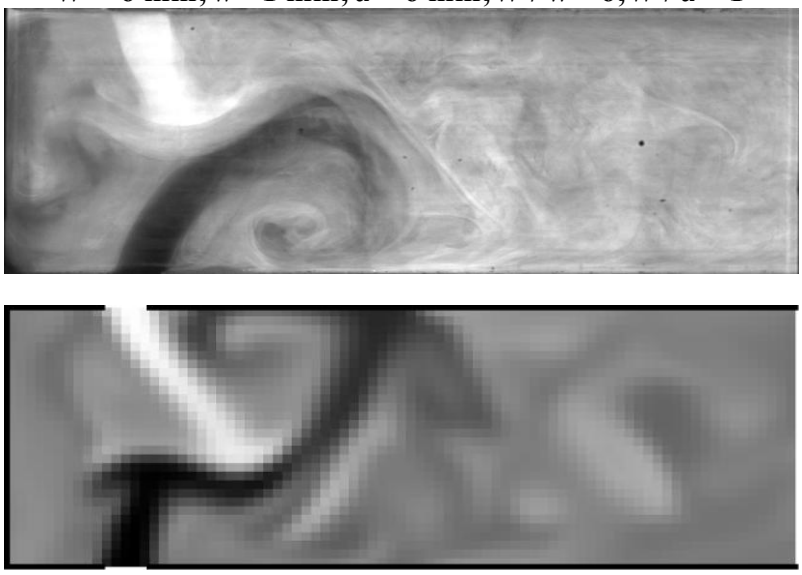

$W = 6$ mm; $w = 1$ mm; $d = 4$ mm; $W / w = 6$; $W / d = 1.5$

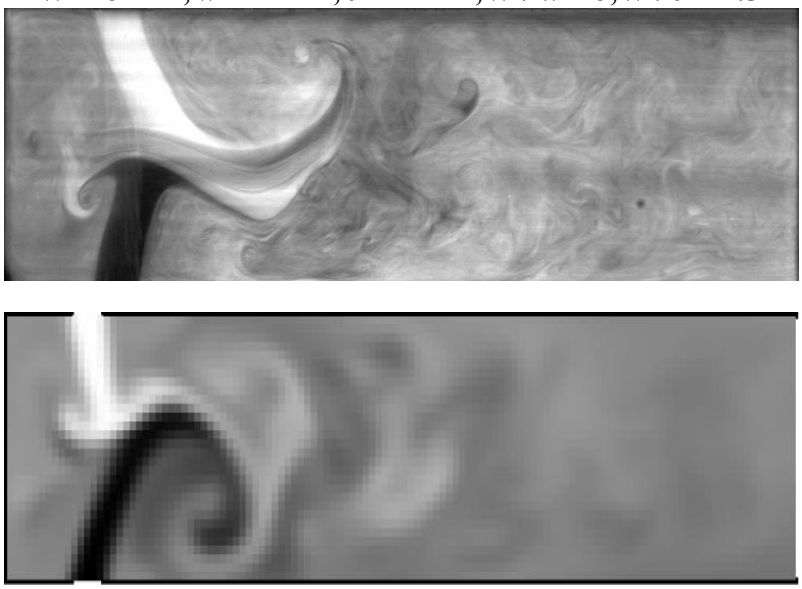

Figure 4.48 Comparison between 3D CFD and experimental results for the geometries with ratio $W / w = 6$ and ratios of $W / d = 1$ and 1.5 for *Re*=300.

$W = 6$ **mm;** $w = 1$ **mm;** $d = 3$ **mm;** $W / w = 6$**;** $W / d = 2$

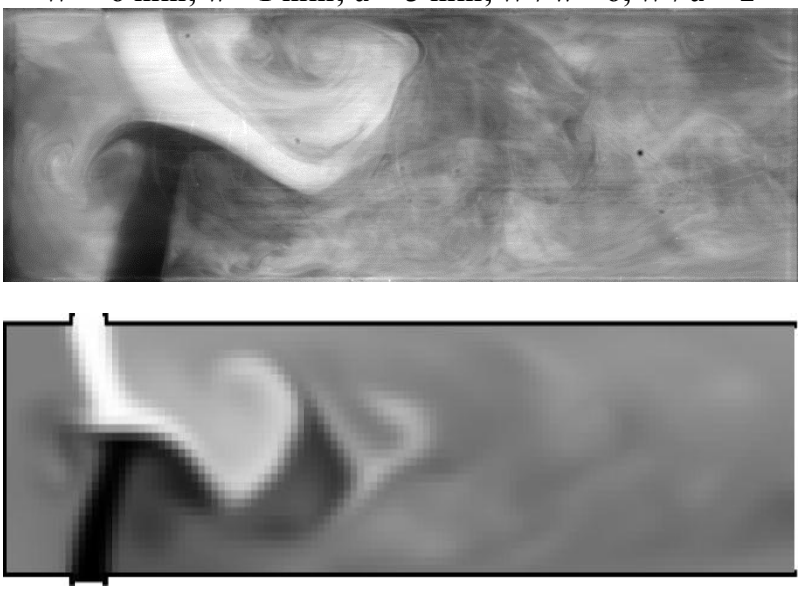

$W = 6$ **mm;** $w = 1$ **mm;** $d = 1$ **mm;** $W / w = 6$**;** $W / d = 6$

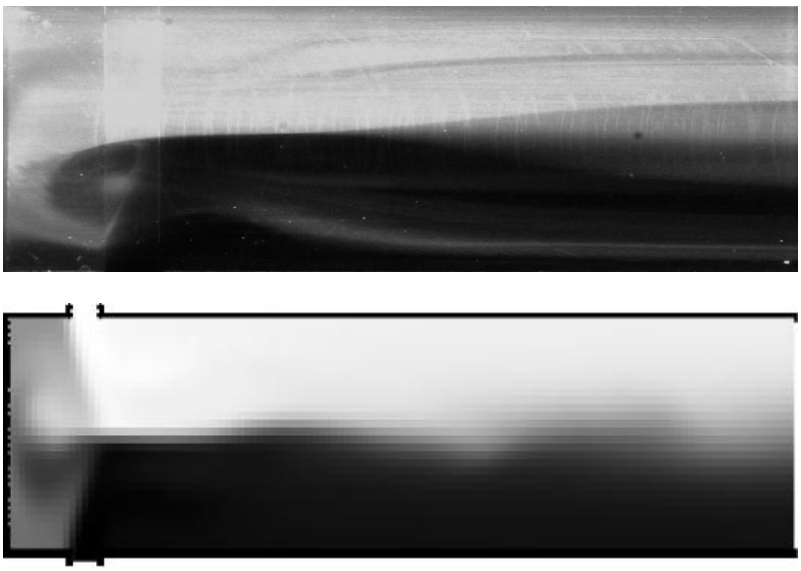

Figure 4.49 Comparison between 3D CFD and experimental results for the geometries with ratio $W / w = 6$ and ratios of $W / d =$ 2 and 6 for *Re*=300.

4.12 Conclusion

4.12.1 **2D CFD**

From the 2D CFD study, W / w was shown to be the most important parameter.

The onset of the vortices that occupy the entire chamber width was observed to depend not only on the Reynolds number but also on the geometrical parameter, W/w. Also this study sets the grounds for an explanation of the different results obtained on T-jets mixers studies using approximately the same jets Reynolds numbers but different geometries.

The effect of W/w on the mixing was also studied with the 2D CFD model using the trajectories of discrete particles. The evolution of the vortices that occupy the entire chamber width towards the outlet is the main mixing mechanisms in this type of mixers. Flow regimes where these vortices are not formed have much lower mixing efficiencies.

The ability of the T-jets mixers to generate vortices, self-sustainable chaotic flow regime, is here related to the geometrical parameter W/w. These vortices are fundamental to operate with high mixing efficiencies.

4.12.2 **3D CFD**

With 3D CFD study, we examined the effect of geometrical parameters chambers width to the jets width ratio, W/w, and chambers width to the chambers depth ratio, W/d, on the flow characteristics in the different T-jets mixers with 3D CFD simulation.

From the grid independence study it was shown that the grid size did not change the flow dynamics in the T-jets mixers. From this study, it could be concluded that the geometrical parameters are as important as the operational parameters, Reynolds number, which was also scrutinized to have a complete insight. In particular, we analysed the evolution of vortices, contributed by the ratio W/w, and W/d, through the y and z vorticity at a particular Reynolds number. The impact of depth was shown in z vorticity maps where the transition Reynolds was high for shallow T-jets mixers than in deep T-jets mixers and the importance of wide mixing chamber was explored. The different flow regimes namely stratified or segregated flow regime, vortex flow regime and engulfment flow regime but through this work we have identified a new flow regime, self-sustainable chaotic flow regime which has not been previously reported in T-jets works (Bothe et al., 2006; Soleymani et al., 2008) which was also identified and confirmed with the experimental results.

The strong association of vortices formation and oscillation of the jets was also analysed with the time histories and power spectra from the υ_x at the jets impingement point and the turbulence intensity plots.

The 3D CFD simulation showed the importance of space above the jets position with the hydrodynamic and spectral analysis and turbulence intensity, it showed that for the formation of vortices which initiates good quality mixing the head space plays an important role.

The tracer simulation reported in this work depicted, the main mixing mechanism in impinging jets is the vortex formation which emerges from the jets impingement in the deeper T-jets mixers than in the shallow T-jets mixers through the contribution of optimum design and operational parameter to promote the homogenization of fluid. The qualitative study of these tracer simulations with intensity of segregation also confirmed the importance of vortex formation. The results also showed that there is an optimum limit of depth above or below which the formation of vortices is dampened and reduces the quality of mixing.

In whole, the simulation results proved the development of vortices is essential for good mixing performance. Furthermore, the work explored the development and occurrence of vortices depends strongly on both operational and geometrical parameter. So it could be concluded that the appearance is not only depended on Reynolds number but also on another dimensionless parameter.

The study suggests that by choosing appropriate design parameters and conditions the T-jets mixers could be fine tuned to attain a particular goal.

4.13 References

Ansys Fluent 14.0 Theory Guide:16.0 Discrete Phase, Last Access Jan.2012, Available from: https://www1.ansys.com/customer/content/documentation/140/flu_th.pdf

Ansys Fluent 14.0 Theory Guide:20.1 Overview of Flow Solvers, Last Access Jan.2012, Available from:https://www1.ansys.com/customer/content/documentation/140/flu_th.pdf

Ansys Fluent 14.0 Theory Guide:20.3.2 Temporal Discretization, Last Access Jan.2012, Available from:https://www1.ansys.com/customer/content/documentation/140/flu_th.pdf

Ansys Fluent 14.0 Theory Guide:7.0 Species Transport and Finite Rate Chemistry, Last Access Jan.2012, Available from: https://www1.ansys.com/customer/content/documentation/140/flu_th.pdf

Ansys Fluent 14.0 Users Guide: 29.14.1 User Inputs for Time-Dependent Problems, Last Access Jan.2012, Available from: https://www1.ansys.com/customer/content/documentation/140/flu_ug.pdf

Ansys Fluent 14.0 Users Guide: 7.3.1 Flow Inlet and Outlet Boundary Conditions, Last Access Jan.2012, Available from: https://www1.ansys.com/customer/content/documentation/140/flu_ug.pdf

Ansys, Online manual, Ansys Fluent 14.0 Users and Theory Guide, Last Access Jan.2012, Available from:https://www1.ansys.com/customer/content/documentation/140/flu_th.pdf Available from:https://www1.ansys.com/customer/content/documentation/140/flu_ug.pdf

Aubin, J., Fletcher, D.F., Bertrand, J., and Xuereb, C., 2005. Characterization of Mixing Quality in Micromixers. Chemical Engineering Science 60, 2503-2516.

Baldyga, J. and Bourne, J.R., (1999). Turbulent Mixing and Chemical reactions. John Willey & Sons.

Bothe, D., Stemich, C., Warnecke, H., 2006. Fluid mixing in a T-shaped micro-mixer. Chemical Engineering Science 61, 2950-2958.

Harris, R.F., Anderson, R.M. and Shannon, D.M., 1992. Speciality Polyurethane Soft segments II Mixing Studies in Micro-RIM Using Polyether Diamine Oligomers Containing Backbone Urea Moieties. Journal of Applied Ploymer Science 46, 1547-1560.

Danckwerts, P.V.,1952. The definition and measurement of some characteristics of mixtures. Applied Scientific Research 3, 279-296.

Gomes, P.J., 2011. The Netmix Reactor: Strategies for optimizing Mixing and Development of New Reactor Designs. Departamento de Engenharia Química. Porto, Universidade do Porto.

Hoffmann,M., Schlüter,M., Räbiger,N., 2006. Experimental investigations of liquid-liquid mixing in T-shaped micro-mixers using μ-LIF and μ-PIV. Chemical Engineering Science 61, 2968–2976.

Kresta, S.M. and Brodkey, R.S., 2004. Mixing and Chemical Reactions. Handbook of Industrial Mixing Science and patrice. John Wiley & Sons, New Jersy.

Lee, L.J., Ottino, J.M., Ranz, W.E., Macosko. C.W.,1980. Impingement mixing in Reaction Injection molding. Polymer Engineering and Science 20, 868–874.

Moon, F.C, 2004. Chaotic Vibrations: An Introduction for Applied Scientists and Engineers. New Jersey: John Wiley & Sons.

Orszag, Steven A., 1970. Analytical Theories of Turbulence. Journal of Fluid Mechanics 41, 363-386.

Santos, R. J., 2003. Mixing Mechanisms in Reaction Injection Moulding - RIM. An LDA/PIV Experimental Study and CFD Simulation. Departamento de Engenharia Química. Porto, Universidade do Porto.

Santos, R.J., Ertugrul, E., Dias, M.M., Lopes, J.C.B.,2009. Dynamic behavior of the flow field in a RIM machine mixing chamber. AIChE Journal 55, 1338-1351.

Santos, R.J., Teixeira, A.M.T., Costa, M. R. P. F. N., Lopes, J.C.B., 2002. Operational and Design Study of RIM Machines. International Polymer Processing 17, 387-394.

Santos, R.J., Teixeira, A.M.T., Lopes, J.C.B., 2005. Study of mixing and chemical reaction in RIM. Chemical Engineering Science 60, 2381–2398.

Santos, R.J., Teixeira, A.M.T., Ertugrul, E., Sultan, M.A., Karpinska, A.M., Dias, M.M., Lopes, J.C.B. 2010.Validation of a 2D CFD Model for Hydrodynamics Studies in CIJ Mixers. International Journal of Chemical Reactor Engineering 8 (A32).

Soleymani, A., Kolehmainen, E. and Turunen, I., 2008. Numerical and experimental investigations of liquid mixing in t-type micromixers. Chemical Engineering Journal 135, S219-S228.

Teixeira, A. M., Santos, R.J., Costa, M. R. P. F. N., Lopes, J.C.B., 2005. Hydrodynamics of the Mixing Head in RIM: LDA Flow-Field Characterisation. AIChE Journal 51(6), 1608-1619.

Tennekes, H., J.L. Lumley., 1997. A First Course in Turbulence. 7th Ed. ed, Cambridge, MIT Press.

Unger, D.R. and Muzzio, F.J.,1999. Laser induced Fluorescence Technique for the Quantification of Mixing in Impinging Jets. AIChE Journal 45, 2477-2486.

Wong, S.H., Ward, M.C.L., Wharton, C.W., 2004. Micro T-mixer as a rapid mixing micromixer. Sensors and Actuators B 100, 359-379.

5. MICROMIXING IN T-JETS MIXER

5.1 Introduction

Mixing and chemical reaction coexists and is related to each other in many chemical mixers such as the static mixers. The phenomena through which the different reactants are brought together have a great impact on the evolution of a chemical reaction. The selectivity of a reaction is affected due to the inadequate mixing of the reactants, which results in undesirable products. The efficiency of many chemical processes depends upon the mixing conditions of the materials. The field of mixing in chemical engineering field is very vast and diverse. This work only considers liquid-liquid phase mixing in a static mixer with opposed jets, the T-jets mixer.

In the literature (Bourne et al., 1990; Bourne et al., 1992) exist several studies on test reaction developed for micromixing studies in aqueous media. In this study, a test chemical reaction introduced by Bourne is used (Bourne, 1981). This reaction was studied previously with stopped-flow analyzer to determine the kinetics of the reactions and then it was used in another reactor introduced at LSRE the NETmix® (Nunes, 2007; Laranjeira et al., 2011). Here this work is extended to study the reaction with an UV-vis spectrophotometer system equipped with an instant online measuring flux cell device.

5.1.1 **Test Chemical Reaction**

The test chemical reaction chosen was first proposed and introduced by Bourne (1984). It is simultaneous coupling of the reactant 1-naphthol (*A*) and diazotized sulfanilic acid (*B*)

$$A + B \xrightarrow{k_{1o-R}} o - R \text{ (fast)} \tag{5.1}$$

$$A + B \xrightarrow{k_{1p-R}} p - R \text{ (fast)} \tag{5.2}$$

$$o - R + B \xrightarrow{k_{2o-R}} S \text{ (slow)} \tag{5.3}$$

$$p - R + B \xrightarrow{k_{2p-R}} S \text{ (slow)} \tag{5.4}$$

where *o-R*, *p-R* and *S* are 2-(4-sulpophenylazo)-1-naphthol, 4-(4-sulpophenylazo)-1-naphthol and 2, 4 –bis (4- sulpophenylazo)-1-naphthol respectively. **Figure 5.1** shows the structure of these chemical species. All the products are coloured and their concentrations can be easily determined by UV-vis spectrophotometer **Figure 5.2**.

The first two reactions (Equation (5.1) and (5.2)) between 1-naphthol (*A*), and diazotized sulfanilic acid (*B*) are very fast and produce two monomer isomer dyes (*o-R* and *p-R*). These *o-R* and *p-R* react with *B* to give the secondary product called bisazo dye *S*; these second reactions (see Equation (5.3) and (5.4)) are slower.

This Bourne reaction was chosen for various reasons: it is one of the most applied reaction in the micromixing studies in a wide range of applications; the reagents and solvents (mainly water) used are not expensive and can be used in studies which require considerable solution volumes (up to 10 litre in each experiment); the reaction products are coloured therefore it allows visualization of the iso-momentum state between the two opposing jets.

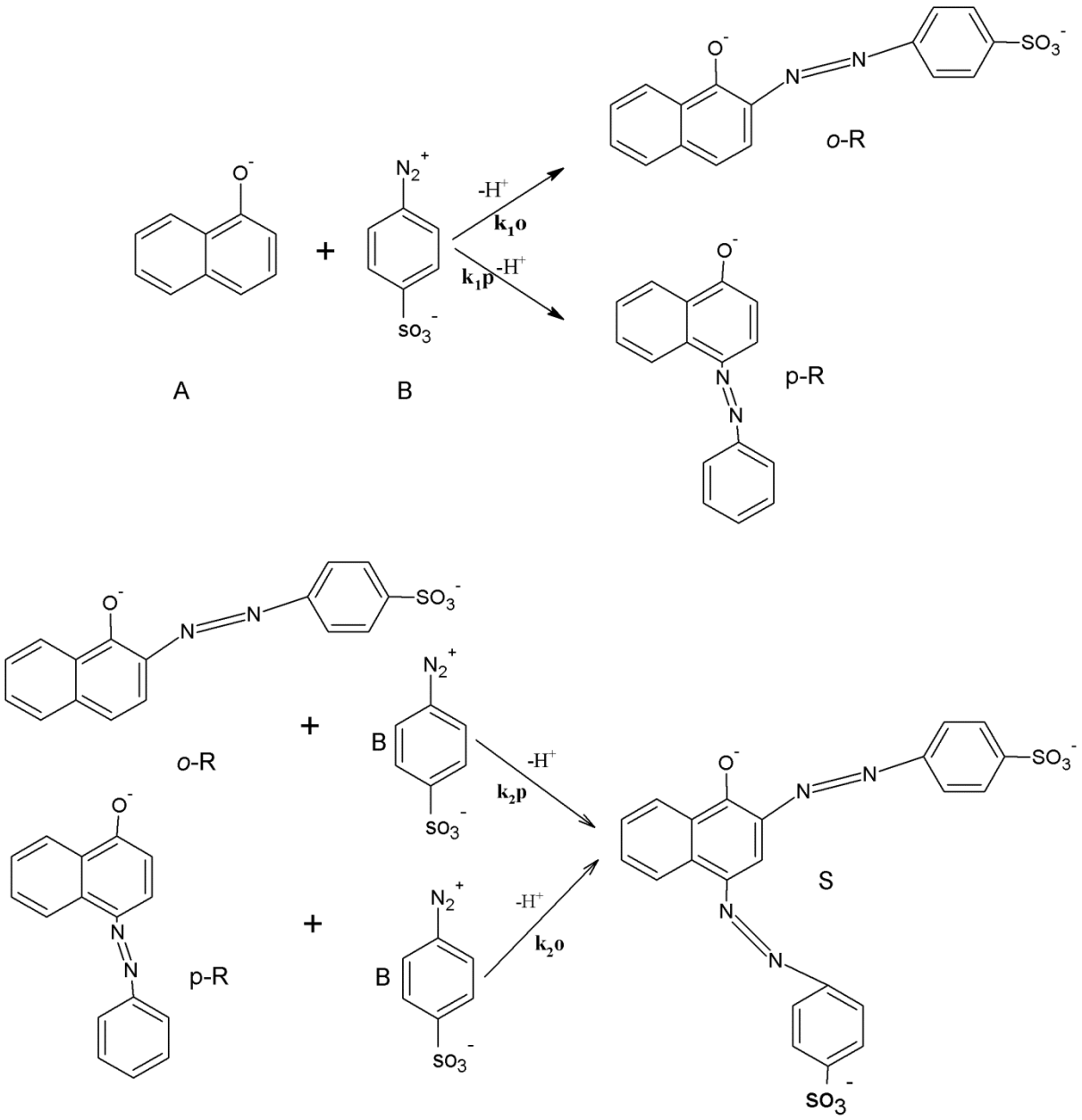

Figure 5.1 Diazo coupling reactions between 1-Naphthol (*A*) and diazotized sulfanilic acid (*B*) (Bourne et al., 1992a)

The test chemical reaction can be simplified using the alternative scheme (Bourne et al., 1990, 1990a)

$$A + B \xrightarrow{k_1} R \text{ (fast)} \tag{5.5}$$

$$R + B \xrightarrow{k_2} S \text{ (slow)} \tag{5.6}$$

where R=*o*-R+*p*-R; $k_1 = k_{1o} + k_{1p}$ and $k_2 = \%o - Rk_{2p} + \%p - Rk_{2o}$. B is used as limiting reactant, and thus S is only formed when an excess of B exists after A reacts with B to form R. If mixing is fast enough, all B is consumed by A, and so the concentration of S is smaller for faster micromixing conditions. This simplification has two advantages: (i) mass balance equations are simpler and easier to work with; (ii) it overcomes some limitations of the analytical method demand due to the fact that the monoazo isomers (*o*-R and *p*-R) have their spectra overlap at pH=9.9, the value utilised in this study. The kinetic rate constants for the first and second reaction at 25 $°C$ are $k_1 = 19 \times 10^3 \text{m}^3\text{mol}^{-1}\text{s}^{-1}$ and $k_2 = 3.99 \text{m}^3\text{mol}^{-1}\text{s}^{-1}$ (Lenzner, 1991; Nunes et al., 2012). The product distribution, X_S, is usually characterised by the fraction of the limiting reactant B which is converted to the secondary S:

$$X_S = \frac{2C_S}{2C_S + C_R} \tag{5.7}$$

where C_S and C_R are the concentration of the product R and S. X_S is called as the segregation index or the selectivity in S and is determined by spectrophotometric analysis of the fluid through the flux cell, after the reaction is complete and all B had been consumed. These competitive-consecutive reactions are sensitive to micromixing effect and X_S gives direct measure of micromixing. The minimum value of X_S is expected with greater homogeneity when the reactants are fully mixed and the mixture is homogeneous at the molecular scale level. (Demyanovich and Bourne, 1989).

The selectivity X_S, has the range from 0 to 1. When X_S tends to zero it indicates good mixing and 1 indicates poor mixing, if the limiting reactant is B and if the first reaction is fast compare to the second reaction. From the work of Baldyga and Bourne (1999) on similar test reaction a range $0.04 < X_S < 0.4$ was defined. The upper limit of X_S is achieved from the stability of the secondary product S and the lower limit is due to analytical errors of the spectrophotometry technique. In this work the X_S value need not lay within these limits

because all the measurements were made on-line and therefore no degradation of the secondary product *S* occurs from sampling to analysis.

The spectrophotometer is the device used to determine the concentration of the each product in the reaction mixture, for this the molar extinction, ε, of the pure products must be known. In this work it was assumed that the Beer-Lambert Law is valid. It is known that the species *R*, and *S* absorb the light independently, which imply that the absorbance at a given wavelength is

$$Abs = \varepsilon_R \delta C_R + \varepsilon_S \delta C_S \tag{5.8}$$

where ε_R and ε_S are extinction coefficient of the product *R* and *S*, respectively $m^2\ mol^{-1}$, δ is the optical path length and C_R and C_S are the concentrations of the *R* and *S*. For determination of concentration of each product, the molar extinction coefficients, ε, of the pure products must be known. These coefficients constitute the calibration spectra of the species and were determined based on the Beer-Lambert law. Reactant *A* is not considered in Equation (5.8) because it is colourless and the range of wavelengths to quantify the products concentration is in the visible region.

From Equation (5.8), an absorbance curve, Abs_{calc}, is calculated, based on the estimations of both products concentrations C_R and C_S. Then, by using the Excel® Solver tool, the curve is fitted to the experimental curve Abs_{calc}, where the fitting variables are C_R and C_S. The fitting to the curve is made through the minimization of the deviation function over the wavelength range of 450-650 nm

$$D^2 = \sum_{450}^{650} (Abs_{\exp\lambda} - Abs_{calc\lambda})^2 \tag{5.9}$$

All T-jets geometries and Reynolds numbers were tested with the same concentration of 1-naphthol (*A*) and diazotized sulfanilic acid (*B*): 0.1 mol m^{-3} of *A* and 0.095 mol $m^{-3}$of *B*. The concentrations ratio is 1.0526. The characteristic reaction time is defined as $1/k_2 C_0$ is equal to 5.2s, where C_0 corresponds to the initial concentration of the limiting reactant (*B* in this case) and k_2 is the second reaction rate constant.

5.2 Chemicals

In this work the reactants used for this Bourne's chemical reaction are 1-naphthol and diazotizes sulfanilic acid. The complete procedure and steps involved including its structure is being discussed in detail in the Appendix A section.

5.3 Experimental Set-Up

This test chemical reaction was performed in eight T-jets mixer geometries and experimental set-up previously described in PLIF experimental study in the **Chapter 3** for the flow field characterization. The list of T-jets mixer is given in **Table 3.1** where W is the mixing chamber width, w is the injectors channels width and d is the depth of the complete geometry. The mixing chamber has a height, $H = 50$ mm respectively.

Similar to the tracer PLIF experimental set up in **Chapter 3**, this chemical reaction experiment comprises two pressurised tanks, one tank is filled with 1-naphthol (*A*), other tank with diazotized sulfanilic acid (*B*) and there volumetric flow rate were monitored and controlled by the two liquid flow controller used in the PLIF experiment of **Chapter 3**.

The flow controllers are factory calibrated for water, therefore they work for water and water with passive tracer fluids as earlier used in PLIF experiments. Here for the solutions of 1-naphtol and diazotized sulfanilic acid, there were slight deviations, less than 10%, and so a calibration curve was made and used for the chemical reaction experiment. This difference of 10% deviation between the flow controllers was due to the alcohol (ethanol) added in 1-naphtol to dissolve it, as it is readily soluble in alcohol and only slightly soluble in water.

The camera DBK 21AU04 FC as shown in the **Figure 5.2** was used to capture the images of the chemical reaction experiment, the *A* and *B* reactants enter the T-jets mixers mixing chamber through opposed injectors. In this setup, complete chemical mixing mechanism and flow regime could be visualized as the Bourne's reaction is coloured. In addition to this setup, differential pressure monitoring system was installed to monitor and control the pressure difference between the feeding inlet jets with a Validyne differential pressure transducer as it is directly related to the balancing of both the opposing jets (Erkoc et al., 2007). The use of

differential pressure reduces the error from 10% to a precision better than 1%. The control of this flow rate, differential pressure was done with the LabView program, see **Figure 5.3** that communicates with the several instruments through a DAQ card from National Instrument. The differential pressure transducer is connected to each of the injectors feeding line, which is coupled to the mixing chamber according to the patented operational procedure. This is the basic concept for patented control scheme for RIM, European Patent EP 1 732 747 A0 and USA Patent US 7708918 (Lopes et al., 2005)

T-jets mixer outlet pipe is connected to flux cell where the absorption spectra is measured. The flux cell has two ports connected to optic fibbers; one port is connected to the UV-vis light source and emits a bean towards the second port, which is connected to the UV-vis spectrophotometer. This UV-vis spectrophotometer from scansci is connected through a USB interface to the same PC that controls the T-jets installation. The complete flowchart is shown in **Figure 5.4**. The PC is installed with the scansci software for measuring the absorbance acquired via UV-vis spectrophotometer. With this spectrophotometer a miniature ScanSource ABS light source model with a continuous spectra in the UV-vis spectrophotometer ranged from 200-1100 nm was connected. This light source is designed particularly to measure the absorbance and the transmittance. The complete equipments such as spectrophotometer, light source and flux cell is shown in the **Figure 5.4**.

The flux cell (SMA-Z-Cell) has two fibre cables; one is connected to the spectrophotometer and other to the light source. The flux cell has fused silica windows as a wetting surface at each fibre optic junction. The flow cell has 10 mm path-length and is made of Plexiglass and this flux cell is completely isolated from the ambient light to reduce the noise during the course of the experiment.

The light that passes through the liquid medium at the flux cell is collected by an optical fibre, which is connected to the UV-vis spectrophotometer where the spectrum of the light is registered in a linear CCD with 2048 pixels. The A/D converter transforms the acquired analog data from the spectrophotometer into digital data. This is transferred to the SpectraScan program through an USB interface.

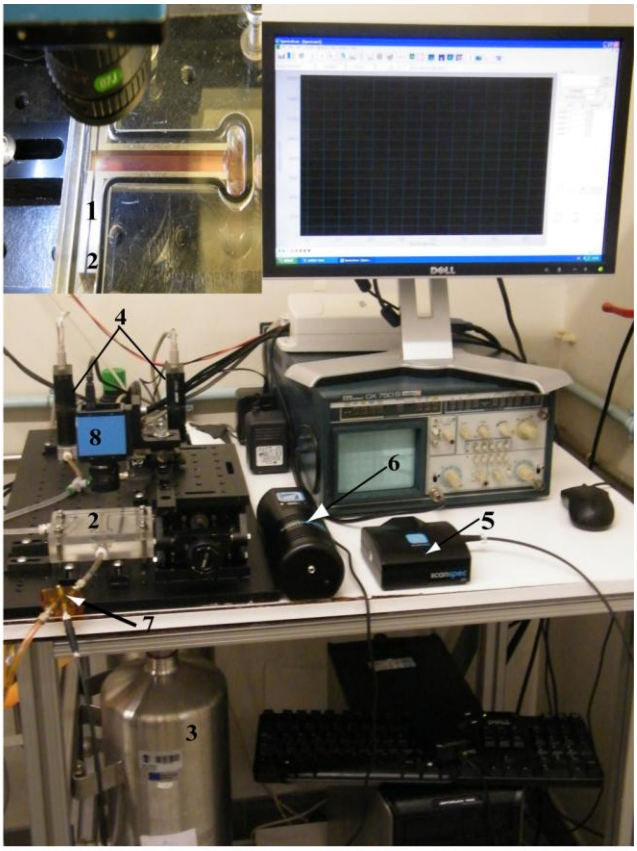

1. T-jets aluminium geometry
2. Transparent acrylic block
3. Pressurised tank with fluids
4. Liquid flow controller
5. Spectrophotometer
6. Light Source
7. Flux cell
8. Camera

Figure 5.2 Chemical reaction experimental set-up.

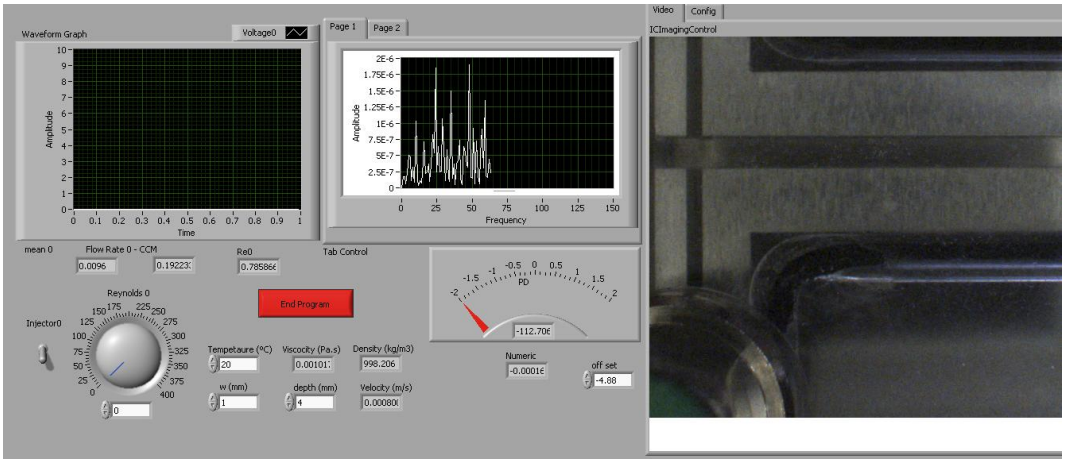

Figure 5.3 View of the control program with pressure and flow controller.

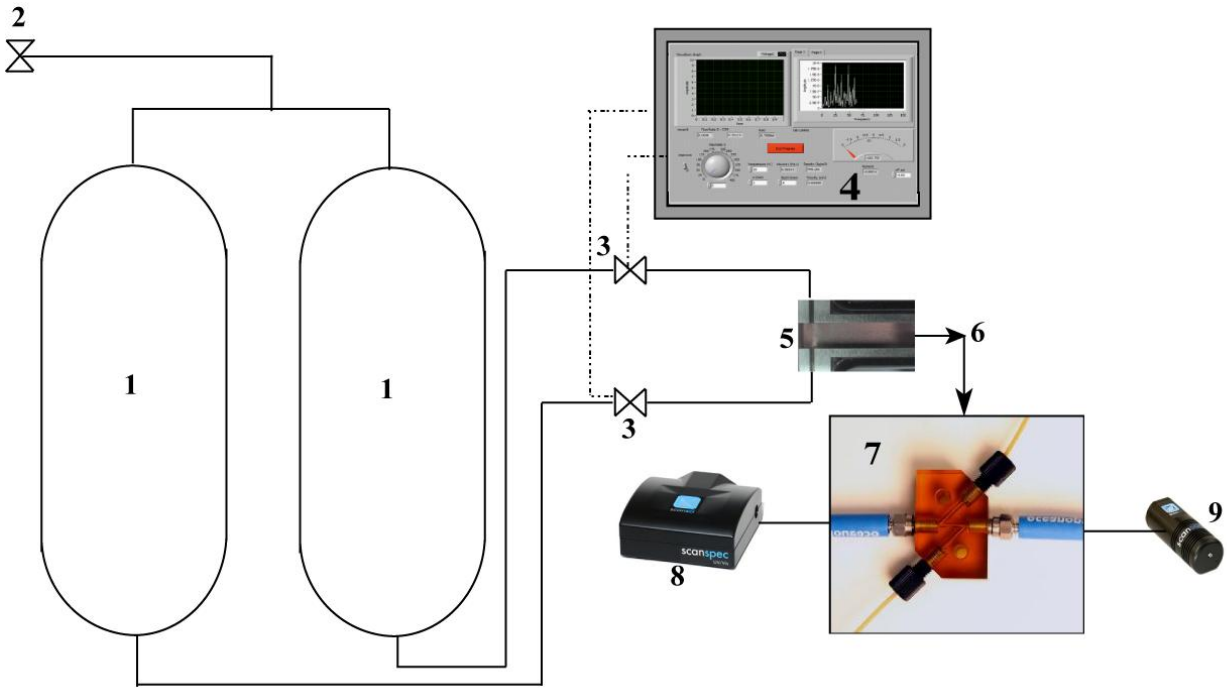

1. Tank
2. Pressure regulator
3. Flow controller
4. PC with flow controller and ScanSCi software
5. T-jets in the acrylic chamber
6. Outlet
7. Flux cell
8. Spectrophotometer
9. Light source

Figure 5.4 Flow chart of chemical reaction experimental set-up.

5.4 Results

The absorbance of the solution at the mixing chamber outlet was monitored on-line over a wavelength range 250-750 nm. The concentrations of S and R were calculated and the selectivity was computed with Equation (5.7).

The chemical reaction experiment was performed with initial concentration of 0.1 mol m^{-3} of 1-naphthol (A) and 0.095 mol m^{-3} of diazotized sulfanilic acid (B) in the T- jets mixers, thus with the initial concentration ratio of 1.0526 ($C_A / C_B = \gamma = 1.0526$) in the eight T-jets mixers geometries listed in the **Table 3.1** of the **Chapter 3**. With visualization experiments, it was

noticed that the initially colourless fluids before jets impingement turns red, which indicates the presence of new species in the reactor, the intensity of red colour liquid depends upon the quality of mixing which differs for the different T-jets mixers studied and the colourless or less intense red colour at the outlet indicates absence the product.

For all geometries and for each Reynolds number the mass balance was always checked, and the maximum measured deviation was approximately 20%. The mass balance did not close, probably due to the fact that all measurements were made on-line, i.e. particularly for low Reynolds number where the mixing time is longer, the probability of the reaction not being completed increases.

For this study the Reynolds number is defined as in **Chapter 3**, using Equation (3.1).

5.4.1 **Selectivity**

The quantification of mixing in the T-jets mixer with chemical reaction is made from the value of selectivity (see Equation (5.7)), X_S. The value of selectivity varies from 0 to 1 depending upon mixing intensity, which has already proven in **Chapter 3** and **Chapter 4**, varies with the Reynolds number.

For the lower Reynolds numbers in all the geometries, the values of selectivity are higher; the flow regime is segregated and mixing occurs only in the interface between the *A* and *B* streams. Increasing the Reynolds number makes the flow regime evolve to either chaotic or engulfment flow regime, which is associated with a steep improvement of micromixing within a short range of Reynolds numbers see **Figure 5.5** and **Figure 5.6**.

5.4.1.1 Effect of (W/d)

For higher Reynolds numbers, the X_S value decreases. The characteristics of the X_S, decrease depend on the T-jets geometry. For the $W/w=6$ in the geometries having larger depths, $W/d=1$ to 2, a steep decrease of X_S, occurs from Re=100 to Re=200. The steep decrease of X_S, is visible in **Figure 5.5**, and is associated with a flow regime transition from segregated steady parallel flow at $Re<100$ to chaotic flow regime with the formation of

vortices having rotation axis normal to the mixing chamber axis. The vortex street promotes a fast homogenization of both reactants, so the onset of the vortices in chaotic flow regime is related to a decrease of an order of magnitude of X_S.

It can be observed that X_S decreases with decreasing of W/d ratio, for the studied range of Reynolds numbers. This is particularly noticeable for the shallower chamber, $W/d = 6$, where the flow regime transition is only reported at $Re > 500$ see **Figure 5.5**.

The depth of the T-jets mixing chamber has a critical effect on the flow regime. In PLIF experiments it was observed that the shallow chambers could not achieve a chaotic flow regime, and so the depth is a critical design parameter. For deeper chambers the depth effect is not so critical, although vortices could be formed further downstream in the mixing chamber at $W/d = 3$ than in deeper chambers, this does not produced an observable effect on micromixing.

Also for $W/d = 1$ where there is evidence from PLIF and CFD data that the flow and mixing dynamics are not as strong as in $W/d = 1.5$ and 2, the differences in selectivity are not clear. The chemical system used, which has a typical reaction time of 5.2s, is probably not so sensitive to distinguish the mixing efficiency of engulfment and chaotic flow regimes. The differences on X_S are only clear between segregated steady flow regime and dynamic flow regime.

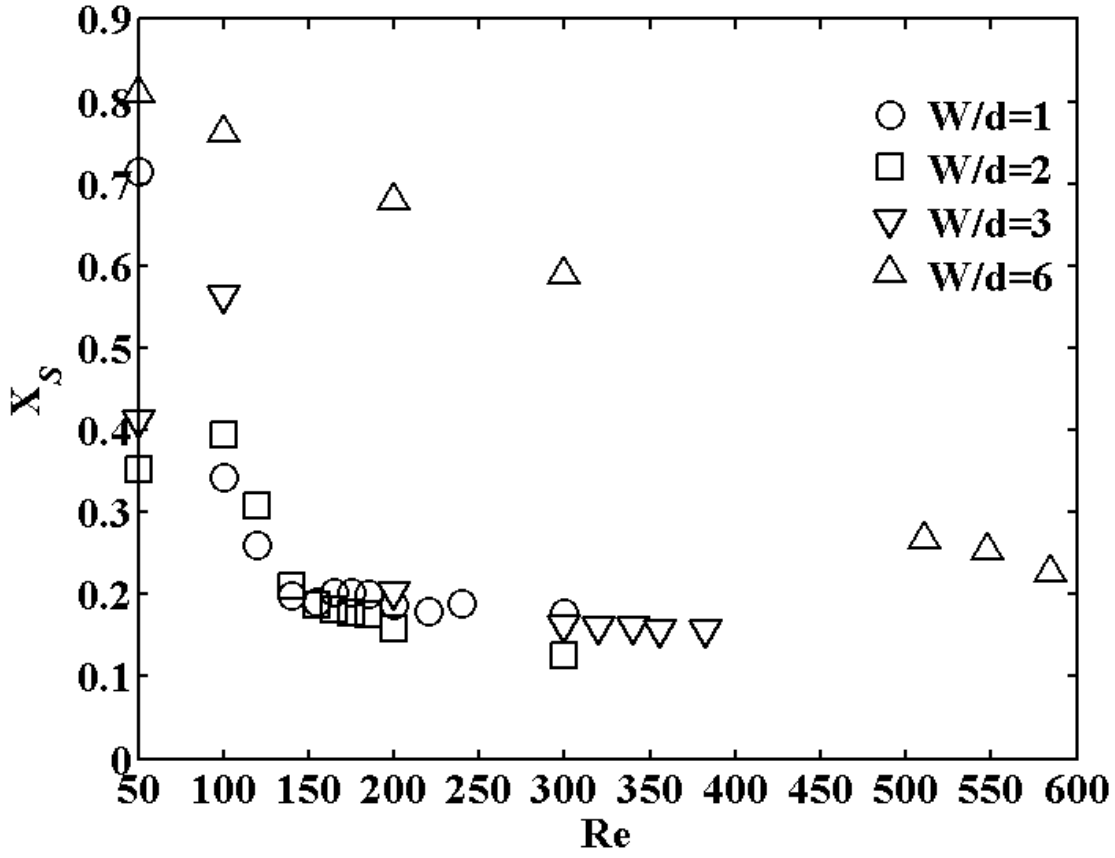

Figure 5.5 Selectivity versus different Reynolds number with fixed $W / w = 6$; with varying W / d .

5.4.1.2 Effect of (W / w)

Figure 5.6 shows the influence on the selectivity of $W / w = 1$, 2 and 4 with fixed ratio $W / d = 0.5$. The flow regimes and mixing in these geometries were previously discussed from PLIF experimental results in **Chapter 3**. For the lower Reynolds numbers in all the geometries, the values of selectivity are higher; the flow regime is segregated and mixing occurs only in the interface between the *A* and *B* streams. Increasing the Reynolds number makes the flow regime evolve to either chaotic or engulfment flow regime, which is associated with a steep improvement of micromixing within a short range of Reynolds numbers.

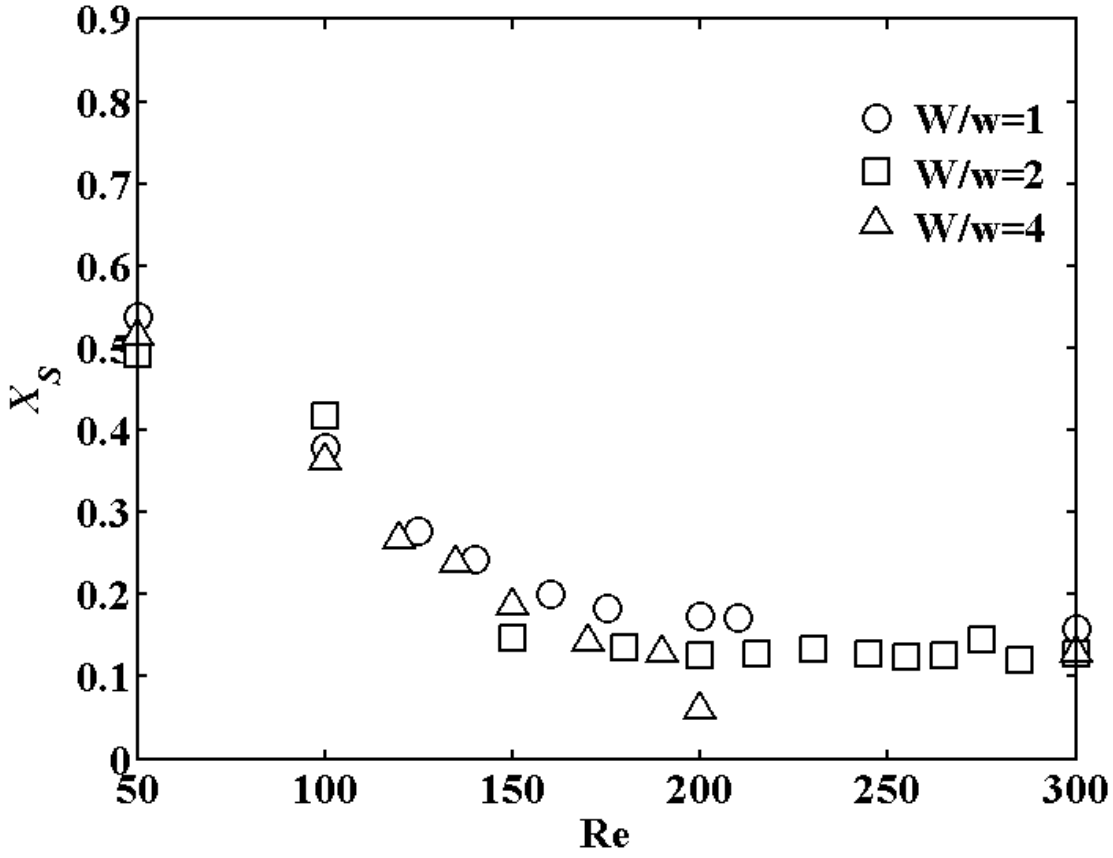

Figure 5.6 Selectivity versus different Reynolds number in different geometries for $W/d = 0.5$ with varying $W/w = 1, 2$ and 4.

The evolution of *S* selectivity with the Reynolds number does not differ significantly with the T-jets geometries. Nevertheless, the macromixing flow patterns are quite distinct. After the transition from the steady flow regime to the dynamic flow regime the effect of the Reynolds number on micromixing is reduced and the selectivity in *S* is maintained roughly constant with *Re*. The transition of flow regime is in the range of Reynolds from 100 to 200 for all geometries of **Figure 5.6**, and therefore the X_S plots are roughly coincident.

5.4.2 **Effect of Flow Rate Ratio**

The balancing of the two opposing jets is an important operational factor on opposed jets reactors. Santos et al. (2010) showed that small deviations from the operation conditions where jets are balanced, compromise the operation of the mixer under chaotic flow regimes. The balancing of the jets is attained by varying the flow rate ratio defined as

$$FR = \frac{Q_A}{Q_B} \tag{5.10}$$

where Q_A is flow rate of 1-naphthol and Q_B is the flow rate of diazotized sulfanilic acid. The flow rate ratio was varied in the range of 0.25 to 2, keeping the concentration ratio, C_{AO} / C_{BO}, constant (these concentrations are referred to concentrations inside the mixing chamber) and equal to 1.2. The geometry used for this study was W / w=6 and $W / d = 1.5$**.**

For small deviations from *RF*=1 one of jets pushes the other against the opposite side of the chamber. Furthermore, the vortex street that issues from the impingement point located in the mixing chamber axis, is only occurring at *RF*=1, which will have a clear impact on micromixing (Nunes 2012).

The results of selectivity in *S* for the W / w=6 and $W / d = 1.5$ geometry at three different Reynolds numbers are shown in **Figure 5.7**. From this figure it can be concluded that increasing the flow rate ratio from 0.25 to 1 improves micromixing. When the flow rate ratio increases from 1 to 2 (maintaining *B* as limiting reactant), the selectivity increases. This means that mixing quality decreases when the flow rate ratio is different from unity. Even for low Reynolds numbers, where the flow is steady, the smallest values of X_S are observed for *RF*=1.

The X_S plots are not symmetrical, i.e. the value of X_S for *RF*=0.5 is larger than for *RF*=2. This is due to the fact that for *RF*=0.5 the stream rich in *B* squeezes the *A* stream and occupies most of the chamber, and so *B* rich regions occupy a larger volume, which enables longer contact times of *B* and *R*. On the other hand when *RF*=2 the regions occupied by *B* are smaller and thus contact of *B* and *R* becomes less likely to occur, which decreased the X_S values see **Figure 5.8**. A similar behaviour of flow rate ratio on micromixing was observed for the other seven geometries, the selectivity plots are shown in **Appendix B**.

$W / w = 6$; $W / d = 1.5$; W =6 mm; w =1 mm; d =4 mm

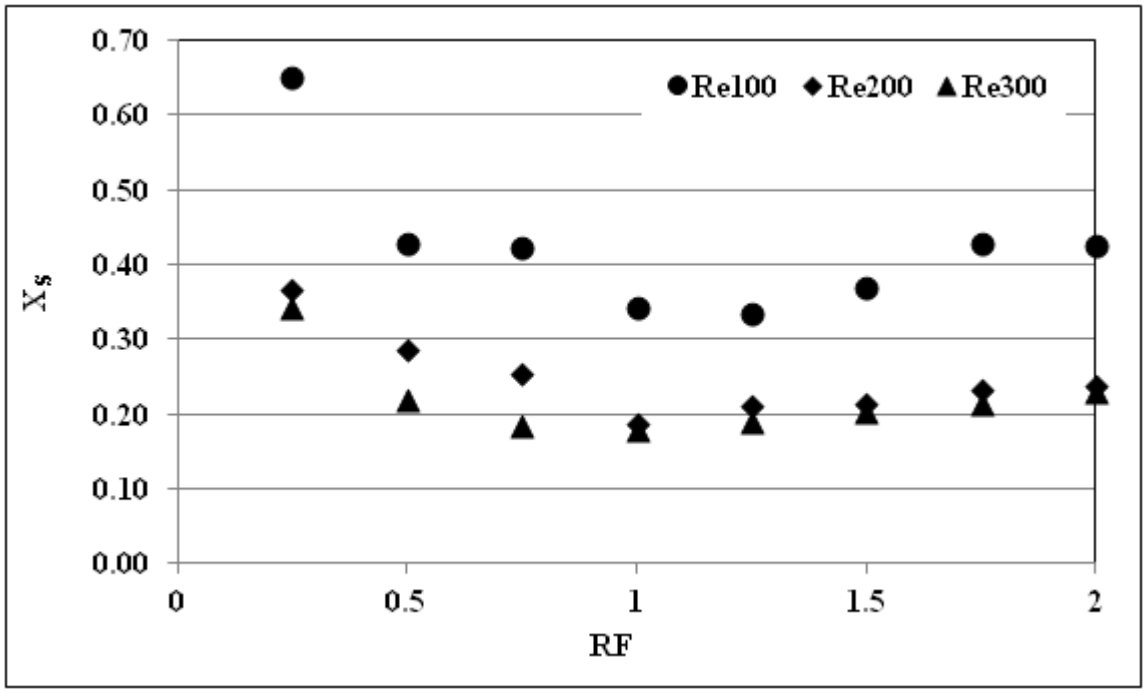

Figure 5.7 Flow rate ratio versus Selectivity at Re = 100, 200 and 300 for ratios W / w=6 and W / d = 1.5.

FR=0.25 FR=0.5

FR=0.75 FR=1

FR=1.5 FR=2

Figure 5.8 Images obtained for different Flow rate ratio at Re = 300 for ratios W / w=6; with and W / d = 1.5.

5.4.3 **Damkholer number**

In this section we study the effect of Damkohler number in the T-jets geometry with ratios W / w=6; $W / d = 1.5$ and measure its effect on the selectivity.

In general, Damkohler number is a dimensionless number applied in chemical reaction to estimate and relate the residence time or the retention time with the reaction time of the chemical species. When *A* and *B* react according to the following kinetic scheme and form the reactant *R*

$$A + B \xrightarrow{k} R \tag{5.11}$$

$$\frac{dC_R}{dt} = kC_A C_B \tag{5.12}$$

where C_A, C_B, C_R are the concentration of the respective species *A*, *B* and *R* respectively and *k* is the specific reaction rate. The Damkohler number is defined as the

$$Da = \tau k C_o^{n-1} \tag{5.13}$$

where C_0 is the inlet concentration of the chemical species and τ is the average residence time in the mixing chamber which is defined as $\tau = V / Q$ where *V* is the volume of the reactor and Q is the volumetric flow rate and *n* repents the reaction order respectively.

The reaction rate constant of n=2 for this test reaction is known from the previous work (Nunes, 2007) on the kinetics reaction rate constant. All experiments were carried out at 25ºC and for this temperature the different Damkohler numbers studied with the different initial concentration are shown in the **Table 5.1**, with the ratio between reagents concentration at 1.2.

Table 5.1 Different Damkohler number studied and their initial reactant concentration.

Damkohler number	C_{A_0} mol/m^3	C_{B_0} mol/m^3
100	0.010	0.008
500	0.048	0.040
1000	0.095	0.080

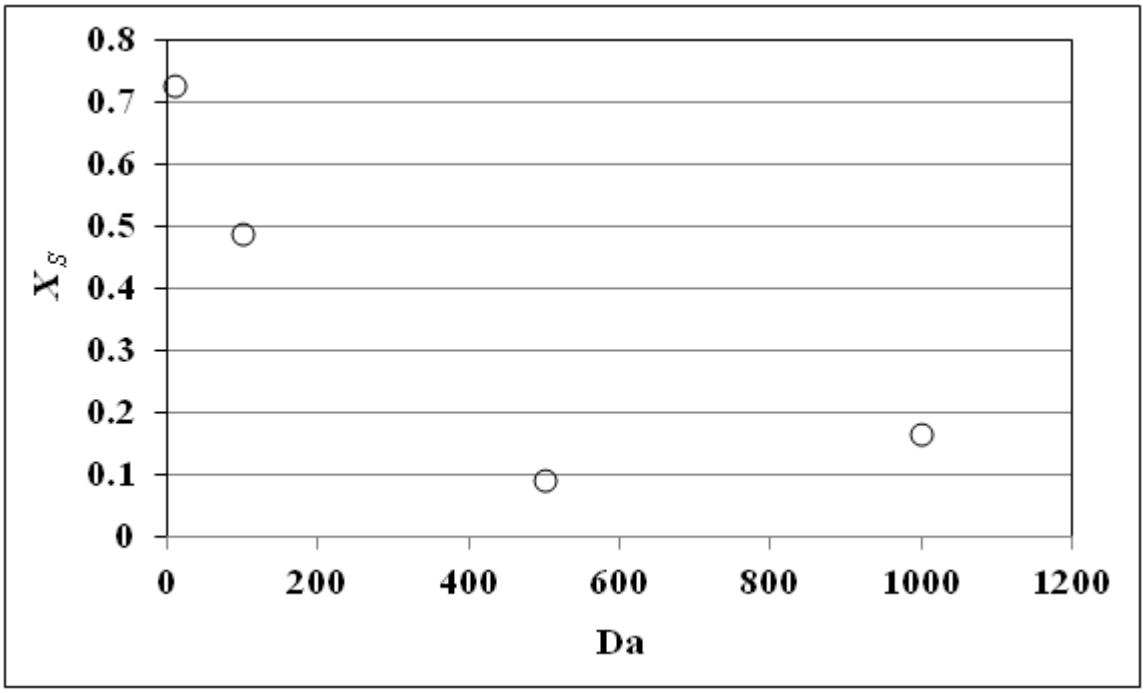

Figure 5.9 Damkholer number versus Selectivity for ratios W/w=6; with varying W/d = 1.5 at Re = 200 .

The **Figure 5.9** shows the plot of selectivity with Damkohler number for the *Re*=200. When the *Da* is increased from 100 to 500, the selectivity decreases. In this case the concentration of limiting reactants is increased from 0.008 to 0.040 mol m^{-3}. When *Da* is increased from 500 to 1000 (the concentration of limiting reactant increases from 0.040 to 0.080 mol m^{-3}) the selectivity also increases.

For the *Da* number of 100, it is observed that the selectivity at *Re* =200 is around 0.49 which is outside the range of 0.4-0.04 limit for it to be valid. Therefore for this low *Da* number the selectivity is very high even at high Reynolds number which clearly indicates that the experiments with this *Da* number could not be performed for micromixing characterisation.

Also for very high Da number the concentrations of the reactants are very high which leads to instability in the product reaction namely product *S*. So therefore it could be concluded that the optimum Da number that could be used for the experiments is Da=500 which is very close to the one used in the experiments.

5.5 T-jets Mixer Micromixing Simulation: - A 2D CFD Study

In this section the test chemical reaction is studied with the 2D CFD simulation in T-jet mixer geometry. The simplified form of the test chemical reaction with four species, which was used in the micromixing experiments, is used in the 2D CFD, see Equation (5.5) and (5.6).

In order to interpret the chemical reaction experiments and compare with the T-jet mixer model results, it is important to have reliable chemical kinetics information. The kinetic constants from the work of Nunes (2007); are being used here for the following reaction kinetics,

$$-r_A = k_1 C_A C_B \tag{5.14}$$

$$r_S = k_2 C_B C_R \tag{5.15}$$

Here the reported data are as follows $k_1 = 18824 \times 10^3 m^3 K^{-1} mol^{-1} s^{-1}$, $k_2 = 3992 m^3 K^{-1} mol^{-1} s^{-1}$ at 25 $°C$ obtained in stopped flow reaction analyser. Since the k_1 is three orders of magnitude higher than k_2, the theoretical model predictions are found to be insensitive to modest variations in k_1 (Chang et al., 1986; Laranjeira et al., 2012) but the same cannot be said for k_2.

The test chemical reaction simulations will be used to depict the mixing mechanism and their role in chemical reaction. The main advantages in the analysis of the results from simulation of chemical reaction coupled with hydrodynamics simulation are:

- The chemical reaction is sensitive to earliness of mixing, contrary to the tracer tests that yield the same result regardless of the time at which the chemical species are contacted;
- The CFD simulation of chemical reaction enables a clear understanding of the interactions of the reactants as the products are formed in the contact regions.

The 2D CFD model of the T-jet mixer for chemical reaction and the boundary conditions are explained below.

5.5.1 **Chemical Reaction Model Description**

The T-jet mixer geometry used is a 2D model of T-jets mixer comprising of injectors connected at opposite sides of a square chamber with a closed top and an outlet which is shown in detail and explained in **Figure 4.1 (a)**. The axes of the opposite injectors are aligned and above the injectors it is formed a cavity or space with a height $h = 2$ mm. The width of the injectors, w, is 1 mm. The chamber has height of $H = 50$ mm and the width of the chamber W is 6 mm

The hydrodynamic model described earlier in the **Section 4.6** is coupled with the advection-diffusion-reaction equation for a species with chemical reaction,

$$\frac{\partial C}{\partial t} + \vec{\upsilon}\vec{\nabla}C = D_m \nabla^2 C + r \tag{5.16}$$

where C is the concentration of the chemical species, $\vec{\upsilon}$ is the velocity vector field at time t and D_m is the molecular diffusivity and r is the rate of reaction by the chemical species.

For a n order elementary chemical reaction the net rate of reaction of the chemical species is

$$r = kC^n \tag{5.17}$$

where k is specific reaction rate.

5.5.2 **Geometry and Boundary Conditions**

The simulated 2D geometry is an axial cut, passing through the centre of the injectors of the T-jet mixer. The following boundary conditions were set to the 2Dsimulation model:

At the chamber walls no slip condition are assumed i.e., both the two velocity components were set to zero at the wall, at the chamber outlet a constant and uniform pressure value was set. In the left injector, the velocity is $\vec{\upsilon} = (\upsilon_{inj}, 0)$ and in the right injector $\vec{\upsilon} = (-\upsilon_{inj}, 0)$, the injector velocity υ_{inj} is fully developed similar to hydrodynamic simulation shown in **Chapter 4**. In **Chapter 4** the injector channel was simulated, while here the fully developed velocity profile was directly set at the line of interception of the injectors with the mixing chamber. For the right injector the velocity profile is defined as

$$\vec{\upsilon}_x(z) = 6\vec{\upsilon}_{inj} \frac{\left(z - \left(h - \frac{w}{2}\right)\right)\left(z - \left(h + \frac{w}{2}\right)\right)}{w^2} \tag{5.18}$$

and for the left injector

$$\vec{\upsilon}_x(z) = -6\vec{\upsilon}_{inj} \frac{\left(z - \left(h - \frac{w}{2}\right)\right)\left(z - \left(h + \frac{w}{2}\right)\right)}{w^2} \tag{5.19}$$

where $\bar{\upsilon}_{inj}$ is the average velocity at the injectors, w is the width of the injector, h is the distance of the injectors centre to the top of the chamber where $z = 0$. The z velocity component is zero at both injectors. The boundary conditions for the mass transfer are represented in term of diffusivity coefficients, D_m, and mass fluxes and concentration of the chemical species. At the boundaries of the chamber interior, the walls, the injectors and the outlet, D_m are set to zero. The mass fluxes are set to zero at the chamber walls. In this simulation the fluid D_m was set to $1 \times 10^{-9} m^2 s^{-1}$.

5.5.3 **Initial Conditions**

In the chemical reaction simulation, volumetric reaction was set for both steady and transient simulation. In the steady state simulation except for the flow equation, a converged solution was obtained with residuals equal to 10^{-4} for all the species involved including the energy equation. The converged solution residuals were also set to 10^{-4} for the flow equations involving x and y velocities components.

The converged solution from steady state was the starting point for the transient chemical reaction simulation including the flow equation. As per the absolute convergence criteria all the residuals involved in transient simulation were set to 10^{-6}.

The solution method was Pressure-Velocity coupling with Coupled scheme for steady state simulations in order to obtain fast convergence. Then the PISO scheme was used for the transient simulation. The spatial discretization gradient was Least Squares Cell based, pressure gradient was Second order for steady state and transient state, the spatial discretization momentum and energy discretization was set as Third Order MUSCL. For the transient simulations, a second order implicit formulation was used.

The dynamic simulations were started from the steady state solution applying a non-symmetric perturbation .i.e. the velocity of the right injector was varied with time as $\upsilon_x(z,t^*)=\upsilon_x(z)f(t^*)$, where $f(t^*)$ is the perturbation time function affecting the steady velocity profile and t^* is defined as $t^*=\bar{\upsilon}_{inj}t/w$. In order that there is no discontinuity in the flow field, a smooth time function with a continuous first order derivative was chosen,

$$f(t^*)=1+\frac{a}{2}(1-u(t^*-b))\left(1-\cos(\frac{2\pi t^*}{b})\right) \tag{5.20}$$

Where $u(t^*-b)$ is the Heaviside function. The parameter a is the maximum amplitude of the perturbation which in this case was set to $a=0.1$. The value of b is the time over which the perturbation is applied to the velocity profile of the right injector and was set to a tenth of the fluid passage time in the mixing chamber which is defined as the,

$$\tau = DH / 2\bar{\upsilon}_{inj} w \tag{5.21}$$

This perturbation has a limited impact in time and small amplitude when compared to the $\bar{\upsilon}_{inj}$ with a maximum value of $0.1\bar{\upsilon}_{inj}$. After the initial $0.1\,\tau$ no further perturbation is imposed to any of the system variables, and the boundary conditions remained constant in time. The influence of the perturbation amplitude and period on the flow dynamics was assessed by Santos et al. (2010). The perturbation has no impact on the flow dynamics after the transient period where the system evolves from the initial steady-state.

Here for the simulation, two cases with different concentration ratios were studied. Firstly, equimolar concentration ($\gamma = C_A / C_B = 1, C_A =$ 1 mol/m^3 and $C_B =$ 1 mol/m^3) and then with an initial concentration ratio of 1.2 ($\gamma = C_A / C_B = 1.2, C_A = 0.720$ mol/m^3 and $C_B = 0.6$ mol/m^3).

5.5.4 **Results**

5.5.4.1 Concentration Maps

Figure 5.10-**Figure 5.13** shows the concentration maps of the species *A*, *B*, *R* and *S* at different time instants for Reynolds number 100, 200, 400 and 600 at equimolar concentration ($\gamma = C_A / C_B = 1$).

For the initial time at *t*=0 sec, the fluid is completely segregated for all the Reynolds number studied .i.e. 100,200,400 and 600, which is shown in **Figure 5.10**, **Figure 5.11**, **Figure 5.12** and **Figure 5.13**, respectively. The jets with *A* and *B* for two streams that flow segregatedly in each side of the chamber as can be seen from the concentration maps in **Figure 5.10** to **Figure 5.13**. The product *R* is only formed in the interface between the two streams *A* and *B* downstream of the jets impingement point. The reacting zone is very thin, and *S* is only formed in the interface between *R* and *B*, because the jets are flowing fast to the outlet, $t =$ 0.5s and 0.08s for $Re = 100$ and 600 respectively. The typical reaction time to form *S* is $1/k_2 C_0 = 0.5$s, so only a small quantity of *S* is formed, which is not observable from the concentration maps in **Figure 5.10** to **Figure 5.13**.

In the upper vortices where the retention time is extremely high, the reaction completely consumes the limiting reagent *B* in each side of the mixing chamber. The transfer of the chemical species to the upper vortices is done by diffusion from the jets, therefore there is always an excess of the reagents in the side of the chamber from where each reactant it is being injected. Diffusion transfers chemical species at slow rate to the upper vortices where they get trapped. The transfer of chemical species between the vortices is also made only through diffusion, thus *A* is slowly transferred into the *B* rich vortex giving enough time for the *R* that was formed to further react with *B* to form *S*. On the other vortex, *A* rich vortex, *A* is always in excess and so almost no *S* is formed.

The dynamics and the evolution of species concentration vary depending upon the Reynolds number.

From **Figure 5.10** for $Re = 100$, it is visible that after the initial perturbation, the initial interface between the two phases is disturbed with oscillation. As the time advances the system tend to non-symmetrical steady state which differs from the initial symmetric state at *t*=0 sec. As observed, the reactants streams entering the injectors are still maintained in their respective position while flowing through the mixing chamber. The interface between *A* and *B* bends increasing the contact area, which slightly increases the formation of both *R* and *S*. Although, the convective transfer mechanisms are not clear from the maps, dragging of small quantities of one stream into the other occur. This is clear at downstream positions where some streaks of *R* and *S* are seen in the middle of *A* and *B* rich streams. In the upper vortices some increase of transfer between *A* and *B* streams is also observable from the decrease in local concentrations of *A* and *B*, while the concentrations *R* and *S* raised.

The simulation for $Re = 100$ after the perturbation of the systems exhibits some transient flow patterns with back flow, which increases the contact time between species, and so for a short period the concentration of *S* increases. When the system stabilizes again, backflow engulfing the two streams disappears and the contact times decrease to values small for significant *S* formation to occur.

As the Reynolds number is increased to $Re = 200$ as observed in **Figure 5.11** there are formation of vortices at the downstream, and the reactants *A* and *B* entering the mixing

chamber from their jets are not anymore in their respective position as seen for $Re = 100$, interface moves across each other initiating mixing which leads to increase in the formation of species *R* and *S* as seen in the concentration map.

Figure 5.12 and **Figure 5.13** shows the concentration maps for $Re = 400$ and 600, it is clear the dramatic change in flow field from $Re = 100$ and 200, with the onset of mechanisms such as the engulfing of fluid from *A* and *B* feeding jets by vortices that are formed downstream the injectors. This flow regime, *self sustainable chaotic flow regime*, is characterized by the formation of a vortex street that was reported by Santos et al. (2005) to be the main mixing mechanism in opposed jets reactors. The engulfment of fluids rapidly homogenizes both fluid streams immediately upon impinging each other, which leads to a generalized formation of product *R* throughout the mixing chamber, as can be seen from the **Figure 5.12** and **Figure 5.13**.

Each vortex core is predominantly formed from fluid from one of the jets, while flowing throughout the mixing chamber the vortex engulfs fluid from the opposite jet homogenizing the concentration profiles. This is clear from mass transfer simulations without chemical reaction of Santos et al. (2005). The vortices that have local maxima of *B* will be the responsible for *B* formation. Increasing the Reynolds numbers the vortices become more random and so the local maxima values of *B* will decrease with Reynolds number for *chaotic flow regimes.*

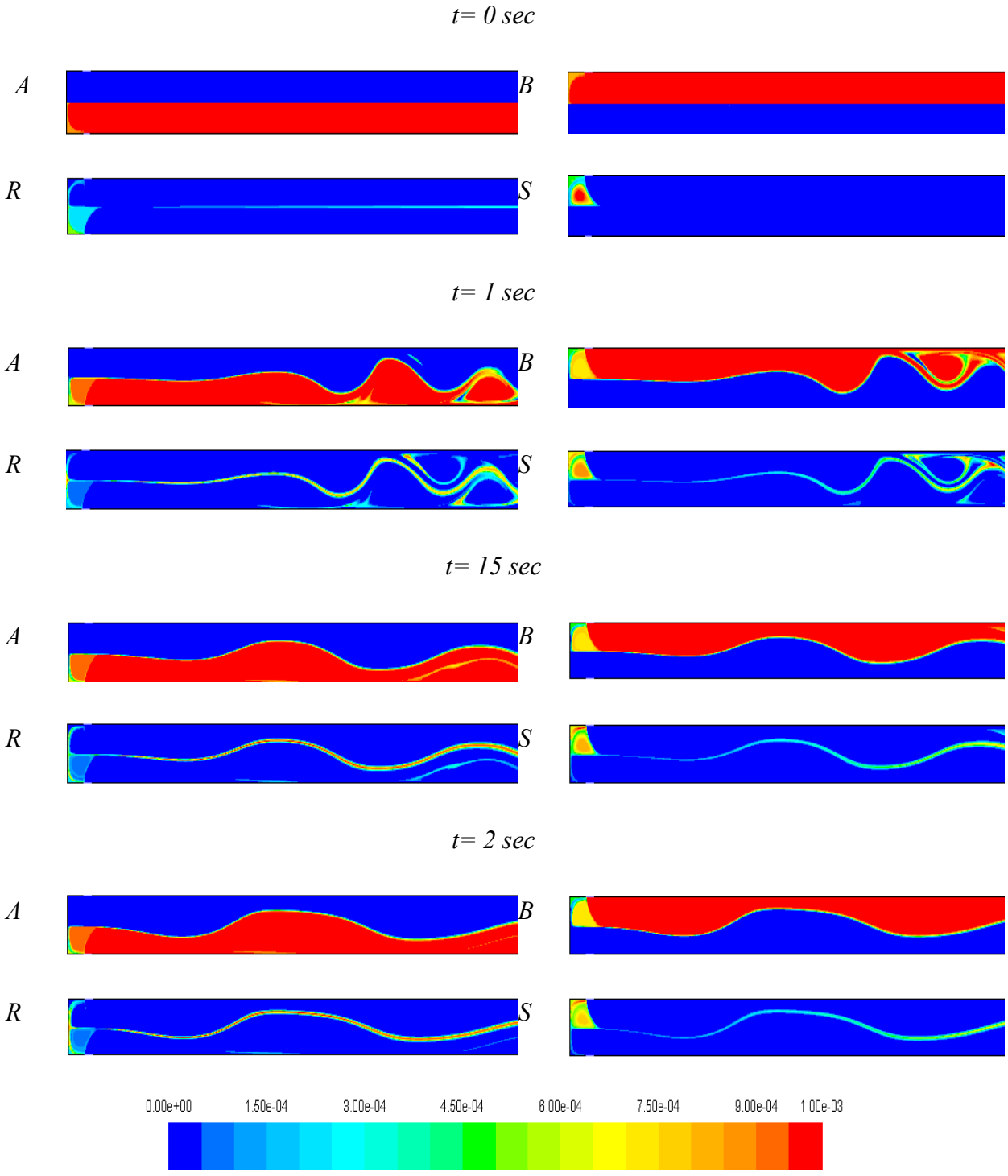

Figure 5.10 Concentration maps of *A*, *B*, *R* and *S* at t=0, 1, 15 and 2 seconds obtained for $Re = 100$.

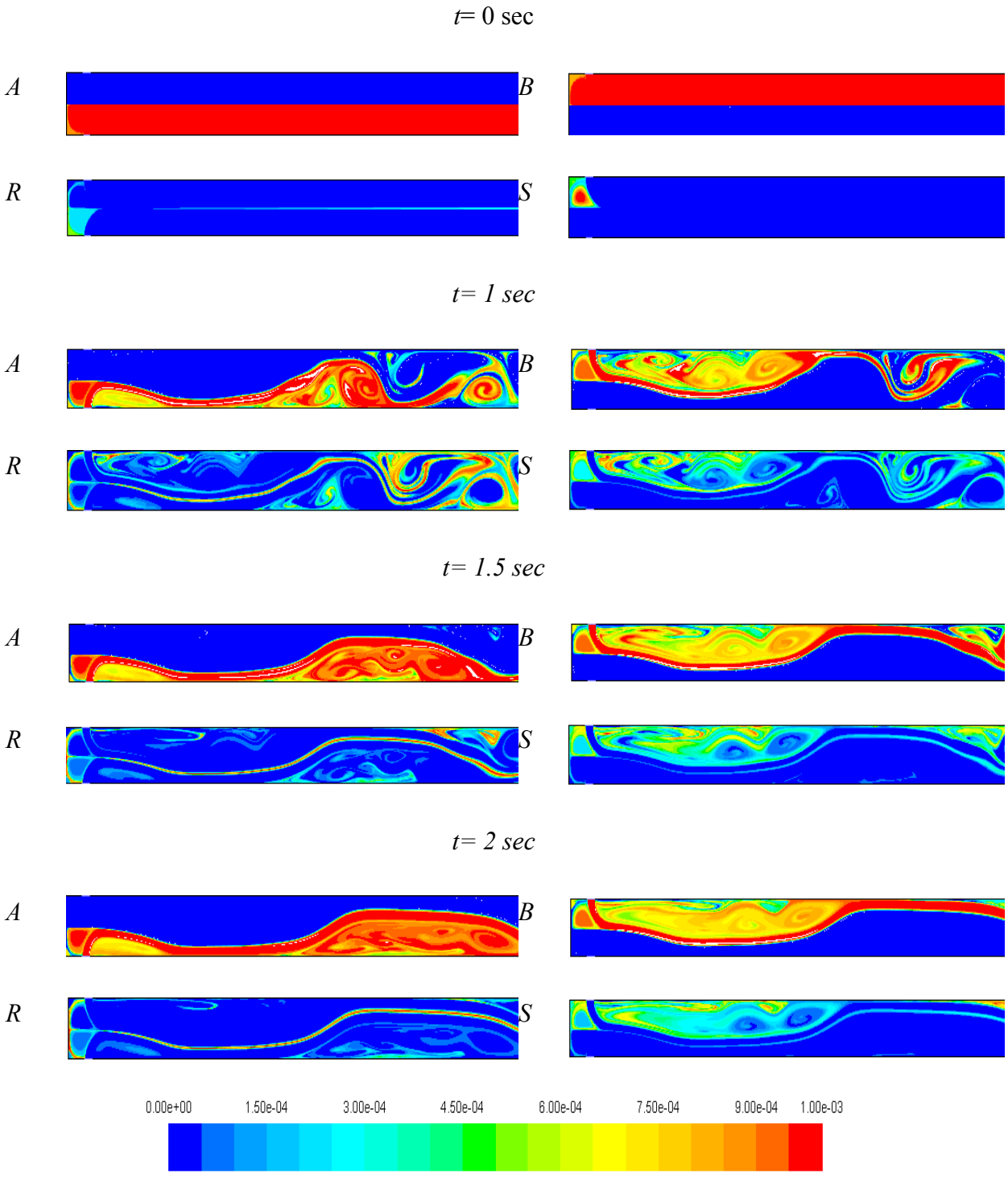

Figure 5.11 Concentration maps of *A*, *B*, *R* and *S* at *t*=0, 1, 15 and 2 seconds obtained for $Re = 200$.

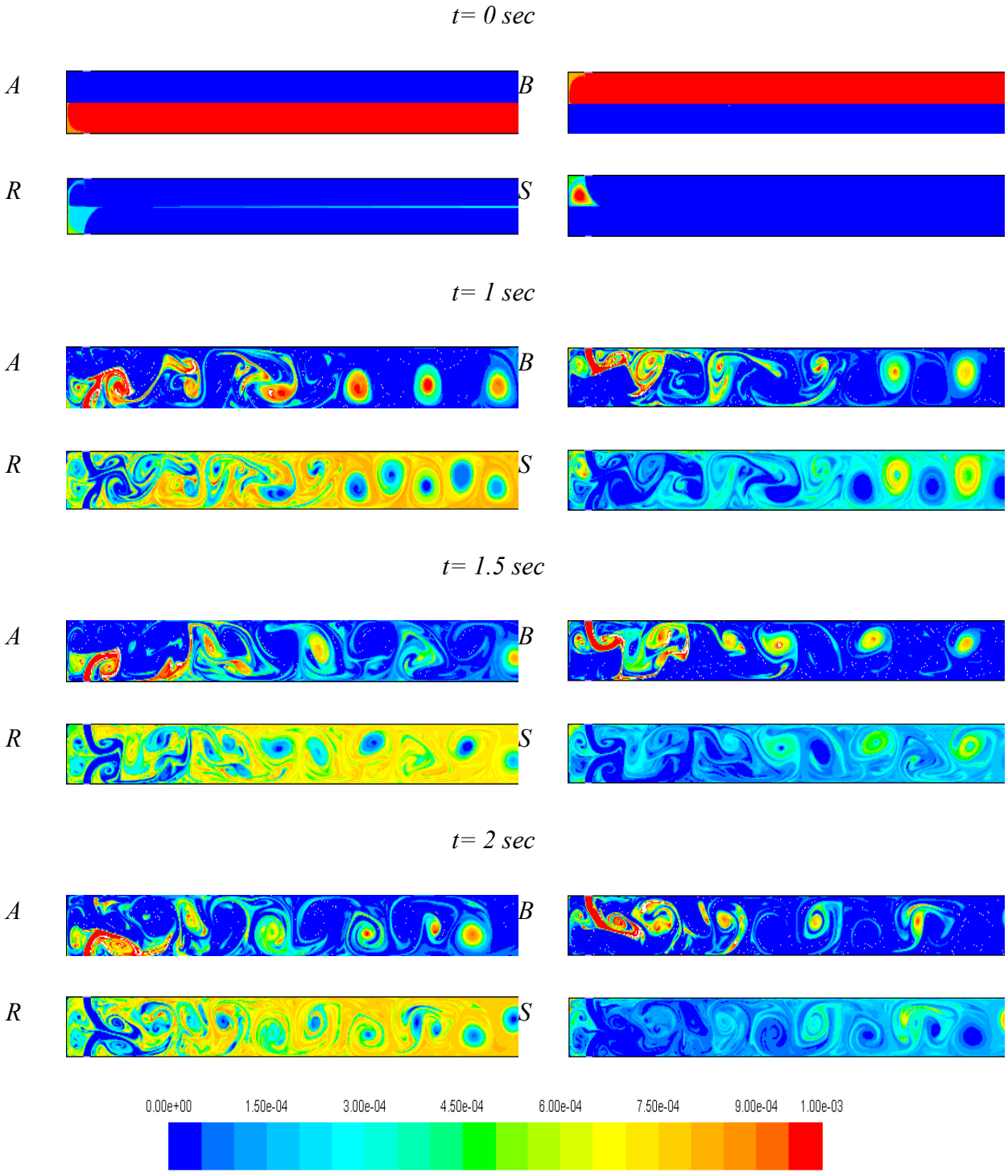

Figure 5.12 Concentration maps of *A*, *B*, *R* and *S* at t=0, 1, 15 and 2 seconds obtained for $Re = 400$.

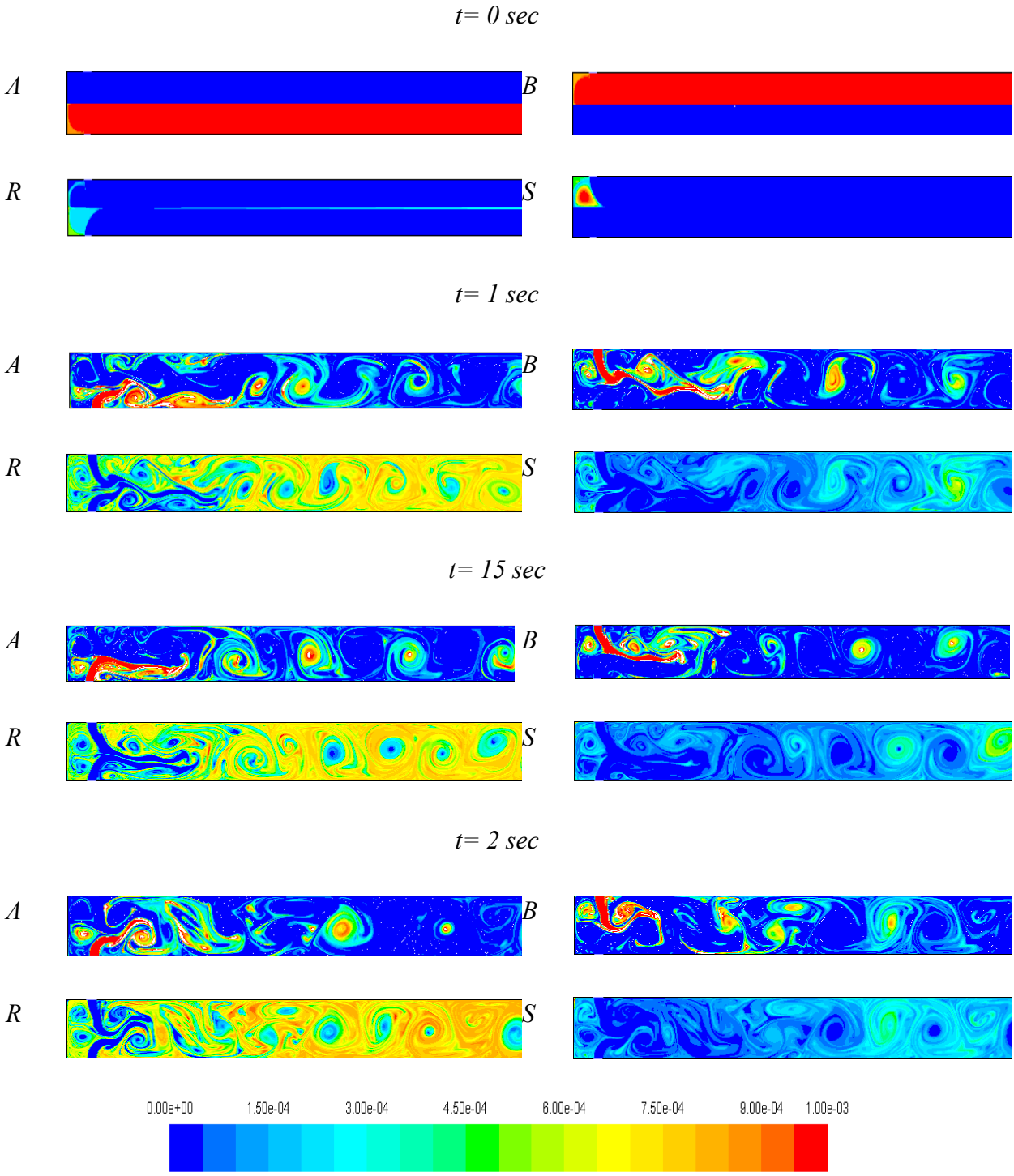

Figure 5.13 Concentration maps of *A*, *B*, *R* and *S* at t=0, 1, 15 and 2 seconds obtained for $Re = 600$.

For the $\gamma = C_A / C_B = 1.2$ similar flow characteristics were visualized therefore it is not shown here.

5.5.4.2 S Selectivity

As explained earlier when the separate reactant streams *A* and *B* are mixed, the products *R* and *S* are formed. The amount of each product formed is dependent on the mixing phenomena as a result of the simultaneous processes of diffusion and reaction which occur during this micromixing. Hence, when the product *B* is the limiting reagent, a well mixed system will form predominantly the primary product *R* and on the other hand, a poorly mixed system favours the formation of secondary product *S*. A measure of the distribution of *B* between the products is the selectivity which is defined as the amount of *B* used to form *S* to the amount of *B* used to form both *R* and *S* (or initially present *B* is the limiting reagent) therefore

$$X_S = \frac{2\overline{C_S}}{2\overline{C_S} + \overline{C_R} + \overline{C_B}} \tag{5.22}$$

where $\overline{C_R}$, $\overline{C_S}$, and $\overline{C_B}$ are the area averaged concentration of the chemical species R, S and B. Here concentration of B must be accounted for, because there is still a considerable amount of unreacted B, particularly at low Reynolds numbers. The selectivity will vary between the limits 0 and 1, $X_S \sim 0$ indicates good micromixing and $X_S \sim 1$ indicates poor micromixing. The selectivity was computed over several lines, normal to the mixing chamber axis, z=10 mm, 25 mm (centre of the mixing chamber) 30 mm, 40 mm and 50 mm (outlet of the mixing chamber) for the two concentration ratio $\gamma = C_A / C_B = 1$ and 1.2. **Figure 5.14** - **Figure 5.18** shows the effect of Reynolds number on the micromixing measured throughout the mixing chamber. The X_S was computed at $t = 2\text{s}$. For lower Reynolds numbers

From **Figure 5.14** to Figure 5.18, line *z*=10 mm to 50 mm X_S increases from $Re = 100$ to $Re = 200$. At the lower Reynolds numbers the flow regime is segregated and mixing mainly occurs by molecular diffusion and some dragging of fluid from opposite streams. So Re=100, where the viscous forces impose the more stable flow has the lowest yield in both *R* and *S*, and so X_S as its lowest values at $Re = 100$.

The trend on X_S from $Re = 200$ to $Re = 400$ it is not clear. On one had the engulfment of streams at $Re = 400$ is promoting chemical reaction and thus *S* formation. On the other hand some recirculation zones at $Re = 200$, where the fluid gets stuck and promotes the local occurrence of *S*, such is the case of line at *z*=10 mm and 25 mm.

From $Re = 400$ to 600 the generalised increase in flow dynamics decrease the stability of the segregation islands rich in *B*, the vortex cores, and so the X_S decreases slightly.

In micromixing study it is a requirement that at the moment of sample collection the limiting reactant, *B*, is fully consumed $(C_{B0} = 0)$, otherwise it is not assured that the reaction has stopped. Here the reaction, particularly for lower Reynolds numbers, $Re = 100$ and 200, would proceed in the sample collecting system where mixing is not controlled, and so the measure values of X_S would be greater than for $Re = 400$ and 600.

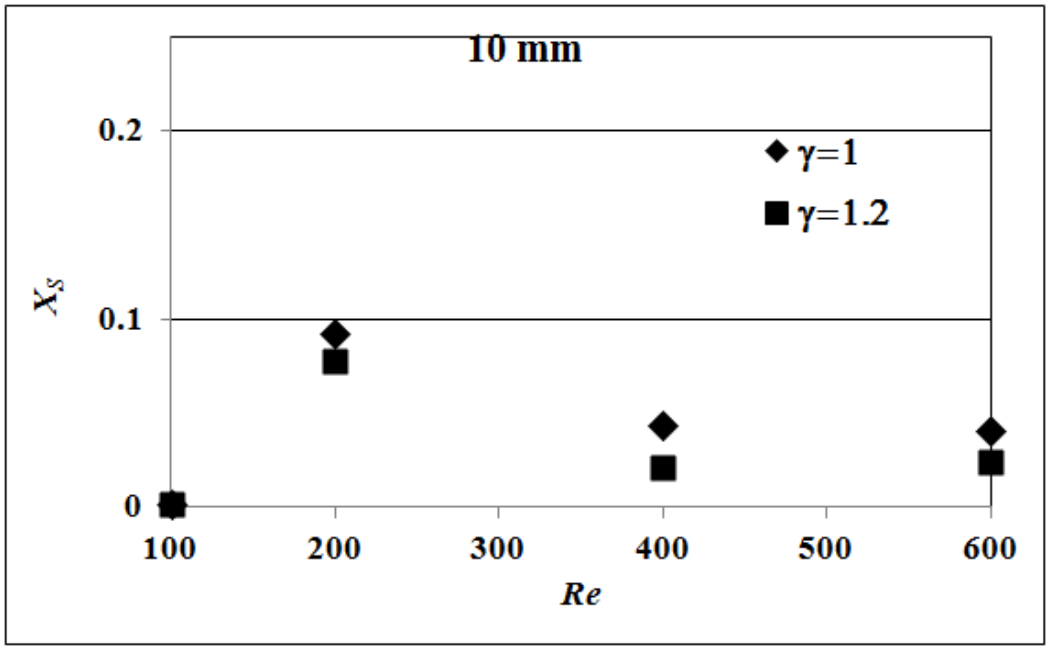

Figure 5.14 Selectivity versus different Reynolds number computed at the 10 mm for different ratios.

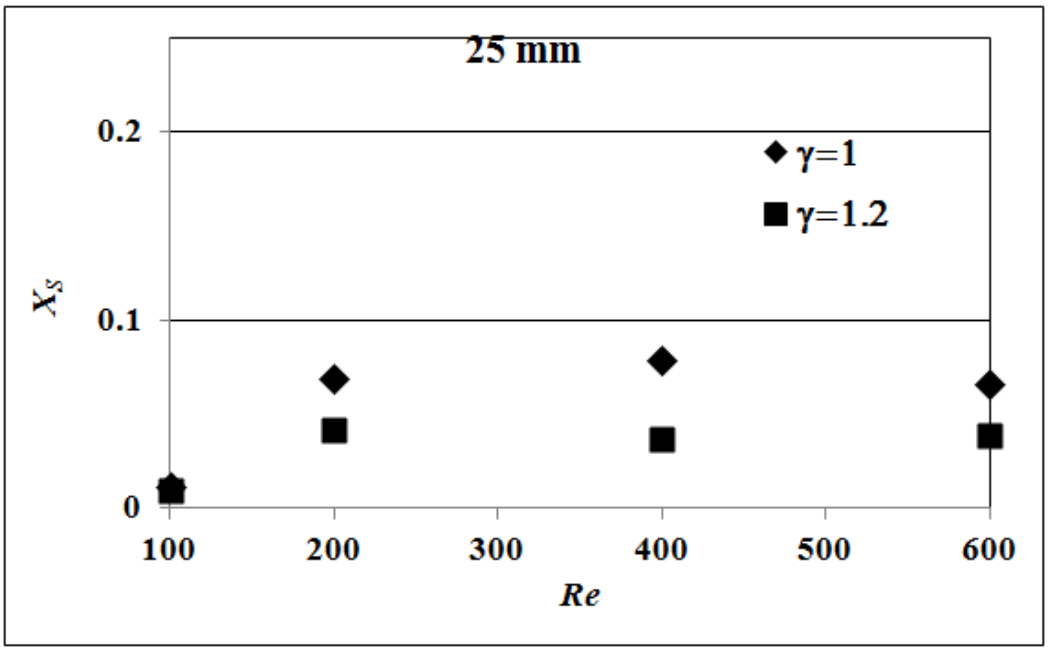

Figure 5.15 Selectivity versus different Reynolds number computed at the 25 mm for different ratios.

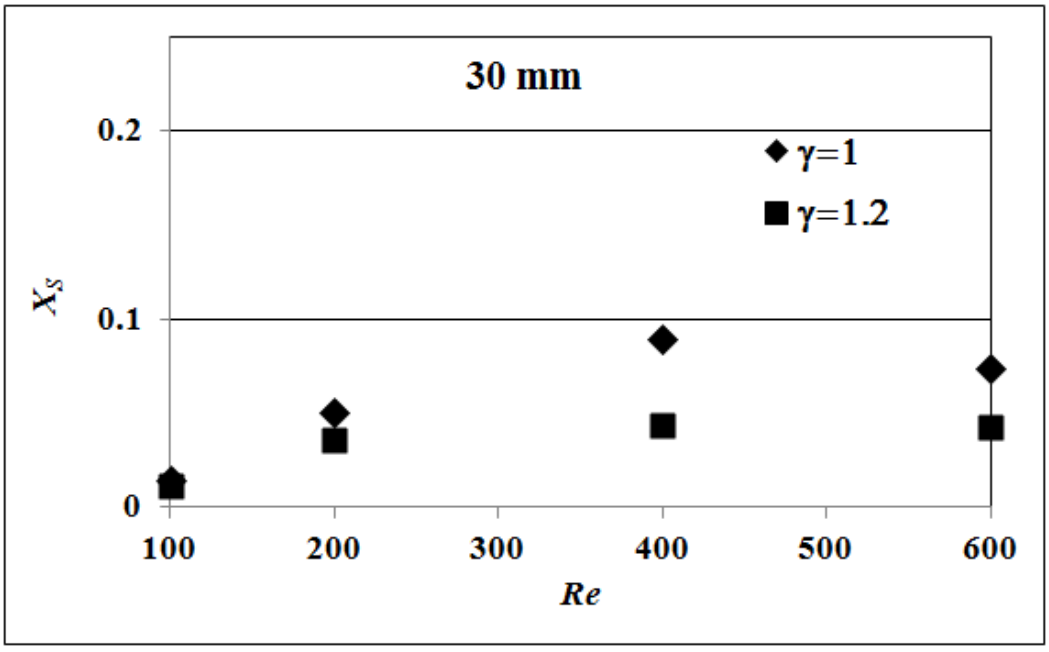

Figure 5.16 Selectivity versus different Reynolds number computed at the 30 mm for different ratios.

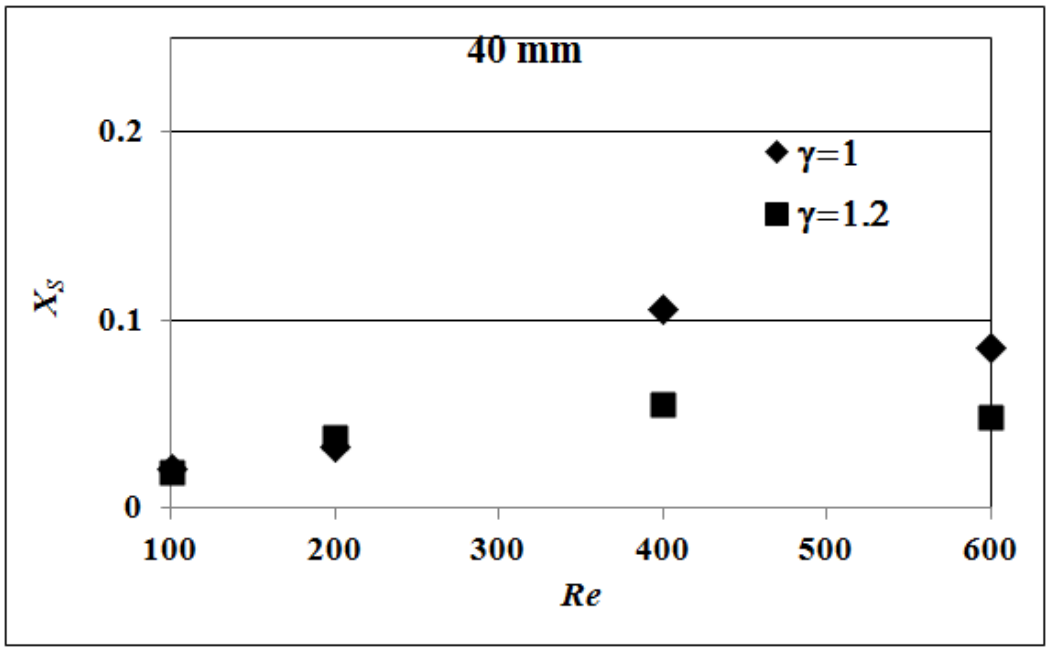

Figure 5.17 Selectivity versus different Reynolds number computed at the 40 mm outlet for different ratios.

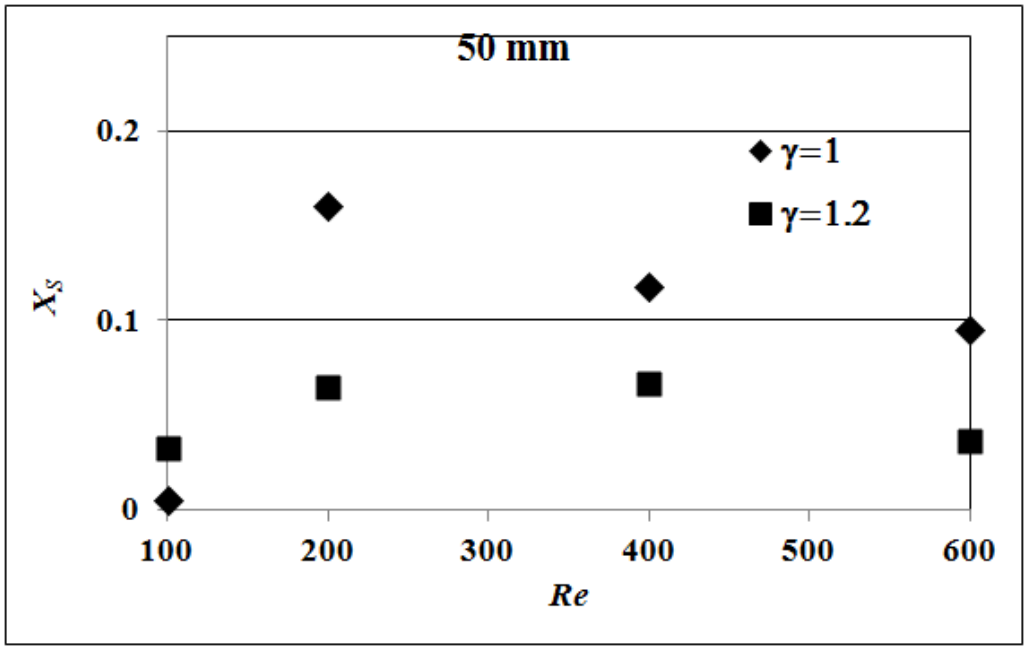

Figure 5.18 Selectivity versus different Reynolds number computed at the 50 mm (outlet) for different ratios.

5.6 Conclusion

In this chapter, micromixing in T-jets mixers was studied with a consecutive competitive test chemical reaction introduced by Bourne (1984). The product distribution of azo-coupling fast

consecutive competitive reaction system, is strongly dependent on the mixing intensity, hence the selectivity in the product *S* was used to assess the mixing in T-jets mixer with chemical reaction.

Initially the experiments, to determine the product distribution at the outlet for all the eight T-jets mixer was carried out at different Reynolds number. Similar to the PLIF experiments with the tracer, it was observed in the micromixing experiments namely the test reaction the effect of the geometrical parameters such as chambers width to the depth ratio (W/d) and the chambers width to the injector's width ratio (W/w) plays an important role in the mixing phenomena. The selectivity of the product *S* decreases with the increase in the W/d ratio and decreases with the increase in the W/w ratio. The results obtained from the experiments indicated the influence of the Reynolds number on the micromixing. For all the geometries studied it was noticed that the increase in the Reynolds number improved the mixing quality, which in turn had effect on the overall product distribution with the decrease in the selectivity.

The effect of different reactants flow ratio on the selectivity was studied and it was shown that for good mixing it is important for the flow rate ratio to be in equilibrium in both the jets. The Damkholer number was studied, the influence of the concentration of both the reactants were tested. The Damkholer number values used in the work are very close to the ones more suited for this kind of test reaction

The T-jets mixer micromixing simulation showed the results mechanisms of formation of the secondary product, *S*, in segregated steady flow regimes, other flows with a weak dynamics of mixing and *self-sustainable chaotic flow regimes.* While in flows with weak dynamics the reaction is mainly limited by diffusion and so in the chamber zones of backflow promote the formation of *S*, for chaotic flow regime *S* is mainly formed due to the occurrence of segregation islands in the vortices cores.

5.7 References

Bourne, J.R., Kozicki, F. and Rys, P., 1981. Mixing and fast chemical reaction—I: Test reactions to determine segregation. Chemical Engineering Science, 36: 1643-1648.

Bourne, J. R., 1984. Micromixing Revisited. IChemE Symposium Series, (ISCRE 8), 797-813.

Baldyga, J., and Bourne, J. R., 1999. Turbulent Mixing and Chemical Recations. John Willey & Sons Ltd, New York.

Bourne, J. R., 1990. Kinetics of the Diazo Coupling between 1-Naftol and Diazotized Sulfanilic Acid. Industrial and Engineering Chemistry Research, 29, 1761-1765.

Bourne, J. R., O.M. Lenzner, J., Maire, H., 1990a. 1-Naftol and Diazotized Sulfanilic Acid. Industrial and Engineering Chemistry Research (ACS Publications), 1761-1765.

Bourne, J. R., O.M. Lenzner, J., 1992. An improved Recation System to Investigate Micromixing in High-Intensity Mixers. Industrial and Engineering Chemistry Research, 31, 949-958.

Chang, L. J., Mehta, R.V., Tarbell, J.M., 1986. Evaluation of Models of Mixing and Chameical reaction with Turbulence Analogy. Chemical Engineering Communications, 42, 139-155.

Demyanovuch, R.J., and Bourne, J. R., O.M. Lenzner, J., 1989. Rapid Micromixing by the Impingement of Thin Liquid Sheets.2. Mixing study. Industrial and Engineering Chemistry Research, 28, 830-839.

Erkoc, E., Santos, R.J., Nunes, M.I., Dias, M.M., Lopes, J.C.B., 2007. Mixing dynamics control in RIM machines. Chemical Engineering Science 62, 5276-5281.

Laranjeira, P., Martins, A., Nunes, M., Lopes, J.C.B., Dias, M.M., 2011. A NetMix®, a New Type of Static Mixer: Experimental Characterization and Model Validation. AIChE Journal, 57, 1020-1032.

Lenzner, J., 1991. Der Einsatz rascher, kompetitiver Reaktionen zur Untersuchung von Mischeinrichtungen, PhD. Thesis, Dipl. Chem. Ing. ETH, Switzerland.

Lopes, J.C.B., Santos, R.J., Teixeira, A.M., Costa, M.R.P.F.N., 2005. Production Process of Plastic Parts by Reaction Injection Moulding, and Related Head Device. World Intellectual Property Organization, International Publication number WO 2005/097477.

Nunes, M.I., 2007. Micromixing in Chemical Recators-Test Reactions. PhD. Dissertations, Porto.

Nunes, M.I., Santos, R.J., Dias, M.M., Lopes, J.C.B., 2012. Micromixing assessmentof confined impinging jet mixers used in RIM. Chemical Engineering Science, 74, 276-286.

Santos, R.J., Teixeira, A.M.T., Lopes, J.C.B., 2005. Study of mixing and chemical reaction in RIM. Chemical Engineering Science 60, 2381–2398.

Santos, R.J., Teixeira, A.M.T., Ertugrul, E., Sultan, M.A., Karpinska, A.M., Dias, M.M., Lopes, J.C.B. 2010.Validation of a 2D CFD Model for Hydrodynamics Studies in CIJ Mixers. International Journal of Chemical Reactor Engineering 8 (A32).

Teixeira, A. M., Santos, R.J., Costa, M. R. P. F. N., Lopes, J.C.B., 2005. Hydrodynamics of the Mixing Head in RIM: LDA Flow-Field Characterisation. AIChE Journal, 51(6), 1608-1619.

Wenger, K.S., Dunlop, E.H., MacGilp, I.D., 1992. Investigation of the Chemistry of a Diazo Micromixing Test reaction. AIChE Journal, 38, 1105-1114.

6. FINAL REMARKS

6.1 Introduction

The main goal of this work is the introduction of large throughput micro/mini T-jets mixers. This chapter start with an analysis of the contribution of this thesis towards T-jets scale-up. After, the main conclusions from this thesis are summarized, and last suggestions of future work to address issues not yet solved from this thesis are made.

6.2 T-jets scale-up

With the knowledge obtained from this study it is possible to introduce a new class of T-jets mixer with a capacity far beyond the current state-of-the-art. Currently the scale-up of microreactors is based on numbering-up of micro devices in order to retain the benefits associated with small-scale processing Hessel et al. (2003) because the reactors geometry and flow regime will change the final product. The required increase in production capacity is thus based on a micro-reactor concept, numbering-up, where the number of reactors or network elements is increased, which means that the flow has to be distributed over large arrays of mixing units. Numbering-up is the current state-of-the-art solution for the implementation of continuous processes, but sometimes it has been proven impractical. Clearly scale-up is not an easy issue for nanoproduct processing, and so this work explores a solution that goes beyond

the state-of-the-art. This is achieved with increasing a non-critical dimension for mixing, in this case the mixer depth, d. This approach is a new concept, surpassing the current state-of-the-art in micro mixers, and has the major advantage of empowering a single unit with the ability to deliver large throughputs, thus reducing the complexity arising from the flow distribution over an array of devices and significantly decreasing the head loss. This new scale-up route does not affect micromixing and thus has the potential to ensure a rapid transition into industrial processes. The only potential limitation to this approach is the capacity of the accessory equipment such as the feeding pumps.

The throughput of the T-jets mixers used in this work is compared to other works in **Table 6.1**. The throughput, q, of the reactors is calculated assuming Reynolds number 300, according to the definition of Equation (3.1) in **Chapter 3**, and normalized by the injectors width, q_{inj} / w, so the results will not be influenced towards the larger T-jets mixers. The geometries yielding q_{inj} / w above 100 mL min^{-1} mm^{-1} were shaded in **Table 6.1**.

The scale-up concept introduced in this paper for T-jets mixers is the increase of the depth while keeping the other dimensions that have a direct impact in mixing, the increase on depth is calculated from

$$\frac{d_2}{d_1} = \frac{q_2}{q_1} \tag{6.1}$$

Where d_1 and d_2 are the T-jets depth, and q_1 and q_2 are the flow rates.

Table 6.1.T-jets throughput from several works for Reynolds number 300 and considering water as the working fluid and geometries.

Other authors	W mm	W / w	W / d	q_{inj} ml.min^{-1}	q_{inj} / w ml. mm^{-1} min^{-1}
Gobby et al. (2001)	0.2	1	1.7	4.3	22
Wong et al. (2004)	0.2	2	2.4	3.0	30
	0.2	2	3.9	1.8	18
	0.1	4	2.0	1.8	74
	0.06	3	1.2	1.8	92
Engler et al.(2004)	0.6	2	2	11	36
Hoffmann et al. (2006)	0.4	2	2	3.6	36
	0.4	2	2	7.2	36
	0.4	2	4	7.2	36
	0.4	2	4	3.6	18
	0.4	4	4	3.6	18
Ito and Komori (2006)	0.5	0.5	1.0	18	18
	0.5	0.5	1.0	18	18
	0.1	0.1	1.0	3.6	3.6
	0.1	0.1	1.0	3.6	3.6
	0.1	0.1	1.0	3.6	3.6
Soleymani et al. (2008)	1.6	4	5.3	11	27
	1	2	3.3	11	22
	0.2	1	1	7.2	36
	0.3	1	1	11	36
	0.1	1	1	3.6	36
	0.2	1	2	3.6	18
	0.8	2	2	14	36
Bothe et al. (2008)	0.2	2	2	3.6	36
Adeosum and Lawal (2009)	0.2	1	1.6	4.5	23
Roudgar et al. (2012)	0.2	2	2.0	1.8	18
This work	6	6	1	216	216
	6	6	1.5	144	144
	6	6	2	108	108
	6	6	3	72	72
	2	1	0.5	144	72
	2	2	0.5	144	144
	2	4	0.5	144	289

6.3 General Conclusions

In **Chapter 2**, a review on the state-of-the-art of mixing in the T-jets mixers was provided. From the published work, the importance of the operational parameters and geometrical parameters to characterize the different flow regimes was summarized from both CFD and experimental approaches.

In **Chapter 3**, the effect of geometric and operational parameters on flow dynamics and on mixing was characterized experimentally using the PLIF technique. The results obtained from these experiments were then quantified with the intensity of segregation. The experiments showed that the operational parameter namely Reynolds number and the geometrical parameters such as the ratio of mixing chamber width to the injectors width, W/w, and the ratio of mixing chamber width to the mixing chambers depth, W/d, has a clear effect on the flow dynamics and mixing performance. From this experimental approach a new flow regime, the self-sustainable chaotic flow regime, was identified. With this experimental approach, a threshold limit for the design parameters were set. The conditions for operation under a self-sustainable chaotic flow regime were set to $Re \geq 150$; $W/d \geq 2$ and $W/w = 6$. The lowest values of intensity of segregation, standing for good mixing, were obtained for the self-sustainable flow regime.

The transition Reynolds numbers from steady flow regimes to dynamic flow regimes, chaotic or engulfment, was identified for T-jets mixers with different geometries. It was shown that the transition Reynolds number increases as W/d ratio increases, i.e. deeper geometries reach dynamic flow regimes at lower Reynolds number.

In **Chapter 4**, a detailed and comprehensive study with both 2D and 3D CFD simulation on T-jets mixers was conducted.

From 2D CFD simulation, it was shown that the ratio of chamber width to the injectors width, W/w, has a clear effect on the flow dynamics and mixing performance. The flow dynamics with 2D CFD results was analysed from the time histories and respective power spectra at particular points in the mixing chamber axis: at the intersection of mixing chamber and inlet channels axes, P1, and at the middle point of the mixing chamber axis, P2. In the 2D geometries the flow patterns depending on the mixer geometry can be such as a vortex street, for wider chamber geometries, $W/w = 8$, or a rippling jet, for narrow chamber geometries,

$W/w=2$. The chamber width influences the flow dynamics, for the same W/w, the flow dynamics was higher for the $W=2$ mm chamber than for the $W=1$ mm chamber. The flow oscillations have higher amplitude for the wider chamber with the $W/w=8$ cases having a stronger flow dynamics. The 2D simulations enabled a clear visualization of the mechanisms underlying the increase of flow dynamics for larger W/w values: the inlet jets occupy a smaller fraction of the chamber width leaving room for the formation of vortices. The turbulence intensity were computed for different geometries from the x velocity time histories, and it was observed that the mixing dynamics in T-jets mixers grows exponentially with W/w ratio.

The effect of W/w on mixing was also studied with the 2D CFD model using the trajectories of discrete particles for chaotic advection analysis. It is showed that the jets in the wider mixing chamber, $W/w=8$ geometry, mix much faster than in the $W/w=2$ geometry. From these simulations it is clear that the main mechanism of mixing, the formation of engulfing vortices, does not occur when the jets width occupies most of the mixing chamber, i.e. $W/w\leq 4$.

Furthermore 3D CFD simulations were performed to study the effect of the operational parameter Reynolds number and geometrical parameters, the ratio of the mixing chamber width to the jets width, W/w and mixing chambers width to the mixing chambers depth, W/d . From the vorticity maps, self sustainable chaotic flow regime was identified in deeper and wider chambers, $W/d\geq 2$ and $W/w\geq 6$. The different flow regimes in T-jets mixers were better characterised from the 3D CFD simulations, namely the segregated, vortex, engulfment, and self sustainable flow regime. The dynamics of these flow regimes were analysed for the first time in this study from the velocity time histories and from the power spectra. Another variable used on mixing assessment was turbulence intensity. It was concluded that the deeper and wider chamber have better mixing associated to the formation of well defined vortices giving rise to chaotic flow regime. Another interesting conclusion was that there seem to be an optimal depth (d) value above which the formation of vortices is hampered and flow dynamics is affected. To study the role of hydrodynamics in the mixing in the T-jets mixer, the mass transfer equations were coupled to the 3D hydrodynamic model and the results were shown in the last section of the **Chapter 4**. From the dynamic visualization of the mass transfer simulation results the role of the vortices in mixing was clearly identified. From these tracer simulation, intensity of segregation was computed. It was shown that the

vortices which were formed in the wider and deeper mixing chamber geometries, are the main mixing mechanism in T-jets yielding lower intensity of segregation.

The **Chapter 5** of this thesis deals with the study of chemical reaction in the T-jets mixer, for this Bourne test chemical reaction was chosen. The chemical reaction results were similar to those obtained with PLIF regarding the geometrical parameters, W/w and W/d and the operational parameter Reynolds number. These results were quantified with the selectivity, which showed that the selectivity tends to decrease with decrease in W/d ratio. Also the selectivity tends to be lowest in the geometries which have chaotic flow regimes accompanied with vortices formation. The effect of different reactants flow ratio on the selectivity was studied and it was shown that unity flow rate ratio is the condition that promotes better mixing. The Damkholer number was studied for test reaction sensitivity in the T-jets mixers.

Chemical reaction was simulated in **Chapter 5** with 2D model enabling greater insight of the role of the flow structures in the T-jets mixers. The chemical reaction simulation clearly shows the role of the vortices engulfing the fluid from both jets, promoting chemical reaction at the interface of the two reactants. These vortices form when the Reynolds number is larger than 100, and the onset of this vortices coincides with a steep decrease in the selectivity of the secondary product of competitive reactions that is associated with worst local micromixing conditions.

6.4 Future Work

The background acquired through this work will be helpful to identify several important research subjects in the field of micromixing. These topic are both experimental and simulation. The suggestions are as follows:

1. The effect of feed streams pulsation on the flow dynamics in the T-jets mixer with different frequencies and amplitudes.
2. Identification of instantaneous flow field from Particle Image Velocimetry (PIV), which enables measuring the instantaneous velocity field in a plane illuminated with a laser sheet by processing of particles displacements.
3. In this work Bourne test chemical reaction coupling of the reactant 1-naphthol (*A*) and diazotized sulfanilic acid (*B*) was studied. This system was found to be slow to characterize the micromixing in high intensity devices. Faster mixers should be

assessed using faster reaction systems, particularly the one introduced by Bourne et al. (1992) and tested in the RIM machine by Nunes et al. (2012).

4. Apply T-jets mixer model on the reactive precipitation processes for nanoparitcles production.
5. The precipitation process studied could be predicted with coupling of Population Balance Model with CFD models, aiming to develop the computational tools and methods for a more robust design of the T-jets mixer.

6.5 References

Adeosun, J.T., Lawal, A., 2009. Numerical and experimental studies of mixing characteristics in a T-junction microchannel

Bothe, D., Stemich, C., Warnecke, H., 2008. Computation of scales and quality of mixing in a T-shaped microreactor. Computers & Chemical Engineering 32, 108-114.

Bourne, J. R., O.M. Lenzner, J., 1992a. An improved Recation System to Investigate Micromixing in High-Intensity Mixers. Industrial and Engineering Chemistry Research, 31, 949-958.

Engler, M., Kockmann, N., Kiefer, T., Woias, P., 2004. Numerical and experimental investigations on liquid mixing in static micromixers. Chemical Engineering Journal 101, 315-322.

Gobby, D., Angeli, P., Gavriilidis, A., 2001. Mixing characteristics of T-type microfluidic mixers. Journal of Micromechanics and Microengineering 11, 126-32.

Hessel, V., Löwe, H., 2003. Components, Plant Concepts, User Acceptance - Part I, II &III. Chemical Engineering and Technology, 26, 531.

Hoffmann, M., Schlüter, M., Räbiger, N., 2006. Experimental investigations of liquid-liquid mixing in T-shaped micro-mixers using μ-LIF and μ-PIV. Chemical Engineering Science 61, 2968–2976.

Ito, Y. and Komori, S., 2006. A vibration technique for promoting liquid mixing and reaction in a microchannel. AIChE Journal 52, 3011-3017.

Nunes, M.I., Santos, R.J., Dias, M.M., Lopes, J.C.B., 2012. Micromixing assessmentof confined impinging jet mixers used in RIM. Chemical Engineering Science, 74, 276-286.

Roudgar, M., Brunazzi, E., Galletti, C., Mauri, R., 2012. Numerical Study of Split T-Micromixers. Chemical Engineering and Technology 35, 1291–1299

Soleymani, A., Kolehmainen, E. and Turunen, I., 2008a. Numerical and experimental investigations of liquid mixing in T-type micromixers. Chemical Engineering Journal 135, S219-S228.

Wong, S.H., Ward, M.C.L., Wharton, C.W., 2004. Micro T-mixer as a rapid mixing micromixer. Sensors and Actuators B 100, 359-379.

A. BOURNE REACTION

A.1 Introduction

In this Appendix, the preparation and calculations of Bourne chemical reaction are presented including the structure, procedure, involving the preparation of reactants.

A.2 Chemicals

A.2.1 1-Naphthols (*A*)

1-Naphthols molecular formula is $C_{10}H_8O$ and its molecular weight is 144.7 is g mol^{-1}. The purity of this reactant 99+ % in this work (ACROS 12819). The structural formula of 1-naphthol is shown in **Figure A.1**.

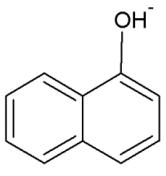

1-Naphthol

Figure A.1 Structural representation of 1-Naphthol (*A*).

1-Naphthol is readily available in the market. The reactant 1-naphthol is slightly soluble in the solvent water but readily soluble in the ethanol. Therefore it is prepared by dissolving it in a small quantity of ethanol and then with the water to prepare the reagent.

In order to prepare a 1litre solution with a concentration of 1 mol m^{-3}, 0.036 g of 1-naphthol is pre-dissolved in small quantity of ethanol (approx 10ml) and then dissolved in distilled water. The solution needs to be buffered with Na_2CO_3/ $NaHCO_3$ to a pH of 10 and so that the ionic strength is equal and maintained to a value of 444.4 mol m^{-3}, so that the product of the reactive species concentration is maximum. The solution was prepared on daily base, and stored in a glass vessel in a dark room devoid of light at room temperature.

The solution concentration of 1-naphthol was checked with UV-vis spectrum and compared with the previously reported data. In order to compare, a diluted solution of 1-naphthol (0.1 mol m^{-3}) is buffered with Na_2CO_3/ $NaHCO_3$. The maximum absorbance occurs at $\lambda max =$ 330nm as seen in **Figure A.2**, the curve obtained in this work for 1-naphthol is in good agreement with the previously published experimental data. These spectra were determined at the conditions similar to the experimental conditions at room temperature of 25 ℃. Also before conducting the experiments with the different T-jets mixers, the concentration of the 1-naphthol solution was confirmed with the spectrophotometry.

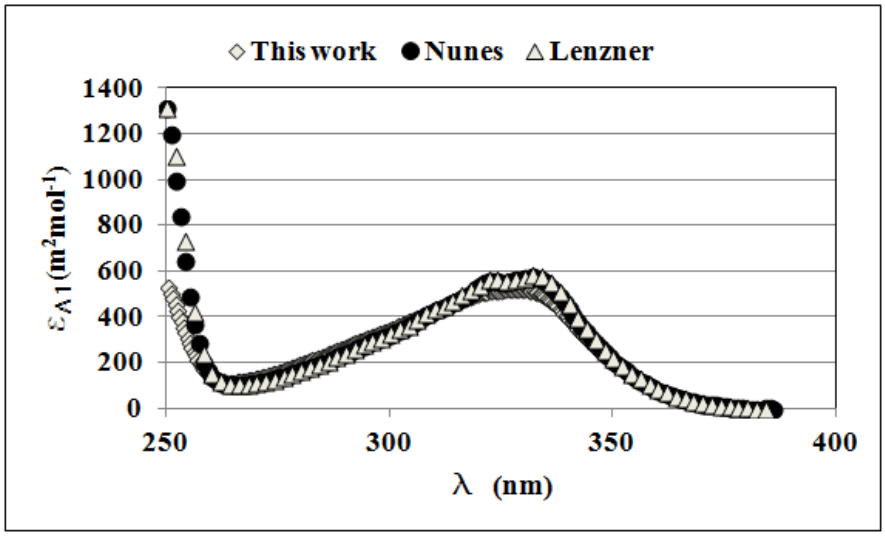

Figure A.2 Molar extinction of 1-naphthol from experimental and published data (I =444.4 Mol m-3 , pH= 10, Temp=25 °C).

The list of eight T-jets mixers used for this chemical reaction study are similar to the ones used for the flow field experimental study (see **Table 3.1**) in **Chapter 3**. The experimental

set-up is similar to the one used for flow field study, with the exception of spectrophotometer, light source and flux cell.

A.2.2 Diazotized Sulfanilic Acid (*B*)

The preparation of diazotized sulfanilic acid involves diazotization of sulfanilic acid with the purity of 99% and above (Fluka 86090). For the experiment, 1liter of diazotized sulfanilic acid with the concentration of 10 mol m^{-3} was prepared.

Diazotized sulfanilic acid solution was prepared by dissolving 0.5300 g of sodium carbonate (Na_2CO_3) in water, and then 1.7319 g of sulfanilic acid was added. A homogeneous solution was achieved through constant stirring and then it was cooled below 4℃. To this homogenous solution 0.717 g of sodium nitrate was added, in parallel a small quantity of water was used to dilute the 1.9 ml of Hydrochloric acid (HCl), 37% w/w and then cooled to a temperature below 4℃. In the burette, the solution of sulfanilic acid with sodium nitrate is introduced which is then added in drop wise in the HCl solution. A white precipitate is obtained, which is then dissolved in water (Nunes, 2007). For the experiment with T-jets mixer, a fresh solution of diazotized sulfanilic acid was prepared half day before the experiment.

A.2.3 Monoazo dye (*R*)

The product *R*, (also known as monoazo dye) is obtained from the first reaction between 1-naphthol and diazotized sulfanilic acid.

Initially, the product *R* was obtained by the addition of *B* to *A* in semi-batch conditions (using a burette). The obtained product was then analyzed with the spectrophotometer and the absorbance spectrum was calculated and compared with the previous published data.

From the reaction between 1-naphthol and diazotized sulfanilic acid, the spectrum was obtained directly. For this, 1-naphthol with the concentration of 0.06 mol m^{-3} and diazotized sulfanilic acid with the concentration of 0.05 mol m^{-3} was prepared. Then the diazotized sulfanilic acid was introduced in a burette and added drop by drop to the solution of 1-naphthol at 25 °C with intense and continuous stirring. The product obtained was assumed a 100% yield.

The product R obtained from the reaction between 1-naphthol and diazotized sulfanilic acid is present in the solution as two isomers, *o-R* (2-[4-Sulfophenyl)azo]-1-naphthol) and *p-R* (4-[4-Sulfophenyl)azo]-1-naphthol). The structural formula of *o-R* and *p-R* is shown in **Figure A.3**. From the chemical analyses it was seen that the percentage of *o-R* and *p-R* in the mixture was about 94% and 6% (Nunes, 2007) respectively.

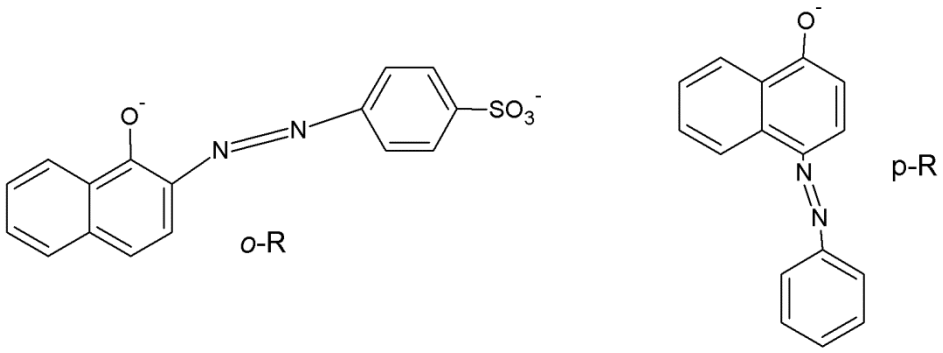

Figure A.3 Structural representation of *o-R* and *p-R*.

In this work, the need for acquiring isolate spectra for both the isomers was not necessary as the spectrum acquired for *R* was enough for the chemical reaction experiments. The absorbance spectrum of product *R* was determined and compared with the previously published spectra data. The molar extinction coefficients was determined using the Beer-Lambert law as given below

$$Abs = \delta \varepsilon C \tag{A.1}$$

where δ is the path-length, in metres, ε is the extinction coefficient in $m^2\ mol^{-1}$ and C is the concentration in mol m^{-3}.

Figure A.4 shows the curves obtained for the monoazo dye *R* to have good agreement with previous published data.

The maximum value of molar extinction coefficient obtained in this work is about $\lambda \max =$ 515 nm (see **Table A.1**). The values obtained are not much different, when compared with other work and also similar to Wenger et al. (1992).

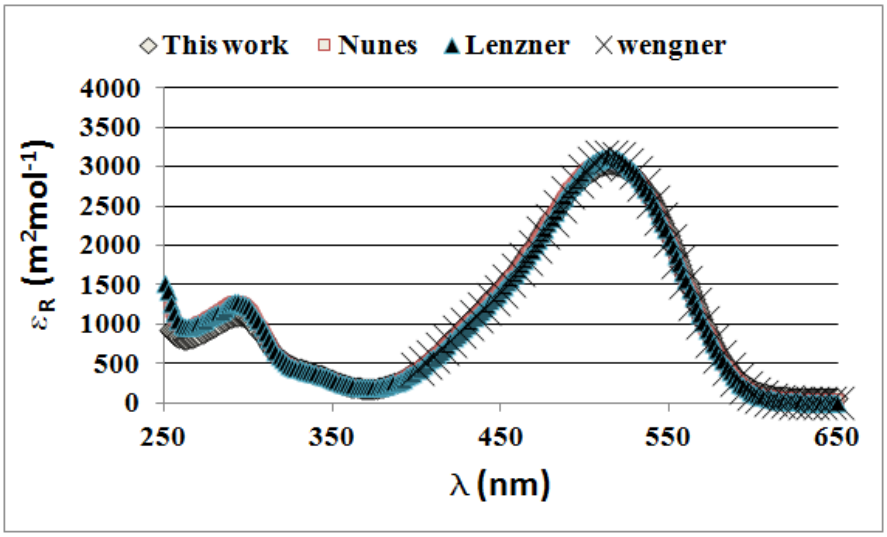

Figure A.4 Comparison between the spectra of monoazo dye *R* obtained in this and previous work at I =444.4 molm^{-3} , pH= 10, Temp=25 °C.

Table A.1 Values of λmax , obtained in this and other work

Reference	$\varepsilon_{R\max}$, m^2 mol^{-1}	λmax , nm
This work	3192	515
Nunes (2007)	3084	513
Lenzner (1991)	3123	514
Wenger et al. (1992)	3141	515

A.2.4 2,4-Bis[(Sulfophenyl)azo]-1-naphthol (*S*)

The product *S*, also known as bisazo dye, is obtained from the second reaction of the Equation (5.6) between the component *R* and *B*. This dye *R* has two isomers: *p*-*R* and *o*-*R*. The reactants *p*-*R* and *o*-*R* are readily available from previous work of Nunes (2007). The final product *S* was analyzed with spectrometer and the obtained spectrum was compared with previous published work.

Due to the slow reaction, it was difficult to predict the time at which the product *S* is formed. The spectrum *S* was obtained from the coupling reaction of *o*-*R* and *B*. The experiment involves the following step: The solution of diazotized sulfanilc acid was introduced into the burette and added dropwise into the solution of *o*-*R*. The experiments were conducted by

varying the stoichiometric ratio of *o-R* to *B* from 1 to 2 and considering *B* as the limiting reagent. The conversion of *B* was assumed total, .i.e. 100%.

Figure A.5 shows the results obtained and compared with other published data. It is observed form the plots, there is slight variations in the spectrum obtained when compared with previous data. With the plots of spectrum *S*, two maximum peaks and one minimum are observed and the wavelength at which these peaks are obtained is listed in the **Table A.2**. The results obtained from this work and previous work is not significantly different.

The results obtained from this work and previous work are similar but in order to compare the shape of the spectra, a term index of purity (see Equation (A.2)) was defined and applied with the spectra values.

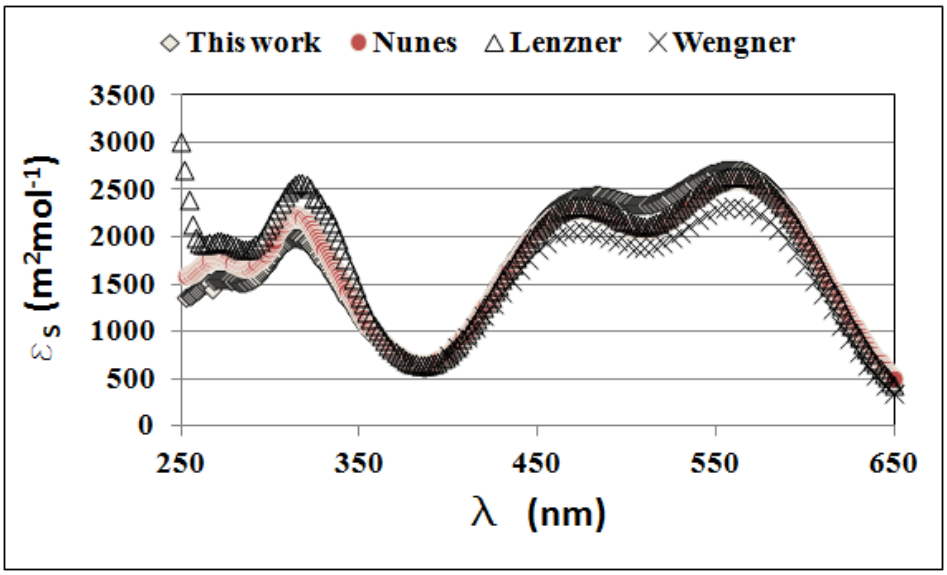

Figure A.5 Comparison between the spectra of bisazo dye obtained in this and previous work, from the coupling reaction of $o-R+B \rightarrow S$ at I =444.4 mol m^{-3}, pH=10 and Temp=25 °C.

Table A.2 Values of max and min wavelength of *S* spectra.

Reference	$\lambda_{1^{st}\ peak}$,nm	λ_{min} nm	$\lambda_{2^{nd}\ peak}$, nm
This work	475	508	557
Nunes (2007)	473	511	559
Lenzner (1991)	475	510	560
Wenger et al. (1992)	474	508	562

The $\varepsilon_{S\max}$ and $\varepsilon_{S\min}$ are the maximum and minimum extinction coefficients of product *S* as given in Equation (A.2). The **Table A.3** shows the index of purity (I_p) values for *S* calculated using the wavelength values of **Table A.2**.

$$I_p = \frac{\varepsilon_{S\max}}{\varepsilon_{S\min}} \tag{A.2}$$

Table A.3.Values of Index of Purity for product *S*.

Reference	$\varepsilon_{1^{st}\,peak} / \varepsilon_{s\min}$	$\varepsilon_{2^{nd}\,peak} / \varepsilon_{s\min}$
This work	1.04	1.07
Nunes (2007)	1.11	1.26
Lenzner (1991)	1.10	1.23
Wenger et al. (1992)	1.10	1.25

From the **Figure A.5** it was observed some variations in magnitude between the curves obtained in this work and earlier works. This variation is due the indexes of purity which is a quantitative confirmation. The age of the reactant could be the major cause for not obtaining the similar spectra for *S*.

A.3 References

Lenzner, J., 1991. Der Einsatz rascher, kompetitiver Reaktionen zur Untersuchung von Mischeinrichtungen, PhD. Thesis, Dipl. Chem. Ing. ETH, Switzerland.

Nunes, M.I., 2007. Micromixing in Chemical Recators-Test Reactions. PhD. Dissertations, Porto.

Wenger, K.S., Dunlop, E.H., MacGilp, I.D., 1992. Investigation of the Chemistry of a Diazo Micromixing Test reaction. AIChE Journal, 38, 1105-1114.

B. FLOW RATE RATIO

$W / w = 6;\ W / d = 1;\ W = 6$ mm; $w = 1$ mm; $d = 6$ mm

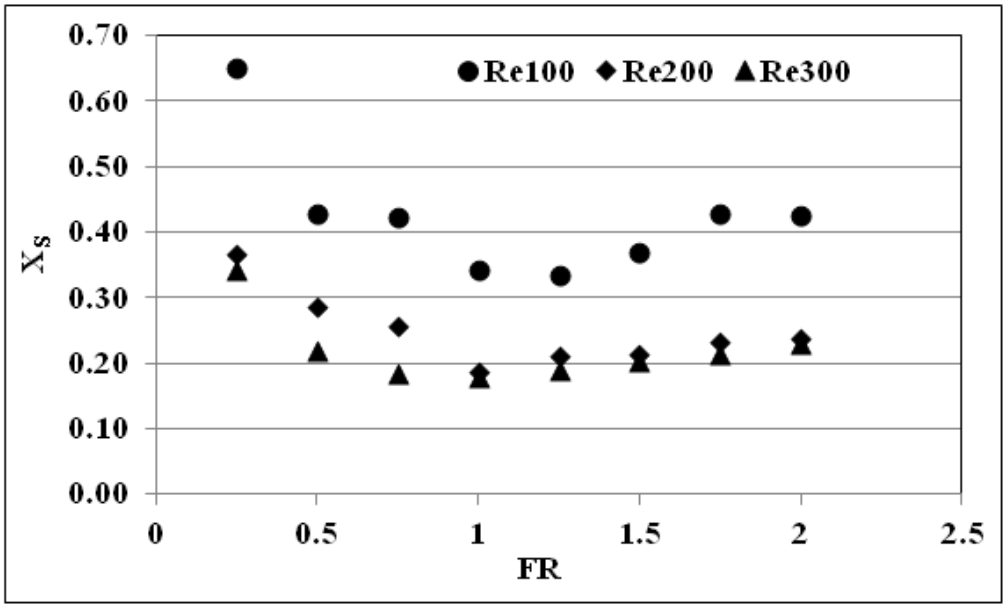

Figure B.1 Flow rate ratio versus Selectivity at Re=100, 200 and 300 for ratios $W / w = 6$ and $W / d = 1$.

$W / w = 6;\ W / d = 2;\ W = 6$ mm; $w = 1$ mm; $d = 3$ mm

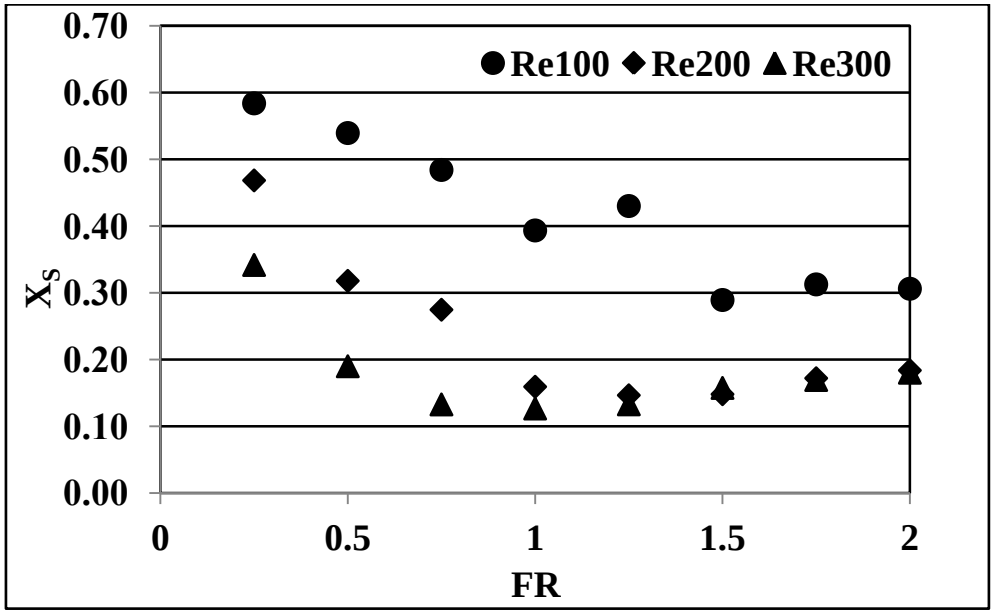

Figure B.2 Flow rate ratio versus Selectivity at Re=100, 200 and 300 for ratios $W / w = 6$ and $W / d = 2$.

$W / w = 6;\ W / d = 3;\ W = 6$ mm; $w = 1$ mm; $d = 2$ mm

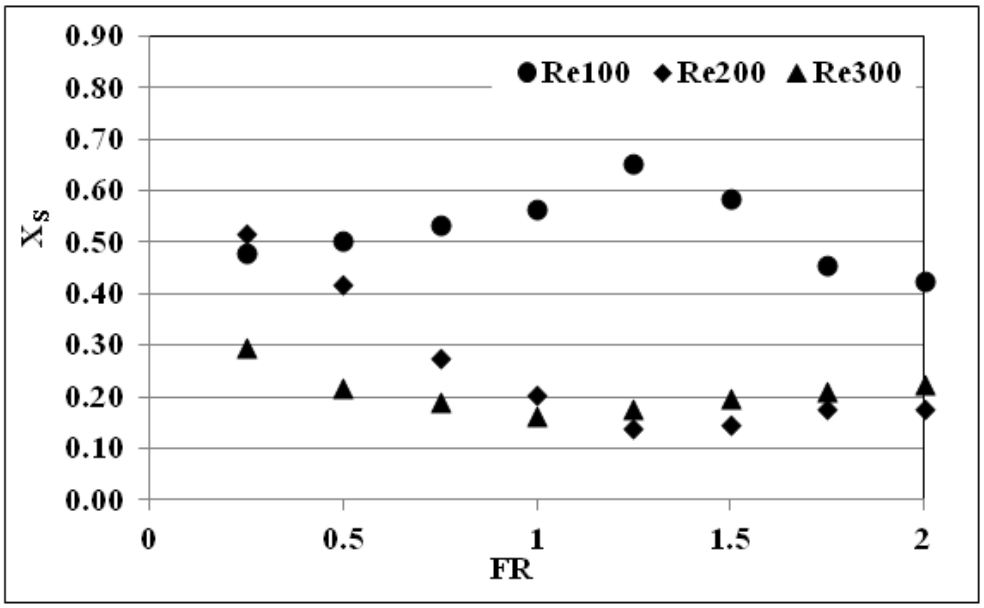

Figure B.3 Flow rate ratio versus Selectivity at Re=100, 200 and 300 for ratios $W / w = 6$ and $W / d = 3$.

$W / w = 6;\ W / d = 6;\ W = 6$ mm; $w = 1$ mm; $d = 1$ mm

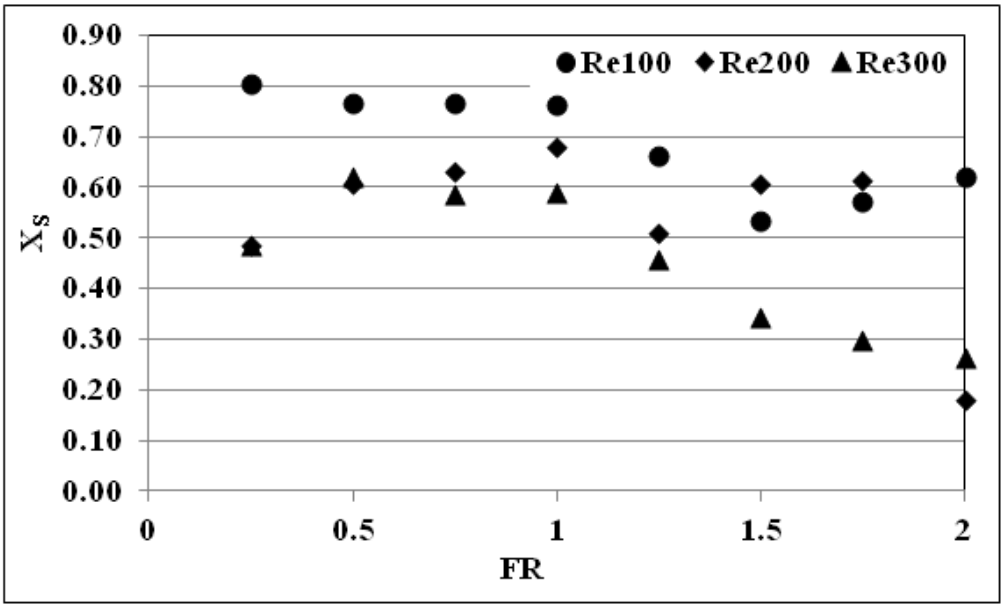

Figure B.4 Flow rate ratio versus Selectivity at Re=100, 200 and 300 for ratios $W / w = 6$ and $W / d = 6$.

$W / w = 1;\ W / d = 0.5;\ W = 2$ mm; $w = 2$ mm; $d = 4$ mm

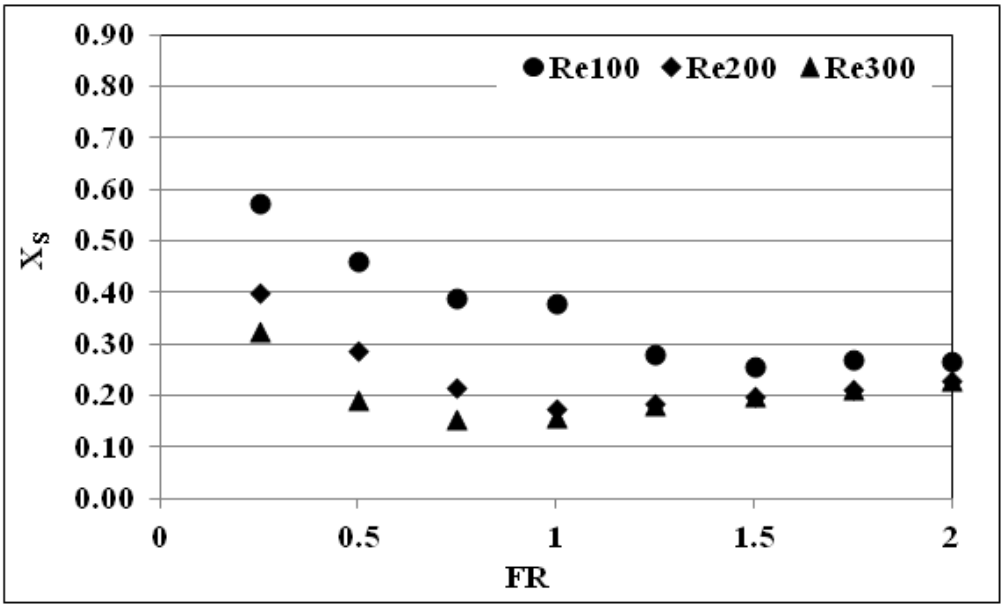

Figure B.5 Flow rate ratio versus Selectivity at Re=100, 200 and 300 for ratios $W / d = 0.5$ and $W / w = 1$.

$W / w = 2;\ W / d = 0.5;\ W = 2$ mm; $w = 1$ mm; $d = 4$ mm

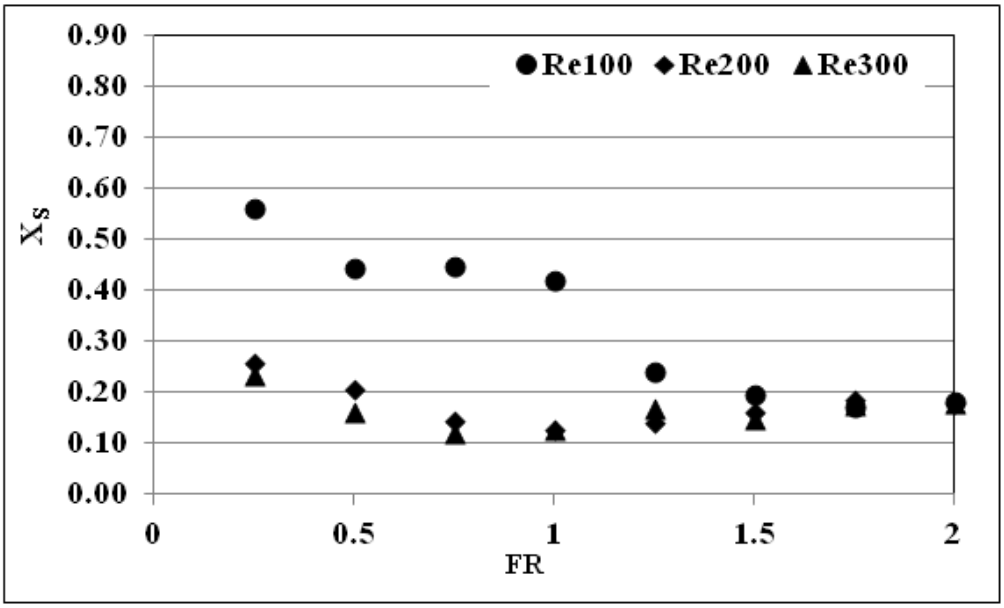

Figure B.6 Flow rate ratio versus Selectivity at Re=100, 200 and 300 for ratios $W / d = 0.5$ and $W / w = 2$.

$W / w = 4;\ W / d = 0.5;\ W = 2$ mm; $w = 0.5$ mm; $d = 4$ mm

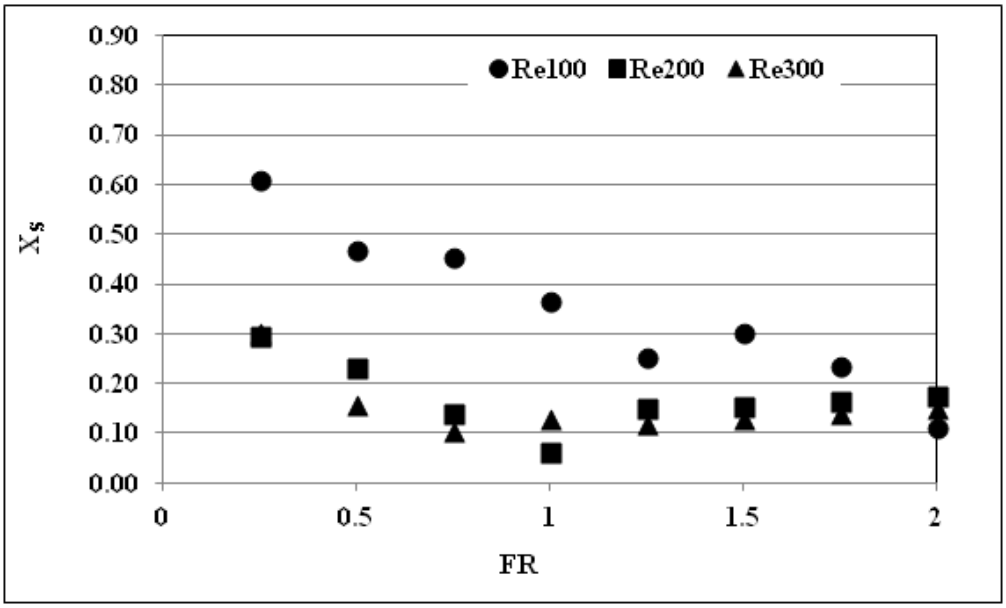

Figure B.7 Flow rate ratio versus Selectivity at Re=100, 200 and 300 for ratios $W / d = 0.5$ and $W / w = 4$.